Prediction of instability and ground movements during tunnel construction in non-homogenous conditions

by

Vasiliki Founta

Diploma in Civil Engineering
National Technical University of Athens (2011)

Master of Science in Civil and Environmental Engineering (2013)
Massachusetts Institute of Technology

Submitted to the Department of Civil and Environmental Engineering
in Partial Fulfillment of the requirements for the Degree of

Doctor of Philosophy in Civil and Environmental Engineering
at the

Massachusetts Institute of Technology
February 2018

Signature redacted

Signature of Author.....
Department of Civil and Environmental Engineering
September 15, 2017

Signature redacted

Certified by.....
Andrew J. Whittle
Professor of Civil and Environmental Engineering
Thesis Supervisor

Signature redacted

Accepted by.....
Jesse H. Kroll
Chair, Departmental Committee for Graduate Students

Prediction of instability and ground movements during tunnel construction in non-homogenous conditions

by

Vasiliki Founta

Submitted to the Department of Civil and Environmental Engineering on September 15, 2017, in Partial Fulfillment of the requirements for the Degree of Doctor of Philosophy in Civil and Environmental Engineering

Abstract

Advances in tunneling technology, notably in the widespread use of closed-face tunneling boring machines, have reduced risks and greatly increased the productivity of underground construction projects. For shallow tunnels in 'soft ground', instabilities can create collapse mechanisms that propagate to the ground surface, while the prediction and control of tunnel-induced ground deformations remain a key challenge. These problems are especially significant for 'mixed face' conditions, where the tunnel boring machine encounters soils of contrasting mechanical and/or hydraulic properties.

This thesis uses finite element simulations to investigate the control of face stability and ground deformations for shallow tunnels in soft ground. The primary control parameters of interest are the face pressures imposed by earth pressure balance (EPB) or slurry shield machines, and the grouting pressures used to control deformations around the tail void at the rear of the tunnel shield. Stability is evaluated by methods of (c-phi) strength reduction, for a range of ground conditions including i) undrained failure in low permeability clays with continuous and discontinuous (mixed face) strength profiles; and ii) drained shearing in high permeability sands above and below the water table, where the closed-face conditions at the tunnel face provide an impermeable membrane. The numerical results are synthesized into a series of generalized design charts for immediate application.

Numerical simulations using 3D finite element models are also used to investigate the factors influencing ground movements for closed-face tunneling operations using a relatively simple

elastic-perfectly plastic model of soil behavior. These analyses show that maximum surface deformations above the tunnel can be estimated by simple addition of constituent sources associated with the face pressure, shield shape (conicity), machine weight (buoyancy) and grouting pressure. The research proposes a simplified method for predicting the surface settlements based on analytical parameterization of the numerical results, enabling direct design of parameters for controlling ground deformations associated with tunneling for mixed-face conditions in clays.

The proposed methodology for predicting ground settlement has been evaluated using data from three well-documented case studies: 1) Crossrail C300 beneath Hyde Park in London, where tunnels were bored through units of stiff clay; 2) Downtown Line DTL3 (C933) in Singapore where tunnels traversed an interface between stiff Old Alluvium and overlying soft marine clays; and 3) northern sections of the MTRA Blue Line in Bangkok, where tunnels were built below the interface between soft and stiff clays. The comparisons between computed and measured data from these projects show that the proposed generic design method achieves comparable agreement to site specific numerical simulations and empirical methods such as ANN. Further studies are now needed to extend the model for mixed face conditions with contrasting permeability.

Thesis Supervisor: Andrew J. Whittle
Title: Professor of Civil and Environmental Engineering

Acknowledgments

First and foremost, I want to thank my advisor Professor Andrew Whittle for helping me to pursue my academic and career interests with his continuous guidance, persistence and support during my studies at MIT. His knowledge, integrity and sincerity enabled me to learn, grow and develop the necessary skills to succeed in this journey and the ones to come. I also want to extend my sincere thanks to Professor Herbert Einstein, Professor John Germaine and Professor John Ochsendorf who served as my thesis committee, offering valuable feedback and sharing their expertise with me during my PhD.

I am deeply grateful for the support from the MIT-Singapore Alliance for Research and Technology (SMART), the Onassis Foundation, Goldberg-Zoino and the State Scholarship Foundation of Greece. Additionally, I am particularly thankful for the help and input provided by Thiri Su in collecting the data from the DTL project and TH Seah for providing us with material for the MRTA Project in Bangkok. Lastly,

I am really grateful to Nina, Zhandos, Yixing, Eva, Ivo, Alessandra, Ilaria, Jialiang, Omar, Bing, Steven, Wei, Chunwei, Despina, and Mauro for sharing their experience and knowledge with me and creating an enjoyable and supportive environment. I also want to thank Jeanette, Kiley, Sarah and Kris for happily helping me so many times.

Then I would like to truly thank my friends Mariam, Themi, Manoli, Katerina, Theodora, Hlia, Kyriako, Afrodith, Dimitri, Sophi, Konstantina, Giorgo, Dimitri, Chara and all the members of the Marney family for making MIT feel like home. I would always cherish the time we spend together.

I want to thank my parents and my brother Vasilis for loving me, patiently supporting me and always being there for me. Finally, I want to thank my loving husband Christos for being so wonderfully calm, strong and positive, giving me a reason to smile every day.

As you set out for Ithaka
hope that your journey is a long one…
Constantine P. Cavafy

Table of Contents

List of Figures

List of Tables

List of Symbols

C	Cover depth of the tunnel
D	TBM shield diameter at the front section
D_T	Depth of the stratigraphic interface below the tunnel crown
D_{tail}	TBM shield diameter at the tail section
EPB	Earth Pressure Balance
FE	Finite Element
FEA	Finite Element Analysis
FS	Safety factor
G	Shear modulus
G_T	Shear modulus for the top clay layer
G_B	Shear modulus for the bottom clay layer
H	Depth to the tunnel springline
H_w	groundwater pressure head at the tunnel
JLE	Jubilee Line Extension Project
K	Settlement trough width parameter
K_0	Lateral earth-pressure coefficient at rest
LF	Load factor
l_{TBM}	TBM shield length
M-C	Mohr - Coulomb
N	Stability ratio
N_c	Critical stability ratio
NATM	New Austrian Tunneling Method
NLA	Numerical limit analysis method
r_G	Slurry unit weight ratio
s_{u0}	Critical undrained strength at the ground surface (FS=1) for face stability
s_{uH}	Critical undrained strength at the springline (FS=1) calculated from the face or grout stability analyses
s_{uz}	Critical undrained strength at the depth z
$\tilde{s}_{uH}$	Critical undrained strength for unsupported (i.e. σ_f or $\sigma_G = 0$) calculated from stability analyses

s_{uH}^{*}	In-situ undrained strength of the clay at the springline
$s_{u\,mob}$	Mobilized shear strength in c-phi reduction method
s_{uT}	Critical undrained strength of the top clay layer
s_{uB}	Critical undrained strength of the bottom clay layer
TBM	Tunnel boring machine
u	Water pore pressures
u_z, u_z^0	Maximum surface settlement occuring above the tunnel centerline
u_ε	Ovalization at tunnel cavity
u_δ	Uniform convergence at tunnel cavity
V_0	Initial volume of the tunnel cavity per unit length
V_L	Volume loss percentage
W_{TBM}	TBM weight [tone]
W_{soil}	Weight of the removed soil equal to the TBM volume
x	Horizontal distance from tunnel centerline
x_i	Location of the inflexion point in the settlement trough
y	Longitudinal distance along the tunnel alignment
z	Depth of interest in the ground
γ	Total unit weight of the soil
γ_{eq}	Equivalent unit weight to account for partial submersion of the tunnel face
γ_d	Dry unit weight
γ_{sat}	Saturated unit weight
$\lvert\Delta u\rvert$	Incremental displacement vectors occurring during a single calculation step
$\lvert\Delta u_{max}\rvert$	Maximum incremental displacement vector over the soil mass
Δu_z	Uniform vertical translation of tunnel cavity
ΔV_g	Volume change in the ground
ΔV_L	Volume loss at the tunnel cavity
ΔV_s	Volume of the surface settlement trough
v	Poisson's ratio
ρ	Rate of strength increase with depth

ρ_g	Mass density of the slurry
ρ_w	Mass density of water
σ_f	Face pressure at the springline level
σ_G	Grout pressure at the springline level
σ_s	Surface surcharge pressure
φ'	Friction angle
φ'_{mob}	Mobilized friction angle
ψ'	Dilation angle

1 Introduction

Tunnel construction can be very demanding due to the hazards[1] and the high costs involved. The introduction of mechanized tunnel excavation with the use of tunnel boring machines (TBMs) in 1857 by Charles Wilson alleviated the dangers associated with traditional excavations methods that relied on explosives and improved construction efficiency by automatizing soil removal and lining support installation (Hemphill, 2012). However tunneling is still a challenging endeavor even today, as it is quite difficult to control and predict tunnel deformations, especially when excavating in unstable conditions involving soft soils or multiple layers of different soil types.

Tunnel boring machines can be classified according to the support provided at the excavated face. In soft soil conditions, closed-face TBMs are preferred over open-face TBMs, as they provide continuous support and can be used in soils that are intrinsically unstable (i.e. cannot stand unsupported, Hemphill, 2012) and provide better control over the induced surface deformations which is of critical importance for urban tunneling projects.

Tunnel design in urban environments requires an accurate prediction and control of the ground deformations to minimize the impact on the overlying structures. Surface settlements in soft ground tunneling can be divided into two main categories: The first (and most important) category is short-term deformations that occur during the tunnel excavation itself. The second category involves long-term deformations due to consolidation and creep occurring after the completion of the tunnel. Figure 1.1 illustrates the main sources of short term settlements for

[1] Cave-ins, poisonous gases, fires

closed-face tunneling (Moller, 2006). An important factor that causes surface deformations as the TBM advances through the soft soil is the stress relief at the face due to soil removal (see point 1 in Figure 1.1). This is controlled by applying face pressure to the exposed boundary using either compressed air, a slurry fluid or earth paste[2] (excavated soil with hydrating agents) (slurry) or a cement-soil mixture. Moreover, additional deformations can be attributed to the conical shape of the shield[3] that overcuts the soil creating a gap between the machine and the surrounding soil boundary (see point 2 in Figure 1.1). Precast segmental lining systems are installed in-place by the machine and have an even smaller diameter. This creates a gap behind tailskin of the shield referred to as tail void, which is responsible for further deformations (see point 3 in Figure 1.1). Ground movements around the tail void are compensated injecting pressured grout. Finally, as the installed lining ring can also deform, as it carries part of the stress from the surrounding soil, introducing additional surface deformations (see point 4 in Figure 1.1).

The current methods for predicting tunnel induced ground deformations can be categorized as empirical, analytical and/or numerical. Empirical and analytical methods are usually preferred due to their simplicity and implied generality; whereas numerical methods provide site specific simulations for specific projects. Current practice uses mostly 2D numerical analyses, due to their lower computational requirements. However, it has been shown (Clough and Leca, 1989, and Swoboda and Abu-Krisha, 1999) that only 3D analyses can accurately represent the details of the tunneling procedure and capture the 3D nature of closed face tunneling.

---

[2] Slurry and earth balance shields have closed face chambers to control pressures during tunneling

[3] external steel cylindrical body of the tunnel boring machine

The main objective of this research is to understand how mechanized tunneling affects the stability and induced ground deformations in homogeneous soil conditions and also for mixed face[4] conditions which is the most typical case occurring in practice (Herrenknecht et al., , 2004). Our goal is to create a framework for predicting surface deformations that is based on a quantitative numerical analyses (3D finite element models) but can be applied in design using specified TBM control parameters (face pressure, grout pressure) and shield geometry, tunnel diameter and cover depth together with basic engineering properties of the soil profile. The methodology is based on extensive parametric studies with 3D finite element simulations involving an array of different parameters (face pressure, grout pressure, TBM properties, soil properties, subsurface stratigraphy, and tunnel geometry) examined through predictions of ground deformations and stability. The results of these analyses are summarized by a global governing equation which can be used to predict deformations by inputting the design parameters. This can help tunnel engineers mitigate adverse effects such as excessive settlements or tunnel instability.

In order to achieve this objective the thesis describes:

- tunnel face (front) stability for limiting soil conditions in high permeability sand (frictional material with drained shearing) and low permeability clay (cohesive material with undrained shearing)

- Numerical predictions of ground movements associated with mechanized tunnel construction for a variety of soil conditions ranging from homogeneous to mixed face

[4] i.e. multiple soil layers at the excavation face

conditions (where there is contrast in shear stiffness and strength occurring at the tunnel face). The predictions are based on simulations developed in prior research (Founta 2013)

- quantitative interpretation of the numerical simulations into a single predictive model for computing induced surface settlements in terms of control parameters (face and grout pressure) and tunnel geometry

- the proposed methodology is validated using monitoring data from the Mass Rapid Transit project in Singapore DTL (Su, 2015), MRTA Bangkok (Suwansawat, 2002) and Crossrail Project in London (Founta 2013, Founta and Whittle, 2016, Ieronymaki, 2015, Ieronymaki et al. , 2016)

This thesis is divided in three main parts. The first part studies face stability in sands, clays and two layered clay. The second part investigates the induced deformations in greenfield conditions (no overlying structures) due to four main factors a) face pressure, b) grout pressure, c) shield dimensions and d) machine self-weight. The third part presents a sensitivity analysis on time effects, exploring how the advance rate and the permeability of the soil can affect the computed ground deformations.

This thesis is organized in the following chapters:

Chapter 2 provides a brief review on the different available methods for construction of tunnels, focusing on two closed-face systems widely used in soft ground conditions: 1) Earth Pressure Balance (EPB) shield and 2) the slurry shield. In all closed-face tunneling systems,

stability must be maintained through controlling the pressure at the tunnel face. Existing methods for evaluating stability are examined for cases involving undrained shearing in low permeability clays and drained shear conditions in high permeability sands. We then review empirical observations and prior predictive analyses for estimating tunnel induced ground movements.

Chapter 3 describes in detail the proposed methodology for studying face stability in unlined and lined tunnels in clay using strength reduction stability analysis implemented in a 3D finite element model created using the Plaxis^{TM} software (Brinkgreve et al., 2012). The main results for the collapse load are presented as function of the construction method, tunnel geometry and soil properties. The framework for homogeneous clays is expanded to study stability for mixed face conditions where soft clay overlies a stiff clay layer. These results depend on the stratigraphic interface elevation relative to the tunnel. Further results for face stability of lined tunnels in sand have focused on the groundwater pressures and unit weight of the slurry in the face chamber.

Chapter 4 uses 3-D finite element simulations to relate ground deformations to face pressures, grout pressures, shield dimensions and TBM. The results of these parametric analyses are then assembled into a generalized predictive formulation for tunneling in homogeneous clays, through superposition of the effects of the four control parameters. This framework is expanded for mixed face conditions where a soft clay layer overlies a stiff clay layer.

Chapter 5 uses monitoring data from the Crossrail (London), Singapore DTL and Bangkok MRTA (Blue line) projects to validate the proposed methods for predicting tunnel induced ground movements.

Chapter 6 presents a sensitivity analysis on effects of partial drainage exploring how the tunnel advance rate and soil permeability can affect the ground deformations for tunnels in low permeability clays.

Chapter 7 summarizes the results of the research, the main conclusions and gives recommendations for future research.

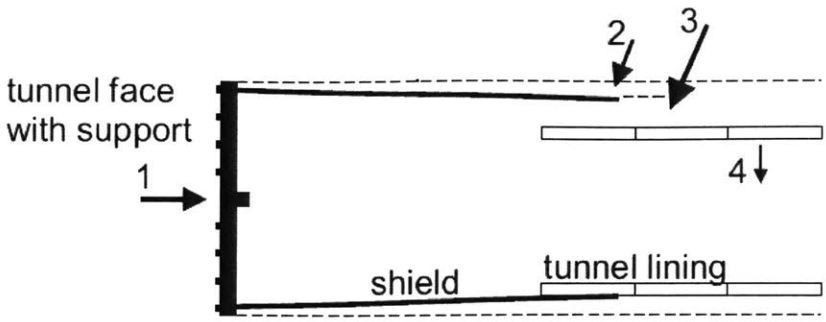

1. Stress relief at excavation face

2. Overcutting, ploughing

3. Tail void

4. Lining deformation

Figure 1.1 Source of short term ground deformations in closed face tunneling methods (after Möller, 2006)

2 Background Overview

2.1 Mechanized Shield Tunneling methods

2.1.1 Introduction

Advances in tunneling technology during recent years, notably in the design of mechanized tunnel boring machines (TBMs), have allowed the construction of tunnels with minimal disruption of the surface in urban areas where the demand for underground structures is the highest (Maidl et al., 2013). Mechanized tunnel construction with the use of TBMs has increased since its first introduction in 1857 (Hemphill, 2012) as it offers great technical and economic advantages compared to alternative excavation methods (e.g. cut and cover was used in original subway systems). Although, mechanized shield[5] tunneling could potentially replace all the other tunnel construction methods, it doesn't always represent the most cost effective or quickest construction solution. Mechanized tunneling offers advantages such as automatization, high advance rates, minimization of surface deformations (that enables construction of shallow tunnels even in low strength soil conditions below the groundwater table) and improved safety conditions. However, it also requires long set-up times for the machine and supporting equipment, the installation of costly and sophisticated facilities on site, decreased flexibility in design[6] (most equipment is limited to circular cross sections, high costs in alternating between different sections of different size) and high performance risks especially when dealing with frequently changing soil conditions (Maidl et al., 2013).

---

[5] The external steel cylindrical body of the tunnel boring machine (TBM)

[6] Crossrail project used EPBs for the construction of the subway tunnels and New Austrian tunneling method (NATM) for station caverns

Mechanized tunnel construction uses an external steel shield to support the tunnel cavity during the excavation until the permanent lining system is installed in place. The excavated material is removed from the face through the shield with the use of appropriate transport systems based on the nature of the excavated soil and the TBM type used, ranging from pumped pipes, conveyor belts, dumper trucks to rail-based systems. The shield acts both as a support for the surrounding soil and as a barrier against any groundwater present along the sides of the tunnels while the face of the excavation is either left unsupported (open face TBMs, see Figure 2.1a) or support pressure is applied using compressed air, slurry or soil mixed with additives (closed face TBMs, see Figure 2.1b). Open-face machines are suitable for stiffer soils with adequate strength to remain temporarily unsupported, while closed-face TBMs are preferred for running soils, such as silt or sand where immediate support at the face is required to avoid collapse or below groundwater to avoid water inflow (Maidl et al., 2013).

2.1.2 Open-face shield tunneling

The main feature of the open-face shield tunneling is that it provides radial support (see Figure 2.1a and Figure 2.2) for the excavated tunnel cavity, while at the same time the tunnel face (heading) remains accessible. In this way the soil stratigraphy ahead of the tunnel can be observed directly by the machine operator, allowing for a quick adjustment of the excavation sequence when needed. An open-face TBM offers the flexibility of tunneling through a range of stratigraphies with different cutting tools which would be almost impossible with a single closed face machine (Herrenknecht, 2017, Maidl et al., 1996). However, the lack of support at

the face, means that additional measures are needed in soft ground[7] and conditions below the water table to protect against excessive deformations and groundwater inflow which significantly increases the cost and complexity of the method counteracting its advantages (Herrenknecht, 2017). Open face TBMs were used for the Jubilee Line Extension (JLE) Project in London (Burland et al., 2001). The project encountered unexpectedly large ground movements which were subsequently attributed to the combination of the absence of continuous support at the excavation face and zones of low strength London clay containing water-bearing silt and sand partings[8] (Standing and Burland, 2006).

The excavation sequence for an open face shield tunnel is depicted in Figure 2.2. The cylindrical steel shield advances into the soil with the help of hydraulic jacks that push against the installed precast segmental lining (Figure 2.3). The inner diameter of the shield has to be bigger than the lining, as the curved precast concrete segments are assembled inside the tail of the TBM to form a complete circular ring. The erected lining rings emerging from the tail of the shield act as both initial and permanent support, significantly accelerating the construction process compared to traditional excavation methods (without the use of TBMs) and minimizing the ground deformations as the lining is already in place to stabilize the excavated ground when the shield advances forward. In order to reduce the radial deformations due to the gap formed between the lining and the soil (tail void), grout is injected at the tail of the shield (Moller, 2006).

---

[7] Soft ground in tunneling refers to cohesive soils, cohesionless soils and silty sands with short stand-up time (time that the excavated face is stable) that usually require continuous support during excavation

[8] i.e. layers < 0.06" (<1.6mm) (Bartlett, 2012)

2.1.3 Closed-face shield tunneling

Closed-face shield tunneling is usually preferred in urban areas, for unstable soil conditions below the groundwater table and for shallow tunnels as continuous low face support limits water inflow and controls excessive deformations (Maidl et al., 2013). There are many advantages that make closed-shield face excavation so increasingly popular: i) it provides a safer working environment, ii) it makes construction faster, iii) it decreases the overall cost for long tunnels, iv) it allows for improved continuous updating of the steering control parameters and v) it makes it possible to excavate beneath the water table (Maidl et al., 2013). However, it should mentioned that closed face TBMs can mostly accommodate circular cross-sections and may present high performance risks when used in alternating geology (excessive settlements, high cutter wear, face instability, water inflow and time delays) (Zhao et al., 2007). The most crucial aspect of tunnel design using a closed face TBM is selecting the appropriate machine type for the soil conditions present to avoid problems such as excessive settlements, slow advance rates and water inflow (Maidl et al., 2013).

Figure 2.4 shows four possible configurations of closed face tunnel boring machines. In stable soils partially mechanized support from the cutting wheel may be sufficient (Figure 2.4a). However continuous face support for unstable soils can be provided through either use of compressed air (Figure 2.4c) or sealed chambers filled with slurry mixture (slurry shield, Figure 2.4d) or the excavated soil paste mixed with lubricating additives such as foams (Earth Pressure Balance method, Figure 2.4b).

The air pressurized shield is mainly used to prevent water inflow in fine-grained[9] soils below the groundwater table that have adequate strength to stand up on their own. This method presents numerous risks for the safety of the tunneling personnel and the stability of the tunnel face as for shallow tunnels the applied pressurized air can escape through the soil mass causing a sudden collapse at the surface (Maidl et al., 2013). The EPB tunneling method is suitable for soft ground conditions ranging from clayey to silty sand soils below the groundwater table (FHWA, 2011), while the slurry shield method is suitable for water bearing silts and sands with fine gravels (FHWA, 2011). The key difference between EPB and slurry is the support medium applied at the face: a bentonite mixture for the slurry compared to the use of the excavated soil mixed with additives. The high support pressures applied for the EPB and slurry methods ensure minimal deformations at the surface. More details about these two methods are presented in sections 2.1.3.1 and 2.1.3.2.

For all methods, the TBM uses a cylindrical steel shield to carry the earth pressures and provide continuous radial support as the tunnel boring machine (TBM) advances forward. The TBM machine moves forward with the help of hydraulic jacks that push against the previous installed lining rings to advance the shield. This process inevitably creates a gap between the excavated soil and the installed precast lining rings what is referred to as tail void. Grout is injected through the lining rings (and/or shield) to infill the tail void and hence, reduces the radial displacements in the surrounding soil. In order to avoid the flow of grout inside the TBM a sealing between the shield and the last lining ring is applied (Figure 2.5).

[9] Soils with particles that are not visible with naked eye (clay,silt) exhibiting low permeability (ability of a fluid to flow in their mass)

In this study, we have developed a 3-D finite element model for simulating the performance of EPB and slurry shields in controlling face stability and tunnel induced ground movements. We present the EPB and slurry methods below and proceed to describe prior work on face stability of the methods for different soils as well as prior work on ground movement estimation.

2.1.3.1 Earth pressure balance (EPB)

The Earth Pressure Balance (EPB) closed-face shield method is commonly used in practice as it enables tunnel construction in soft and unstable ground conditions, ranging from clay to clayey and silty sand, particularly below the groundwater table. The EPB tunneling method, Figure 2.6, controls pressures with a sealed cutter head chamber filled with excavated debris (labelled (1) in Figure 2.6). Pressures are released as material is removed through the screw conveyor (3) and the shield is advanced by pushing against the previously constructed lining rings (2)(Moller, 2006, NFM Technologies, 2017). The face advance rate and chamber pressures are adjusted as the machine advances in order to control and mitigate adverse effects such as tunneling-induced ground deformations and their impacts on the overlying structures.

Additives, such as foam, are injected into the face chamber to break up pieces of soil and ensure flowability through the screw conveyor. The revolution speed of the screw conveyor extracting the soil from the chamber behind the cutting wheel and the pressure and volume of the injected additives control the pressure at the face. Talmon and Bezuijen, (2002); and Merritt and Mair, (2008) have developed theoretical models that describe the operation of a screw conveyor and relate its operational parameters to the face pressure.

2.1.3.2 Slurry shield

The closed-face slurry shield TBM enables tunnel construction in silts and sands with fine gravels below the groundwater table. The slurry shield design, Figure 2.7, controls pressures at the face by filling the head chamber (labelled (1) in Figure 2.7) with a pressurized bentonite slurry (that is supplied externally). The excavated soil is mixed into the slurry and is concurrently removed from the extracted slurry-soil mixture (6) in a separation plant so that the slurry can be reused. The applied slurry pressure is controlled by a pressurized air chamber (5) that connects to the slurry filled chamber.

Depending on the permeability of the soil and the slurry consistency there are two models that can describe the behavior of the slurry at the excavation face as shown in Figure 2.8:

1. The *membrane model* (Figure 2.8a) is applicable for low permeability soils and slurry with high bentonite content. The suspension penetrates the soil forming an impermeable mud layer (also known as a filter cake) which ensures that the face pressure will be maintained even when the slurry stops penetrating the soil further and that there will be no water inflow from the soil at the face. This impermeable membrane is formed quite quickly, in about 1–2 seconds ensuring stability of the tunnel face (Maidl et al., 2013).

2. The *penetration model* (Figure 2.8b) can occur in high permeability coarse grained soils for which the filter cake isn't formed even at high bentonite content. The penetration depth of the slurry within the soil skeleton results in reduction of the applied face pressure. This phenomenon can be remedied by an appropriate increase of the applied

face pressure to compensate for the pressure loss and/or by increasing the advance rate to decrease the penetration depth (Anagnostou and Kovari, 1996).

The formation of the filter cake is crucial for a successful application of the slurry method to ensure that the control pressure applied through the air chamber is maintained at the face.

Similarly to the EPB method the permanent support for the slurry method is applied using precast segmental linings that are erected at the tail of the TBM. The machine advances forward pushing against the erected rings while grout is injected in the gap (tail void) formed between the excavated soil and the lining to minimize the volume loss.

2.2 Face stability in tunnels

One of the most critical factors in controlling the induced settlements is to apply appropriate face pressure needed for stability of the tunnel face. When analyzing the stability of a heading we need to differentiate between frictional high permeability materials (sands) and cohesive low permeability materials (clays), as they require different methodologies to study each of them. In this work, we will examine face stability for both of those cases as well as mixed conditions where different layers of soil appear at the face of the excavation.

2.2.1 Cohesive soils (clays)

2.2.1.1 Empirical and analytical solutions

Over the years a variety of models have been developed using analytical, empirical or numerical methods to estimate the face pressure required to ensure stability for undrained tunnel excavation in cohesive low permeability materials. Broms and Bennermark, 1967 developed

one of the first empirical relationships studying the stability of a borehole (vertical shaft) in an undrained cohesive material, assuming a Tresca yield criterion:

$$\left|\frac{\sigma_1 - \sigma_3}{2}\right| \leq s_u \tag{2.1}$$

where s_u the undrained shear strength (Figure 2.9). They defined the stability number as

$$N = \frac{\sigma_s - \sigma_f + \gamma H}{s_u} \tag{2.2}$$

where σ_s the surface load, H is the depth to the tunnel axis, σ_f the face support pressure and s_u the undrained shear strength of the clay. Broms and Bennermark concluded that a stability number larger than 6 would lead to collapse, based on field observations and laboratory extrusion tests.

Davis et al, (1980) studied the stability of tunnels in clay, considering different unsupported lengths P (Figure 2.10a). For the fully unlined tunnel (P=∞) they used the plane strain model in Figure 2.10b and derived upper and lower bound plasticity solutions presented in Figure 2.11a. For the fully lined tunnel case (P=0) Davis et al, (1980) proposed two different lower bounds (Figure 2.11b) for a 3D circular tunnel heading with:

1. A cylindrical stress field:

$$N = 2 + 2\,ln(\frac{C}{R} + 1) \tag{2.3}$$

2. A spherical stress field:

$$N = 4\,ln(\frac{C}{R} + 1) \tag{2.4}$$

The solutions indicate that higher support face pressures are required for the unlined case (P=∞, Figure 2.11 higher stability number) compared to the fully lined case (P=0). The results also show the dependency of stability on the cover depth to diameter ratio, C/D, with higher ratios corresponding to deeper tunnels. Kimura and Mair, (1981) conducted an experimental study (1-g centrifuge model tests) and proposed a design line for lined tunnels in undrained conditions (P=0) which shows that the lower bound solutions by Davis et al. (1980) are conservative.

2.2.1.2 Numerical solutions

A variety of numerical methods has been developed over the years to calculate the undrained stability of tunnels in clay. In practice, the limit equilibrium method has been quite popular for the estimation of the failure load (e.g. Morgenstern and Price, 1965). However, one of the limitations of this method is the difficulty in establishing a unique safety factor. The introduction of the numerical limit analysis (NLA) method (Sloan, 1989, Lyamin and Sloan 2002a and 2002b) enables rigorous upper and lower bound solutions to be obtained numerically based on predefined undrained strength properties of the clay. NLA uses finite element interpretation methods to simulate the stress and velocity fields that are compatible with defined boundary conditions. The true collapse load is bounded by i) an upper bound solution corresponding to a kinematically admissible velocity field (which satisfies compatibility and associated flow at yield) and ii) a lower bound, statically admissible stress field solution (which satisfies equilibrium and yield criterion).

In their initial studies Sloan and Assadi, (1992) introduced the dimensionless parameter to describe stability at the tunnel face:

$$N = \frac{\sigma_s - \sigma_f}{s_{u0}} = f\left(\frac{C}{D}, \frac{\gamma D}{s_{u0}}, \frac{\rho D}{s_{u0}}\right) \quad (2.5)$$

where σ_s is the surface load, C the overburden depth, σ_f the support pressure, s_{u0} the undrained shear strength at the ground surface, and ρ, the linear rate of undrained strength increase with depth.

Recently Wilson et al., (2011) improved on the solutions for NLA for an unsupported tunnel excavation in clay using the plane stain model (Figure 2.10b). Wilson et al. 2011 examined a variety of geometries and geologies assuming the undrained strength profile increases linearly with depth and improved the accuracy of the prior Sloan and Assadi, (1992) solutions, achieving almost perfect convergence between the upper bound and the lower bound solutions, and a very good match with experimental data (Mair, 1979) as shown in Figure 2.12.

Although there is an abundance of methods studying unlined tunneling in clay, there are significantly fewer studies that consider face stability for a lined closed-face tunnel excavation in clay. The main reason is that the unlined case is readily represented in a 2D plane strain problem while the lined case requires a 3D model to accurately represent potential failure mechanisms.

Augarde et al., (2003) and Tschuchnigg et al., (2015) used plane stain models to study the lined tunnel excavation in clay (assuming P=0, Figure 2.10a). Augarde et al., (2003) studied a wide variety of geometries and soil properties using the finite element limit analysis method for

calculating upper bound and lower bound solutions which then compared to upper bound analytical solutions assuming a rigid block mechanism (Figure 2.13) and the lower bound (Eq. 2.4) analytical solutions proposed by Davis et al. (1980).

Figure 2.14 summarizes the results of the FE bound analyses in the form of dimensionless charts for selected values of the weight to strength ratio, $\gamma D/s_{u0}$ = 0, 1, 2 and 3 and strength inhomogeneity parameter $\rho D/ s_{u0}$ = 0-1.

Tschuchnigg et al, (2015) compared the upper and lower bound NLA solutions with the strength reduction method used in conjunction with displacement-based finite element method. The stress reduction method (or c-phi reduction) is widely used in practice due to its simplicity and is available with commercially available geotechnical software, such as Plaxis^{TM} (Brinkgreve et al., 2012). This method calculates the factor of safety FS by incrementally reducing the input Mohr-Coulomb strength parameters of the soil (cohesion, friction angle) until the mobilized strength reaches a value that leads to soil collapse,

$$FS = \frac{\tan\varphi'}{\tan\varphi'_{mob}} = \frac{c'}{c'_{mob}} \qquad (2.6)$$

Tschuchnigg et al., (2015) concluded that both the stress reduction method and NLA solution methods produced accurate predictions of the collapse load and are safe to use in practice. In the current research, we use the stress reduction method to study the tunnel face collapse load for a wide variety of soil conditions and tunnel geometries.

Sloan, (2013) used the NLA method to study the plane strain models (Figure 2.10a and b) as well as a 3D model of the tunnel heading for different unsupported lengths, P. Figure 2.15a

shows the developed 3D failure mechanism for the fully lined (P=0) case. It is readily apparent that a 3D model is needed to simulate the collapse mechanism.

The computed critical face pressures (σ_f/s_u) using 3D FE upper and lower bound solutions are depicted in Figure 2.15b for a variety of support lengths, (P/D). Sloan compared the results to centrifuge data by Mair, (1979) which was close to the lower bound solution but outside the upper-bound lower-bound band, which was attributed to the fact that more refined 3D adaptive limit analysis methods are still needed.

2.2.2 Frictional soils (sand)

Drained face stability problems in high permeability frictional soils have been studied extensively using theoretical, empirical, experimental and numerical methods. Leca and Domieux, (1990) developed analytical upper and lower bound solutions for lined tunnels (P=0, lined case) in frictional soils under dry conditions. Their solution considers a 3D failure mechanism with conical shaped blocks (Figure 2.16), while for the lower bound they used stress fields similar to those of Davis et al., (1980). Mollon et al., (2009, 2010) extended the kinematical method along the lines proposed by Leca and Domieux and refined the assumed failure mechanism surface by using a spatial discretization technique to achieve more realistic failure mechanisms that represent more accurately the collapse conditions. Mollon et al., (2010) upper bound solution was 25% lower than those proposed by Leca and Domieux (1990). Both upper bound solutions agreed well with centrifuge model experiments in dry homogeneous sand reported by Chambon and Corte, (1994).

Anagnostou and Kovari, (1996) used limit equilibrium analyses with a sliding wedge mechanism proposed by Horn, in 1961 (Figure 2.18) to calculate the minimum support pressure needed for stability of lined tunnel in a frictional material considering both membrane and the filtration models. As described in section 2.1.3, for the slurry shield method (commonly used with sands) we expect the formation of a filter cake at the face to ensure the applied pressure is maintained. However, in coarse soils this impermeable layer cannot always form so the slurry infiltrates into the soil (Figure 2.8). Anagnostou and Kovari, (1996) studied the effect of the slurry infiltration on face stability by considering various factors such as the advance rate, the permeability and grain size of the sand, the bentonite concertation in the slurry and the excess slurry pressure. They describe how the stabilizing force due to the applied face pressure decreases in relation to the infiltration depth. More recently, Anagnostou (2012) has refined the initial model by combining the limit equilibrium method with the method of slices to improve the estimation of vertical stresses inside the wedge (Figure 2.19) while Anagnostou and Perazzelli, (2013) studied the effect of the slurry unit weight on face stability for different friction angles (Figure 2.20).

Vermeer et al., (2002) used a 3D FE model with strength reduction (Figure 2.21a) to study tunnel heading stability for lined tunnels. They estimated the collapse load by incrementally reducing the support pressure until excessive deformations occurred at a control point shown in Figure 2.21b. The resulting collapse load at the tunnel heading for a non-cohesive soil (c=0) can be described by:

$$\frac{\sigma_f}{\gamma D} = \frac{1}{9tan\varphi} - 0.05 \text{ for } \varphi > 20^o \text{ and } H/D > 1 \qquad (2.7)$$

where φ is the internal friction angle of the soil sand.

Figure 2.22 shows that this collapse load is in good agreement with centrifuge data (Chambon and Corte, 1994) and 1-g experiments in dry homogeneous sand (Kirsch, 2010), as well as centrifuge experiments in saturated sand (Plekkenpol et al., 2006).

2.2.3 Mixed face conditions

Mixed ground conditions have always presented a challenge for tunneling engineers due to the difficulty arising when encountering two or more soil layers of contrasting shear strength, stiffness and/or hydraulic conductivity occur at the face of the tunnel excavation. It can be quite difficult to select an appropriate set of control parameters to avoid problems, such as large settlements or sinkholes. Shirlaw, (2008) reviewed seven major EPB tunneling projects in Singapore and Canada (86 km of tunneling) with 59 reported cases of sinkholes or large settlements, 21 out of which were associated with mixed face conditions and transitions from stable to unstable soils while the rest were associated with maintenance, mechanical failures, shield launching/breaking out (Shirlaw, 2008). A tunnel collapse can have catastrophic consequences for a project especially when constructing in a sensitive urban environments, so addressing the challenges involved in mixed face tunneling is crucial for the tunneling community.

Due to recent technology advances in shield tunneling technology, an increasing number of new tunnels are constructed using EPB in mixed face conditions (Herrenknecht et al., 2004). Hence, the need arises to extend the prior studies in homogeneous soil conditions to account for mixed face conditions in order to identify which factors control ground response for more

complex stratigraphies. As the 3D finite element methods become faster and more efficient, such an investigation is now feasible and could provide answers regarding the coupled effect of soil layers with contrasting soil properties.

2.3 Methods for predicting ground movements

Most available prediction methods for ground deformations due to tunneling focus on greenfield conditions where either there are no structures present or the overlying structures are assumed to respond passively to the tunnel induced movements. Tunnel-induced movements in soft ground tunneling can be divided in two categories: 1) short-term deformations associated with tunnel construction, and 2) long-term (post-construction) deformations associated with changes in ground stresses and pore water conditions (these are often connected to seepage boundary conditions at the tunnel face; Mair, 1999, Laver & Soga, 2012).

Predictions of tunnel-induced ground movements are often estimated using empirical interpretations of data for prior projects, while there is now an extensive database of tunnel induced ground settlements; there have been very few studies that attempt to link measurements of ground movements to the method of tunneling or specifically to the control parameters for tunnel-boring machines. The current thesis use 3D finite element methods to predict the effects of control parameters such as the face pressure, shield dimensions, tail void grout pressure and advance rate on predicted ground movements during construction. The research focuses mainly at the short term response (occurring during the timeframe of the construction process). There are a few case studies which consider long-term ground

movements. For example Mair (1999) reports large settlements for the Jubilee Line Extension (JLE) tunnels in London associated with changes in groundwater pressures around semi-permeable tunnel lining system.

2.3.1 Empirical methods for ground movements

Empirical methods for tunnel-induced ground movements were first proposed by Peck (1969) and Schmidt (1969) and are still widely used in geotechnical practice. The following paragraphs survey the current state of empirical methods

Peck 1969 and Schmidt 1969 proposed a Gaussian function to describe the transversal surface settlement trough (Figure 2.23):

$$u_z\,(x,y) = u_z^0\, exp\left(-\frac{x^2}{2{x_i}^2}\right) \qquad (2.8)$$

where x is the horizontal distance from tunnel centerline, u_z^0 is the surface settlement at the tunnel centerline, and x_i the location of the inflexion point in the settlement trough.

The volume of the surface settlement trough ΔVs per unit length of the tunnel can be found by integrating equation (2.1):

$$\Delta V_s = \sqrt{2\pi}\, u_z^0\, x_i \qquad (2.9)$$

The total volume loss ΔVs at the surface can be described by:

$$\Delta V_s = \Delta V_L + \Delta V_g \qquad (2.10)$$

where ΔV_g is the volume change in ground and ΔV_L is the volume loss at the tunnel.

For tunnel construction in drained conditions (i.e. sands), ΔV_s differs from ΔV_L due to dilation or contraction in the soil mass ($\Delta V_g \neq 0$). However for tunneling under undrained conditions, $\Delta V_g = 0$, so $\Delta V_s = \Delta V_L$.

Mair and Taylor (1997) proposed a linear relationship between the location of the inflexion point x_i and tunnel depth H:

$$\frac{x_i}{H} = K \qquad (2.11)$$

where K is the trough width parameter estimated using measured data from prior projects. Mair and Taylor (1997) reported a mean value K=0.5 for tunnels in clays and K=0.35 for sands, Figure 2.25.

Mair and Taylor (1997) observed that the ground movements relate to the tunneling method, and the displacement direction for EPB tunneling is controlled by the magnitude of the face pressure. Macklin (1999) correlated the load factor N/N_c (where N is the face stability ratio defined in eq. (2.2) and N_c is the critical face stability ratio at collapse as defined by eq. (2.3) and (2.4)) to the observed ground movement described by the observed ground loss, V_L by proposing an empirical equation based on analyzed field and laboratory data[10] shown in Figure 2.24:

$$V_L\,(\%) = 0.23\, e^{4.4LF} \qquad (2.12)$$

[10] The database used for this empirical equation is mostly for tunnels in stiff London clay

Mair and Taylor (1997) showed that the width of the subsurface settlement trough is also well correlated with the depth of the tunnel, H, and to characteristics of the overlying soil. The Gaussian trough extended by varying the trough width parameter:

$$x_i = K(H - z) \tag{2.13}$$

where K increases non-linearly with depth (Figure 2.26). For tunnels in clay Mair et al. (1993) proposed the following equation:

$$K = \frac{0.175+0.325\,(1-\frac{z}{H})}{1-\frac{z}{H}} \tag{2.14}$$

For tunnels in sand Jacobz (2002) proposed a modified equation:

$$K = \frac{0.09+0.26\,(1-\frac{z}{H})}{1-\frac{z}{H}} \tag{2.15}$$

The most common empirical expressions for estimating horizontal surface displacements assume that the vectors of transverse surface displacements are directed to a point at or close to the center of the tunnel (after Attewell, 1978 and O'Reilly & New 1982):

$$u_x \approx \frac{x}{H-z}\, u_z \tag{2.16}$$

However there is much less data available to validate this expression.

It has been shown by Celestino et al. (2000), Jacobsz (2002) and Vorster et al. (2005) that the simple Gaussian curve (Eq. 2.8) does not always represent accurately observed settlement

troughs. Vorster (2005) conducted centrifuge tests in sand and achieved an improved fit to the measured data using a modified Gaussian curve:

$$u_z\,(x,y) = \frac{\mathrm{n}u_z^0}{(n-1)+exp\left(\alpha\left(\frac{x}{x_i}\right)^2\right)} \tag{2.17}$$

where n the shape function parameter controlling the width of the profile described by:

$$\mathrm{n} = \exp(\alpha)\frac{2\alpha-1}{2\alpha+1} + 1 \tag{2.18}$$

and α the parameter that imposes the location of the inflection point x_i to be the same as the one used for the Gaussian curve (Eq. 2.10), while Eq. (2.17) matches the Gaussian curve for α =1 and n=0.5. Figure 2.27 shows how the n the shape function parameter affects the surface trough shape.

Marshall et al., (2012) concluded that the modified Gaussian curve by Vorster et al. (2005) provided a slightly better fit to the data compared to the Gaussian curve by Peck (1969) when used to fit the data from centrifuge experiments they conducted in sand but adds a level of complexity as it considers three degrees of freedom. Figure 2.28 shows the fitted monitored settlement trough using the simple Gaussian and the modified Gaussian curves. The quality of fit for the Gaussian curve by Peck (1969) was shown to slightly decrease at higher volume losses due to the reduction of the trough width (i.e. formation of a chimney-like displacement mechanism above the tunnel).

Attewell and Woodman (1982) proposed a method for estimating the longitudinal settlement trough that considers the effect of tunneling by considering the tunnel as a point source of

volume loss progressing along the tunnel alignment. The overall effect can be estimated by superimposing the incremental settlement troughs caused by a single point of loss along the tunnel alignment. Following the assumption that the incremental settlement troughs can be described by a Gaussian function (2.8), they derived the longitudinal settlement trough as a superposition of the Gaussian settlement curves for infinite points along the tunnel axis. As a result the longitudinal settlement trough is given by the cumulative function of the Gaussian distributions:

$$u_z(y) = u_{z,max} \exp\left(\frac{-y^2}{2x_i}\right)\left[1 - G\left(\frac{y}{x_i}\right)\right] \quad (2.19)$$

where y is the longitudinal location of the examined point relatively to the face of the excavation (as defined in Figure 2.29), G a probabilistic function (G(0)=0.5 and G(∞)=1), u_z is the longitudinal settlement, $u_{z,max}$ the maximum settlement which can be calculated from Eq. (2.10).

Attewell and Woodman (1982) proposed the assumption that half of the maximum deformation occurs when the shield face is passing, which was validated with data from the Jubilee Line Extension (JLE) Project in London clay for open face tunneling. However, Mair and Taylor, (1997) showed that for closed-face tunneling the surface displacement, occurring when the TBM face passes the examined cross section (y=0) corresponds to one quarter of the maximum longitudinal displacement, so the empirical model can be accordingly modified to capture this case (Figure 2.29).

Empirical models are a useful tool and they are widely used in practice, however their applicability and accuracy is heavily limited by their considered calibration dataset. As a result caution should be exercised when applying them for different tunnel geometries, construction methods and soil conditions.

2.3.2 Machine Learning Algorithms

Suwansawat and Einstein (2006) developed a method for predicting the maximum surface settlement using Artificial Neural Networks (ANN). This approach accounts for single or twin tunnel geometry, TBM control parameters and the underground stratigraphy. The ANN is trained using an extensive database of monitoring data from the Bangkok MRTA project. Different training scenarios were considered to assess which provided the best predictions for the monitoring data. Typically a subset of the dataset corresponding to a subsection of the tunnel is selected for training of the model which is then used to predict performance for the remaining tunnel alignment (Suwansawat, 2002). As shown in Fig, the accuracy of the method was higher when trained and evaluated with data within the same section (Root Mean Squared Error, RMSE≈7 when ANN trained and evaluated in section A) but decreases when assessed with different cross-sections (RMSE≈16 when trained for section A and evaluated in section B). Pourtaghi and Yaghin, (2012) used a combination of ANN together with wavenet theory, applying the Morlet wavenet function for the MRTA dataset which performed slightly better than ANN (15% reduction in RMSE).

2.3.3 Analytical solutions for ground movements

Analytical solutions have also been proposed for estimating tunnel-induced ground deformations. These solutions are based on simplifications of soil behavior (e.g., assuming soil is a linearly elastic material) but otherwise satisfy the principles of continuum mechanics. They use only a small number of input parameters that can be easily calibrated from field data and therefore offer a semi-empirical approach with greater predictive range than existing empirical methods. The analytical solutions also provide a useful tool for checking the accuracy of numerical solutions.

Sagaseta (1987) described tunnel deformations based on the assumption that the final shape of the tunnel cavity can be represented by two mode shapes, uniform convergence, u_ε and the ovalization, u_δ (Figure 2.31**)**. His proposed analytical solutions consider a concentrated ground loss occurring in linear elastic, isotropic, homogeneous medium under and undrained conditions (incompressible) and superimposed the singularity solutions to represent the two shape modes of the tunnel cavity. Verrujit and Booker (1996) expanded this framework for drained soils, while Verruijt (1997) introduced conformal transformation solutions that related deformations around the tunnel cavity to those at the ground surface. Pinto and Whittle (2013) compared the closed-form solutions obtained by superposition for singularity solutions (after Sagaseta, 1987, Whittle and Sagaseta, 2003) with more 'exact' solutions obtained by representing the finite dimensions of a shallow tunnel in elastic soil (Verruijt, 1997).

Table 2.1 summarizes the analytical solutions proposed by Pinto and Whittle (2013) for describing the transverse field of ground deformations around a shallow tunnel based on

displacement modes shown on Figure 2.31. The solutions allow the estimation of both vertical and horizontal displacements at any depth. The tunnel cavity deformation modes: uniform convergence u_ε, ovalization u_δ are used as input parameters, while the vertical translation Δu_z is calculated to satisfy the boundary condition of zero vertical displacements at the far-field.

Figure 2.32 depicts the effect of the relative distortion, $\rho = -\frac{u_\delta}{u_\varepsilon}$ on the estimated settlement troughs. Pinto et al. (2013) found good agreement between the approximate analytical solutions and measured data from tunnels excavated through different ground conditions using a variety of closed and open-face construction methods, while Zymnis et al. (2013) used this method to integrate ground movements for open face construction of the Jubilee Line Extension (JLE) tunnels in St. James Park for assumptions of isotropic and anisotropic stiffness of London Clay.

Ieronymaki et al. (2015), extended this framework using a 2D numerical model that simulated the effects of three independent cavity deformation parameters, the uniform convergence u_ε and ovalization u_δ along with the vertical translation Δu_z (which was a dependent parameter in prior analytical solutions). The simulations optimized the three parameters for the deformations observed due to the EPB, at certain sections of the Crossrail project and achieved a good fit for both simple (M-C) soil model and more complex (MIT-S1) soil model (Ieronymaki et al., 2016).

2.3.4 Numerical simulations of tunnel construction

Although, empirical and analytical methods are valuable tools for design, they have certain limitations as discussed in the prior sections. Numerical simulations are becoming increasingly

popular as the computation time even for 3D models has decreased to a point that it is feasible to use for practical purposes. 2D simulations for tunnel construction offer a relatively simple and fast way to estimate ground displacements. However, it is clear that since 2D models assume plane strain conditions they cannot represent critical details that control deformations in mechanized tunneling, such as the applied face pressure, the shield body, the grouting of the tail void, the erection of the lining support system. Hence, 2D models cannot capture the 3D nature of shield tunneling (e.g. Clough and Leca, 1989). Mair et al. (1981) claimed that 2D models performance might be improved when more sophisticated soil models are considered.

Due to the limitations of 2D models, nowadays 3D models are employed for most of the current tunnel projects in engineering practice (Moller, 2006). The majority of the available 2D methods are simulating the 3D tunneling process by imposing an appropriate boundary condition at the tunnel cavity that:

1. Reduces the stiffness of the surrounding soil (Progressive softening method or α-method developed by Swoboda, 1979)

2. Reduces the initial geostatic stress applied by the excavated soil by a certain factor (Stress reduction method or β-method, after Panet and Guenot, 1982) or until a certain volume loss is achieved (Volume loss control method by Addenbrooke et al., 1997)

3. Imposes a contraction at the tunnel cavity until a certain vertical gap is formed between the crown and the lining while the invert is fixed in place (Gap method introduced by

Rowe at el., 1983) or until a prescribed contraction value is reached while the springline of the tunnel remains fixed (Contraction method by Vermeer and Brinkgreve, 1993).

Comparative studies between 2D and 3D analyses have been performed by Moller, (2006) to improve the performance of the stress reduction method (Figure 2.33), which found that different β-factors were required to produce the same surface deformations and lining forces observed in a 3D model by a 2D model. Due to the limitations and the inherent inability of a plane strain analyses to reproduce important aspects of the mechanized tunneling process, especially the stress relief at the face due to the removal of the soil and the deformations at the shield tail due to the grouting process, we decided to mainly focus on the 3D FE methods for this study.

Non-linear 3D finite element analyses have been a valuable tool in studying the ground displacements induced by soft ground shield tunneling and usually employ a step-wise procedure to simulate the tunneling process. Each step corresponds to a fixed incremental advance equal to the width of the lining rings (or a fraction thereof). The TBM is represented either as an advancing solid body (Kasper and Marschke, 2004) or in a simplified manner by applying a pressure boundary condition (Moller, 2006). Moller, (2006) developed a 3D model using the commercial geotechnical software Plaxis 3D^{TM} which used step-by-step methods to simulate the excavation procedures for slurry shield tunnels. Figure 2.34 shows that excavation procedure is simulated in series of steps. At each step one row soil element is removed, simulating the excavated soil mass. Each soil volume generally has a circular cross-section and standard width that corresponds to the selected round length for the tunnel (lining width). The

support effect from the shield is represented by a pressure boundary condition (instead of using stiff shell elements). Normal tractions are used to simulate the slurry pressure at the face of the tunnel, and the radial pressure behind the shield due to fresh grout fluid injected in the tail void. The grout pressure is radially applied to the excavated soil surface for two rings behind the shield, while the soil is allowed to freely deform until it comes into contact with the lining (representing the formed tail void). For the subsequent steps, solid elements representing the hardened grout are activated and the radial pressure is switched off. So at each step i, the soil element i is deactivated, a radial pressure is applied for elements i to i-n+1 to simulate the shield, radial pressure is applied for elements i-n and i-n-1 to represent the grout and the lining element i-n-2 is activated (where n the number of steps that correspond to the shield length). Möller (2006) suggested that a similar sequence can be applied also for the EPB tunneling method, with the use of a modified pressure boundary or a contraction boundary condition to simulate the overcutting and the conical shape of the EPB shield.

Kasper and Meschke, (2004) have developed an in-house finite element model based on the FE framework KRATOS (Dadvand et al. 2010) to simulate the shield as an advancing deformable body in frictional contact with the soil (Figure 2.35). The TBM shield advances through the soil with the use of hydraulic jacks (represented by truss elements) that push against the emplaced lining system to steer the machine forward. The tunneling construction is modeled in steps that consist of three stages (see Figure 2.35). In the first stage the jacks are contracted (Figure 2.35a), in the second stage the jacks extend pushing the machine forward into the soil (Figure 2.35b) and at the third stage the soil elements from excavation face are removed and the area is re-meshed, connecting the new nodes to the TBM head (Figure 2.35c). When the TBM has

advanced forward by the length of one lining ring, new elements representing the lining are activated and the jack elements now connected to the edge nodes of the new lining.

Founta et al., (2013) modified the Moller (2006) methodology to simulate an EPB machine applying a contraction boundary condition on the activated plate elements to represent the conical shape of the shield (Figure 2.36a) and then compared results with the "ekate" model of Kasper and Meschke, (2004) (Figure 2.36b) for the case of the Crossrail project in London. They concluded that a detailed representation of the tunneling process is important but simplified models can also yield equally good results with less computational effort (Founta et al., 2013).

Limited parametric analyses were conducted to investigate how the TBM control parameters, face pressure, grout pressure, advance rate and tunnel geometry are controlling surface deformations (Kasper and Meschke, 2006a and 2006b, Nagel and Meschke, 2011, Su, 2015, Founta and Whittle, 2017). Kasper and Meschke, (2006a) conducted an indicative number of analyses and found that effects due to the face pressure, grout pressure and conical shape and length of the shield can be significant, while effects due to the TBM and trailer weight have minor effects on surface deformations. Kasper and Meschke, (2006b) extended the prior analyses investigating effects due to soil properties and tunnel geometry. They found that the tunnel cover depth over diameter ratio and the friction angle of the soil significantly affected deformations, while the over consolidation ratio and permeability of the soil had minor roles. Founta and Whittle, (2017) also investigated the effects of face pressure and grout pressure on the surface deformations for the Crossrail Project in London (Appendix A). It is shown that large variations of the applied face pressure and grout pressure result small changes on the surface

deformations which is attributed to the stiff properties of the London clay. These initial parametric studies provide a good understanding on the importance these parameters can have on controlling the developed deformations. However they don't provide a clear relationship indicating for which case parameters such as the applied face pressure can be important and for which little effect is observed on the ground deformations. It is crucial to understand the underlying mechanisms involved in the formation of the surface settlements and identify the critical cases for which extra care should be given in ensuring the appropriate control parameters are selected.

Typically simple soil models such as elasto-plastic M-C or Modified Cam-Clay are used due to their simplicity and the low number of input parameters (Melis et al, 2002, Broere and Brinkgreve, 2002, Kasper and Meschke, 2004, Moller, 2006, Galli et al. 2004, Founta et al. 2013). Generally, care should be given as MC has been shown to predict smaller ground settlements compared to more advanced soil models (Do et al., 2013). However, although sophisticated soil models are undeniably superior at simulating soil behavior, simplified elastic perfectly plastic soil models (such as Mohr Coulomb) have been shown to provide quite reliable results for cases that the soil behavior remains mostly linear[11] (Founta and Whittle, 2017 see Appendix) when compared to more sophisticated soil models (MIT-S1 by Pestana and Whittle, 1999). As a result, they can provide a reliable estimation, especially in cases where there is only limited field or lab data available. Most tunneling analyses in clay consider undrained conditions that account only for the short-term effects due to tunneling and ignore long term effects occurring due to the dissipation of the developed excess pore water pressures. Swoboda and

[11] small zone of yielding around the tunnel

Abu-Krisha, (1999) analyzed the effects of TBM tunneling in clay using a 3D FE model that employs an incremental procedure and accounts for time effects (i.e. consolidation due to the dissipation of the developed pore pressures with time). They examined effects due to the applied face pressure and grout pressure, concluding that higher support pressures may lead to higher overall excess pore pressures hence longer dissipation times. Further investigation is needed to better understand the effect of partial drainage on the observed tunnel deformations for different soil properties (permeability) and advance rates of excavation.

There are a limited number of studies exploring the induced deformations due to shield tunneling in mixed face conditions. These include interpretation of measured settlements (Clough and Leca, 1993), risk analysis (Sousa and Einstein, 2012) and 2D and 3D Finite Element analyses (Nunes and Meguid, 2009; Zhang et al. 2015, Su, 2015). Broere, 2001 developed a 3D modified wedge model (Horn, 1961 see Figure 2.18) to study face stability in heterogeneous soils above and in front of the tunnel face, while Hu, 2012 extended this model to include both the modified wedge stability model and the modified Terzaghi model to study the influence of the heterogeneity of the soil and the slip angle on the minimal support pressure. Su, (2015) studied the case of mixed face conditions in clay for the Bendemeer station (contract C933) of the Mass Rapid Transit (MRT) project in Singapore (Su, 2015) using a 3D model developed with the GeoFEA Finite Element Program (Figure 2.37). The model captured the layered stratigraphy including the Old Alluvium and Kallang formations and simulated the applied face pressures using the monitored pressure values for this section. The FE results provided good approximation of the observed settlements but generally underestimated the observed deformations. Similarly, most 3D FE studies in literature explore mixed face conditions in

relation to a specific project. This practice indeed satisfies perfectly the specific needs of each examined project. However, a more general framework is needed to provide a more spherical understanding of the effect mixed face conditions can play on the observed surface deformations.

$$\textit{Convergence}: \begin{cases} u_x^{\,c} = 4 \cdot u_\varepsilon \cdot R \cdot \left\{ \dfrac{(1-\nu)\cdot x}{x^2+(y-H)^2} - \dfrac{(y-H)\cdot x\cdot y}{\left[x^2+(y-H)^2\right]^2} \right\} \\ u_z^{\,c} = 2 \cdot u_\varepsilon \cdot R \cdot \left\{ \dfrac{2\cdot(y-H)\cdot x^2 + H\cdot\left[x^2-(y-H)^2\right]}{\left[x^2+(y-H)^2\right]^2} - \dfrac{2\cdot(1-\nu)\cdot(y-H)}{x^2+(y-H)^2} \right\} \end{cases}$$

$$\textit{Ovalization}: \begin{cases} u_x^{\,c} = \dfrac{8\cdot u_\delta \cdot R}{3-4\cdot\nu} \cdot \left\{ \begin{array}{l} x\cdot\dfrac{x^2+y^2-H^2}{\left[x^2+(y-H)^2\right]^2}\cdot(1-\nu) - \ldots \\ \ldots - x\cdot y\cdot\dfrac{y\cdot(x^2+y^2)+2\cdot H\cdot(H^2-x^2)-3\cdot y\cdot H^2}{\left[x^2+(y-H)^2\right]^3} \end{array} \right\} \\ u_z^{\,c} = \dfrac{8\cdot u_\delta \cdot R}{3-4\cdot\nu} \cdot \left\{ \begin{array}{l} \dfrac{x^2\cdot(2\cdot H-y)-y\cdot(y-H)^2}{\left[x^2+(y-H)^2\right]^2}\cdot(1-\nu) - \ldots \\ \ldots - \dfrac{(y-H)\cdot\left\{H\cdot y\cdot(y-H)^2 - x^2\cdot\left[(x^2+y^2)+H\cdot(y+H)\right]\right\}}{\left[x^2+(y-H)^2\right]^3} \end{array} \right\} \end{cases}$$

$$\textit{Ovalization}: \frac{\Delta u_z}{u_\delta} = \frac{2}{3-4\cdot\nu}\cdot\frac{R}{H}\cdot\frac{(1-8\cdot\nu)\cdot\left(\frac{R}{H}\right)^4 + (11-8\cdot\nu)\cdot 4\cdot\left(\frac{R}{H}\right)^2 - 32}{\left[4+\left(\frac{R}{H}\right)^2\right]^3}$$

$$\textit{Convergence}: \frac{\Delta u_z}{u_\varepsilon} = 4\cdot\frac{R}{H}\cdot\frac{8\cdot(1-\nu)-(1-2\cdot\nu)\cdot\left(\frac{R}{H}\right)^2}{\left[4+\left(\frac{R}{H}\right)^2\right]^2}$$

Table 2.1 Analytical solutions for ground deformations around a shallow tunnel (after Pinto and Whittle, 2013)

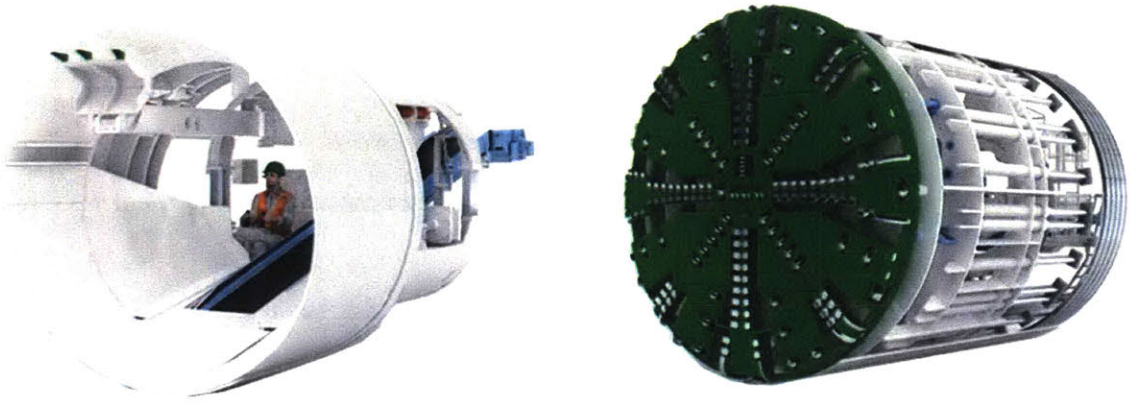

a) Open face TBM

b) Closed face TBM

Figure 2.1 Open face vs closed face TBMs (Herrenknecht, 2017)

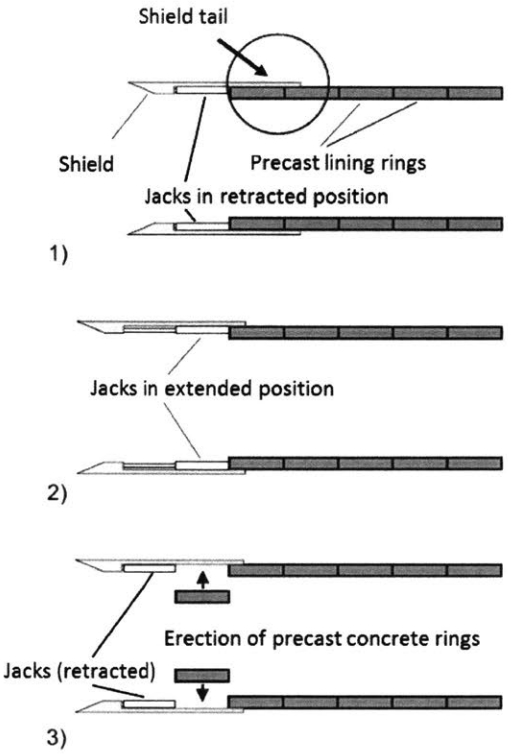

Figure 2.2 Excavation sequence for open face shield tunneling (modified from Moller, 2006)

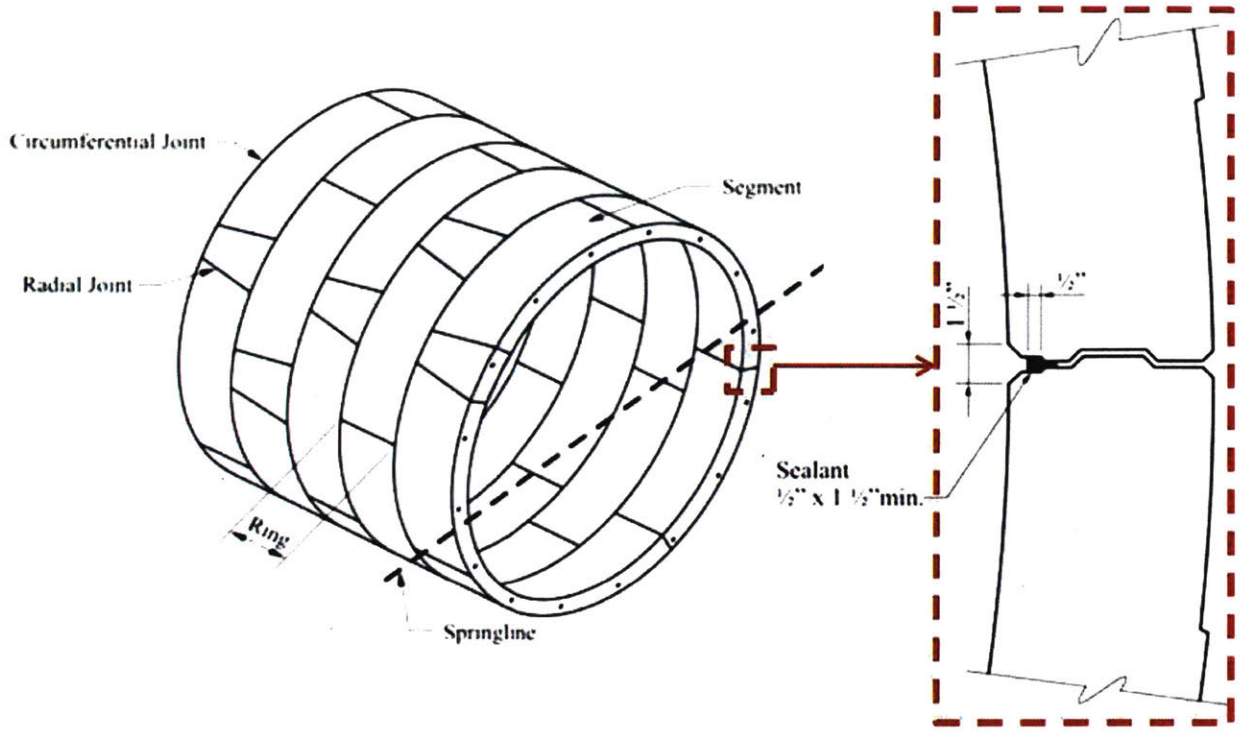

Figure 2.3 Schematic figure of the assembled precast segmental lining (after FHWA, 2011)

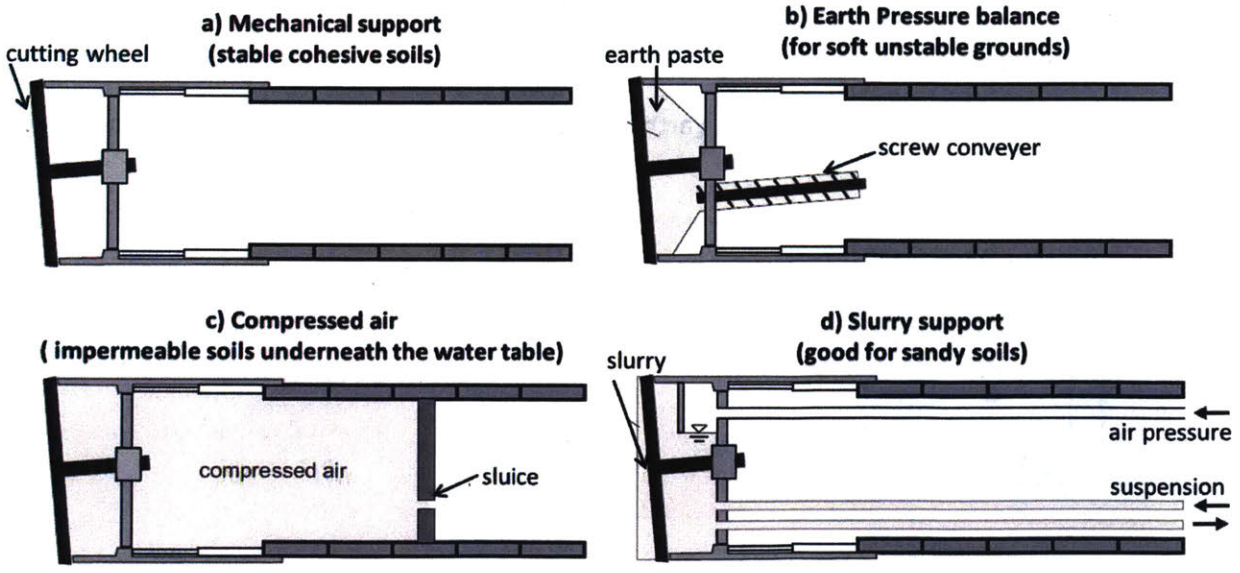

Figure 2.4 Closed face shield tunneling methods (after Moller, 2006)

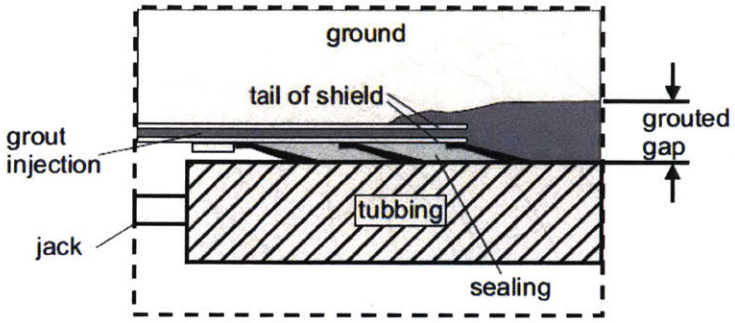

Figure 2.5 Schematic figure of grout injection in the tail void (after Moller, 2006)

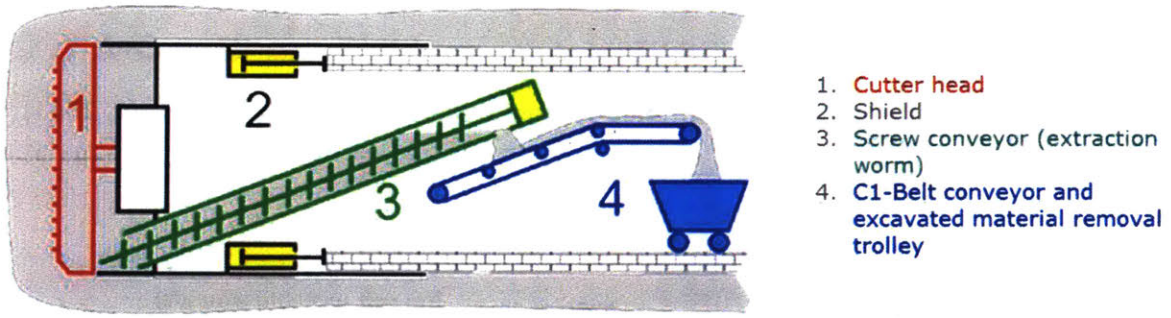

Figure 2.6 Excavation sequence for Earth Pressure Balance (EPB) machine (after NFM-Technologies, 2017)

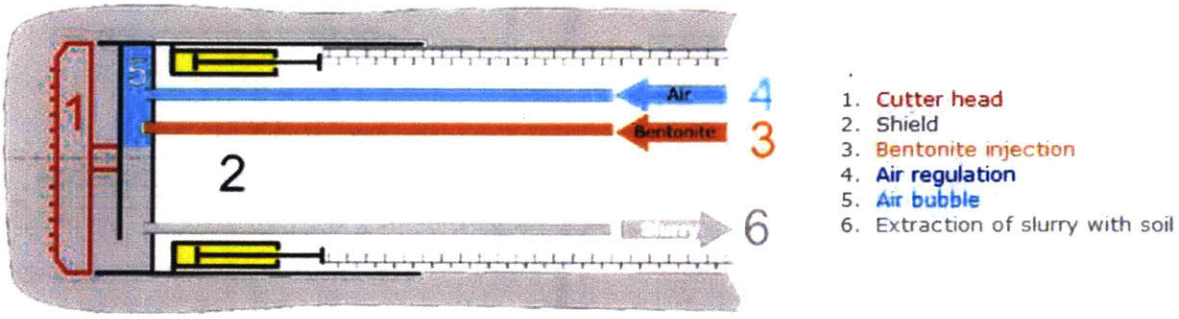

Figure 2.7 Excavation sequence for slurry machine (after NFM-Technologies, 2017)

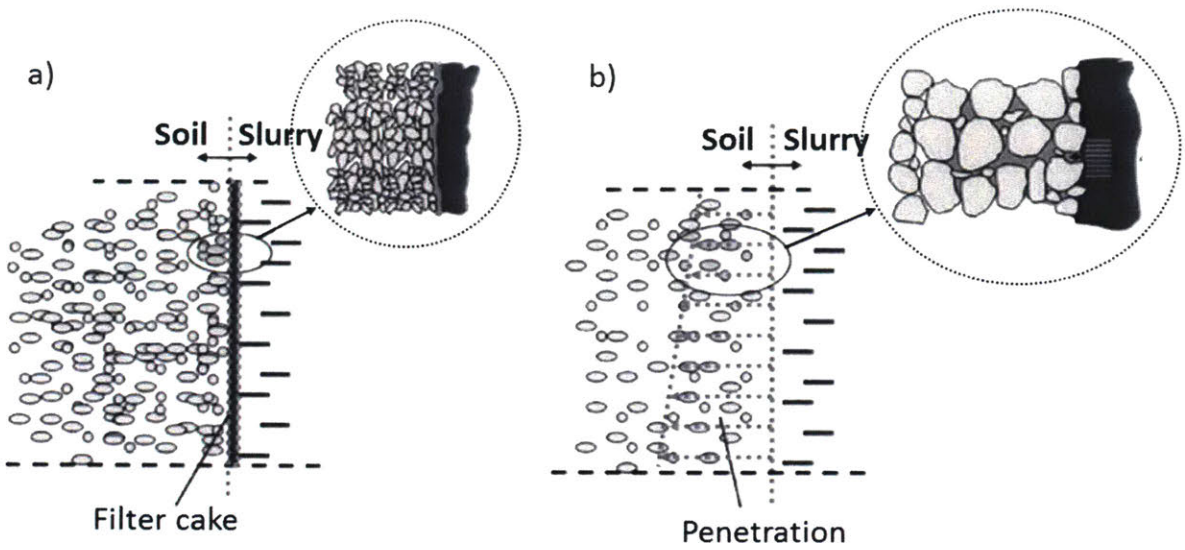

Figure 2.8 Slurry penetration models a) membrane model b) penetration model (modified from Maidl et al., 2013)

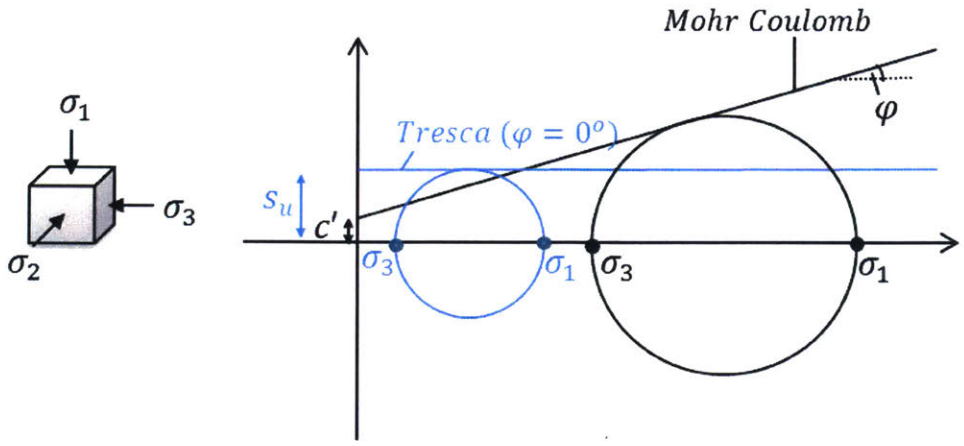

Figure 2.9 Tresca and Mohr Coulomb yield criteria

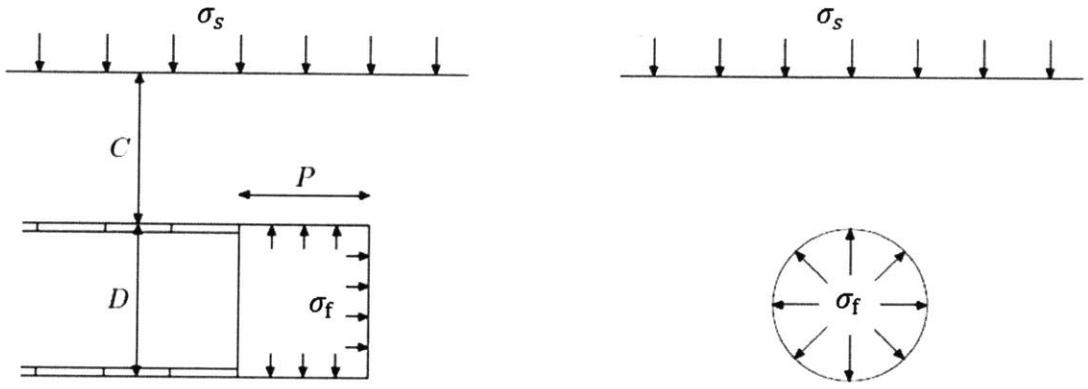

a)Plane stain longitudinal model

b)Plane stain tranverse model (unlined, P=∞)

Figure 2.10 Approximation of face support conditions used in stability analyses by Davis et al., (1980)

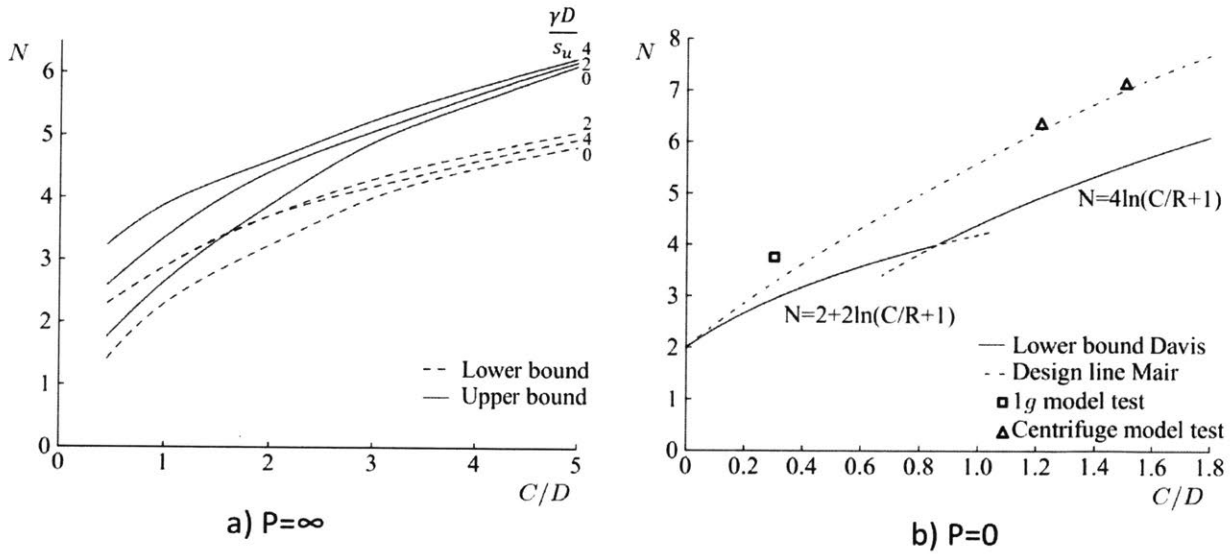

Figure 2.11 Upper bound and lower bound solution by Davis et al., (1980) for (a) a plane strain unlined tunnel (P=∞) and (b) lined tunnel (P=0)(after Broere, 2001)

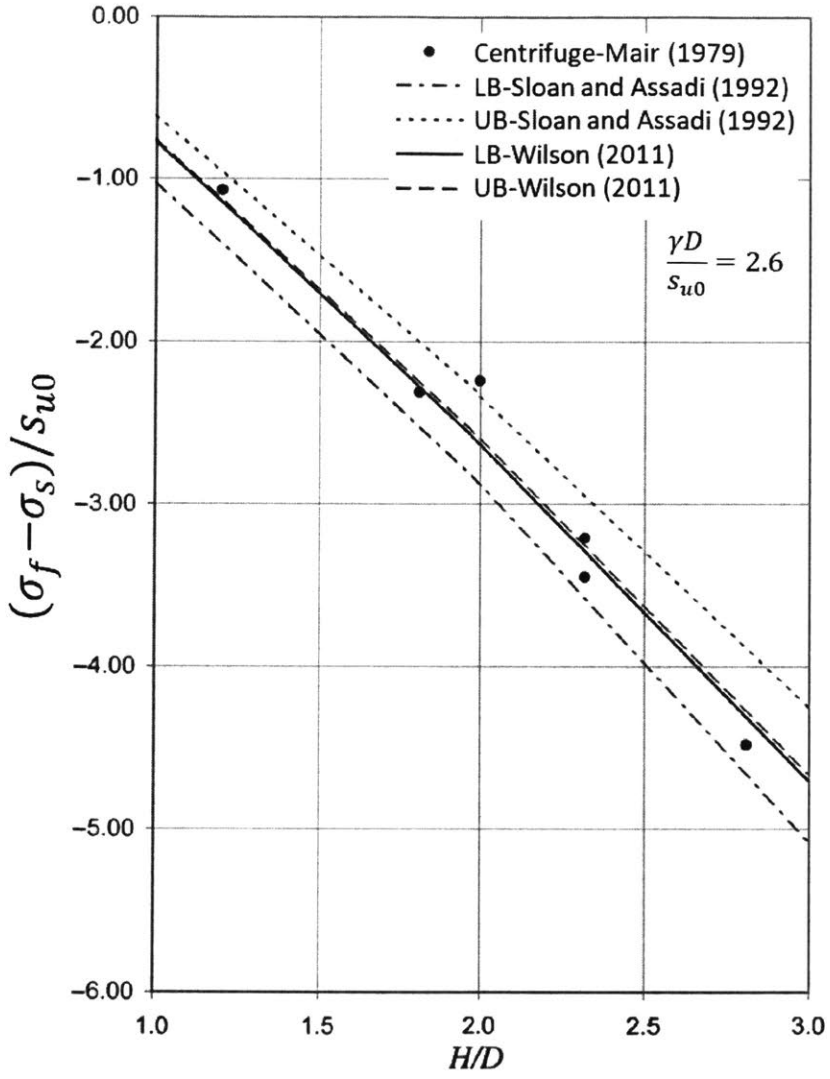

Figure 2.12 Upper bound and lower bound solution for plane strain unlined tunnel in undrained clay (after Wilson et al., 2011)

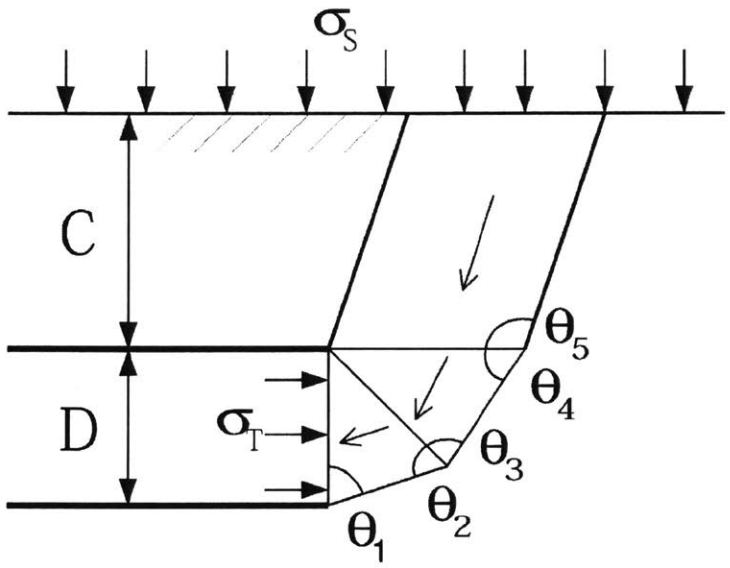

Figure 2.13 Rigid block mechanism for analytical upper bound solution considered by Augarde et al., 2003 to study face stability of lined tunnels in clay

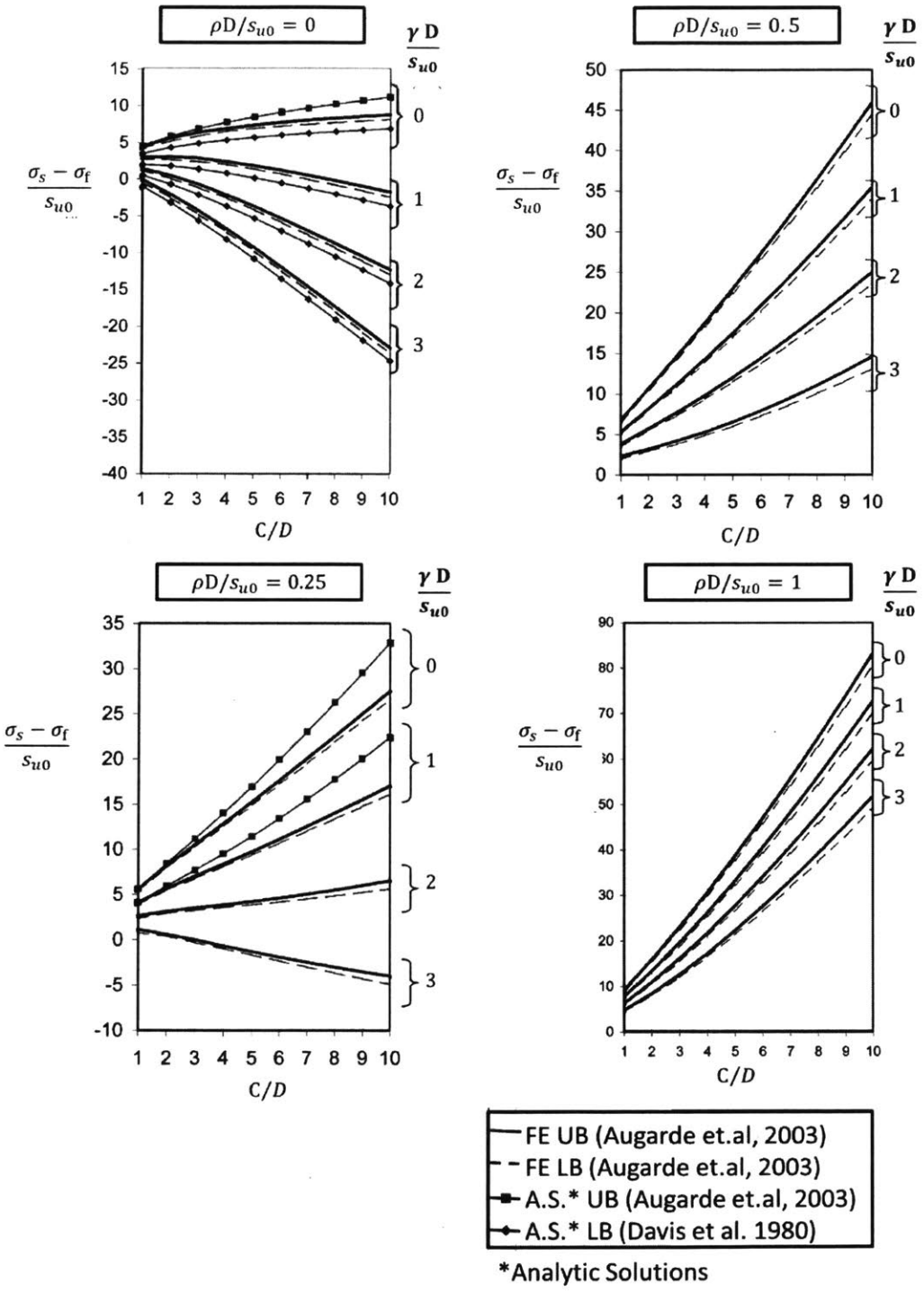

Figure 2.14 Plane strain finite element upper bound and lower bound solutions of face stability compared to analytical solution for lined excavation in clay (Augarde et al., 2003, Davis et al., 1980)

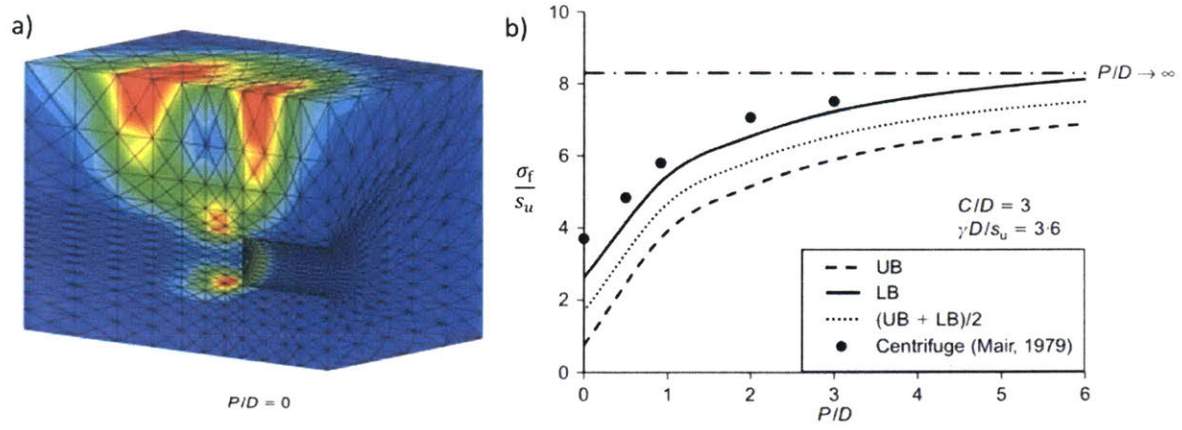

Figure 2.15 Failure mechanisms for fully lined tunnel in clay with $\gamma D/S_{u0}$=3.6 (after Sloan, 2013)

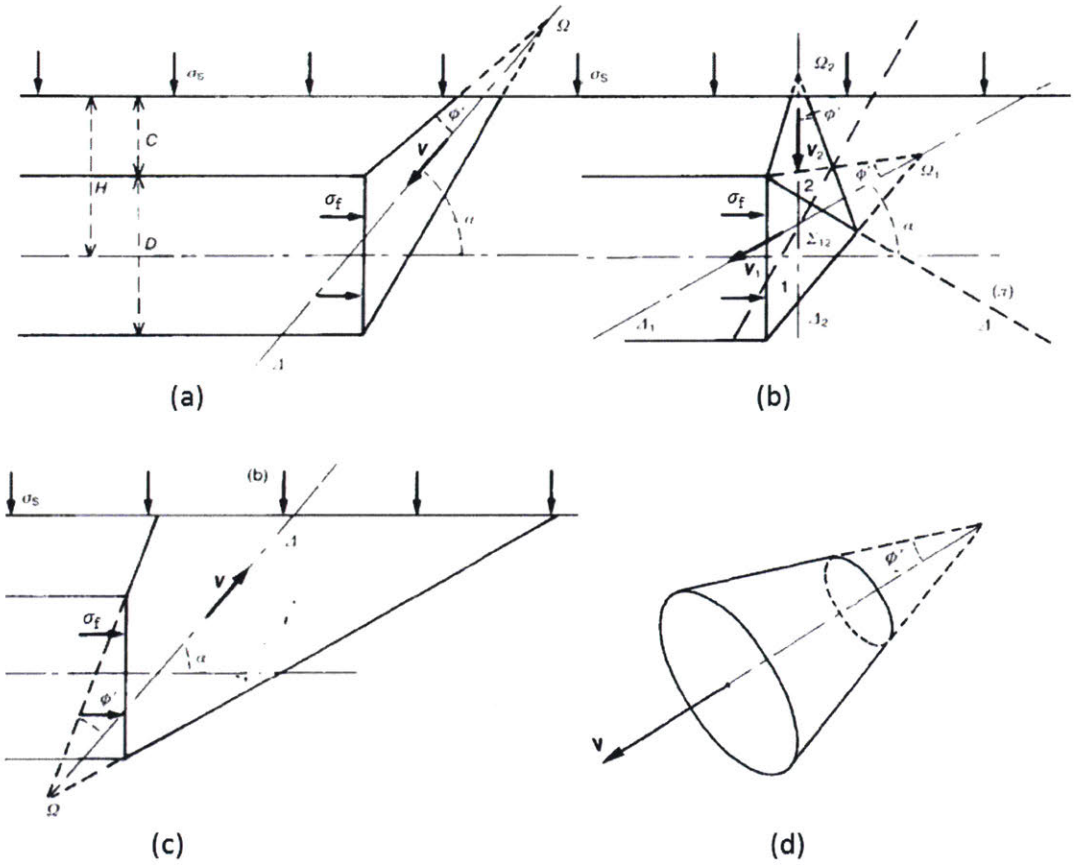

Figure 2.16 3D conical failure mechanisms a, b and c considered for the upper bound solutions and d) the conical block used (after Leca and Dormieux, 1990)

Figure 2.17 3D failure mechanisms considered for the upper bound solutions (after Mollon et al., 2011)

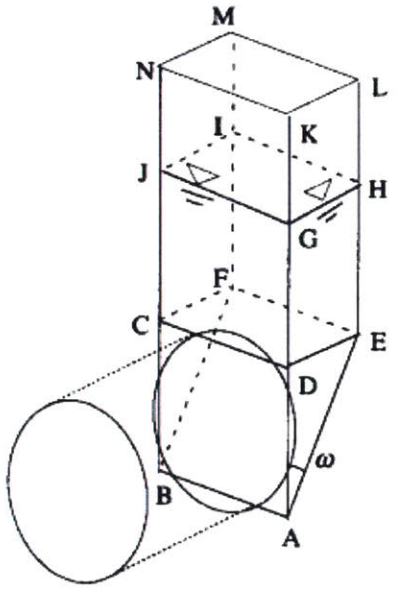

Figure 2.18 Wedge mechanism by Horn, 1961 assumed by Anagnostou and Kovari, 1996 (source Anagnostou and Kovari, 1996)

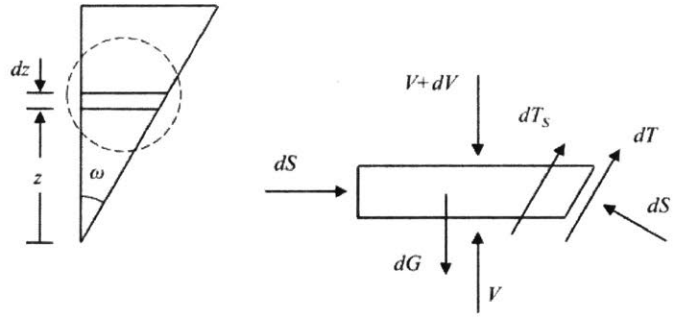

Figure 2.19 Method of slices used by Anagnostou, 2012 (source Anagnostou, 2012)

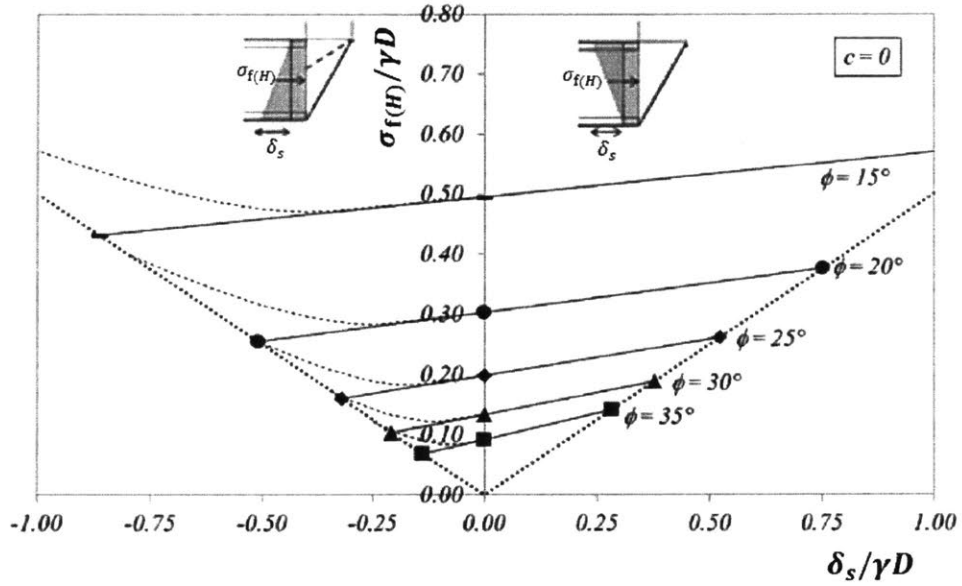

Figure 2.20 Normalized support pressure at the tunnel axis $\sigma_{f(H)}/\gamma D$ and as a function of the normalized gradient of the support distribution $\delta_s/\gamma D$ for different friction angles (Anagnostou and Perazzelli, 2013)

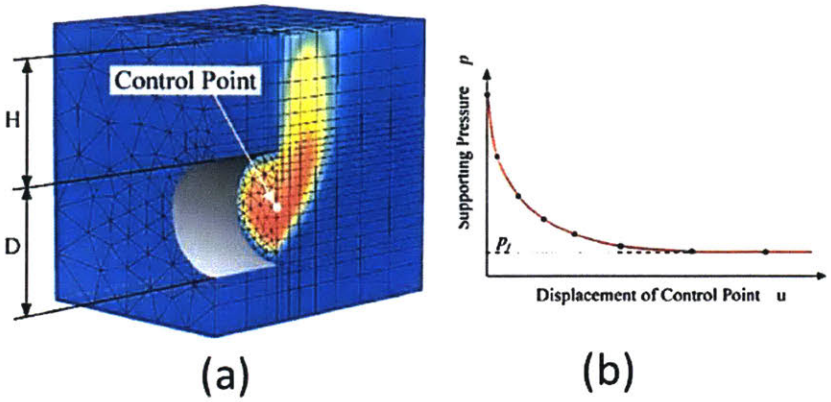

Figure 2.21 3D FE modeling of lined tunnel in sand (a) Collapse mechanism observed and (b) Displacements as a function of the support pressure (source: Vermeer, 2002)

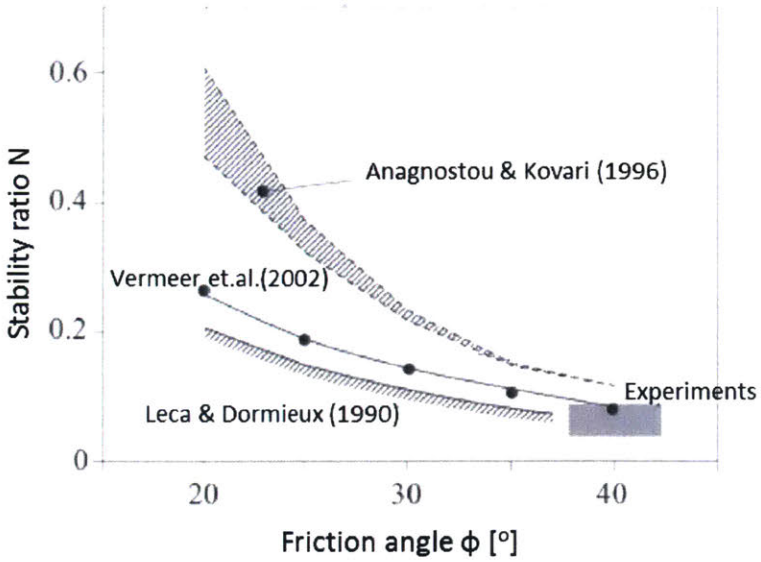

Figure 2.22 3D finite element solutions of face stability compared to centrifuge data, 1-g experiments and solutions using the limit equilibrium method or limit analysis for lined tunnels in sand (Vermeer et al., 2002, Chambon and Corte, 1994, Plekkenpol et al., 2006, Kirsch, 2010, Anagnostou and Kovari, 1996, Leca & Dormieux, 1990)

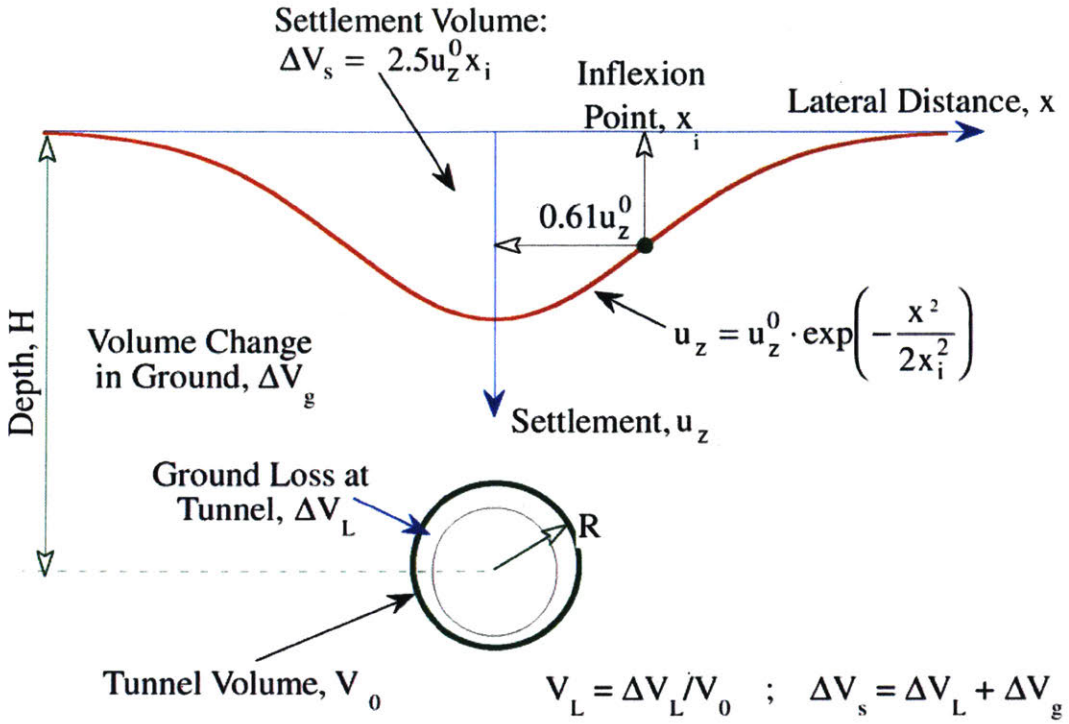

Figure 2.23 Empirical function for transversal settlement trough (after Peck, 1969 and Schmidt 1969)

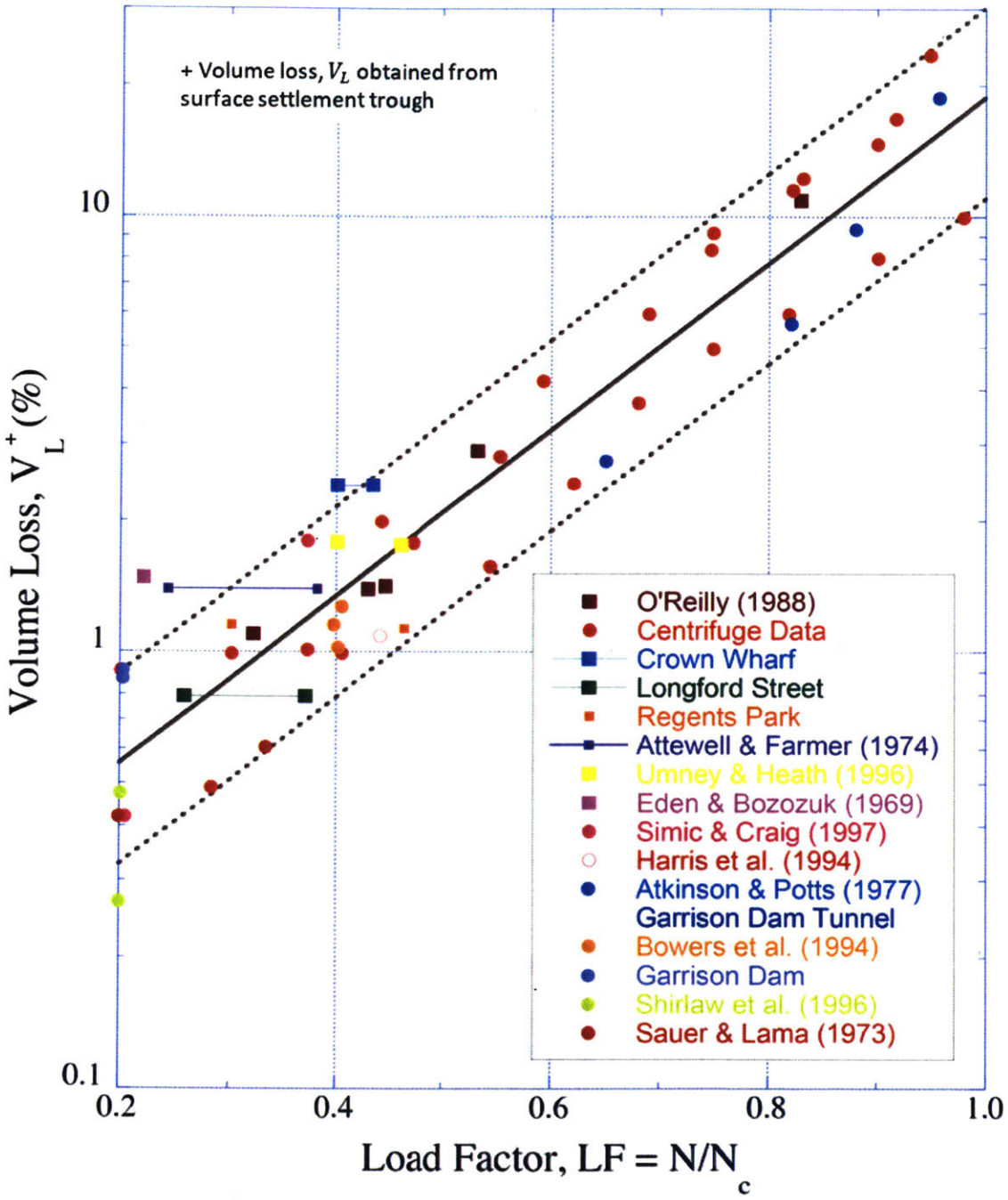

Figure 2.24 Correlation of volume loss V_L and load factor from field and laboratory monitoring data for clays (after Macklin, 1999)

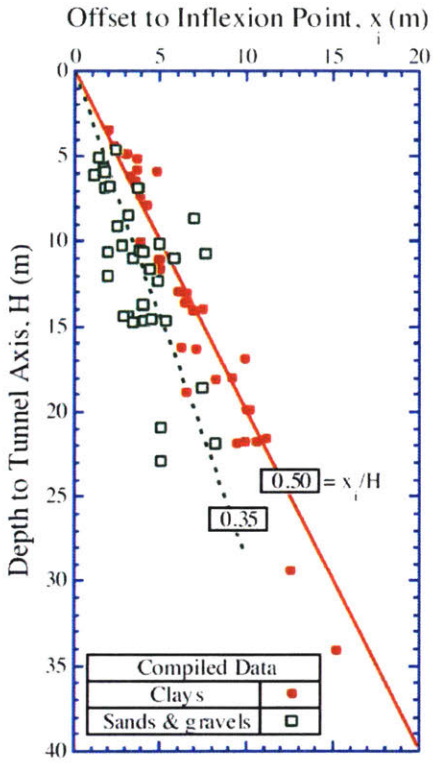

Figure 2.25 Empirical estimation of inflexion point (after Mair and Taylor, 1997)

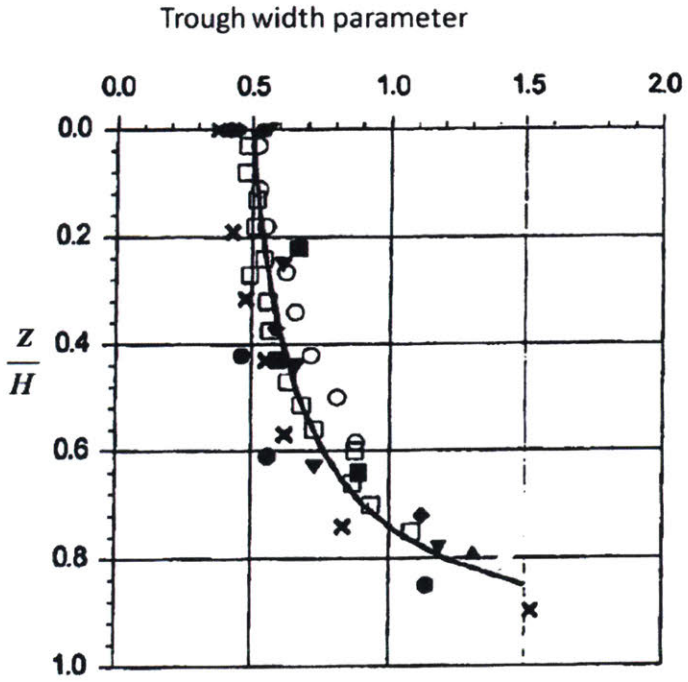

Figure 2.26 Variation of trough width parameter K with normalized depth (z/H) for tunnels in clay (Mair et al., 1993)

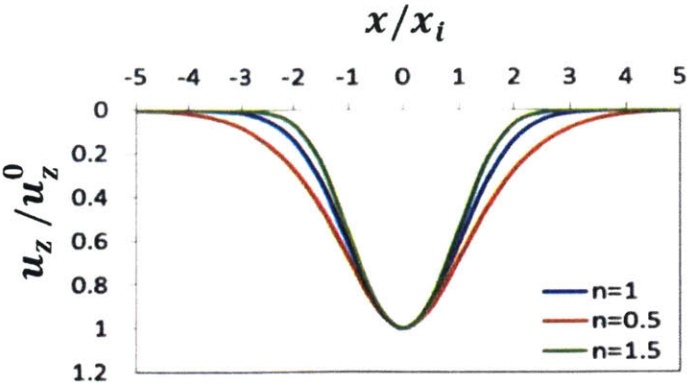

Figure 2.27 Modified Gaussian curve proposed by Vorster, 2005 (source: Ieronymaki, 2015)

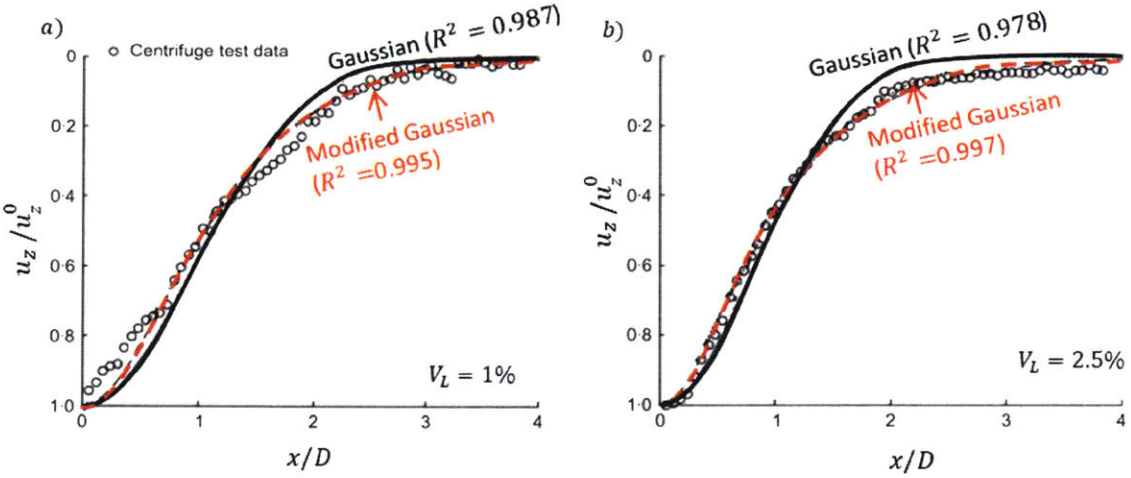

Figure 2.28 Comparison of Gaussian and modified Gaussian fit on surface settlement data from centrifuge model tests in sand for volume loss at the tunnel a) 1% and b) 2%

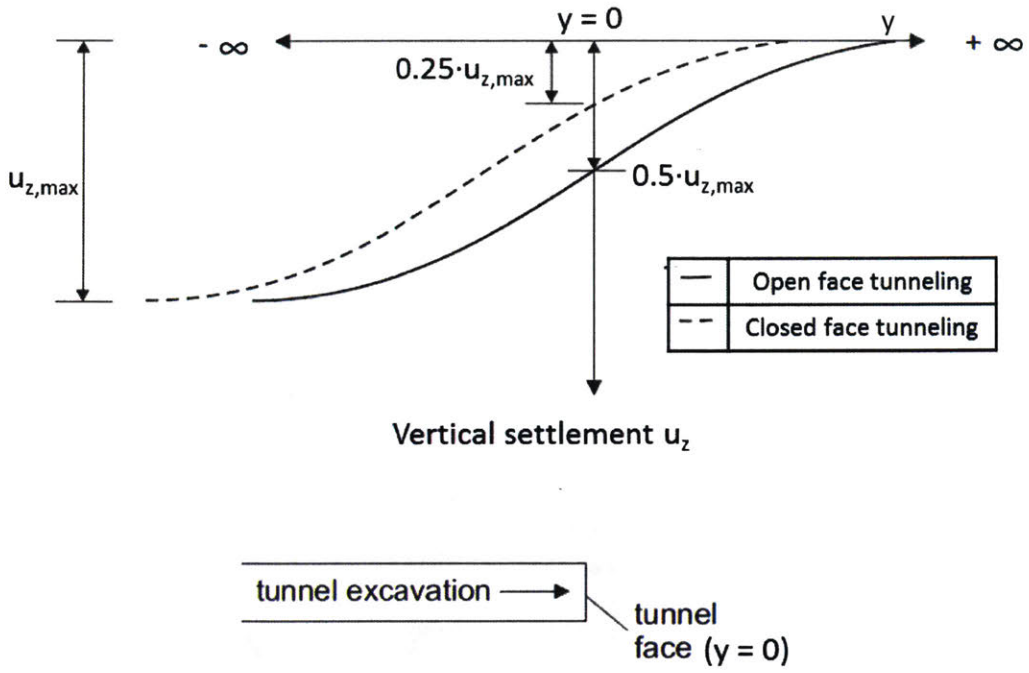

Figure 2.29 Longitudinal surface displacement above tunnel centerline (after Attewell et al., 1986)

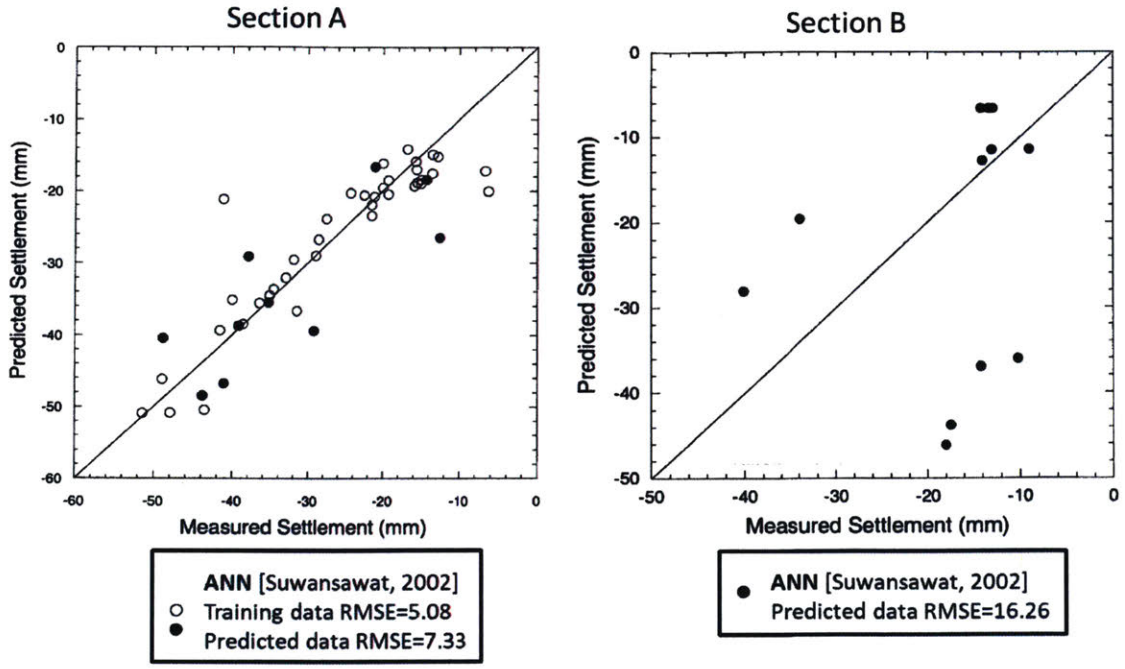

Figure 2.30 Performance of ANN when trained for a subsection of section A and used to predict deformations for a) section A and b) section B (Suwansawat, 2002)

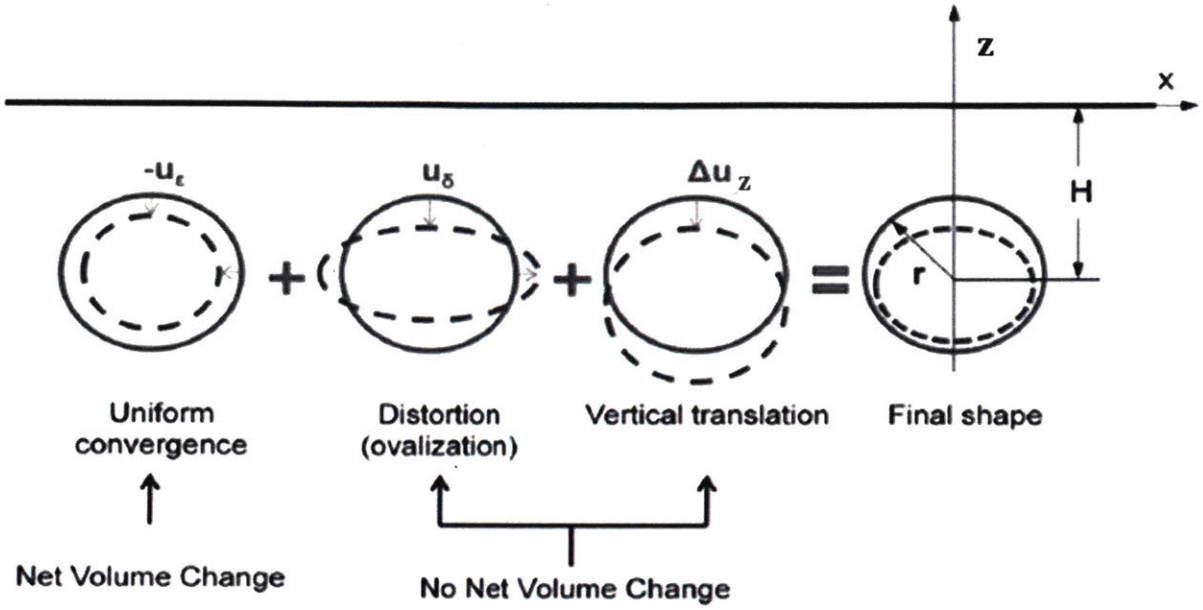

Figure 2.31 Deformation modes around tunnel cavity (after Whittle and Sagaseta, 2003, Pinto and Whittle, 2013)

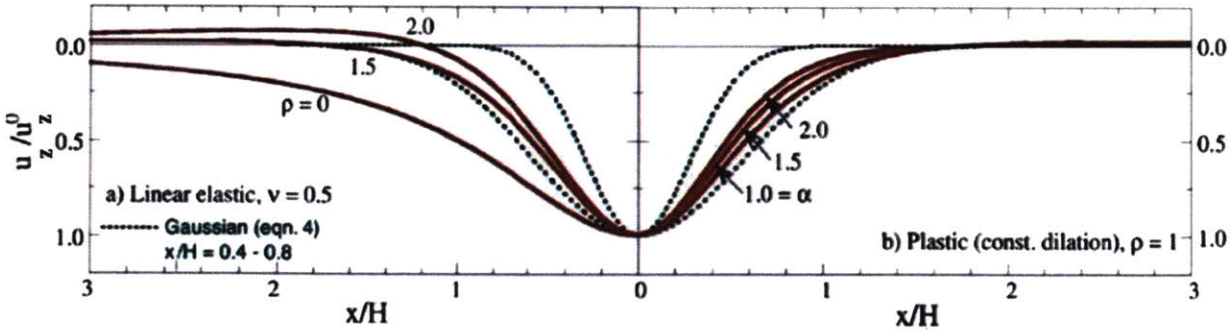

Figure 2.32 Effect of input parameters on surface settlement distribution (Whittle and Sagaseta, 2003)

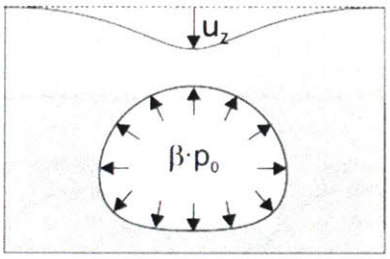

Figure 2.33 Stress reduction method (Möller, 2006)

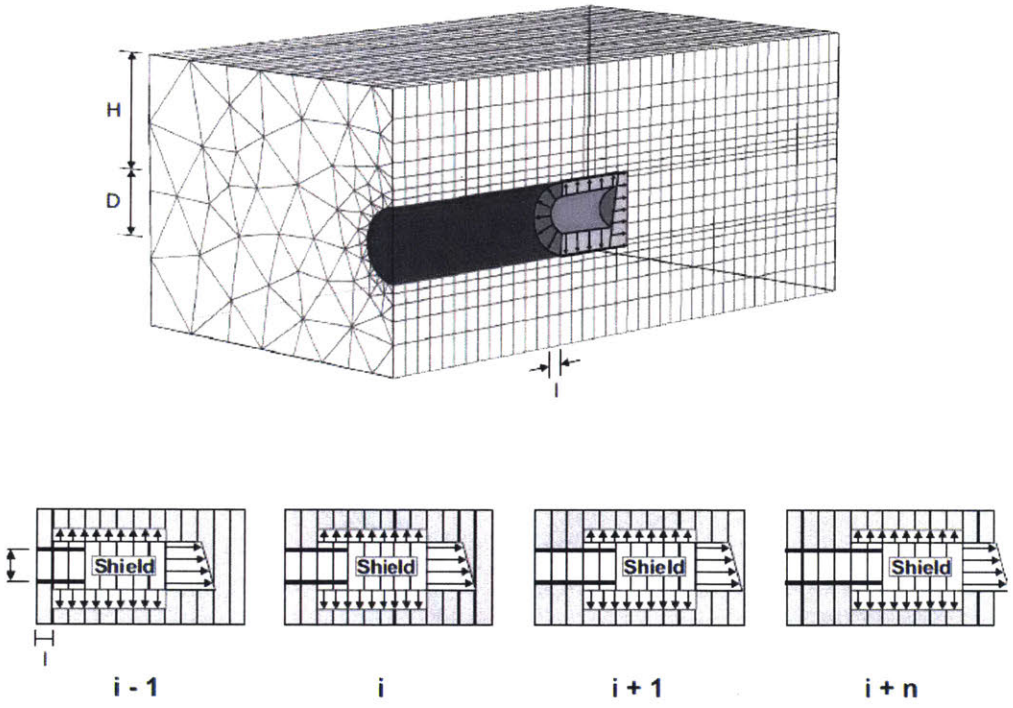

Figure 2.34 Step-by-step simulating of closed face, shield tunneling (Möller, 2006)

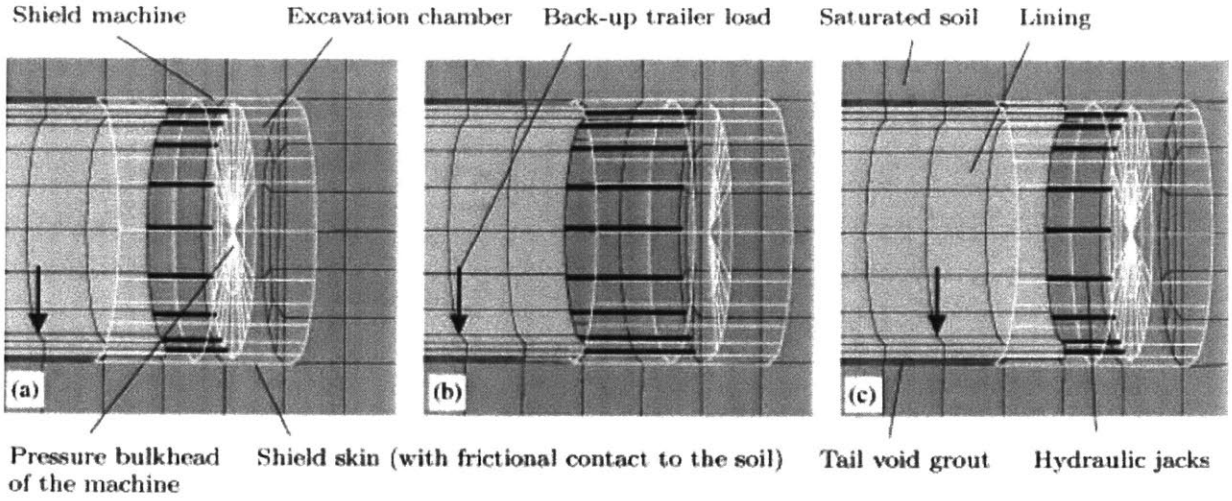

Figure 2.35 Step-by-step simulation of mechanized tunneling: (a) End of previous excavation step; (b) advance of the TBM; and (c) excavation of the soil and introduction of elements representing the tail void grout and the lining (Kasper and Meschke, 2004)

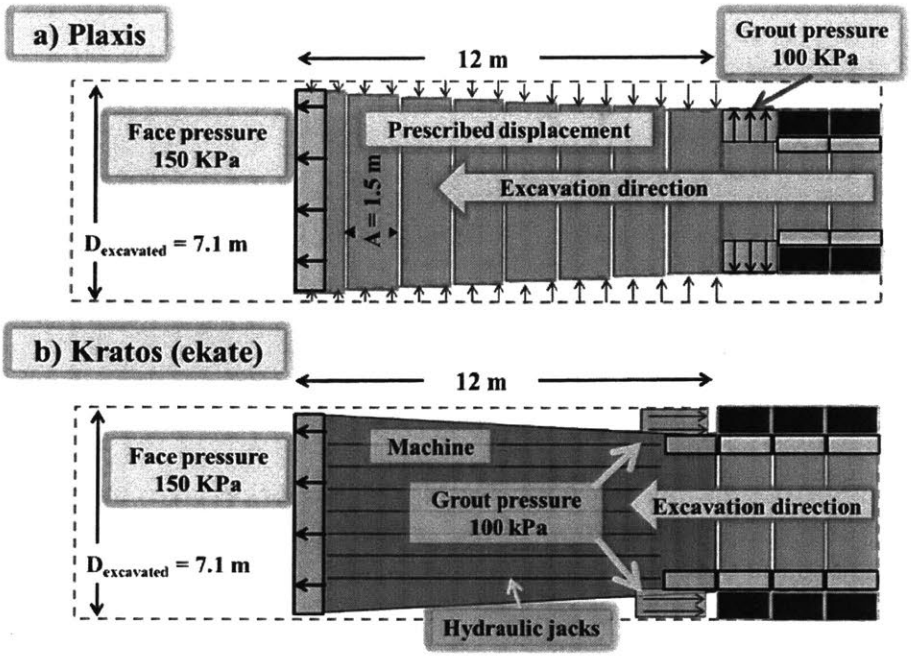

Figure 2.36 Modelling approaches for EPB mechanized tunneling using: a) Plaxis 3D^{TM} b) Kratos-Ekate for the Crossrail Project in London (Founta et al., 2013)

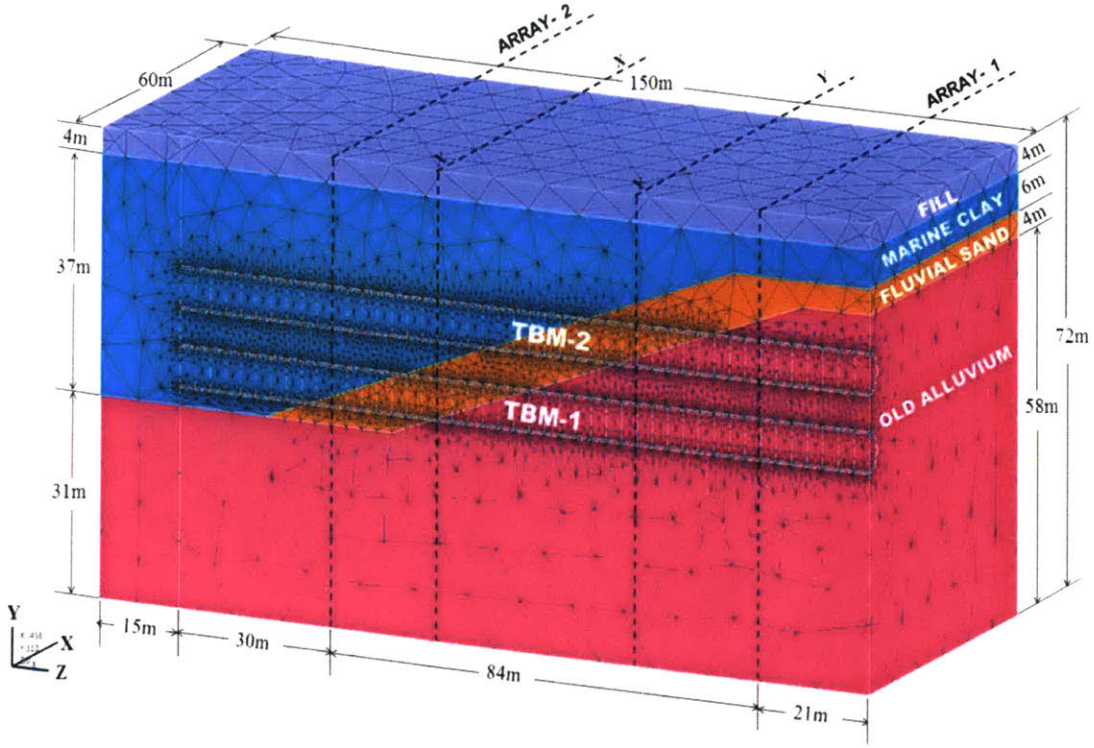

Figure 2.37 3D finite element model used to study mixed soil conditions in the (MRT) project in Singapore (Su, 2015)

3 Analysis of face stability

3.1 Introduction

Ensuring face stability can be one of most demanding tasks in a shield tunneling project especially when dealing with mixed face conditions involving soil layers with contrasting strength and hydraulic properties. Although, the control of face pressures helps to minimize the surface settlements, it is not uncommon large settlements or sinkholes to disrupt the construction of a project[12] (Shirlaw, 2008). A tunnel collapse can have catastrophic consequences for a project and our main goal is to provide a clear understanding of how different factors including soil type (cohesive vs frictional), soil stratigraphy, soil properties, closed face control parameters and tunnel geometry can affect stability. A review of the commonly used methods to estimate face stability was presented in section 2.2. The current analyses are compared with prior results published in literature and included new results for face stability in frictional materials (sands), cohesive materials (clays) and mixed face conditions.

3.2 Undrained Face Stability in Clays

In this section we compare the stability of a tunnel heading excavated in a uniform clay layer for i) the unlined case (no lining system present), $P=\infty$, Figure 2.10) and ii) the fully lined case (immediate support directly behind the heading, P=0, Figure 2.10). We describe in detail the different methodologies used for the development of each model and we analyze how the

[12]A detailed list of notable tunnel failures is provided by CEDD (2015)

collapse mechanism depends on lined vs unlined conditions, tunnel geometry and clay properties.

Figure 3.1 shows the geometry of interest for undrained tunnel instability in low permeability clay. The numerical analyses consider a circular tunnel of diameter, D with cover depth, C embedded in uniform clay stratum of total unit weight, γ. We consider stability for two cases: i) an unlined tunnel, represented as a plane strain problem, where stability is maintained by an internal pressure (σ_f; Figure 3.1a) and ii) a fully lined tunnel where face stability is controlled by a uniform pressure, σ_f (Figure 3.1b, 3D geometry). In all cases we assume that the tunnel is embedded within a deep layer of clay, where undrained shear strength can vary linearly with depth, z:

$$s_{uz} = s_{u0} + \rho z \qquad (3.1)$$

where s_{u0} the undrained shear strength at the surface.

3.2.1 Unlined tunnel

The case of an unlined tunnel excavation is simulated using a 2D plane strain model with a single stratigraphic unit using Plaxis 2D-AE^{TM} software (Brinkgreve et al., 2014). Figure 3.2 shows a typical mesh (C/D=2) used in baseline analyses. The current example uses a reference tunnel diameter, D=7.1m (cf., Founta and Whittle, 2016) with far field boundaries far from the tunnel centerline to minimize effects on ground deformations and stability mechanisms. The clay unit is simulated using the linearly-elastic, perfectly-plastic Mohr-Coulomb (M-C) model.

The current implementation assumes undrained shear conditions[13] (i.e., there is no migration of pore water within the clay mass over the time frame of tunnel construction) with friction angle $\varphi = 0^o$, undrained shear strength at the ground surface $s_{u0} = 10 - 150\ kPa$, Poisson's ratio $v' = 0.25$ ($v_u \approx 0.5$, for undrained conditions) and total unit weight, $\gamma = 20\ kN/m^3$. The analyses assume that the groundwater table is coincident with the ground surface with hydrostatic initial pore pressures, and in situ stresses with $K_0 = 1.0$. Unlined tunnel excavation is modeled by deactivating the solid elements inside the tunnel section, and applying a uniform radial pressure σ_f over the tunnel cavity.

The stress reduction technique, also known as 'c-phi' reduction method (Brinkgreve and Bakker, 1991) was used to calculate the global safety factor, FS, as explained in section 2.2.1. According to this method, the shear strength parameter, s_u is successively reduced to a value $s_{u\,mob}$ at which failure occurs in the soil body (i.e. uncontrolled soil deformations). Each analysis is preformed using a step advancement that gradually decreases the initial strength, s_u by an incremental multiplier M_{sf}, until both soil mass collapses (this can be checked by ensuring that a failure mechanism has formed in the soil mass) and a constant ΣM_{sf} value is achieved (see example in Figure 3.3a). Hence, we find the mobilized undrained strength $s_{u\,mob}$ that would lead to failure, as follows:

$$\frac{s_u}{s_{u\,mob}}\left(= \Sigma M_{sf}|_{failure}\right) \rightarrow FS \qquad (3.2)$$

where $s_{u\,mob}$ is the undrained strength at which equilibrium is lost at a selected support pressure, σ_f and s_u (the undrained strength value used as an input in our analysis, Figure 3.3b).

[13] i.e. Method B in the terminology of Plaxis

For the typical case presented in Figure 3.3 we consider an unsupported unlined tunnel with C/D=2 and s_u=150 kPa. The numerical analysis produced a value of $\Sigma M_{sf}|_{failure}$=1.6, so the critical value of undrained strength that would lead to collapse is calculated as $s_{u\,mob}$ =94 kPa. The subsequent figures use the reference undrained strength $s_u = s_{u\,mob}(i.e. FS = 1)$, when considering collapse mechanisms and presenting the undrained strength, tunnel depth and face pressure combinations that would lead to collapse.

A variety of tunnel geometries were considered for the analyses ranging from shallow tunnels, $\frac{C}{D}$ = 1 to deeper tunnels, $\frac{C}{D}$ = 5. Figure 3.4 compares the effects of cover depth ratio, C/D, on the ratio of cavity pressure to the reference undrained strength, σ_f/s_{u0}, where s_{u0} is the reference strength at the ground surface for conditions simulated in centrifuge model tests reported by Mair (1979). The physical models used homogeneous kaolin with $\rho = 0$ and $\frac{\gamma D}{s_{u0}} = 2.6$. Figure 3.4 shows that the computed stability ratio can be described by a linear relation:

$$\frac{\sigma_f}{s_{u0}} = 2.105\frac{C}{D} - 1.5363 \qquad (3.3)$$

which provides a very good match to the experimental results by Mair (1979).

Results examining the effect of different undrained strength gradients, ρ, were compared to upper and lower bound solutions obtained by Numerical Limit Analysis method (NLA; Wilson et al., 2011) for ratios $\frac{\rho D}{s_{u0}} = 0 - 1$. As shown in Figure 3.5, the current results are within the reported upper and lower bounds for all selected soil properties and hence we have a successful baseline that can be used to examine more complicated profiles and geometries.

In order to understand the mechanisms involved in face stability it is important to observe how the completed failure mechanisms change for different cover-diameter ratios, C/D. Figure 3.6 depicts the failure mechanisms for unsupported (σ_f =0) unlined tunnel excavations in homogeneous (ρ=0) clay with cover-diameter ratios C/D=1.0 – 4.0. The failure mechanisms are illustrated using the magnitudes of incremental ("instantaneous") displacement vectors, $|\Delta u|$ occurring during a single calculation step at the point of collapse, normalized by their maximum value, $|\Delta u_{max}|$. The contours of the normalized displacement increments $\Delta u/\Delta u_{max}$ are very useful for observing the developed mechanisms when failure occurs (Brinkgreve et al., 2012). For C/D=1 (shallow tunnel) the failure mechanism extends to the surface with large displacement increments ($|\Delta u|/|\Delta u_{max}|$ >0.75) occurring right above the tunnel axis, whereas for deeper tunnels (C/D≥4) the mechanism changes with the larger displacement increments now localized around the tunnel cavity and smaller displacements $|\Delta u|/|\Delta u_{max}|$ <0.5 at the surface.

A variety of normalization methods were considered in order to interpret the results for inhomogeneous clay profiles ($\rho \neq 0$), using a dimensionless analysis according to the Buckingham π theorem (Buckingham, 1914). The current analyses, (contrary to prior work) uses s_u as one of the independent variables, while selecting the soil unit weight, γ and the tunnel diameter, D as repeating variables. In this way, we are able to study the dependency of the face stability on undrained strength of the soil, s_{u0}, strength gradient, ρ, and tunnel cover, C using four dimensionless groups:

$$\frac{\sigma_f}{\gamma D} = f\left\{\frac{s_{u0}}{\gamma D}, \frac{\rho}{\gamma}, \frac{C}{D}\right\} \quad (3.4)$$

The computed stability results are then re-plotted using the aforementioned normalization as shown in Figure 3.7. Figure 3.7a shows the case of an unsupported tunnel cavity, $\frac{\sigma_f}{\gamma D} = 0$ (zero pressure at the tunnel cavity) . For homogeneous soil profiles, ($\frac{\rho}{\gamma} = 0$), a higher reference strength s_{u0} is required to ensure stability for deeper tunnels. This is reasonable as increased tunnel depth is associated with higher geostatic stresses and hence, higher strength to ensure stability. The relationship between the critical value of s_{u0} and C/D becomes linear for tunnels with C/D>3 (see Figure 3.8) and this can be attributed to the fact that there is a switch in the failure mechanism from shallow to deep tunnels (as suggested in Figure 3.6). At higher strength gradients, $\frac{\rho}{\gamma}$, lower values of reference shear strength at the surface, s_{u0} are required. This can be attributed to the strong dependency of tunnel stability on the soil strength at the springline elevation ($s_{uH} = s_u|_{z=H}$) rather than at the ground surface level. It is interesting to observe that for $\rho/\gamma \approx 0.17$, the required undrained shear strength at the surface, s_{u0} remains constant for different tunnel cover ratios, C/D (Figure 3.7a). This case corresponds to values of undrained strength at the springline, s_{uH} that are appropriate to ensure stability for each tunnel geometry. Similarly, we note that for $\rho/\gamma > 0.17$, the strength increase with depth becomes so large that lower reference strength, s_{u0} is required to ensure stable conditions for deeper tunnels. The effect of the strength profile with depth is also examined for the cases of radial support pressure ratios $\frac{\sigma_f}{\gamma D} = 0.7$ and 1.4 (Figure 3.7a, b and c).

Figure 3.9, shows contour lines for the three related support ratios at the tunnel cavity, $\frac{\sigma_f}{\gamma D} = 0$, 0.7 and 1.4. These have been combined in order observe directly the effects of the four key parameters on face stability. At higher support ratios, the critical strength decreases as the contour lines corresponding to the same ρ/γ value are horizontally translated towards smaller strength ratios. Figure 3.7 and Figure 3.9 graphs can be used to calculate the required shear strength to ensure stability for the case of unlined tunnels for non-homogeneous clay layers. The critical safety factor can be calculated for the in situ undrained strength value, s_u^*, as follows:

$$FS = \frac{s_u^*}{s_u} \qquad (3.5)$$

where s_u is the critical undrained strength calculated from the stability analyses.

3.2.2 Lined Tunnel

The prior framework developed to study stability for unlined tunnels in clay is extended to study stability in fully lined tunnels, where face pressure is applied at the heading. This case involves a 3D geometry which is developed using Plaxis 3D^{TM} (Brinkgreve et al., 2012). Figure 3.10 shows the model with typical parameters based on a prior study for Crossrail (Founta and Whittle 2016, Appendix B). The model uses curved plate elements to represent the lining system, for the tunnel embedded within the clay stratum. The current analyses assume a

uniform pressure, σ_f, acting over the face of the tunnel. This approach ignores self-weight of the earth paste[14] or slurry in the face chamber (for EPB and slurry shields, respectively).

The 3D model used to study the lined tunnel excavation in homogeneous clay is presented in Figure 3.10. The selected model dimensions were 60m by 60m by 25m for the depicted C/D=2 (D = 7.1m) case and were appropriately adjusted for deeper tunnels to ensure that the computed failure mechanism isn't affected by boundary proximity. The MC soil model was used for the clay assuming undrained shear conditions (i.e., there is no migration of pore water within the clay mass over the time frame of tunnel construction), the groundwater table is coincident with the ground surface with hydrostatic initial pore pressures, and in situ stresses assume K_0 = 1.0. Tunnel excavation is simulated by the deactivation of the soil elements within the tunnel cavity, the activation of the plate elements representing the lining and the application of uniform support pressure with depth σ_f at the face of the excavation.

As in the previous 2D simulations, a c-phi stress reduction method (Brinkgreve and Bakker, 1991) was used to calculate safety factor while subsequent results report the critical stability condition for a reference undrained shear strength, s_{uH} (Figure 3.10). A variety of tunnel geometries were considered, ranging from shallow, C/D=1 to deeper tunnels, C/D=5. Three different strength profiles with depth were examined starting with ρ = 0 (representing the homogeneous clay layer) to increasing strength with depth for $\frac{\rho D}{s_{u0}} = 0.5$ and 1.0.

[14] In practice the weight of the earth paste is modified by mixing foam and other soil conditioning additives used with EPB machines

An initial set of analyses was conducted to study the effects of different cover depth-diameter ratios, C/D, to face stability. The numerical analyses results were compared to prior published results to ensure that appropriate mesh and model dimensions were used (Figure 3.11). These included upper (kinematic approach) and lower (static approach using spherical stress field) bound solutions by Davis et al. (1980), upper bound limit analysis solution (kinematic approach) and 3D numerical analyses by Mollon et al., (2013), upper bound (kinematic approach) and lower bound (static approach) solutions by Sloan, (2013) and an empirical design line based on centrifuge model tests by Kimura and Mair (1981). The current results fall in the middle of the range of the predictions of the different methodologies and are in good agreement with the upper bound solutions by Sloan, (2013) and Mollon et al., (2013).

In order to understand how face stability for the lined case is affected by the cover-diameter ratio, C/D it is helpful to compare the computed failure mechanisms. Figure 3.12 depicts the developed failure mechanisms for unsupported (σ_f=0) lined tunnel excavations in homogeneous (ρ=0) clay with cover-diameter ratios C/D = 1.0 – 5.0. The plotted contours correspond to normalized incremental ("instantaneous") displacements, $|\Delta u|/|\Delta u_{max}|$, at the point of collapse. For C/D=1 (shallow tunnel) the failure mechanism extends to the surface with large displacement increments ($|\Delta u|/|\Delta u_{max}|$ >0.75) occurring close to tunnel invert and small deformations ($|\Delta u|/|\Delta u_{max}|$ <0.1) occurring at the ground surface. The mechanism changes for deeper tunnels (C/D≥3) as the failure envelope does not reach the surface and the mechanism is localized around the tunnel face.

The subsequent analyses study face stability by normalizing the critical support pressure, σ_f, using the same dimensionless groups used for the unlined case (Eq. 3.4). Figure 3.13 summarizes face stability for tunnels at cover depth to diameter ratios, C/D = 1.0 - 5.0 at the selected levels of face pressure, $\sigma_f/\gamma D$ = 0.0 (open face), 0.5, 1.0. Figure 3.13 depicts the relationship between the cover depth ratio C/D, the critical undrained strength ratio $\frac{s_{u0}}{\gamma D}$, the support ratio $\frac{\sigma_f}{\gamma D}$ and the strength profile with depth. Generally, we can observe a trend similar to the unlined case, where for deeper tunnels a higher s_{u0} is required to ensure stability. For the case of an unsupported heading, $\frac{\sigma_f}{\gamma D} = 0$ and a constant strength profile with depth, $\frac{\rho}{\gamma} = 0$, there is an almost linear relationship between $\frac{s_{u0}}{\gamma D}$ and C/D, for C/D= 1 to 3 (and a small change in gradient for C/D>3). This seems to be the case for all the different strength profiles, $\frac{\rho}{\gamma} =$ 0 to 0.1, with a change in gradient at C/D≈3. This switch can be attributed to the transition from a mechanism extending to the surface (shallow tunnel) to a local failure mechanism (deep tunnel, cf. Figure 3.12). As the face pressure increases ($\frac{\sigma_f}{\gamma D} = 0.5, 1.0$, Figure 3.13 b and c) stability can be maintained in clays with lower shear strength.

A clearer understanding of the dependency between the four considered parameters is given in Figure 3.14, which overlays results for the three selected values of face pressure. The contour lines show a distinct change in slope at C/D = 2.5 – 3.0 reflecting changes in predicted failure mechanisms (Figure 3.12) while there is a more gradual impact of cover depth-diameter ratio on results for higher face pressures. The contour lines corresponding to the same ρ/γ value appear to have a generally similar orientation, being horizontally translated towards smaller

strength ratios as the applied pressure ratio increases, that means that the effect of the face pressure to the required soil strength is independent of the tunnel elevation.

As discussed in the previous paragraph there is a linear dependency of the required shear strength to the tunnel springline depth, H (i.e. the geostatic stresses at the level of the tunnel). In order to remove effects of geostatic stresses on the face stability, the results have been replotted normalizing the critical support pressure, σ_f, and the referenced undrained strength at the springline elevation s_{uH}, by the unit weight-springline depth factor, γH. This revised normalization allows a better understanding of the dependency of the tunnel stability to the selected parameters by using the resulting four dimensionless groups:

$$\frac{\sigma_f}{\gamma H} = f\left\{\frac{C}{D}, \frac{s_{uH}}{\gamma H}, \frac{\rho}{\gamma}\right\} \qquad (3.6)$$

Figure 3.15 compares the behavior of lined and unlined tunnels with unsupported heading ($\frac{\sigma_f}{\gamma H}$ =0) in homogeneous clay in order to study the effect of the tunnel depth on the required strength. Both the lined and unlined cases follow a similar trend with requiring significantly larger strength ratio close to the surface due to the change in the collapse mechanism for shallow tunnels. As expected the lined case requires less soil strength for stability since the lining provides full support to the tunnel cavity and only the face is prone to collapse.

The results for the homogeneous analyses demonstrate that the critical undrained strength ratio $s_{uH}/\gamma H$ is independent of the strength distribution with depth, ρ/γ, and hence, stability of the tunnel depends only on the undrained shear strength at the tunnel springline $s_{uH}/\gamma H$

(Figure 3.16). This can be easily explained if we consider that the springline is the most vulnerable location as it receives the least support from the lining.

Based on the previous observation that $s_{uH}/\gamma H$ ratio is independent of the strength increase ratio ρ/γ, all the computed data for the single clay stratum, can be combined into Figure 3.17a and b. These results can then be used to calculate the minimum required face support for any lined tunnel in clay (required input: dimensions and soil properties). Figure 3.17a shows that for cover depths C/D>3, the critical undrained strength ratio $s_{uH}/\gamma H$ remains constant (Figure 3.17a). This can be attributed to the transition from a global mechanism that extends to the surface (shallow tunnel) to a local failure mechanism (deep tunnel, C/D>3), as depicted in Figure 3.12. For deeper tunnels the cover depth is no longer part of the failure mechanism and hence no longer affects stability in itself[15]. In Figure 3.17b we can see that there is an almost linear correlation between the reference undrained shear strength at the tunnel springline $s_{uH}/\gamma H$ and the critical support pressure, σ_f:

$$s_{uH} = \tilde{s}_{uH}\left(1 - \frac{\sigma_f}{\gamma \mathrm{H}}\right) \qquad (3.7)$$

where $\tilde{s}_{uH}$ is the reference undrained strength that would lead to collapse for an unsupported heading ($\sigma_f = 0$)[16]. Figure 3.17 can be used to provide a quick estimation of the safety factor for a lined tunnel excavation by calculating the required reference shear strength, s_{uH} to

---

[15] The effect of the tunnel depth in stability due to the increase in geostatic stresses is removed by the considered normalization (Eq. 3.5).

[16] In order to achieve stability in a medium with zero shear strength ($s_{uH} = 0$), which essentially behaves like a fluid, we would need to apply pressure equal to the geostatic stresses at the springline to ensure stability.

ensure stability dividing it with the in situ measured strength of the clay, s_{uH}^{*} (according to Eq. 3.5).

3.3 Undrained Stability for Mixed Face Conditions

The previous section has analyzed the face stability where excavations occur in either homogeneous clay or a single clay unit exhibiting a linear variation in undrained strength with depth. More complex face stability conditions occur when the tunnel face involves two clay units with strongly contrasting differences in undrained strength. This is one example of a mixed face condition commonly encountered during tunneling projects. This section extends the prior analyses for a two layer system, Figure 3.18, where a soft overlying layer with undrained shear strength, s_{uT}, overlies a much stiffer unit ($s_{uB} > s_{uT}$). The current set of analyses introduces the embedment ratio D_T/D(Figure 3.18), where D_T is depth of the stratigraphic interface below the tunnel crown. Cases with D_T/D>0, correspond to mixed face conditions that involves excavation of both clay types (in the face chamber of the EPB mode). In the current analyses use ratios of $\frac{D_T}{D}$= -0.75 to 0.75 for C/D=1-5, and a relative strength ratio, s_{uB}/s_{uT} = $1.5, 2.0, 5.0, 10.0$. The method of analyses uses the c-phi strength reduction method (Brinkgreve and Bakker, 1991) to establish instability where:

$$FS = \frac{s_{uT}}{s_{uT\,mob}} = \frac{s_{uB}}{s_{uB\,mob}} \qquad (3.8)$$

where $s_{uT\,mob}$ and $s_{uB\,mob}$ are reduced strength, needed to destabilize the face. Instability occurs when FS=1, $s_{uT} = s_{uT\,mob}$ and $s_{uB} = s_{uB\,mob}$.

The effects of mixed face conditions can be summarized by considering how collapse failure mechanisms change for different embedment and relative strength ratios (D_T/D, s_{uB}/s_{uT}). Figure 3.19 shows the effect of the embedment ratio, D_T/D, for the case C/D=2, s_{uB}/s_{uT}=2 for unsupported heading ($\frac{\sigma_f}{\gamma H}$=0). The tunnel is fully embedded within the stiff layer for the cases, $D_T/D \leq 0$. For these cases the location of the layer interface has small effect on the required strength, $s_{uT}/\gamma H$. For D_T/D=-0.75 stability is controlled by the homogeneous stiff clay layer (with no effect of the overlying soft layer), forming a failure mechanism similar to the homogeneous case as shown in in Figure 3.12 for C/D=2. For $D_T/D \geq 0$ the tunnel becomes gradually embedded within the top soft layer, and higher values of undrained strength, $s_{uT}/\gamma H$ are required to maintain stability. The failure mechanism changes when the tunnel becomes embedded in the soft layer and the larger incremental deformations ($|\Delta u|/|\Delta u_{max}| > 0.75$) now occur in the upper part of the face within the soft clay layer.

The effect of the relative strength ratio, s_{uB}/s_{uT} is presented in Figure 3.20, for the case of C/D=2 and D_T/D=0.25. It is very interesting to observe the transition from a failure mechanism that involves the full face in the homogeneous case, $s_{uB}/s_{uT} = 1$, to a failure mechanism where the larger incremental deformations ($|\Delta u|/|\Delta u_{max}| > 0.75$) occur only within the upper soft layer for s_{uB}/s_{uT}=2 or the majority of the mechanism ($|\Delta u|/|\Delta u_{max}| > 0.05$) is enclosed within the upper layer for $s_{uB}/s_{uT} = 10$. For relative strength ratio, $s_{uB}/s_{uT} \geq 4$, any further increase of the strength ratio s_{uB}/s_{uT} has minimal effect on the critical strength, $s_{uT}/\gamma H$ at collapse.

As discussed in section 3.2.2 there is a linear correlation between face pressure $\sigma_f/\gamma H$ and strength ratio s_u described by Eq. 3.7: $s_u = \tilde{s}_u\left(1 - \frac{\sigma_f}{\gamma \mathrm{H}}\right)$, where $\tilde{s_u}$ is the required strength at zero face pressure. Consequently, in order to understand how the critical undrained strength $s_{uT}/\gamma H$ depends on the embedment ratio D_T/D and strength ratio s_{uB}/s_{uT} for two layered clays, we can initially focus on the case of zero support pressure at the face, $\sigma_f = 0$ as shown in Figure 3.21a and b. It is interesting to observe that for a given embedment ratio D_T/D there is a threshold reference strength ratio, s_{uB}/s_{uT}, which defines the lower bound of $\tilde{s}_{uT}/\gamma H$. This threshold ratio decreases as the embedment ratio D_T/D increases. In the cases where $D_T/D \rightarrow 1$, for all values of s_{uB}/s_{uT} we have that $\tilde{s}_{uT}/\gamma H$ = 0.12 (i.e. the critical undrained strength ratio for the uniform case, see Figure 3.17) hence stability depends only on $\tilde{s}_{uT}$, whereas for $D_T/D \rightarrow -1$, $\tilde{s}_{uB}/\gamma H = 0.12$ (i.e. $\tilde{s}_{uT}/\gamma H = 0.12/(s_{uB}/s_{uT})$) hence stability depends only $\tilde{s}_{uB}$.

Figure 3.22 and Figure 3.23 summarize the effects of the embedment ratio on the face stability for shallow, C/D=1 and deep tunnels, C/D>3 with s_{uB}/s_{uT}=5. For the case of $D_T/D = 1.0$, face stability is only affected by the upper clay unit strength, $s_{uT}/\gamma H$ and the results match the predictions for homogeneous clay presented previously in section 3.2.2. For example, at C/D=1 with $\sigma_f/\gamma H$=0, $s_{uT}/\gamma H$ = 0.12 which agrees with the homogeneous case in Figure 3.14. At the opposite extreme (when $D_T/D = -1.0$), the tunnel is embedded in the lower, stiff clay layer and the heading stability is only affected by the lower clay unit strength, $\frac{s_{uB}}{\gamma H}$. Hence, for the previous example at C/D=1 with $\sigma_f/\gamma H$=0, $\frac{s_{uB}}{\gamma H}$ is now equal to the homogeneous value of 0.12 and thus $\frac{s_{uT}}{\gamma H}$ = 0.12 / 5 = 0.024 (as s_{uB}/s_{uT}=5). The complete results in Figure 3.22 and Figure 3.23 show how the mixed face transition affects the face pressure required to ensure stability

(for s_{uB}/s_{uT}=5). For example, if C/D=1, D=10m (H=15m) and γ=20kN/m^3, then the values s_{uT}=15kPa and s_{uB}=75kPa. This corresponds to $s_{uT}/\gamma H$=0.05. In this case, stability of the mixed face can be interpreted from the contour of $s_{uT}/\gamma H$=0.05 in Figure 3.22. The required face pressure then increases from $\sigma_f/\gamma H$=0 at D_T/D=0.2, to 0.6 at D_T/D=1.

For the case of a deep tunnel, C/D>3, with a top layer with an undrained strength, $s_{uT}/\gamma H = 0.02$ and $s_{uB}/s_{uT} = 5$, we can see that for full embedment within the stiff layer, $D_T/D = -1$, the face is stable without any support ($\sigma_f/\gamma H = 0$), while as we transition to the soft layer, $D_T/D = 1$, a face support of $\sigma_f/\gamma H < 0.8$ would lead to collapse.

3.4 Drained face stability in sands

This section considers the face pressures needed to control the stability of a lined tunnel in cohesionless sand. The analyses make the key assumption that the slurry in the face chamber provides an impermeable membrane (of section 2.1.3) while there are free drainage conditions within the surrounding high permeability sand mass.

Water pressures are hydrostatic and fully defined by the groundwater table. Figure 3.24 shows the reference problem geometry and boundary conditions. The selected model dimensions were 60m by 40m by 25m (for the depicted C/D=2 case with D ≈ 7m and were appropriately adjusted for deeper (C/D=3) or shallower tunnels (C/D=1) to ensure that the computed failure mechanism isn't affected by boundary proximity. The groundwater pressure at the tunnel is H_w. The face stability of the homogeneous sand profile is studied under dry, fully or partially submerged water conditions ($H_w \leq 0$, $\frac{H_w}{D} \geq 1, 0 \leq H_w/D \leq 1$, respectively). Additionally, the

effect of the slurry density on the tunnel face stability is examined for density ratios $r_G = \rho_g/\rho_w = 0\ to\ 1.5$, where ρ_g is the mass density of the slurry and ρ_w the mass density of water. Sand behavior is simulated using the Mohr-Coulomb, M-C (linearly elastic perfectly plastic soil model) with a constant internal friction angle, ϕ, (cohesionless case, c=0), Poisson's ratio $\nu' = 0.25$ with initial equilibrium stresses defined by $K_0 = \sigma'_{ho} = \sigma'_{vo} = 1.0$. The FE analyses assume zero dilation at failure ($\psi = 0^o$) and hence the MC model assumes a non-associated flow rule.

The tunnel excavation is simulated by i) the deactivation of the soil elements within the tunnel cavity, ii) simultaneous activation of the impermeable curved plate elements representing the linin and iii) the application of a slurry pressure, σ_f, at the face of the excavation (increasing hydrostatically with depth based on the assumed value of ρ_g) and the activation of a no flow boundary at the excavation face that simulates the formation of filter cake (as described in section 2.1.3, see Figure 2.8) that prevents water from entering the tunnel cavity .

The stress reduction technique also known as the c-phi reduction method (Brinkgreve and Bakker, 1991, Sloan, 2013, Tschuchnigg et al., 2015) is used to calculate the global safety factor, FS:

$$FS = \frac{tan\varphi'}{tan\varphi'_{mob}} \qquad (3.9)$$

where φ'_{mob} is the mobilized friction angle needed to induce failure (for FS=1, $\varphi' = \varphi'_{mob}$).

For the performed analyses we selected the dimensionless groups to study based on the Buckingham π theorem and recommendations from prior work. Chambon and Corte (1994) showed a linear relationship between the measured support pressure at failure and the

diameter of the tunnel (in centrifuge model tests), making appropriate the selection of the tunnel diameter, D, as one of the key normalizing variables.

The second normalizing variable is the equivalent unit weight of the soil which is adjusted to reflect the different groundwater conditions as shown in Table 3.1. The value of γ_{eq} varies from $\gamma_d \leq \gamma_{eq} \leq \gamma'$ to represent the transition from dry to fully submerged conditions. We then study the effective support pressure and the buoyant unit weight for the soil and slurry using the following dimensionless groups:

$$\frac{[\sigma_f - u]_H}{\gamma_{eq} D} = f\left\{\frac{C}{D}, \frac{H_w}{D}, \varphi, r_G\right\} \qquad (3.10)$$

where H is the springline depth, $\sigma_f(z = H)$, and u$(z = H)$, are the face pressure and pore at the springline, D the tunnel diameter, C the cover depth, H_w the water table measured from the tunnel soffit. The soil strength is represented by the friction angle of the soil, φ, and the slurry by $r_G = \rho_g/\rho_w$ unit weight ratio (see Table 3.1 for definition).

3.4.1 Stability in Dry and fully submerged conditions

An initial set of analyses was conducted under dry conditions assuming a uniform pressure distribution that remains constant with depth ($r_G = 0$) in order to compare with experimental data by Chambon & Corte, (1994), Kirsch, (2010) and Plekkenpol et al., (2006) as well as published analyses by Anagnostou and Kovari, (1996), Anagnostou, (2012), Leca and Domieux, (1990), Mollon, (2010), Vermeer et al., (2002) as presented in section 2.2.2. Figure 3.25 a-c illustrates the effects of the friction angle, ϕ', on the computed failure mechanisms in dry sand. The figure shows the magnitude of the incremental displacements, $|\Delta u|$ occurring during single

step advancement normalized using the maximum occurring incremental displacement $|\Delta u_{\max}|$ at the point of failure. The failure mechanism propagates from near the invert of the tunnel at an angle but does not extend to the ground surface at higher friction angles. Vermeer and Ruse, (2001) and Mollon et al., (2011) reported that for that for the common values of C/D ≥ 1 and ϕ ≥ 20° the failure mechanism does not extend to the ground surface due to the arching effect, which supports the ground cover independent of the magnitude of its thickness. Figure 3.26 compares the computed face pressure from the current analyses, with experimental results and prior analytical solutions for dry sand. The current analyses are in very close agreement with numerical results presented by Vermeer et al., (2002) who estimated the collapse load by incrementally reducing the support pressure until collapse occurred. The results also show that limit equilibrium solutions by Anagnostou, (2012), upper bound solutions by Leca and Dormieux, (1990) and Mollon et al., (2011) are in good agreement with the current analyses.

Figure 3.27a and b summarize the effects of the friction angle on face pressures at collapse for dry and fully submerged tunnels at cover depth-diameter ratios of C/D = 0.7-3.0, respectively. The results show that the behavior is independent of C/D in both cases. This is in agreement with prior observations from centrifuge tests by Chambon & Corte, (1994), and 1-g model tests by Kirsch, (2010). Furthermore, the effective face pressure $(\sigma_f - u)/\gamma_{eq} D$ is independent of the friction angle for ϕ' ≥ 30°.

3.4.2 Effect of Groundwater Pressure

We have extended the analyses to consider face stability for homogeneous sand in conditions where the water table varies for H_w=0.0-1.0 as shown in Figure 3.28. In order to compare the

calculated collapse pressure for the different water levels we normalized the face pressure using the equivalent unit weight, γ_{eq}, and have compared the effective face pressure at the tunnel invert (z = C+D) as a reference level that ensures continuity among all these cases. The normalized support load at collapse is adapted to $\frac{[\sigma_f - u]_{z=C+D}}{\gamma_{eq} D}$. Here, Figure 3.28, clearly shows the role of the water table on face stability enabling control of σ_f at the invert. As explained previously the stability depends only on the conditions present at the tunnel opening while the overlying soil does not affect the critical face pressure. Hence, the face pressure remains constant for submerged ($H_w/D \geq 1$) or dry ($H_w \leq 0$) conditions respectively. The dry and fully submerged cases form an upper and a lower bound that encase all other cases ($0 \leq H_w/D \leq 1$). It should be noted that interpreting this graph can be misleading as the submerged case corresponds to a lower required effective face pressure compared to the fully submerged case. In order to clarify this, we can combine the case of a sand with $\varphi = 30°$, $\gamma_d = 16\ \mathrm{kN}/m^3$ and $\gamma_{sat} = 20\ \mathrm{kN}/m^3$ and a tunnel with a cover depth - diameter, C/D=1 (and D=7m) and compare the collapse load for dry, $H_w/D = 2$ and fully submerged cases, $H_w = 2D$ (water level coincides with the ground surface). The normalized face pressure at failure for the dry case is $\frac{[\sigma_f - u]_{C+D}}{\gamma_{eq} D}$ = 0.13 corresponding to $\sigma_f \approx 15$ kPa, while $\frac{[\sigma_f - u]_{C+D}}{\gamma_{eq} D}$= -0.05 for the fully submerged case, which implies $\sigma_f \approx 136.5$ kPa, i.e. although the effective normalized pressure is smaller for the submerged case, the magnitude of the actual support pressure is about 9 times larger!

3.4.3 Effect of slurry pressure

The effect of the slurry density on the tunnel face stability has been examined for a range of support with unit weight ratios, $r_G = 0$ - 1.0 in both dry and fully submerged cases. In Figure 3.29, we can observe the effect of the support pressure distribution with depth on the collapse mechanism, for the case of a friction angle ϕ = 30°. For a constant support pressure with the depth, $r_G = 0$, the computed collapse mechanism involves the whole face of the tunnel, while for a larger gradient, $r_G = 0.25$, only the top part of the cross-section is more vulnerable leading (i.e. the failure mechanism is limited to the upper part of the face). At this point, it is crucial to note that although the springline is the most vulnerable position for the exposed cross-section, there is a gradient r_G, for which the face pressure applied at the crown is so much smaller compared to the springline that a local collapse involving only the top part of the face is formed. This explains why for higher support pressure gradients, r_G we might require a higher support pressure at the springline. An indicative range of the most common tunnel construction methods is presented for dry and submerged conditions, such as slurry, EPB and pressurized air. It is very interesting to observe how the combination of the water conditions present along with the selected construction method can have significant effect on the required support pressure to ensure stability.

Figure 3.30 compares the current analyses with prior results from Anagnostou and Perazzelli, (2013) who employ a limit equilibrium method (with the method of slices). Overall, there is a very good agreement between the two methods especially for friction angles higher than $\phi > 20°$, which is very encouraging considering that quite different methodologies were used

(i.e. Anagnostou and Perazzelli, (2013) used a rectangular cross section to approximate the tunnel face).

Table 3.1 Definition of equivalent soil unit weight γ_{eq} and support unit weight ratio r_G

Water level		Equivalent soil unit weight γ_{eq}	Support unit weight ratio r_G
Dry	$H_w \leq 0$	γ_d	$\frac{\gamma_G}{\gamma_d}$
$0 \leq H_w \leq D$		$\frac{H_w}{D}\gamma' + (1 - \frac{H_w}{D})\gamma_d$	Not Applicable
Submerged	$H_w \geq D$	γ'	$\frac{\gamma_G - \gamma_w}{\gamma'}$

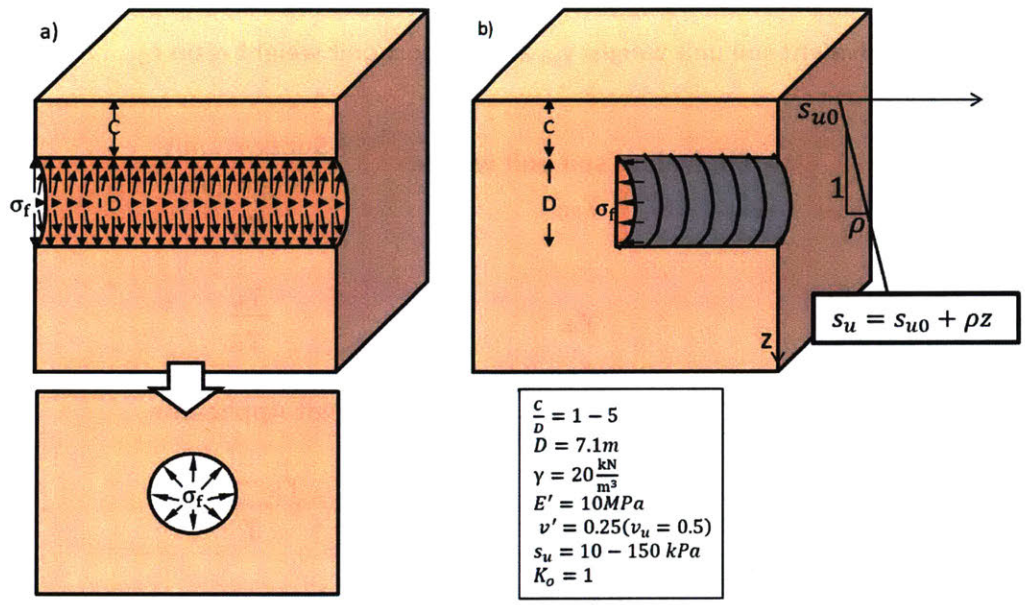

Figure 3.1 Geometries and properties considered for the a) 2D and b) 3D models

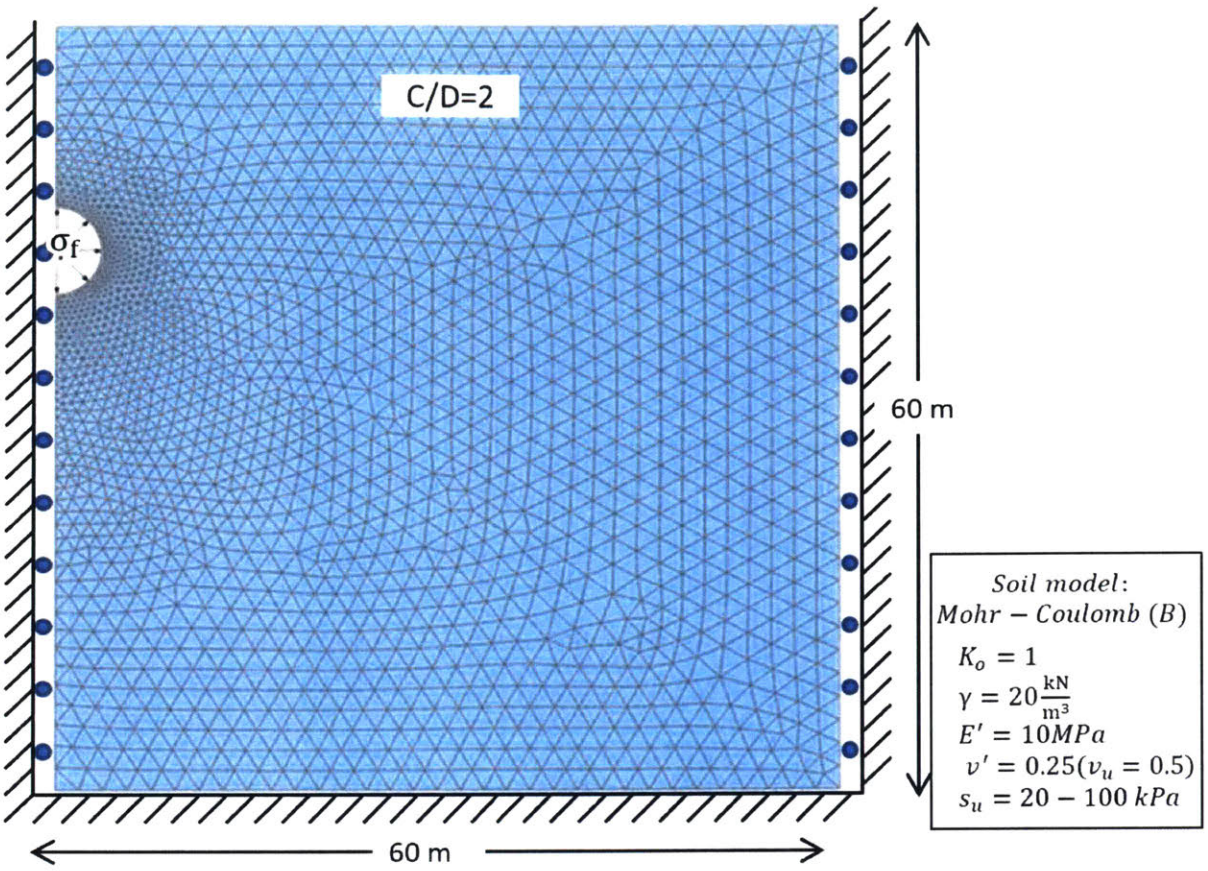

Figure 3.2 a) Example of finite element mesh and boundary conditions for Mesh and dimensions for unlined tunnel in clay with C/D=2

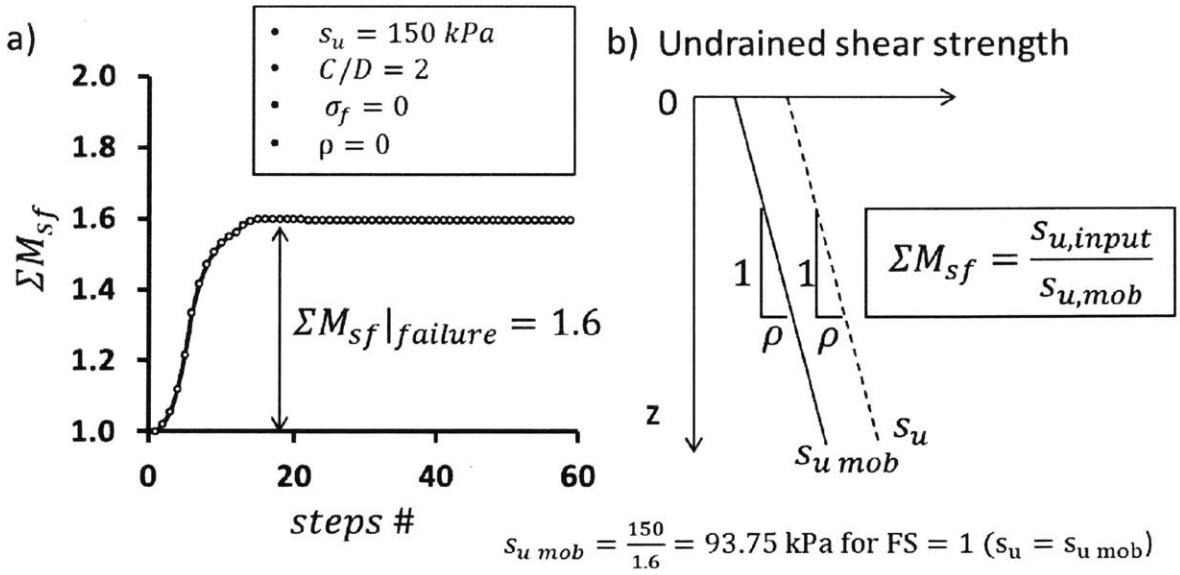

Figure 3.3 a) Load advancement steps vs strength reduction factor ΣM_{sf} and b) safety factor for strength reduction method

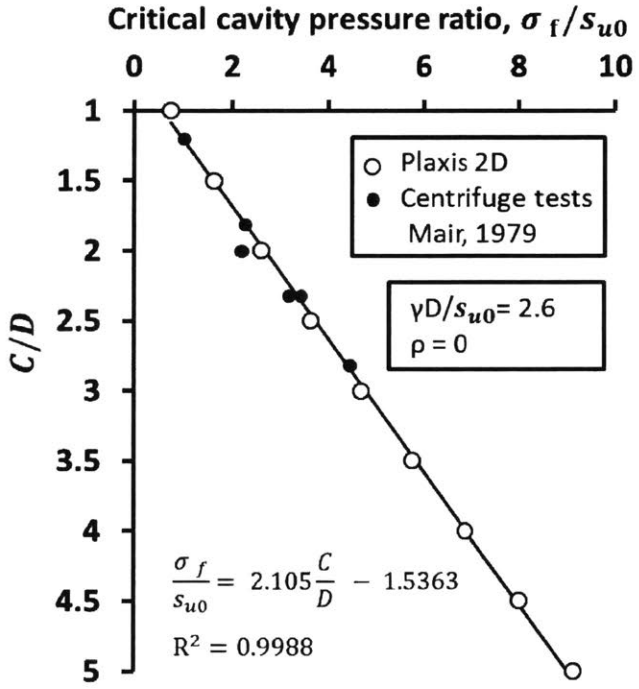

Figure 3.4 2D FE results using the safety reduction method compared to centrifuge data (Mair, 1979) for homogeneous soil profile and $\gamma D/s_{u0}$=2.6

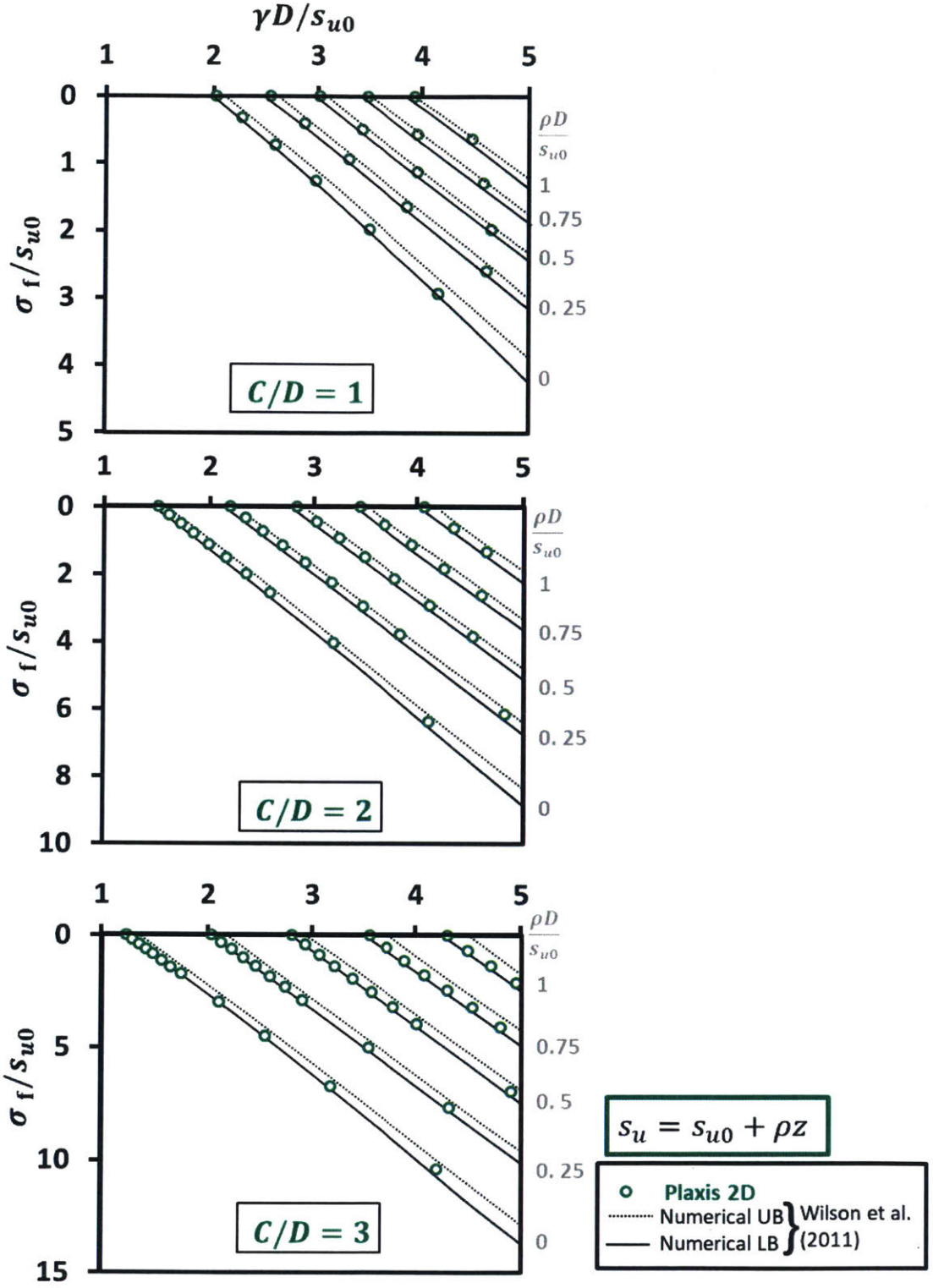

Figure 3.5 Comparison of 2D FE results using the safety reduction method with the upper bound and lower bound solution by Wilson et al., 2011 for a plane strain unlined tunnel in clay

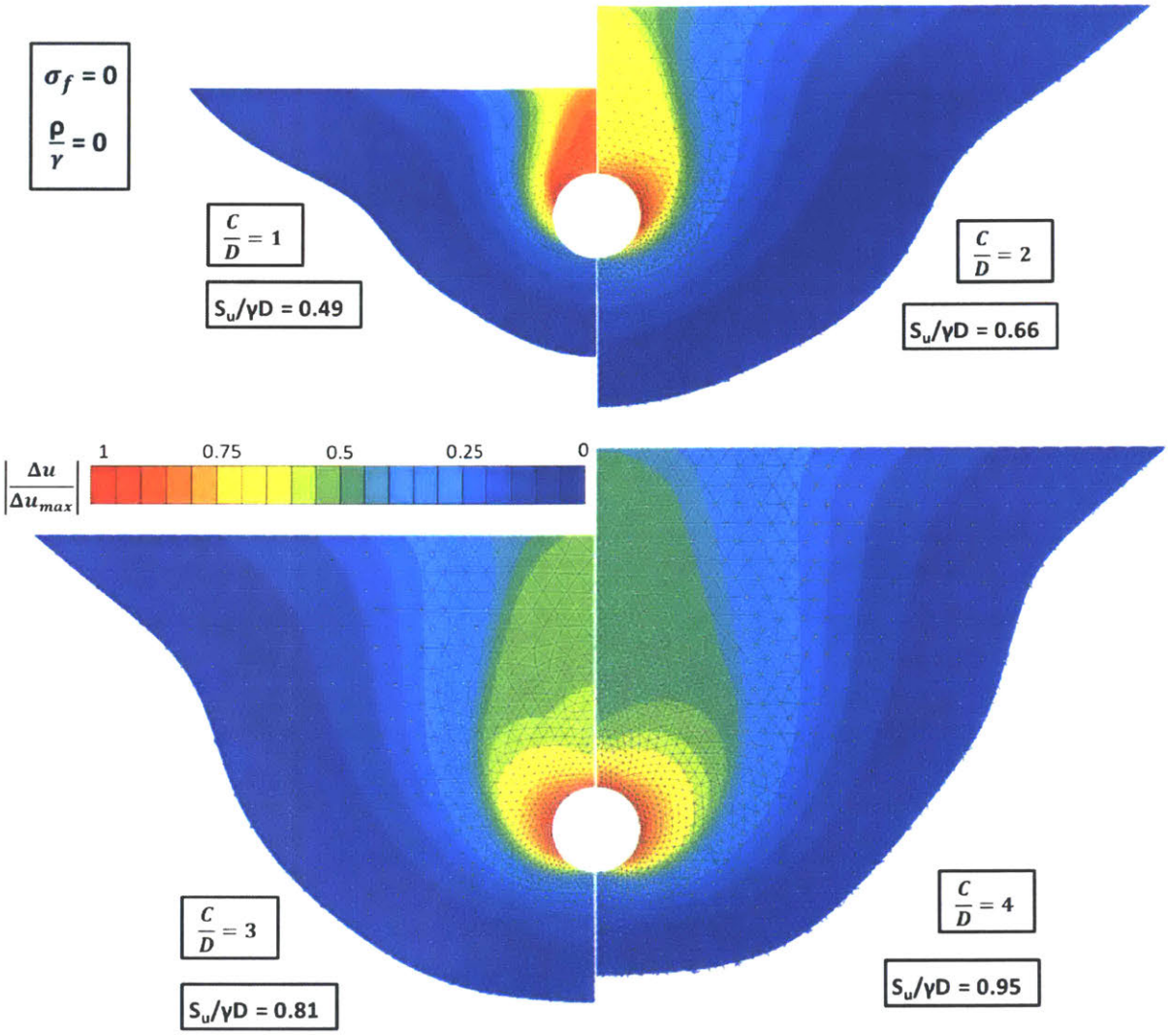

Figure 3.6 Failure mechanisms for unsupported (σ_f=0) excavation in homogeneous (ρ=0) clay for cover-depth-diameter ratios, C/D=1, 2, 3 and 4. Plots show $|\Delta u|/|\Delta u_{max}|$ at point of collapse

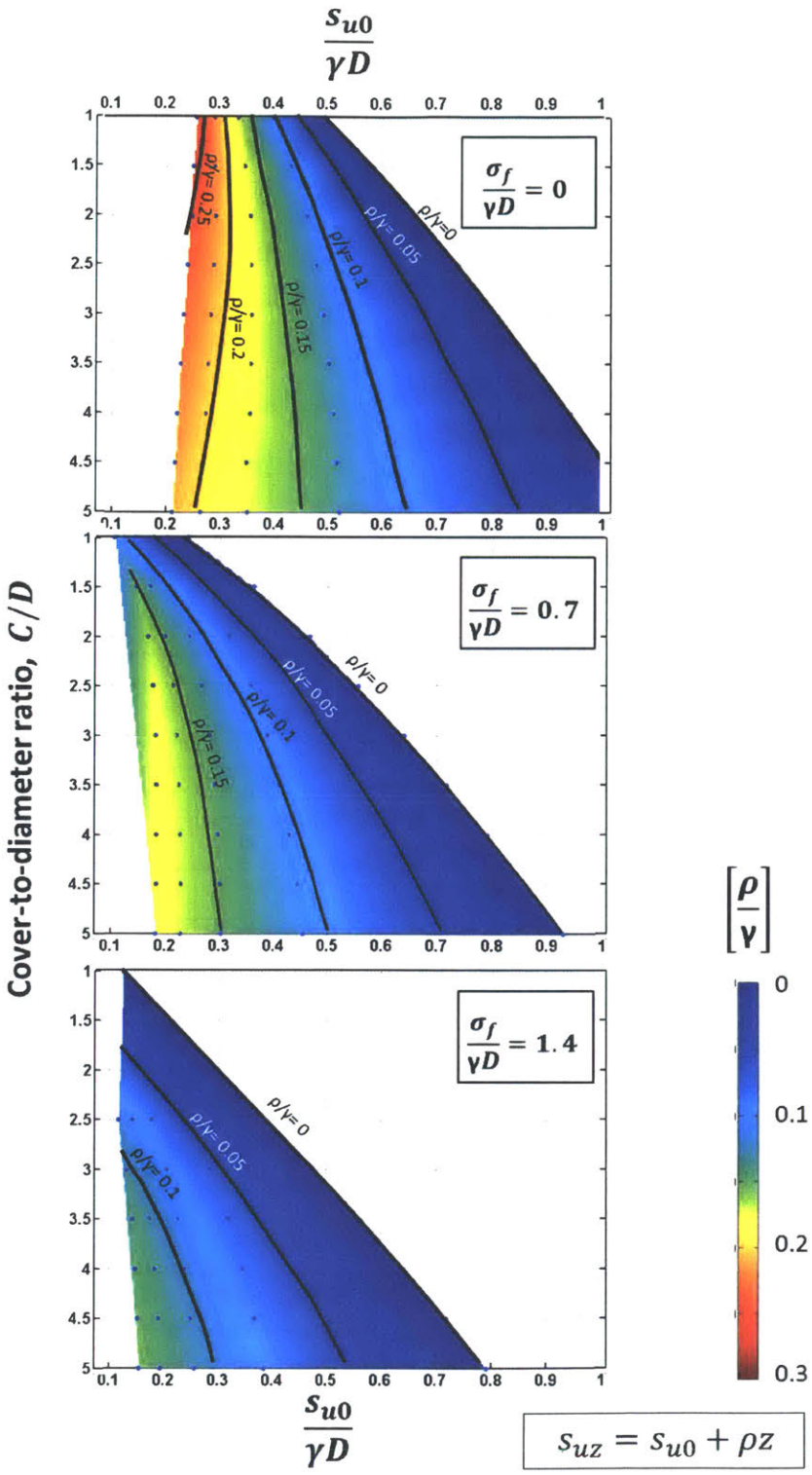

Figure 3.7 Contour plots of strength gradient with depth over unit weight ratio, ρ/γ in cover-depth-diameter ratio, C/D vs undrained strength at the surface ratio, $s_{u0}/\gamma D$ space for different support ratios at the tunnel cavity, $\sigma_T/\gamma D$ for the unlined case in clay.

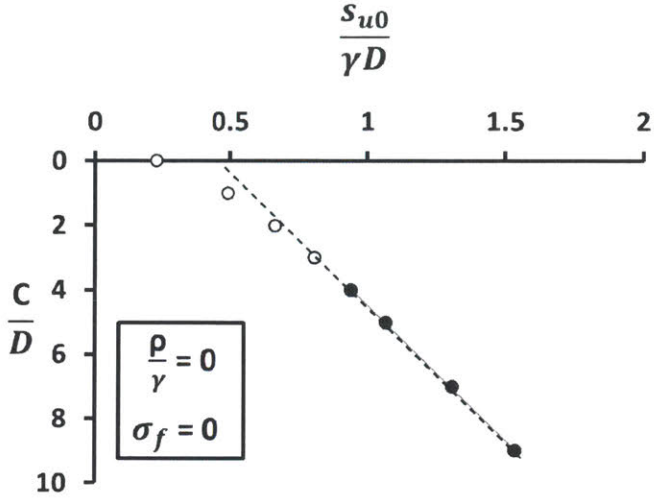

Figure 3.8 Effect of cover-depth-diameter ratio, C/D ratio on the critical undrained strength at the surface for homogeneous (ρ=0) clay for an unsupported face(σ_f=0) unlined tunnel.

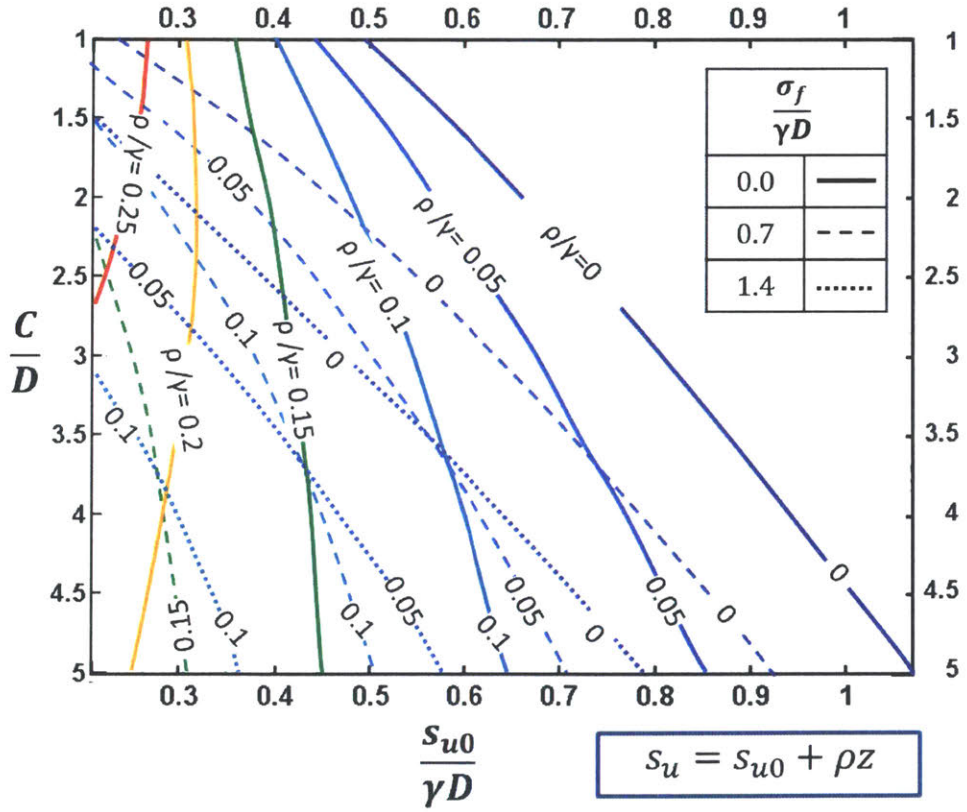

Figure 3.9 Contour plots of strength gradient with depth over unit weight ratio, ρ/γ and face support ratios, σ_f/γD in cover-depth-diameter ratio, C/D vs undrained strength at the surface ratio, s_{u0}/γD space for the unlined case in clay.

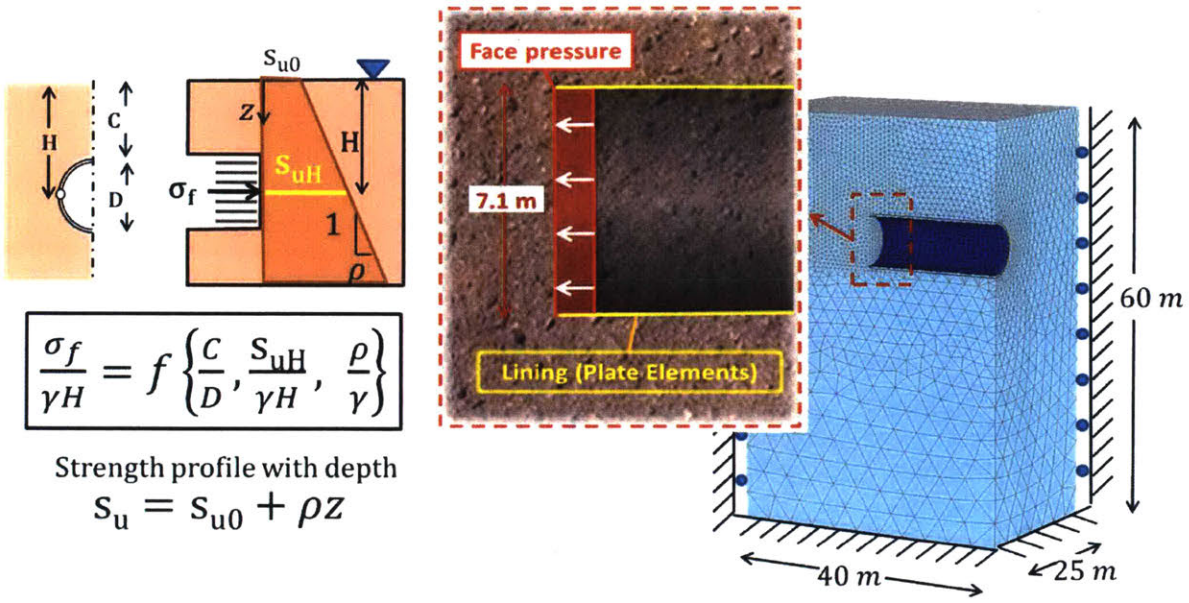

Figure 3.10 Schematic representation of the notation and normalized parameters (left), excavation process (middle) and mesh and dimensions (right) for the 3D Finite element model for lined tunneling in homogeneous clay

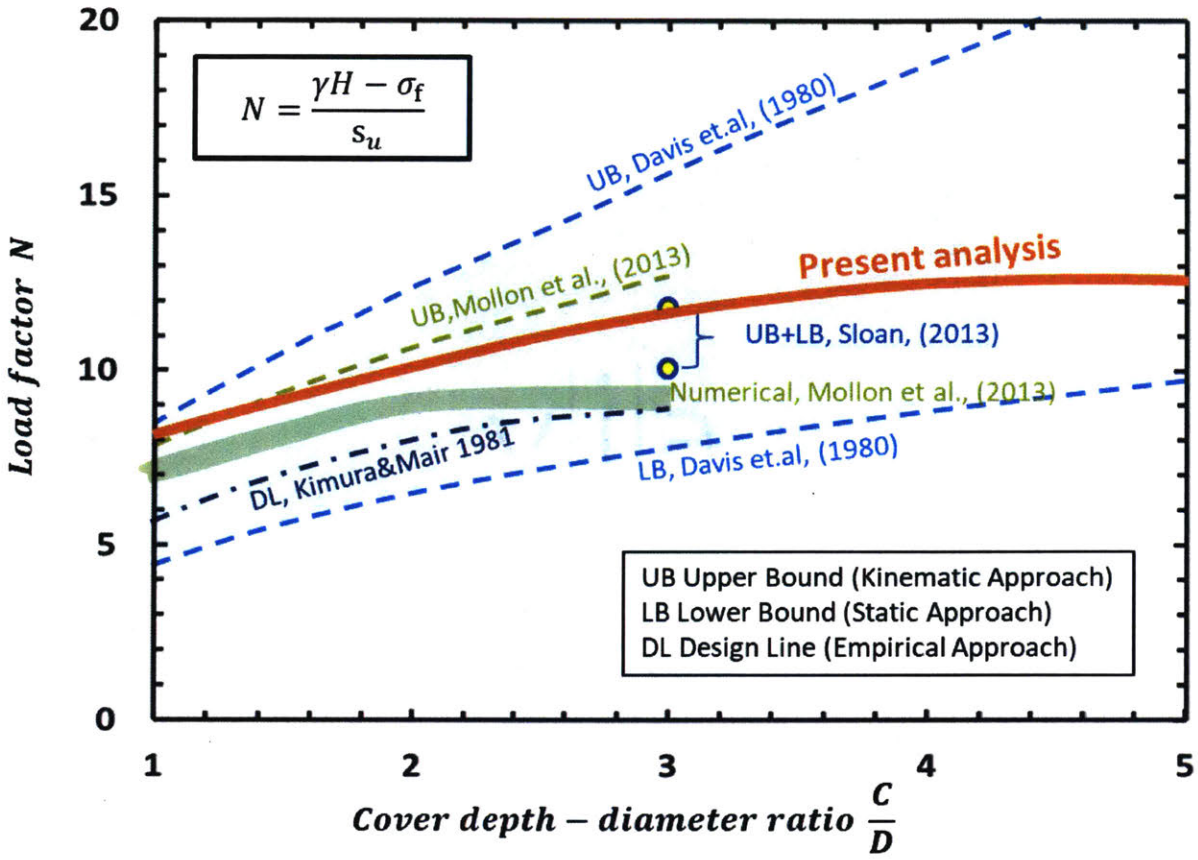

Figure 3.11 Comparison of 3D FE results using the safety reduction method to an array of methods from other researchers including upper and lower bound solutions, FE analyses and experimental data for fully lined tunnels

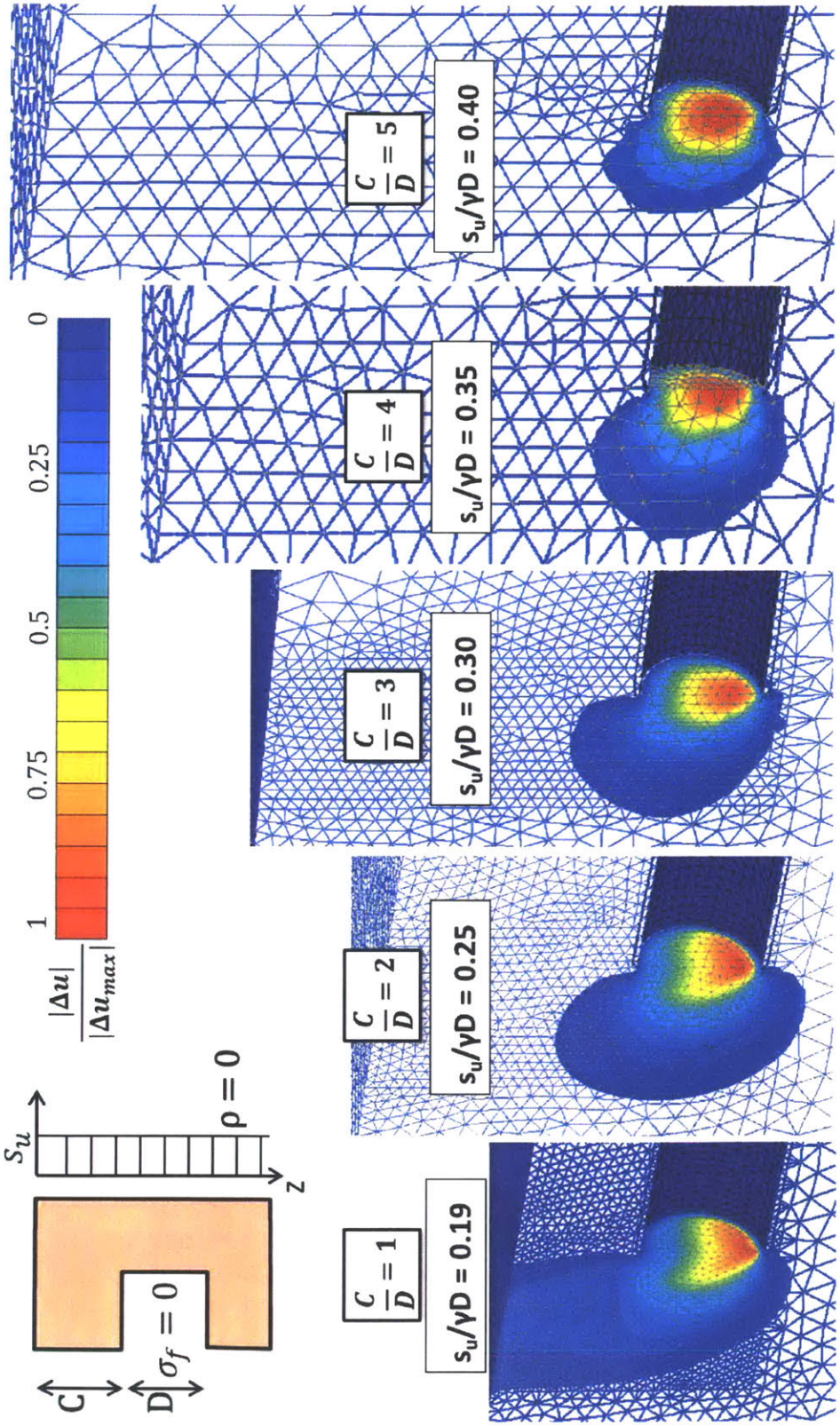

Figure 3.12 Failure mechanisms for unsupported face for different tunnel cover depths

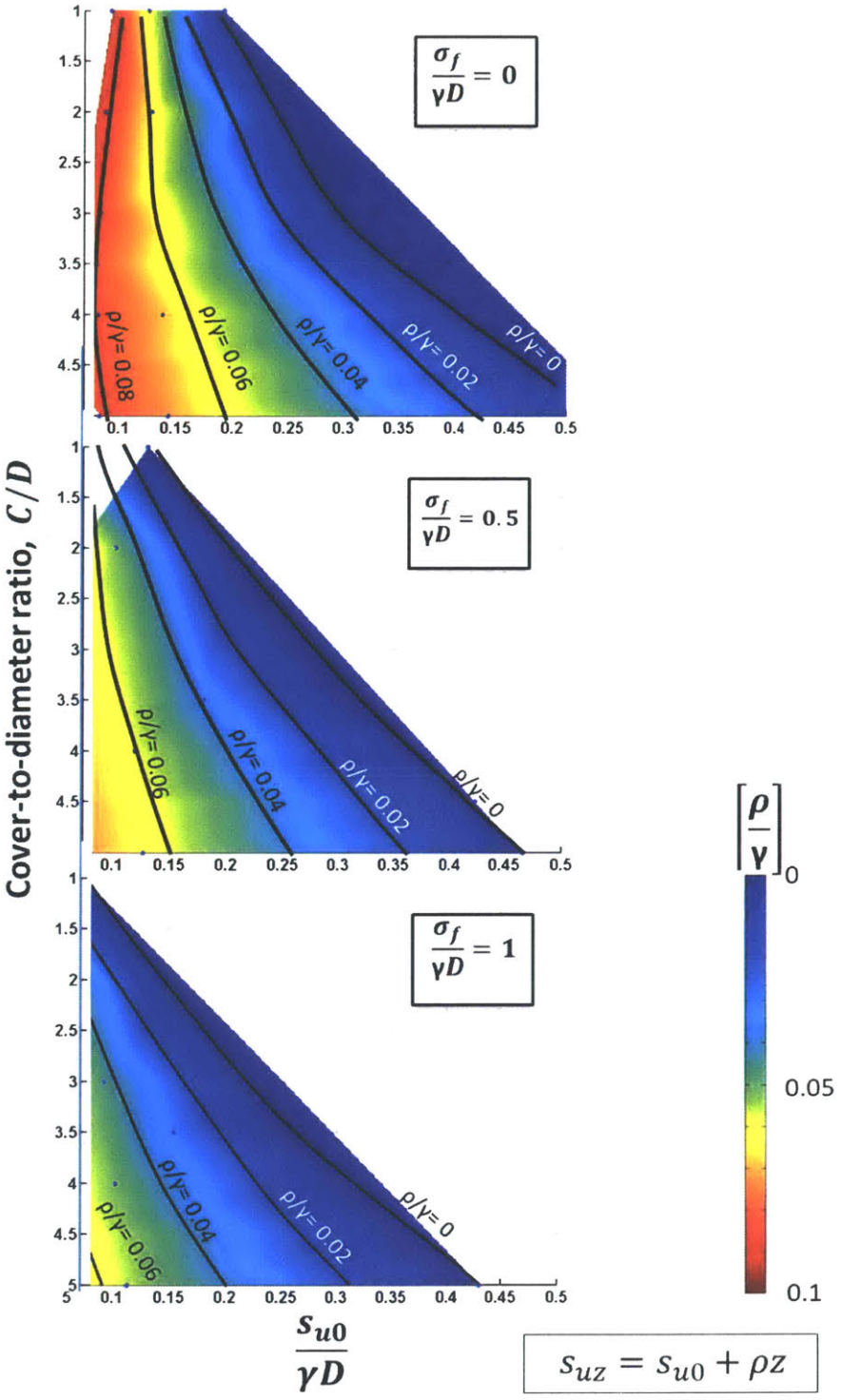

Figure 3.13 Contour plots of strength gradient with depth over unit weight ratio, ρ/γ in cover-depth-diameter ratio, C/D vs undrained strength at the surface ratio, $s_{u0}/\gamma D$ space for different support ratios at the tunnel cavity $\sigma_f/\gamma D$ for the lined case in clay

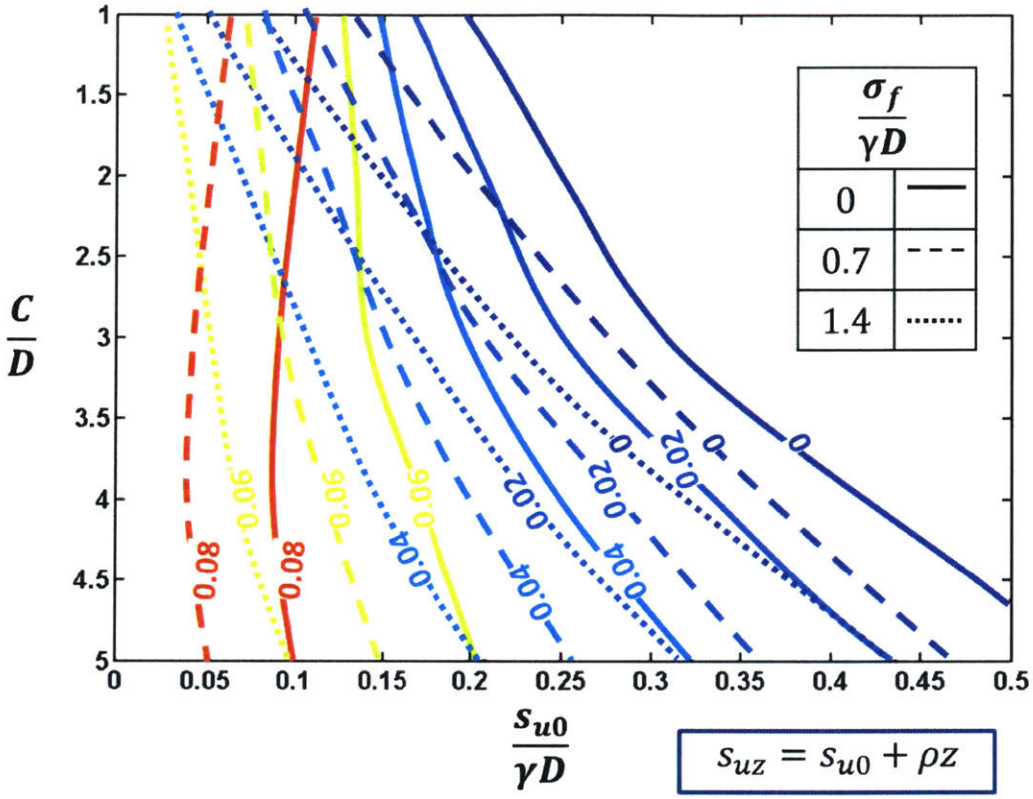

Figure 3.14 Comparison of contour plots of strength gradient with depth over unit weight ratio, ρ/γ and support pressure ratio, $\sigma_f/\gamma D$ in cover-depth-diameter ratio, C/D vs undrained strength at the surface ratio, $s_{u0}/\gamma D$ space for the lined case in clay

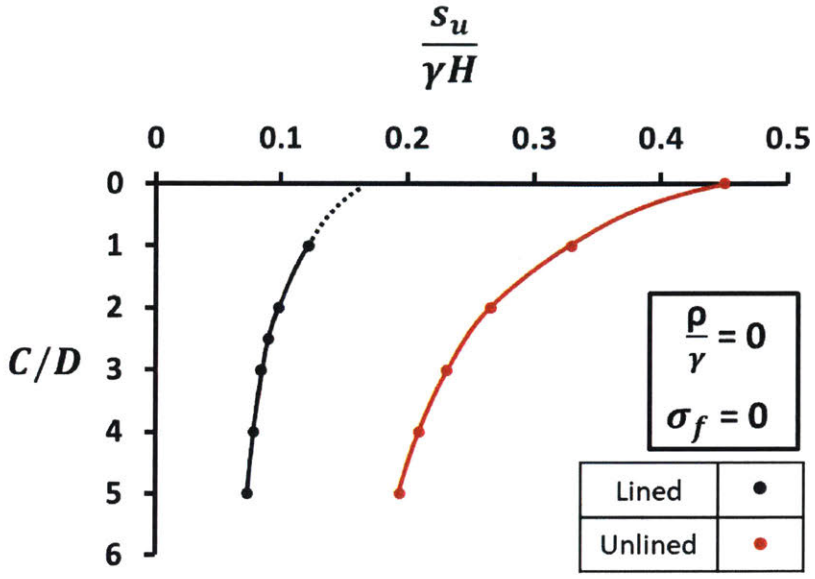

Figure 3.15 Comparison of the effect of cover-depth-diameter ratio C/D on the critical undrained strength in a homogeneous (ρ=0) soil profile with zero support pressure at the face (σ_f=0) for lined vs unlined excavation in clay

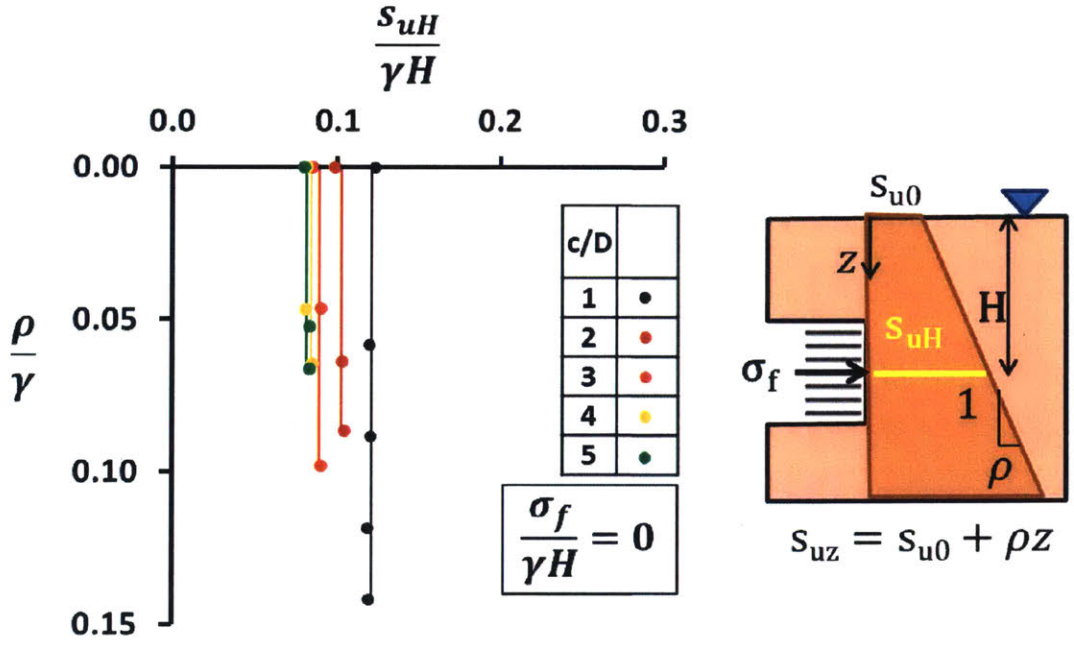

Figure 3.16 Effect of strength gradient with depth over unit weight ratio, ρ/γ on the critical undrained strength ratio at the springline, $s_{uH}/\gamma H$ for cover-depth-diameter ratio C/D=1 to 5

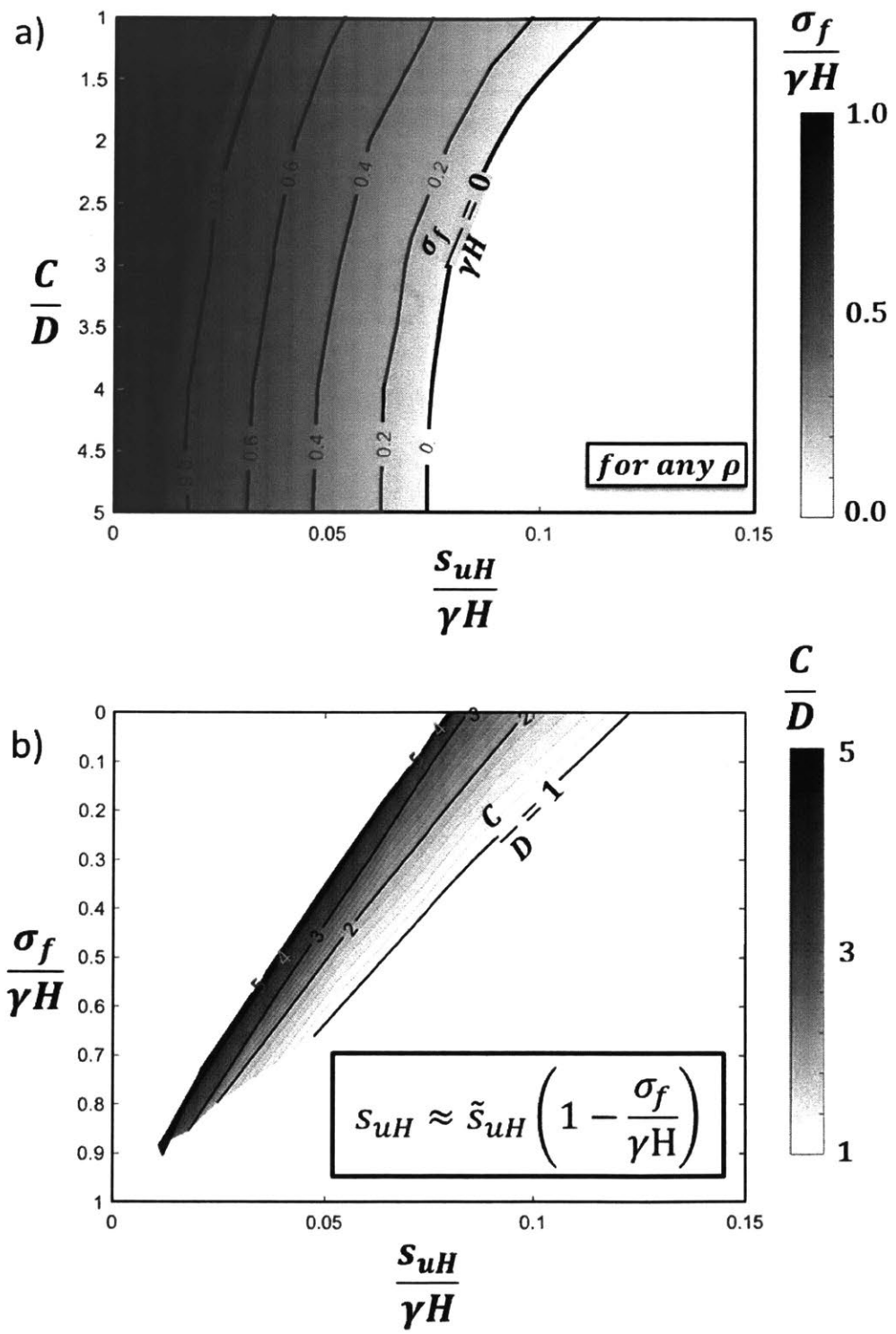

Figure 3.17 Contour plots of critical undrained strength ratio at the springline, $s_{uH}/\gamma H$ in relation to face support pressure, $\sigma_f/\gamma H$ and cover-depth-diameter ratio, *C/D*

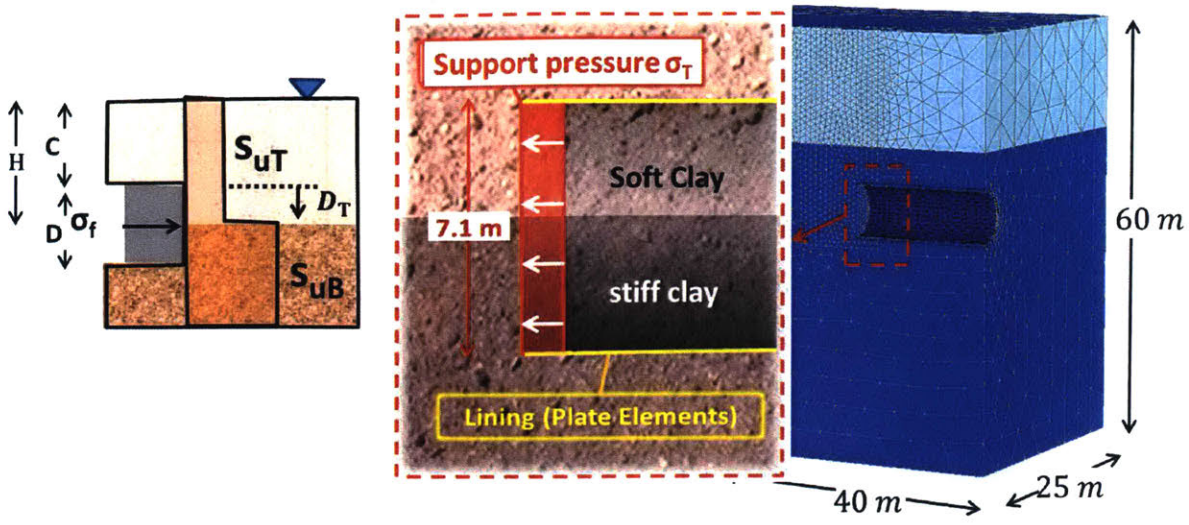

Figure 3.18 Schematic depiction of 3D model used for face stability analyses in mixed face conditions in clay

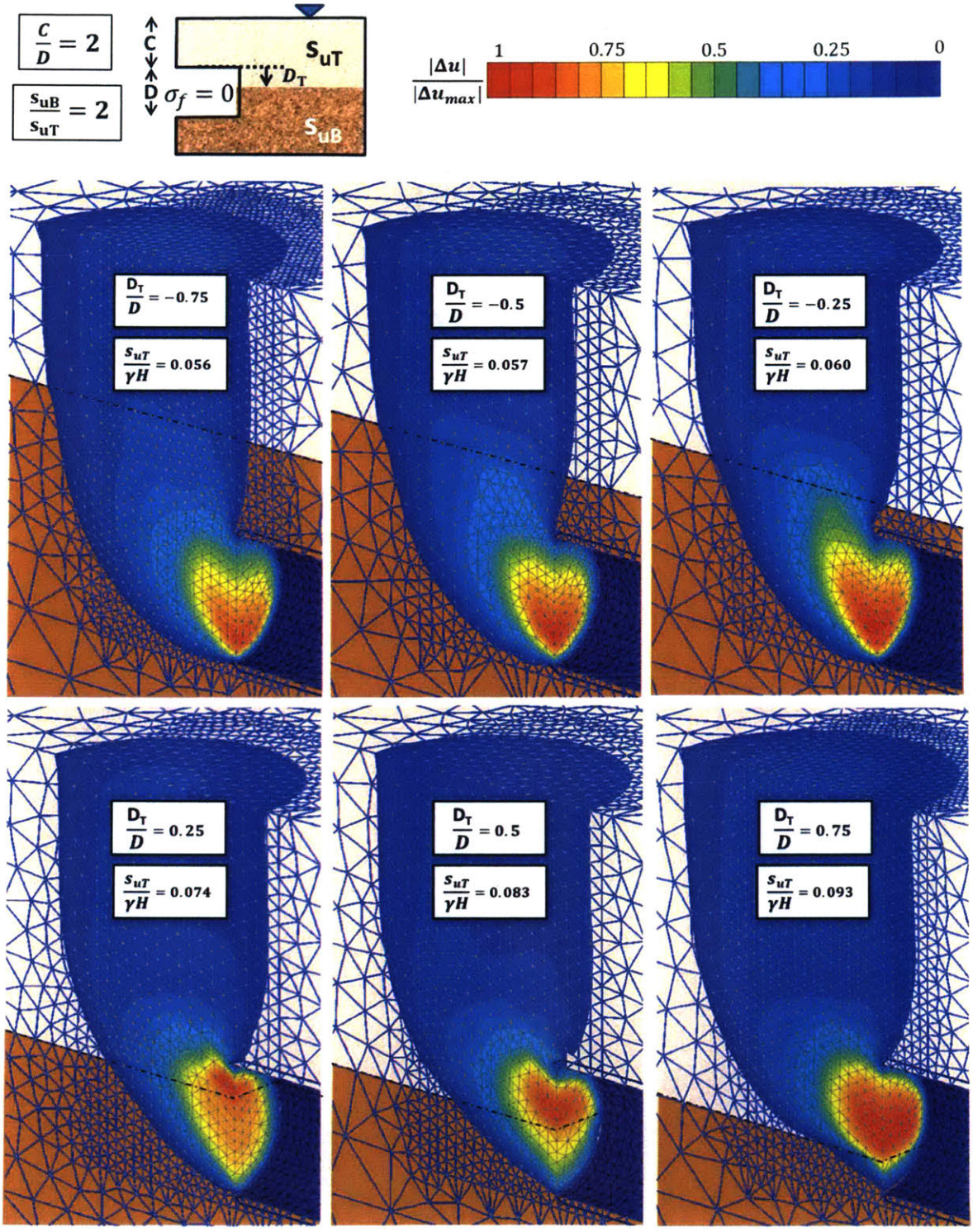

Figure 3.19 Effect of embedment ratio, D_T/D on collapse mechanisms for mixed face tunnel with cover-depth-diameter ratio, C/D=2, strength ratio, s_{uB}/s_{uT}=2 and unsupported face, $\sigma_f/\gamma H$=0

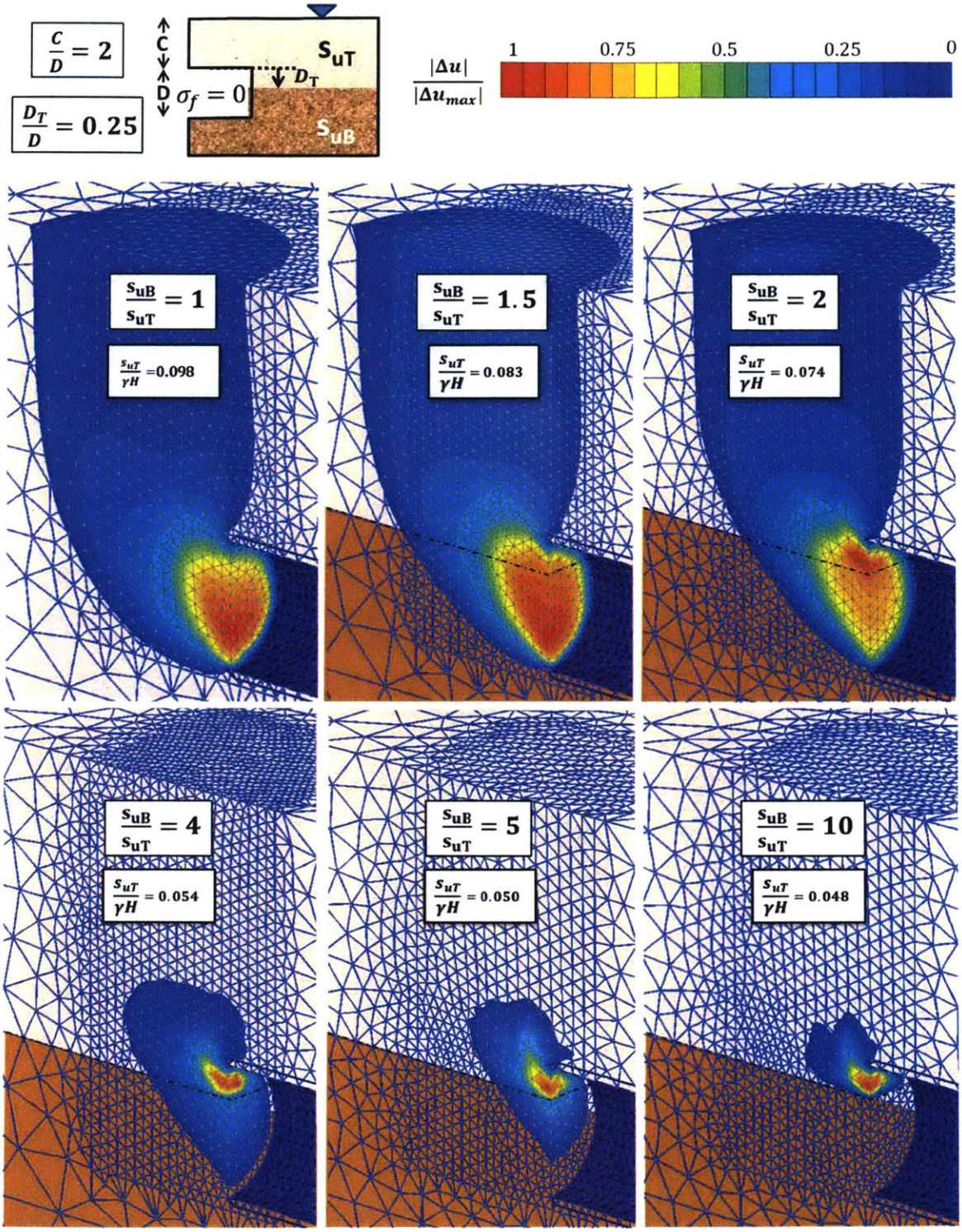

Figure 3.20 Effect of relative strength ratio, s_{uB}/s_{uT} on collapse mechanisms for mixed face tunnel with C/D=2, D_T/D=0.25 and $\sigma_f/\gamma H$=0

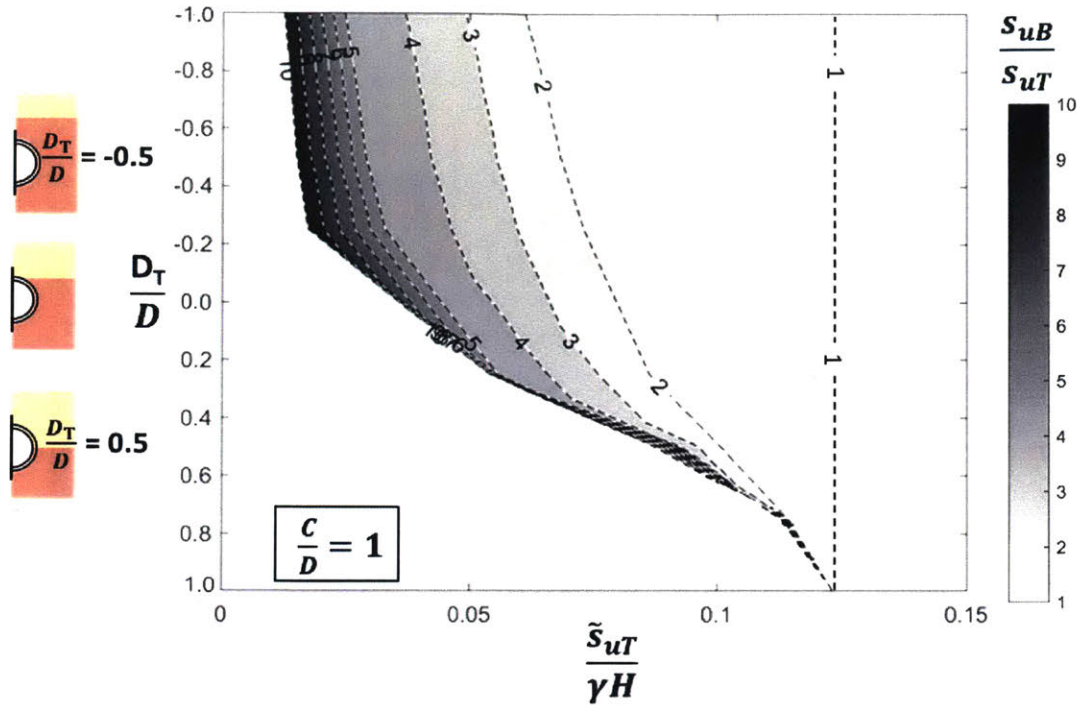

a) Results for shallow tunnel, C/D=1

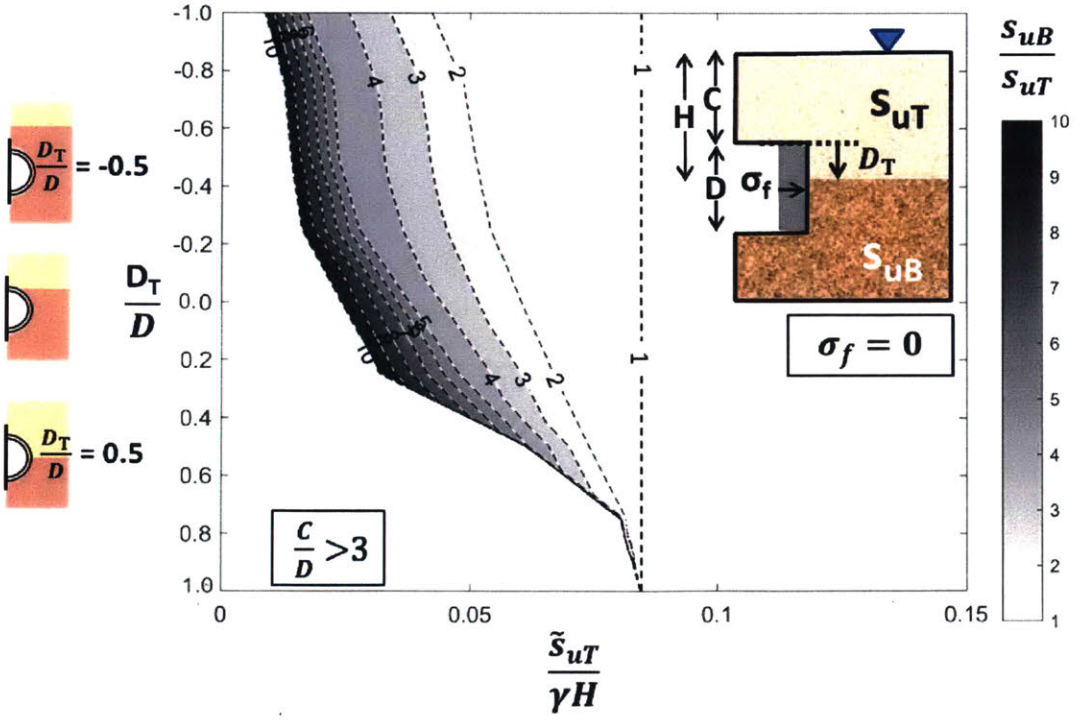

b) Results for deep tunnel with C/D>3

Figure 3.21 Effect of embedment ratio D_T/D and relative strength ratio s_{uB}/s_{uT} on the critical undrained strength for unsupported face, $\sigma_f/\gamma H=0$.

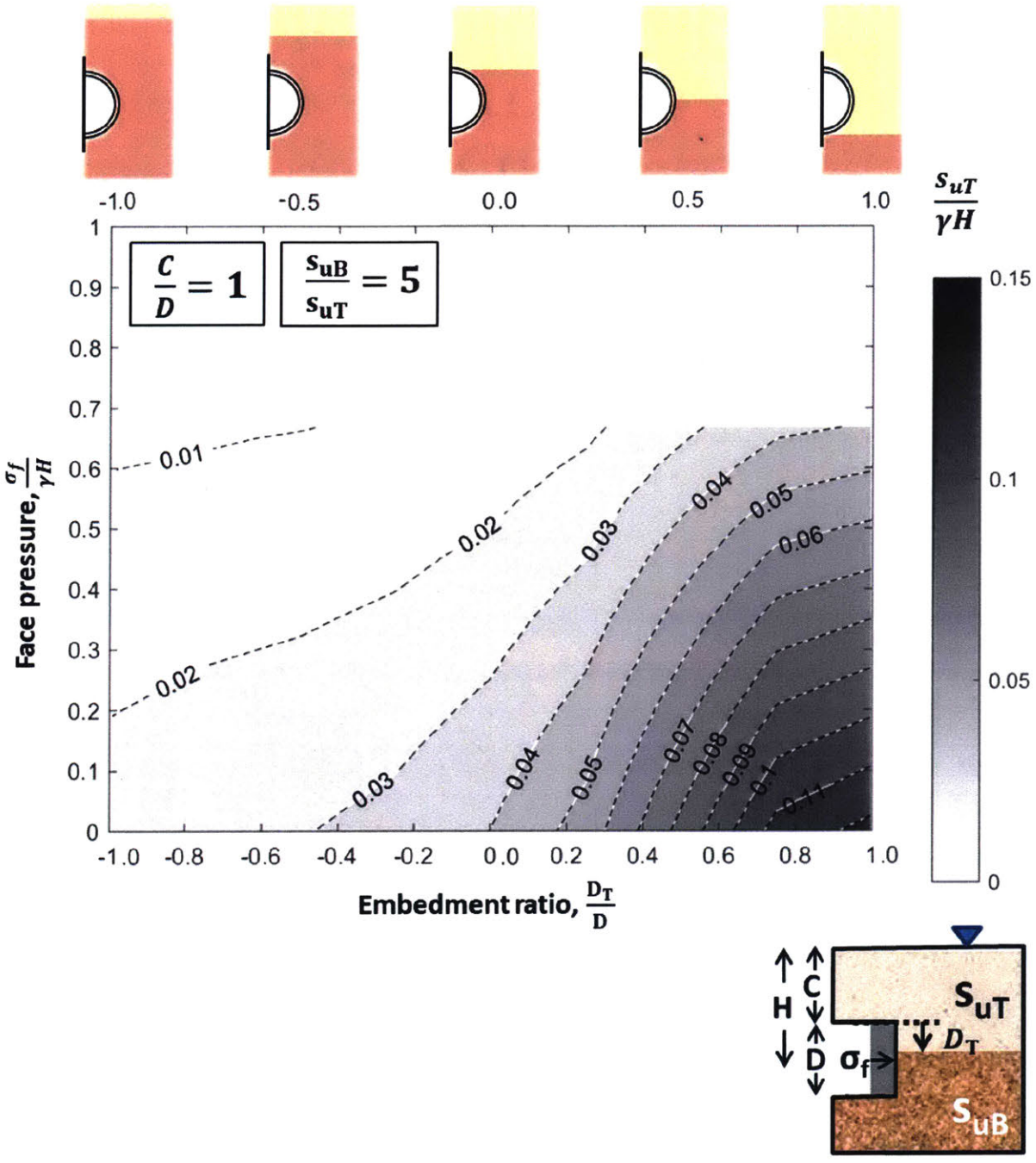

Figure 3.22 Effect of embedment ratio D_T/D and undrained strength on the required support pressure $\sigma_f/\gamma H$ for shallow tunnel, C/D=1 and relative strength ratio s_{uB}/s_{uT}=5

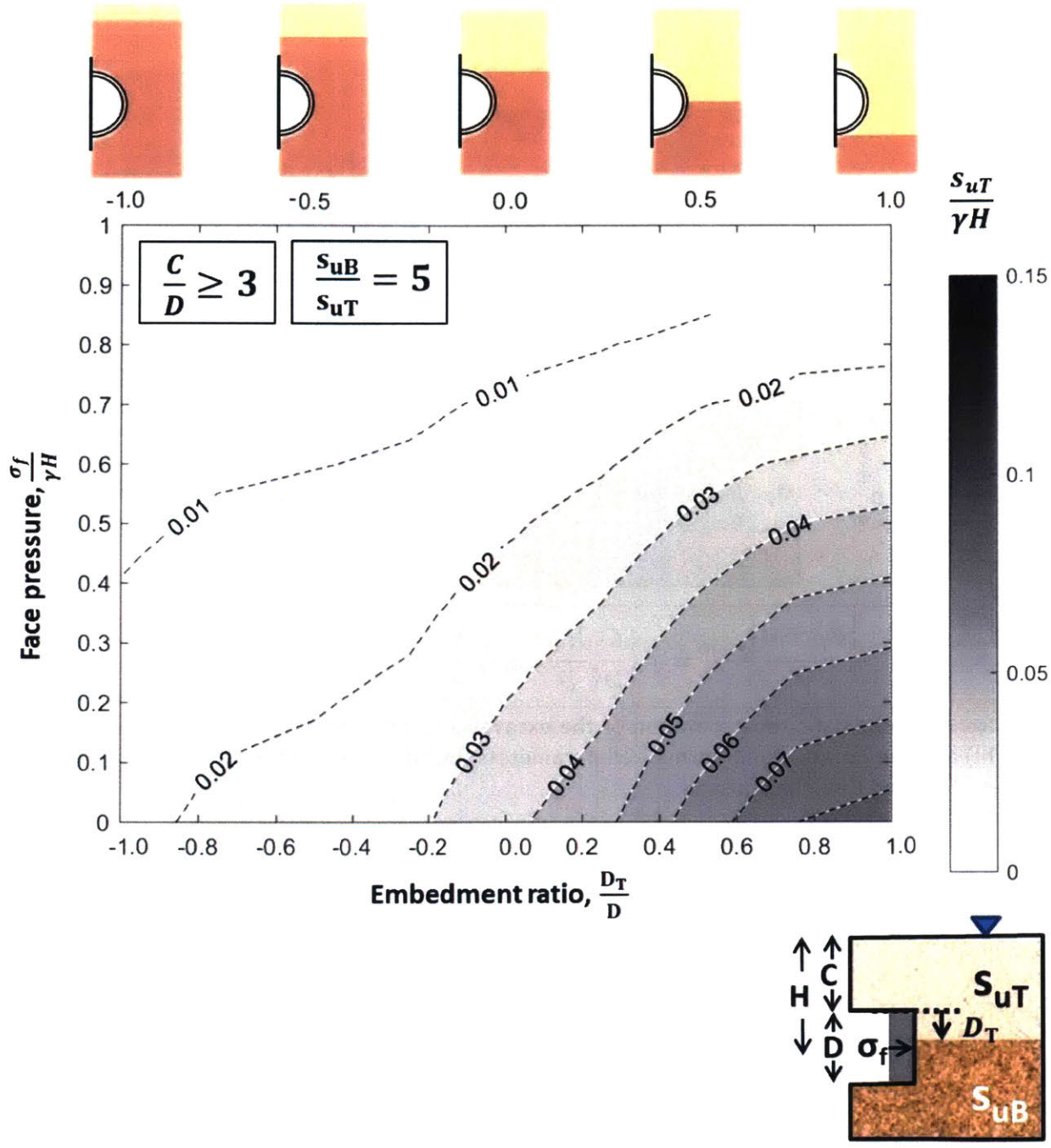

Figure 3.23 Effect of embedment ratio D_T/D and undrained strength on the required support pressure $\sigma_f/\gamma H$ for deeper tunnels, $C/D \geq 3$ and relative strength ratio $s_{uB}/s_{uT}=5$

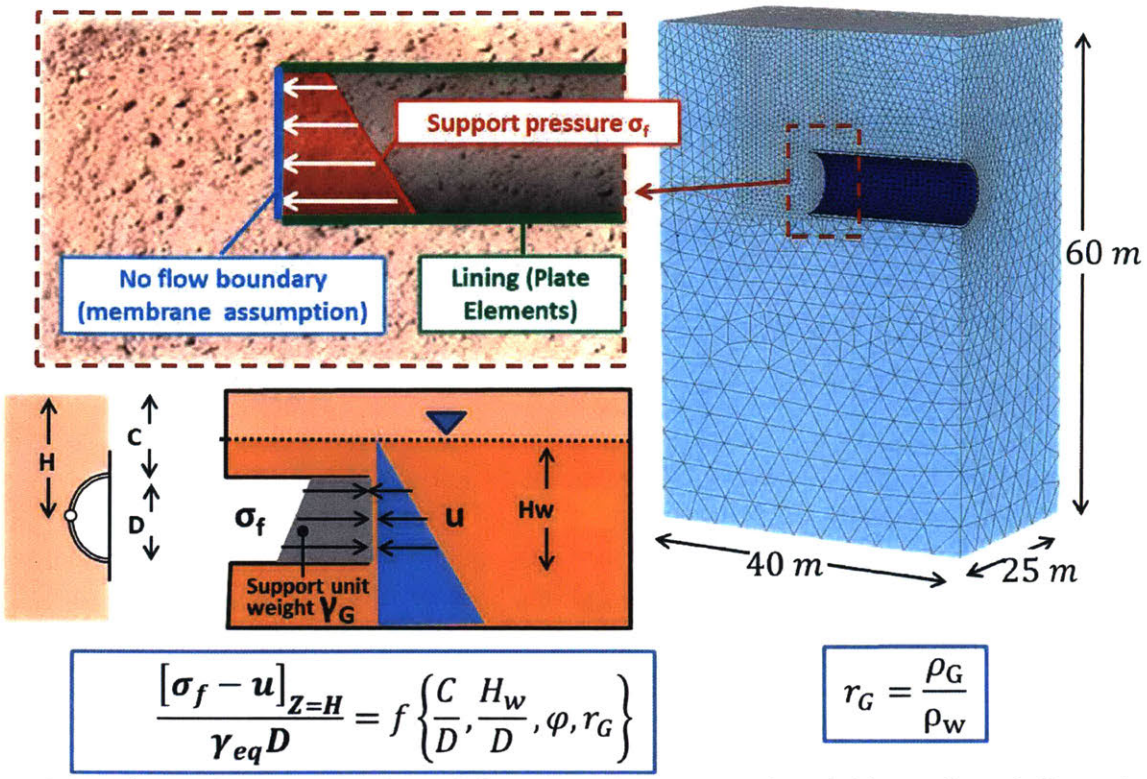

Figure 3.24 Schematic representation of the excavation process (top-left), mesh and dimensions (right) and the notation and normalized parameters (bottom-left) used for the 3D Finite element model for lined tunneling in sand

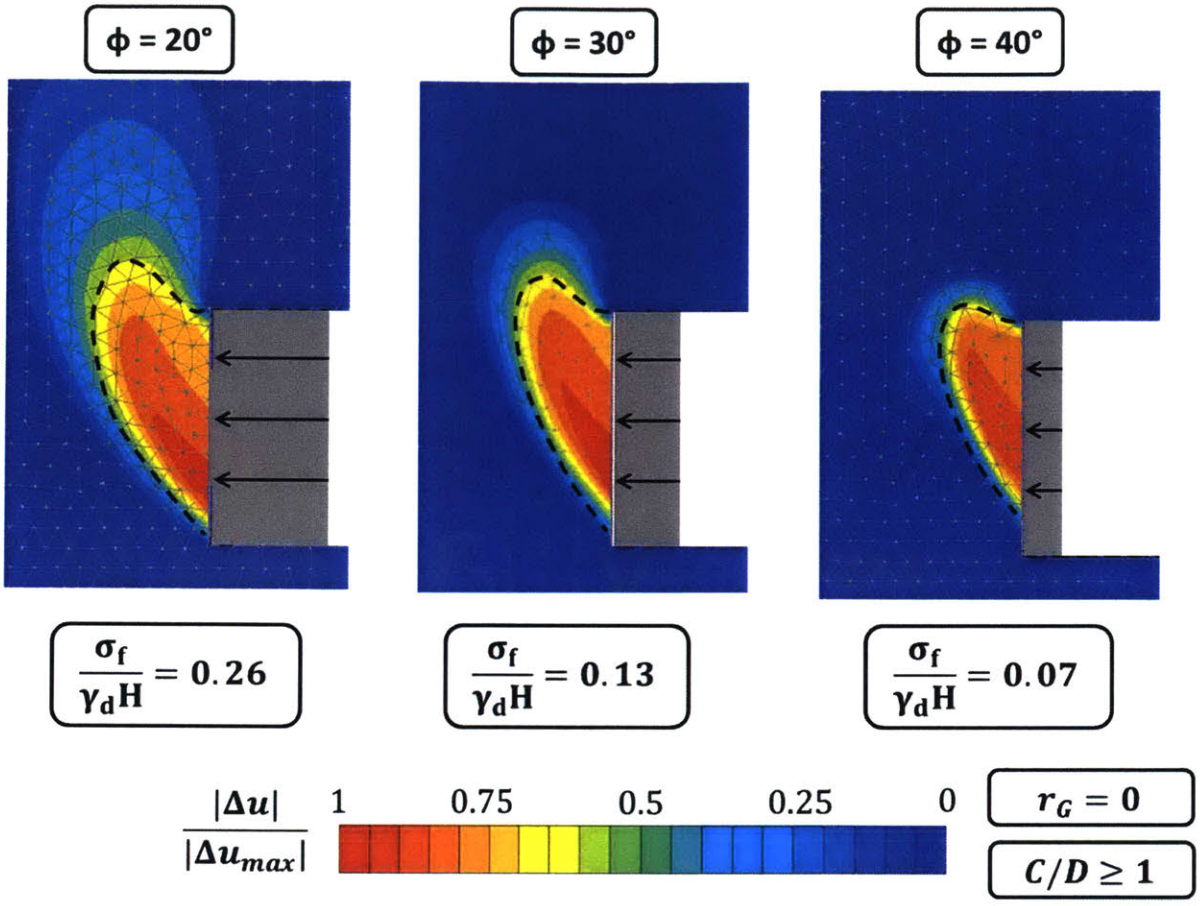

Figure 3.25 Developed collapse mechanisms for increasing friction angle when uniform support is applied at the tunnel heading in dry conditions in sand

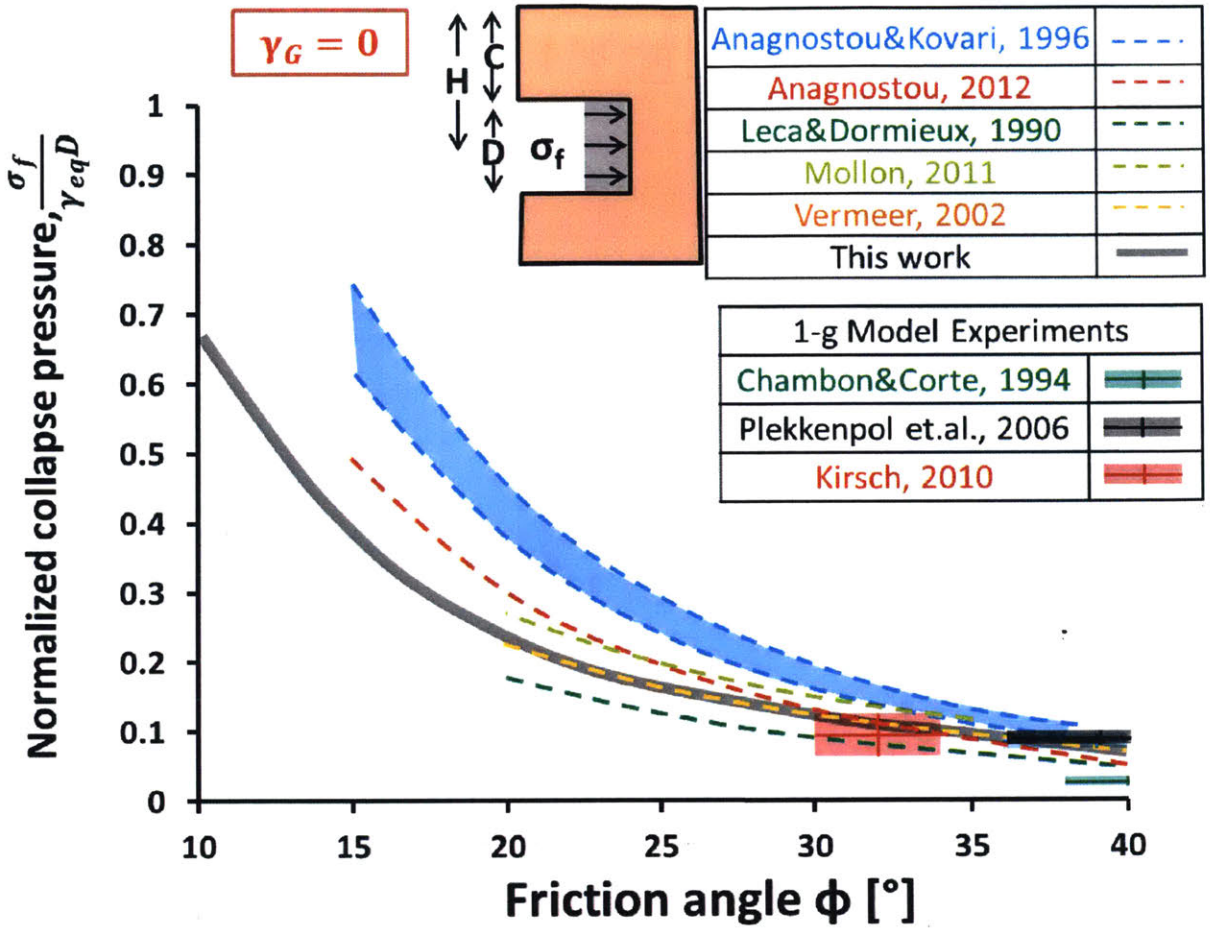

Figure 3.26 3D FE results using Plaxis 3D are compared to experimental, analytical and numerical results of previous studies for a tunnel excavation with constant support pressure in dry sand

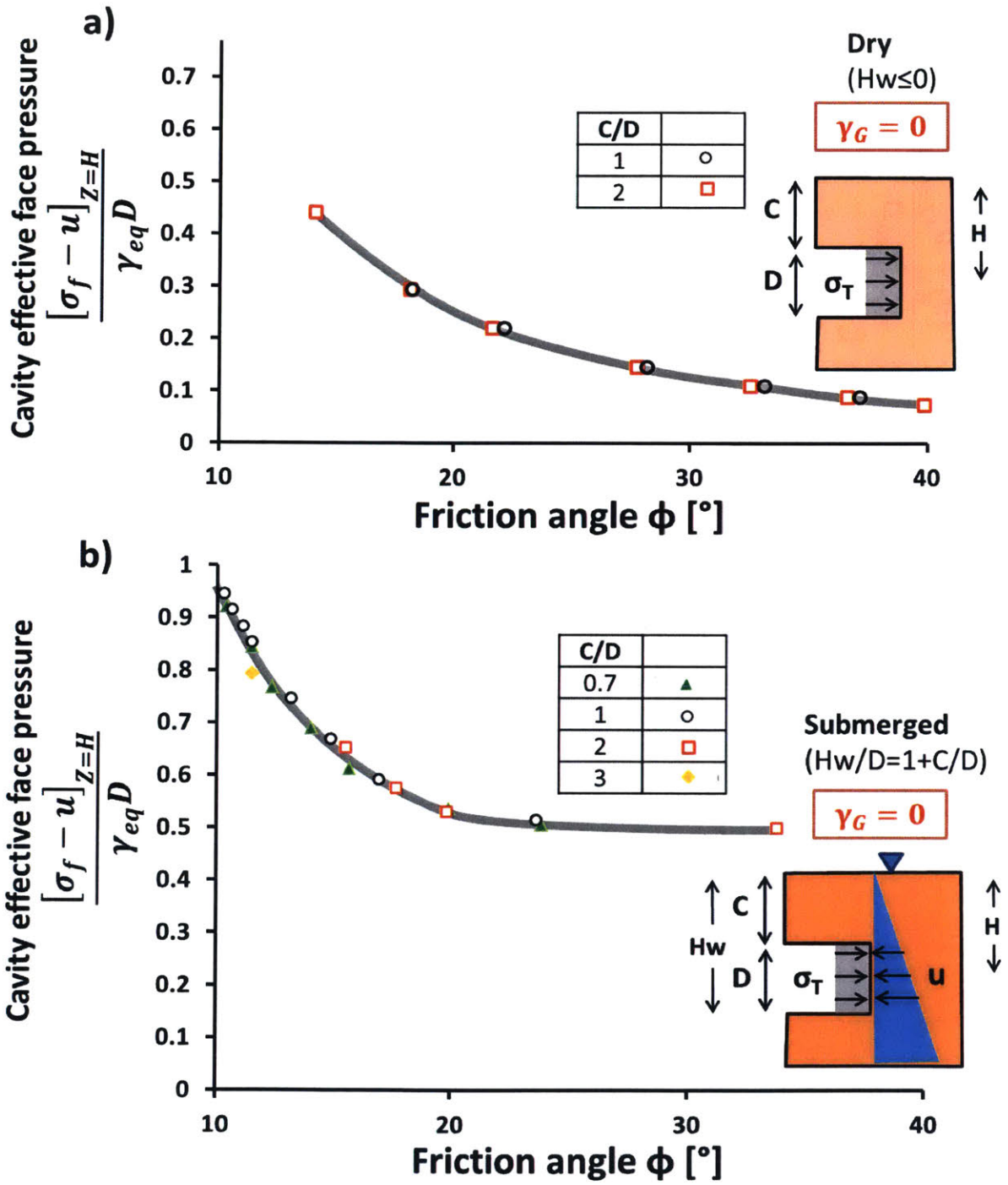

Figure 3.27 Influence of the cover depth over tunnel diameter ratio C/D on the normalized face pressure for uniformly supported heading in a) dry conditions and b) fully submerged tunnel in sand

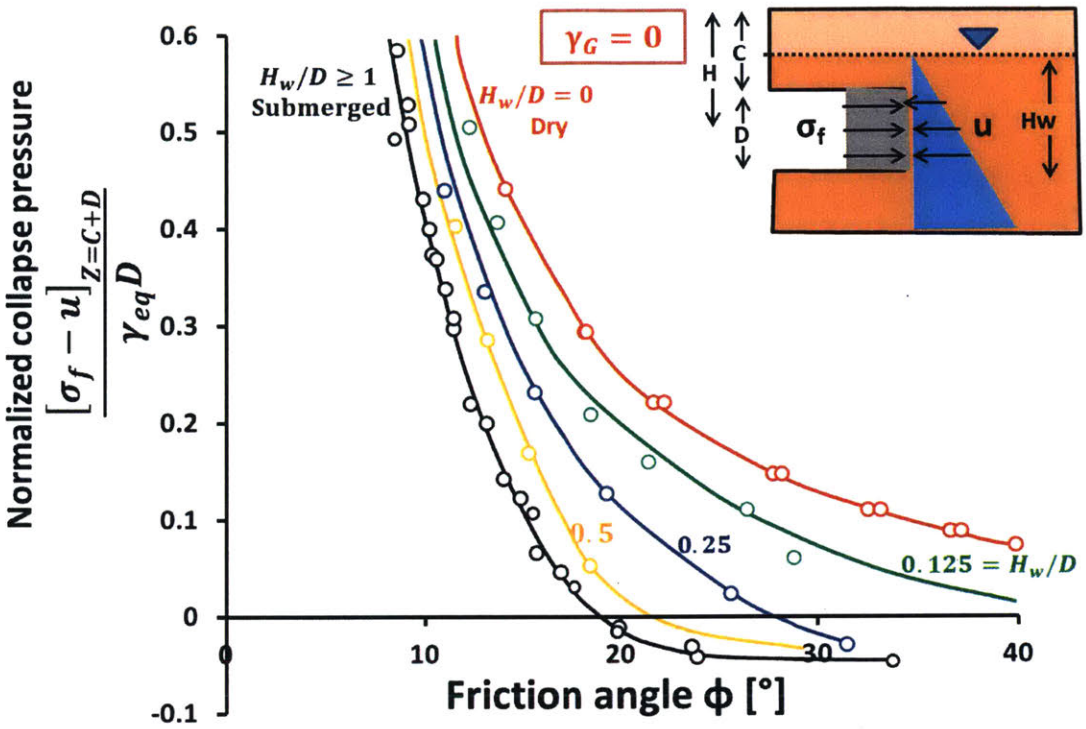

Figure 3.28 Effect of water level on the face pressure at failure for a tunnel excavation with constant support pressure

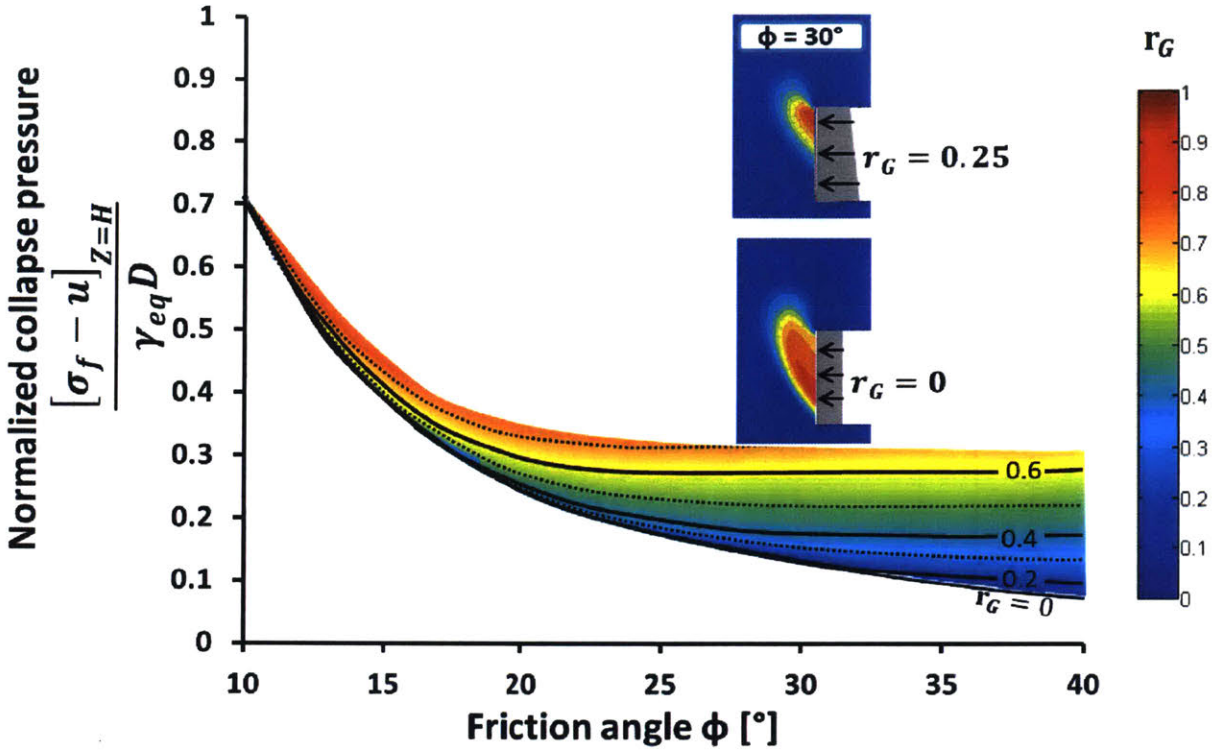

Figure 3.29 Effect of the support medium unit weight on the critical face pressure for a tunnel excavation in sand

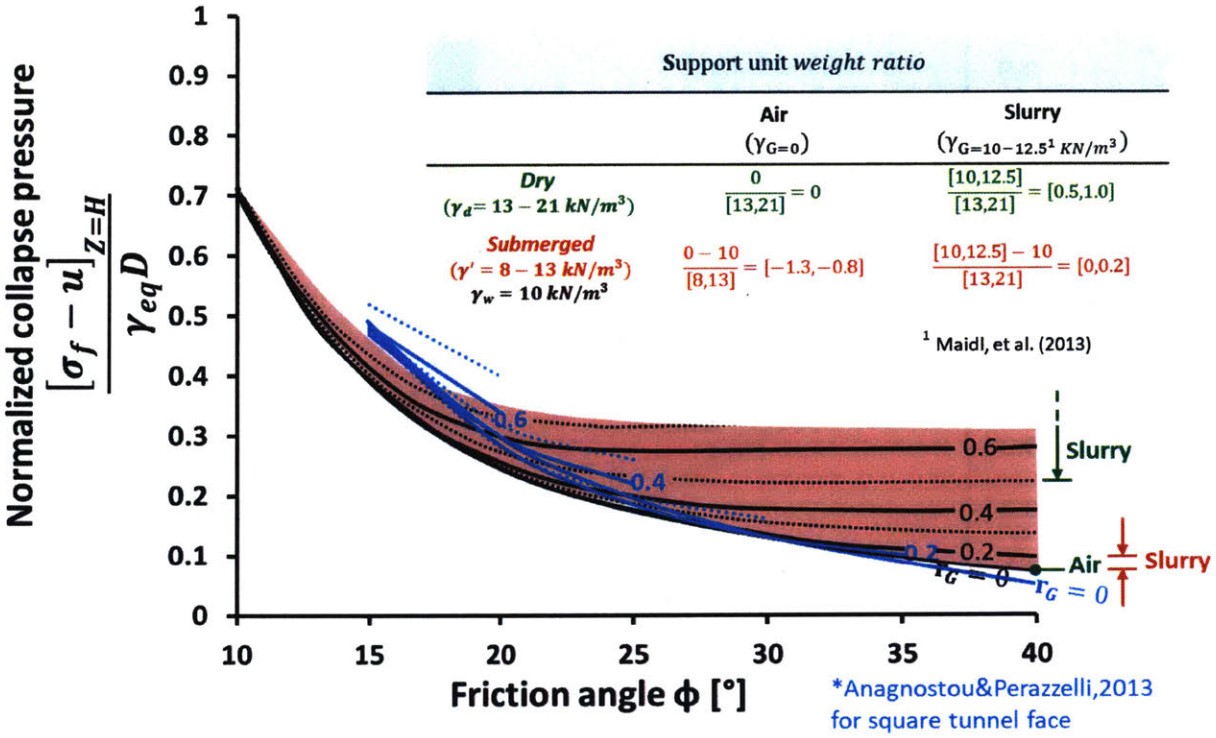

Figure 3.30 Comparison of the effect of the support medium unit weight on the critical face pressure at failure for a tunnel excavation in sand with prior work of Anagnostou&Perazzelli, 2013

4 Predictions of Ground Settlements Caused by Mechanized Tunneling

This chapter proposes a new method for predicting the magnitudes of ground movements caused by mechanized tunnel construction in clay. The proposed method is based on numerical simulations using 2D and 3D Finite Element methods, using the relatively simple elasto-plastic (MC) soil model. The underlying assumption is that ground movements due to tunnel construction can be estimated by considering 4 separate sources of settlement (cf. Figure 1.1) as shown in Figure 4.1:

1. The effects of face pressure, σ_f, on stability of mechanized tunnels has been investigated in detail in the preceding chapter. Closed-face mechanized tunneling achieves control of face pressure using either the excavated earth paste (EPB) or a viscous fluid slurry (slurry shield). Ground movements inevitably occur because of differences between the in-situ ground stresses and the pressures in the face chamber.

2. All soft ground TBM's inject grout to compensate for the tail void between the trailing edge of the shield and the most recently installed sequential lining ring. The grout is injected under pressure to fill the space and is generally designed to set within hours (Founta, 2013, Founta and Whittle, 2017, see Appendix B). The grout pressure reacts against the lining ring and the surrounding soil and hence, can induce ground movements.

3. The rotating cutter head often overcuts the diameter of the shield in order to reduce frictional resistance as the shield is advanced. Similarly most shields are fabricated with

a diameter that decreases from the front to the tail section. These subtle features of shield conicity allow the surrounding soil to move around the shield but also create potential far-field ground movements.

4. Soil excavation from within the tunnel cavity produces a net buoyancy of the tunnel that is potentially offset by the weight of the tunnel boring machine.

The subsequent section describes how these sources of ground movement are analyzed as separate contributions to ground movements.

4.1 Face pressure

The effects of face pressure can vary significantly depending on the specific aspects of each project (soil properties, tunnel geometry etc.) ranging from tunnel projects where we observe minimal deformation even when the face is unsupported in cases where even a small variation in soil properties or applied face pressure can lead to excessive settlements. The initial goal of the current analyses is to help tunnel engineers identify projects that fall into the second, more critical category and take the appropriate counter measures to control ground movements.

In order to study the control of induced-deformations due face pressure, we extended the previously developed 3D Finite Element model (for studying face stability) to simulate deformations associated with steady advancement of the TBM. The model initially considers homogeneous clay conditions as depicted in Figure 4.2, and represents the excavation process as a sequence of discrete steps. During each step an annulus of soil is deactivated, plate elements are activated to model the TBM shield and lining, and a constant face pressure

boundary condition is applied at the newly exposed heading (ignoring the effects of the shield conicity, tail void grouting and TBM weight). The model assumes a constant stiffness and strength profile with depth and adopts the MC soil model (assuming undrained shear conditions for low permeability clay). The groundwater table is coincident with the ground surface and in situ stresses are estimated by K_0 = 1.0. For a homogeneous clay, the prior analyses show that face stability depends only on the ratio of undrained shear strength to overburden pressure at the tunnel springline $s_{uH}/\gamma H$ (Figure 3.16 shows the critical values of this ratio for FS=1.0).

Figure 4.2 show the methodology adopted in this research for calculating the ground surface settlement above the centerline of the advancing tunnel in homogeneous clay:

1. Each advancement step (Figure 4.2a) Δy corresponds to the creation of a new lining ring (typically Δy =1.0-1.5m) and is associated with a longitudinal distribution of incremental settlements at the ground surface δu_z (above the center of the tunnel axis). The largest incremental movement typically occurs right in front of the location of the face. Each point in this distribution describes the movements relative to a fixed location of the tunnel heading. Hence, by integrating the distribution of the incremental movements, it is possible to define the settlement for a given face pressure.

2. In practice the FE assumes initial equilibrium for the tunnel embedded within the soil mass (Figure 4.2b). Steady state conditions (i.e., steady state of incremental ground movements) must be established empirically by examining the incremental deformations for each advancement step.

3. The net settlement caused by the advancing TBM is found by integrating the incremental settlements δu_i over integer multiples of the advancement step, i along the TBM axis:

$$u_z = \sum_{i=-k}^{i=+k} \delta u_i \qquad (4.1)$$

We considered incremental settlement troughs when the face of the TBM was in the middle of the 270m long model and observed that the trough shape remained steady in subsequent steps. For the purpose of this study we will focus on the maximum net surface settlement u_z above the tunnel axis.

Figure 4.3 illustrates a typical example of this methodology for the case with C/D=3, $s_u^* = 100\ kPa$ and $\sigma_f = 0$ (where s_u^* is the in situ undrained strength). The incremental settlement troughs are plotted for steps 1, 5, 10, 15, 20 and 25 (Figure 4.3a), while the total settlement is calculated by integrating along the tunnel axis using Eq. (4.1) for each step (Figure 4.3b). The net settlement stabilizes to the value, u_z=11mm after approximately 7 steps (reached steady state conditions), which corresponds to the residual settlement after passage of the TBM. A similar methodology is used to calculate the net ground settlement for each numerical analysis reported in this chapter.

We used the Buckingham π theorem (Buckingham, 1914) to select the appropriate dimensionless groups to study the effect of the face pressure on surface deformations. The current implementation, uses the maximum surface settlement, u_z, the difference between the in situ, s_u^* and critical undrained strength, s_u, $\Delta s_u\ (= s_{uH}^* - s_{uH})$, face pressure, σ_f and

springline tunnel depth, H as independent variables, while the soil unit weight, γ and the tunnel diameter, D and the shear stiffness, G are selected as repeating variables. In this way, we are able to study the dependency of the surface deformations on the face pressure, σ_f, tunnel geometry and soil properties using four dimensionless groups:

$$\frac{u_Z G}{\gamma D^2} = f\left\{\frac{\Delta s_u}{\gamma D}, \frac{\sigma_f}{\gamma D}, \frac{H}{D}\right\} \qquad (4.2)$$

4.1.1 Effect of Face Pressure on Surface Settlements

Figure 4.4a,b summarize the computed net ground settlements associated with tunnel advance at three ratios of face pressure to overburden stresses, $\frac{\sigma_f}{\gamma \mathrm{H}}$ for shallow (C/D=1) and deep tunnels (C/D≥3), respectively. Characteristically, these results show large (unbounded) values of the normalized settlement, $\frac{u_Z G}{\gamma D^2}$, for stability numbers, $\frac{s^*_{uH}}{\gamma \mathrm{H}}$ (s^*_{uH} corresponds to the undrained strength of the soil) at the springline below the critical stability strength ratio, $\frac{s_{uH}}{\gamma \mathrm{H}}$, found from results in Figure 3.17. As the stability number increases to $\frac{s^*_{uH}}{\gamma \mathrm{H}} \approx 0.5$, there is a significant drop in the surface settlements. The stability number has small influence on settlements for $\frac{s^*_{uH}}{\gamma \mathrm{H}} \geq 0.5$. The data were fitted by the rectangular hyperbola using the least squares method. The resulting equation was

$$\frac{u_Z G}{\gamma D^2} = a\left[\frac{\gamma \mathrm{H}}{\Delta s_u}\right]\left[1 - \frac{\sigma_f}{\gamma \mathrm{H}}\right] \qquad (4.3)$$

where $\Delta s_u = [s^*_{uH} - s_{uH}]$, s_{uH}, is the critical undrained strength value at the springline for FS=1 calculated from the stability analyses, s^*_{uH} is the in-situ undrained strength of the clay and

a is a constant coefficient derived from the numerical analyses. The numerical results are consistently described by a=0.012 for all homogeneous cases.

The rectangular hyperbola fits closely the computed results for both shallow (C/D=1, Figure 4.4a) and deep tunnels (C/D>3, Figure 4.4b) for homogeneous clay. Using the analytic expressions, Figure 4.5a,b show the effects of the stability number $\frac{s_{uH}^*}{\gamma \mathrm{H}}$ and face support pressure ratio , $\sigma_f/\gamma H$, on the induced settlements. There is a linear relationship between the magnitude of the observed settlements and the applied face pressure, such that settlements decrease as the face pressure increases (note that $u_Z \rightarrow 0$ for $\frac{\sigma_f}{\gamma H} \rightarrow 1$) . In contrast, there is a highly nonlinear dependency of the observed settlements on the stability number, resulting in infinitely large deformations (i.e. failure) when the undrained strength becomes equal to the critical undrained strength calculated from the stability analyses (corresponding to the vertical asymptote of the rectangular hyperbola cf. Figure 4.4a,b).

Although, the magnitude of the observed settlements depends linearly on the applied face pressure, the rate of increase varies according to the undrained strength of the soil s_u. This results in minimal increase rates for large s_u and very large increase rates for undrained strength ratios approaching the critical undrained strength of each tunnel geometry. This can lead to a very sensitive behavior during construction, requiring careful adjustment of the face pressure as even small variations in soil strength occurring naturally within the same layer can significantly affect the observed displacements.

4.2 Grouting of Tail Void

The process of filling the tail void with grout plays an important role in controlling the induced deformations. The pressure of the injected fluid supports the tunnel cavity temporarily until the mixture hardens and provides a permanent support along with the erected lining. The grout injection is a complicated process which has been studied extensively in our prior work on the Crossrail project (Founta, 2013, Founta and Whittle, 2017, see Appendices A and B). For the purpose of this study we examine how the applied grout pressure can affect ground deformations at the surface depending on ground properties and tunnel geometry.

In order to study the effect of grout pressure on the induced deformations due to mechanized tunneling we adapted the previously developed 3D finite element model to isolate the effect of the grout pressure as shown in Figure 4.6b. The model simulates the grouting process as a sequence of discrete steps, where the shield is simulated as an infinitely long body from curved plate elements (to avoid effects from the face). During a single step advance the plate element, corresponding to the tail of the undeformed shield, is deactivated and a radial pressure simulating the liquid phase of the grout pressure is applied over a single segment (width, $l_G = 1.5m$), while immediately behind the pressure supported segment a plate element is activated representing the hardened grout-erected lining system.

The FE model represents grout activation in two phases:

1. The freshly injected grout is assumed to behave as an incompressible fluid with very low stiffness. This stage is assumed to extend over one tunnel segment (based on typical tunnel advance rates and grout setup properties (as presented in Founta, 2013,

Appendix B), and is represented by a constant radial pressure with depth, σ_G, around the cavity annulus. The grout is generally designed to harden within hours (Figure B.5) to minimize deformations in the tail void. In cases using a mixture that requires a longer timeframe to harden, the effect of the longer liquid phase (extending over one lining segment) on the surface settlements should be assessed.

2. In the hardened state (i.e. the adjacent step) the grout is simulated by activating plate elements with high stiffness (i.e. $E_{grout-lining} >> E_{soil}$) representing the grout-lining system. This assumption is based on prior work on the effects of grouting (Founta, 2013, Appendix B) and ignores the actual tail void geometry and any deformations of the hardened grout and precast-lining system. Parametric studies examining the effects of grout stiffness, showed that the displacements are mainly affected for values lower than the stiffness of the surrounding soil (see Appendix B, Figure B.13) and that, generally, the grout stiffness becomes significantly higher than the stiffness of the surrounding soft soil after one ring advancement (Figure B.5 shows that for the Crossrail project, the grout stiffness after a single ring advancement is about 30 times larger than the stiffness of the surrounding soil).

The effects of grout pressure on ground settlement can be computed using a similar methodology of integrating incremental deformations spatially (i.e. similar to results for the face pressure in Figure 4.2). The residual settlement $\boldsymbol{u_Z}$ for any point is equal to the sum of the incremental settlements $\boldsymbol{\delta u_i}$ at all locations corresponding to integer multiples i of the step distance along the TBM axis as described by Eq. 4.1.

4.2.1 Effects of Grouting on Ground Settlements

A series of analyses were conducted to calculate the ground settlements due to grout pressure for different tunnel geometries and soil properties. Figure 4.7a and b summarize the computed normalized ground settlements at three selected grout pressures, as functions of the stability number for shallow (C/D=1) and deep (C/D>3) tunnels, respectively. There is a nonlinear dependency of the observed settlements on the undrained strength, resulting in infinitely large deformations (i.e., failure) when the in-situ undrained strength, s_{uH}^{*} becomes equal to the critical undrained strength calculated from prior stability analyses, s_{uH}. These results are qualitative similar to those previously shown for the face pressure and can also be represented by a rectangular hyperbola:

$$\frac{u_z G}{\gamma D^2} = b\left[\frac{\gamma \mathrm{H}}{\Delta s_u}\right]\left[1 - \frac{\sigma_G}{\gamma \mathrm{H}}\right] \qquad (4.4)$$

where $\Delta s_u = [s_{uH}^{*} - s_{uH}]$, s_{uH},is the strength associated with failure, s_{uH}^{*} is the in-situ strength and b is a constant coefficient derived from the numerical analyses. The current analyses find b=0.004 for the homogeneous case. The critical undrained strength s_{uH} can be estimated from Figure 4.6a, using a similar concept to the face pressure case with:

$$s_{uH} = \tilde{s}_{uH}\left(1 - \frac{\sigma_G}{\gamma \mathrm{H}}\right) \qquad (4.5)$$

Equation 4.4 can be used in practice to predict the maximum surface settlement due to the applied grout pressure by inputting: i) the soil properties, s_u, G, ii) the grout pressure σ_G, iii) the tunnel geometry H, D.

The dependency of the induced settlements on the grout pressure (as described by Eq. 4.4) follows similar trends to those observed for the face pressure. As expected a grout pressure equal to the geostatic stresses $\frac{\sigma_G}{\gamma H} \rightarrow 1$, results in zero settlements u_z, whereas u_z increases as the applied radial pressure, σ_G decreases following a linear pattern.

4.3 Shield Geometry

The conical shape of the TBM shield allows for an easier and faster advancement of the tunnel construction. However the decreased diameter at the tail of the shield results in a contraction of the tunnel cavity which affects significantly the surface settlements. The effect of the tunnel contraction has been investigated in prior work on the Crossrail project (Founta, 2013, Founta and Whittle, 2016, see Appendix A). For this work we modify and expand our previous framework to isolate the effects of shield geometry on the induced ground surface settlements.

A 2D, plane strain finite element is used to study effects of the diameter of the shield on ground movements. The selected mesh and dimensions of the model are presented in Figure 4.8. The model simulates the shield conicity by applying an appropriate radial contraction boundary condition at the initial undeformed cavity of diameter D so that it converges to the diameter at the tail of the TBM D_{tail} (assuming a zero gap between the tunnel cavity and the exterior of the shield). The model assumes a constant stiffness and strength profile with depth and adopts the MC soil model, assuming undrained shear conditions, groundwater table coincident with the ground surface and in situ stresses with assumed $K_0 = 1.0$.

4.3.1 Effects of Shield Geometry on Surface Settlements

The conducted analyses study how the shield contraction, $\varepsilon = [\Delta D/D]$, (where D is the diameter at the cavity face, and $\Delta D = |D_{tail} - D|$, is the difference in diameter between the cavity face and the tailskin of the shield) affects the induced displacements for cover depth-diameter C/D=1-5 and soil rigidity, $\frac{G}{s_u}$ =25-200. Figure 4.9 shows how ground settlements are affected by the magnitude of the shield contraction. The normalized deformations, $u_z/\Delta D$ in Figure 4.9 are plotted as a function of the shield contraction, ε for ratios of shear to undrained shear strength, G/s_u. We observe that the value $u_z/\Delta D$ is apparently constant for small values of contraction, ε<1%. The relative stiffness-strength ratio affects the results for shallow tunnels C/D=1 with large contractions, ε>2%. This is because the tunnel cavity contraction, ε (which controls the shear strain level γ at the soil) and the parameter G/s_u control the radius of the plastic zone and hence, the surface deformations. This effect becomes more pronounced for shallow tunnels. In particular for each G/s_u there is a critical contraction ε_y that signifies the switch from purely elastic to elasto-plastic behavior. Similar observations were made by Pinto and Whittle, (2013) and Yu and Rowe (1999), who provided a closed form solution to describe the critical contraction ε_y that causes yielding at the tunnel cavity. This solution can be simplified for undrained conditions as:

$$\varepsilon_y = \frac{S_u}{4G} \qquad (4.6)$$

For contraction levels larger than the critical value a plastic zone is formed around the tunnel cavity resulting in plastic deformations, while for levels lower than the critical value the deformations remain elastic, corresponding to a constant normalized displacement $u_z/\Delta D$

value. We illustrate this effect in Figure 4.10a for a shallow tunnel, C/D=1 with soil rigidity, $\frac{G}{s_u} = 100$ (ε_y=0.25%). These results show how the zone of plasticity and ground settlements are affected by the magnitude of the shield contraction. In this example, plastic strains are limited to a local zone around the shield for $\varepsilon < 1.5\%$, but for larger values of ε extend to the ground surface.

As discussed above, the surface deformations, u_z are proportional to the contraction, ε, and independent of the $\frac{G}{S_u}$ ratio for sufficiently deep (C>3) tunnels (i.e. the local plastic zone formed around the tunnel is far enough to have a minimal effect on surface deformations) and/or small contractions, ε<1% (i.e. the size of the plastic zone is too small to have any effect on surface deformations). Figure 4.11 shows how the normalized settlements, $\frac{u_z}{\Delta D}$ depend on the tunnel depth, H. The computed results were fitted using the least squares method. The resulting equation was:

$$\frac{u_z}{\Delta D} = 0.45\frac{D}{H} \qquad (4.7)$$

where $\Delta D = |D_{tail} - D|$, D the shield diameter at the front section, D_{tail} the shield diameter at the tail section and H is the depth to the tunnel springline. For shallow tunnels with large cavity contractions, ε, Figure 4.9 should be used to predict the induced maximum settlement at the surface, while for all other cases Eq. 4.7 can also be applied.

4.4 TBM Weight and Tunnel Buoyancy

The weight of the TBM machine, W_{TBM} is usually less than the weight of the excavated soil, W_{soil} resulting in a net upward force on the completed tunnel (i.e. buoyancy effect). This effect can be considered favorable as it leads to a decrease in the surface settlement (in contrast to the prior three factors). However, it is important to understand cases where buoyancy can have a substantial effect and the factors which affect its magnitude.

A 2D finite element model is used to study the effects of the TBM weight, W_{TBM} on induced ground deformations, assuming plane strain geometry as shown in Figure 4.12. The selected mesh and dimensions of the model are presented in Figure 4.12. Different ratios of model depth to width MD/MW were considered. The value MD/MW= 4 was selected as it was the smallest model that could ensure zero interference with the transverse boundaries. The model uses the MC soil model, assuming undrained shear conditions, groundwater table coincident with the ground surface and in situ stresses with K_0 = 1.0. An array of different model depths was examined to investigate the effect of the layer depth for the range MD$\in [50, 800](m)$. A homogeneous stratigraphy was studied with soil unit weight of $\gamma = 20\ KN/m^3$, varying shear strength $s_u \in [30,100](kPa)$ and elastic stiffness $G \in [3,10](MPa)$. The reference tunnel had characteristics similar to prior analyses with D=7m and cover depth to diameter, C/D $\in [1, 5](m)$. The model simulates the shield weight effect by deactivating the soil elements inside the tunnel cavity and activating stiff plate elements (the TBM is considered an undeformed body) on which a uniform load was applied corresponding the weight of the shield. Various weights for the TBM were studied ranging from zero weight to the case that the

machine weight is equal to the removed soil weight (e.g. $W_{TBM} = 0.5W_{soil}$ for the Crossrail Project, Founta, 2013, Founta and Whittle, 2016).

4.4.1 Effects of Buoyancy on Surface Settlements

Initially a parametric study focusing on the net buoyancy ratio, W_{TBM}/W_{soil}, for shallow tunnel (C/D=1) with $\frac{G}{s_u} = 100$ was conducted. Figure 4.13a shows that there is a linear dependency between the normalized surface settlement and the buoyancy ratio, W_{TBM}/W_{soil}. The maximum induced heave at the surface above the tunnel centerline can be described by the following equation:

$$\frac{u_z}{u_{zmax}} = 1 - \frac{W_{TBM}}{W_{soil}} \qquad (4.8)$$

where $W_{TBM}$is the TBM weight, $W_{soil} = \gamma\pi D^2 l_{TBM}$ the weight of the removed soil, l_{TBM} the TBM shield length and u_{zmax} is the maximum heave induced for the case when $W_{TBM} = 0$. We can now focus on studying the dependency of u_{zmax} on the model depth, MD and then combine with Eq. 4.8 to calculate the deformations for a specific tunnel case.

As before, the computed displacements are represented by the dimensionless group $\frac{u_{z,max}G}{\gamma D^2}$ where the elastic shear modulus, G, the tunnel diameter, D and the soil unit weight γ are used as repeating variables (based on the π theorem). By multiplying the induced deformation with the shear stiffness modulus, we can account for its effect on the induced deformation and can then focus on the effect of other parameters. Figure 4.13b shows that there is a logarithmic

relationship between the normalized deformations and the ratio of soil thickness to tunnel springline depth, MD/H. This relationship is fitted using the least square method:

$$\frac{u_{z,max}G}{\gamma D^2} = \left[3\log\left(\frac{MD}{H}\right) - 0.02\right]x10^{-3} \qquad (4.9)$$

where MD model depth and H depth at the tunnel springline.

The buoyancy effect due to the TBM weight can be described by combining Eq. (6.4) and (6.5) into one general equation:

$$\frac{u_z G}{\gamma D^2} = \left[1 - \frac{W_{TBM}}{W_{soil}}\right]\left[3\log\left(\frac{MD}{H}\right) - 0.02\right]x10^{-3} \qquad (4.10)$$

This equation can be used in practice to predict the maximum surface heave due to the shield weight by inputting: i) the shield characteristics W_{TBM}, l_{TBM}, ii) the tunnel geometry D, H, and iii) the soil properties γ, G.

4.5 Surface Settlements for Mixed Face Conditions

Mixed face conditions present a challenge for tunnel engineers due to the difficulty arising in selecting the appropriate parameters to control ground deformations. Results in section 3.3 have shown how the face pressure, σ_f, must be adjusted to control stability for mixed face tunneling in clay. This section extends the method proposed for homogeneous conditions for prediction of ground movements for mechanized tunneling in mixed clays.

In order to study the effect of face pressure during mechanized tunnel construction in mixed face conditions, we adapted the previously developed 3D finite element model for the homogeneous case (Figure 4.2) and introduced a two layer stratigraphy characterized by i) an interface located at depth, D_T, below the crown ; and ii) a contrast in undrained shear strength between the upper and lower clay layers ($s_{uT}/s_{uB}; G_T/G_B$). This current analysis focuses only on the effect of face support, ignoring other effects (shield conicity, the grouting process and TBM weight), as this is the main source of deformation for most tunnels and it is highly dependent on the soil conditions encountered at the face of the excavation. The effect of TBM conicity can be calculated separately from the proposed methodology in sections 4.3 as it is independent of the soil properties for small contractions, whereas average soil properties can be used to provide an estimate of the deformations due to grouting and TBM weight (sections 4.2 and 4.4). The analysis uses the same methodology described in section 4.1 to compute the net ground surface settlement based on steady state incremental movements.

An array of analyses was conducted to calculate the induced displacements for different tunnel geometries and mixed face soil properties. Figure 4.14 shows how the computed net surface settlements vary as a function of the embedment ratio, D_T/D. The analyses consider a combination of three different face pressure ratios $\frac{\sigma_f}{\gamma H} = 0, 0.2, 0.4$ and three strength profiles $\frac{s_{uT}}{\gamma H} = 0.08, 0.1, 0.2$ in the upper clay for the case of a deep tunnel (C/D=3) and a small contrast in shear strength and stiffness ($s_{uB}/s_{uT} = G_B/G_T$=2). The figure shows the transition from full embedment in the stiff clay layer ($\frac{D_T}{D} = -1$) to the soft clay layer ($\frac{D_T}{D} = 1$). If a constant face pressure is maintained for each soil profile the displacements increase significantly. For the

case with $s_{uT}/\gamma H$=0.08 and zero face pressure ($\sigma_f/\gamma H$=0) the tunnel is stable in the stiff clay layer but becomes unstable in the soft clay, while settlements in the soft clay can be controlled by increasing the face pressure.

Prior simulations show that surface deformations for homogeneous clays (i.e. $\frac{D_T}{D} = -1{,}1$) can be described by a rectangular hyperbola with a single coefficient $\alpha = \alpha_{hom}$. The mixed face can then be simulated by fitting the transitional effects of D_T/D and strength ratio $\frac{s_{uB}}{s_{uT}}$ using logistic dose response curve (Joseph et al., 2010) with a least squares method (Figure 4.15). The resulting equation can be applied to calculate the fitting parameter a as follows:

$$a = a_{hom}\left\{\left(1 - (\tfrac{s^*_{uT}}{s^*_{uB}})^2\right)\left[\left(\frac{\frac{D_T}{D}+1}{2}\right)^5 - 1\right] + 1\right\} \qquad (4.11)$$

where a_{hom}=0.012 obtained from Figure 3.17 and $s^*_{uT,}\, s^*_{uB}$ the in-situ undrained strength of upper and lower clay units . The surface settlements can be then calculated for the properties of the upper clay layer:

$$\frac{u_Z G_T}{\gamma D^2} = a\left[\frac{\gamma H}{\Delta s_{uT}}\right]\left[1 - \frac{\sigma_f}{\gamma H}\right] \qquad (4.12)$$

where $\Delta s_{uT} = \left[s^*_{uT} - s_{uT}\right]$, s_{uT} is the strength causing face instability (see Figure 3.22, Figure 3.23, Figure 4.16), and a is computed from Eq.(4.11). Figure 4.16 illustrates how the proposed method can be applied in mixed face conditions by using as input the face pressure and soil properties ($s^*_{uT}, G_T,\ s^*_{uB}, G_B$) and geometry specifics (tunnel depth C/D, underground stratigraphy, $\frac{D_T}{D}$). The critical unstrained strength can be calculated from eq. 3.7: $s_{uT} =$

$\tilde{s}_{uT}\left(1-\frac{\sigma_f}{\gamma \mathrm{H}}\right)$, combined with the unsupported critical undrained strength $\tilde{s}_{uT}$ calculated for the examined geometry (C/D and $\frac{\mathrm{D_T}}{D}$) from Figure 4.16 for s_{uT}/s_{uB} =2 or Figure 3.21, Figure 3.22, Figure 3.23 and Figure 4.16 for different relative strength s_{uT}/s_{uB} ratios.

Figure 4.17 summarizes the effects of the face pressure ratio, $\sigma_f/\gamma H$, and embedment ratio, D_T/D, on the induced settlements for four cases of different top layer undrained strength ratios $s_{uT}/\gamma H$= 0.05, 0.01, 0.015, 0.02 with a relative strength ratio $s_{uB}/s_{uT} = 2$ and cover depth ratio $C/D = 3$. We can use these graphs to estimate the necessary increase in the applied face pressure that would provide control over deformations as we transition from the stiff to the soft clay layer. For instance, if we consider the case with $s_{uT}/\gamma H$= 0.05 ($s_{uB}/\gamma H$= 0.10), if we plan to maintain a maximum normalized deformation of $\frac{u_Z G_T}{\gamma D^2}$ = 0.3, the analyses show applied face pressure must increase by a factor of 6 from $\frac{\sigma_f}{\gamma \mathrm{H}} = 0.1$ to 0.6 during the transition from stiff to soft clay. Rates of change in the support pressure are less significant at higher support pressures. A support ratio of $\frac{\sigma_f}{\gamma \mathrm{H}} = 0.35$ in the stiff layer would translate to a ratio of $\frac{\sigma_f}{\gamma \mathrm{H}} = 0.75$ in the soft layer for maintaining a deformation of $\frac{u_Z G_T}{\gamma D^2}$ = 0.1, corresponding to a factor of increase of about 2. Similar trends can be observed for other three higher undrained strength cases (i.e. $\frac{s_{uB}}{s_{uT}} = 1.0 \rightarrow 5.0$; using Eq. 4.11 and 4.12).

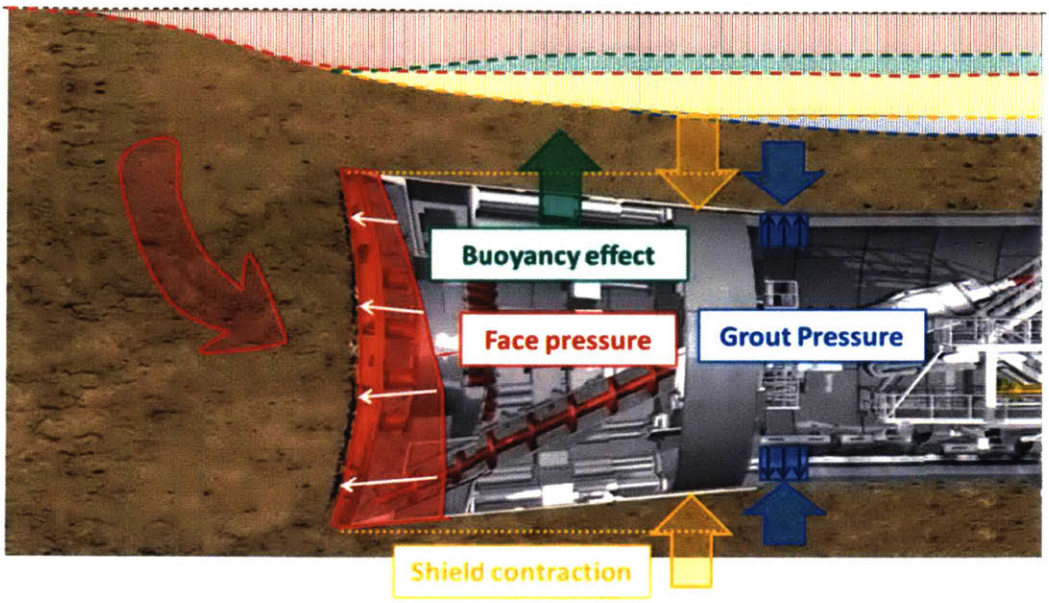

Figure 4.1 Schematic of the combined effect of the four examined parameters considered for the deformation analyses

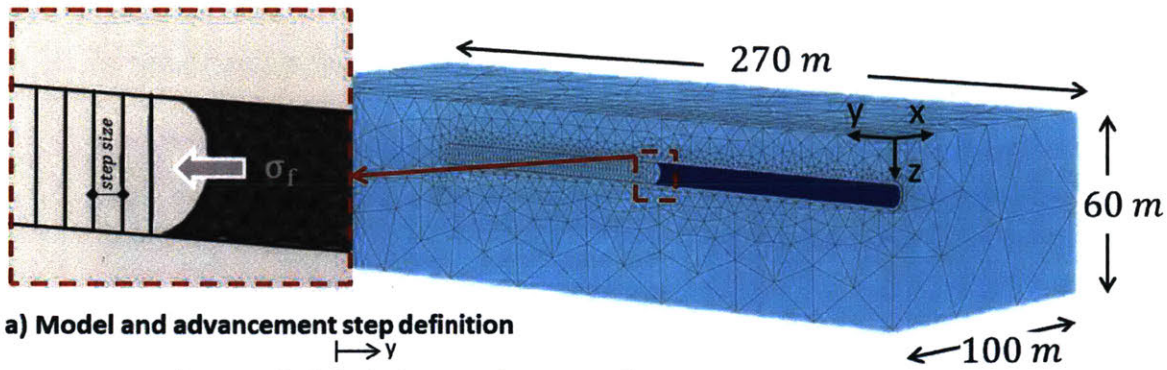

a) Model and advancement step definition

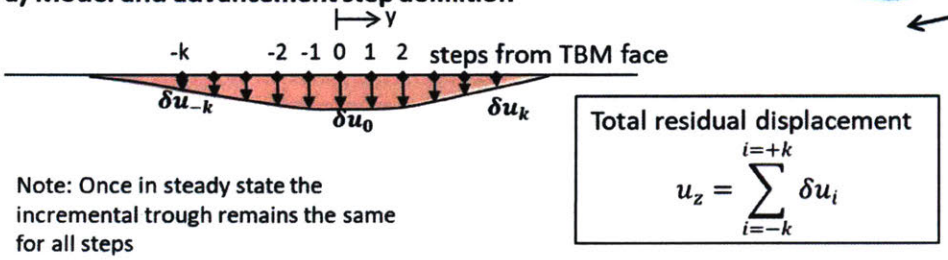

Note: Once in steady state the incremental trough remains the same for all steps

Total residual displacement

$$u_z = \sum_{i=-k}^{i=+k} \delta u_i$$

b) Incremental ground displacements for a single advancement step

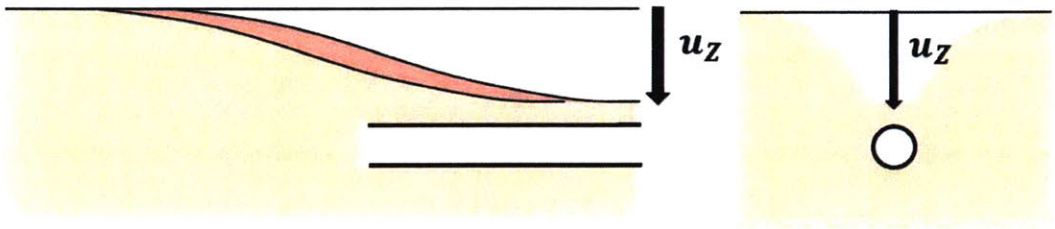

c) Longitudinal settlement trough

Figure 4.2 Schematic depiction of 3D model and methodology used to study the induced deformation due to tunneling in homogeneous conditions in clay

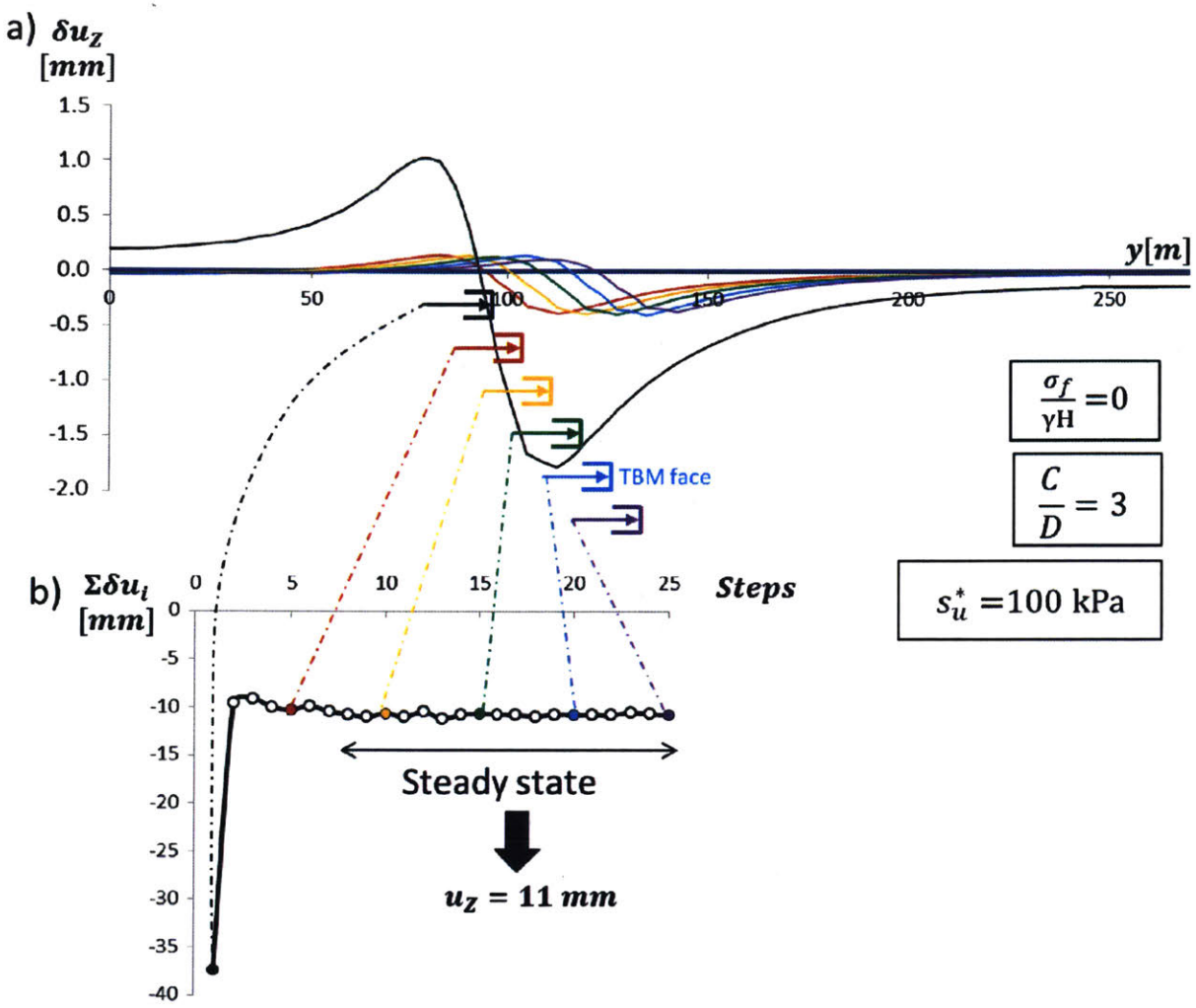

Figure 4.3 Example of methodology used to calculate residual settlements for C/D=3, s_u=100kPa and σ_f=0 a) incremental settlement troughs and b) settlement integrals for steps 1,5,10,15,20,25

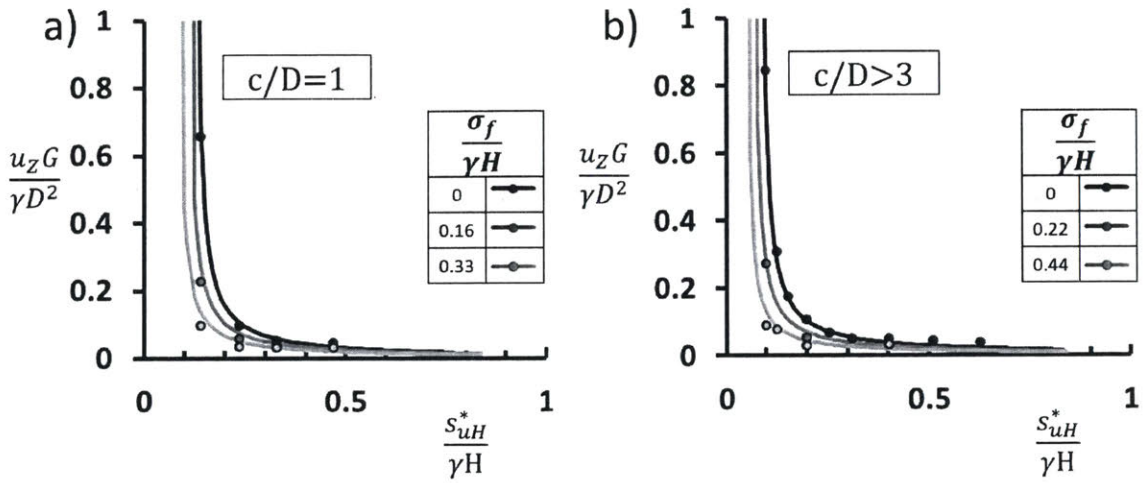

Rectangular Hyberbola

$$\frac{u_z G}{\gamma D^2} = a\left[\frac{\gamma H}{\Delta s_u}\right]\left[1 - \frac{\sigma_f}{\gamma H}\right]$$

$$\Delta s_u = s^*_{uH} - s_{uH}$$

Fitted for the analysis data

$$a_{hom} = 0.012$$

Figure 4.4 Computed deformations due to face pressure fitted with rectangular hyperbola, followed by the proposed design charts for a) shallow and b)deep tunnels

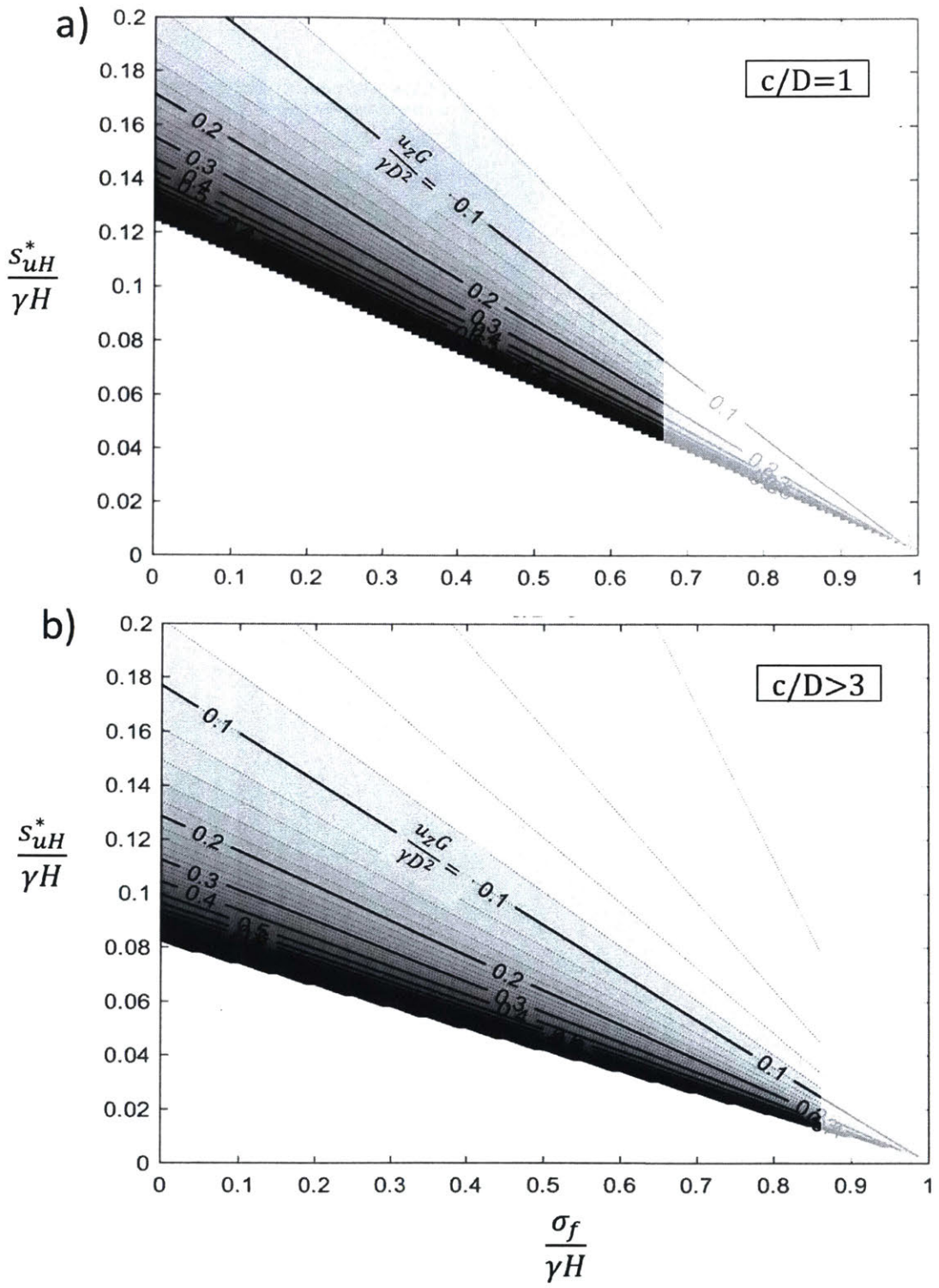

Figure 4.5 Design charts for method of displacements for homogeneous clays for a) shallow and b)deep tunnels

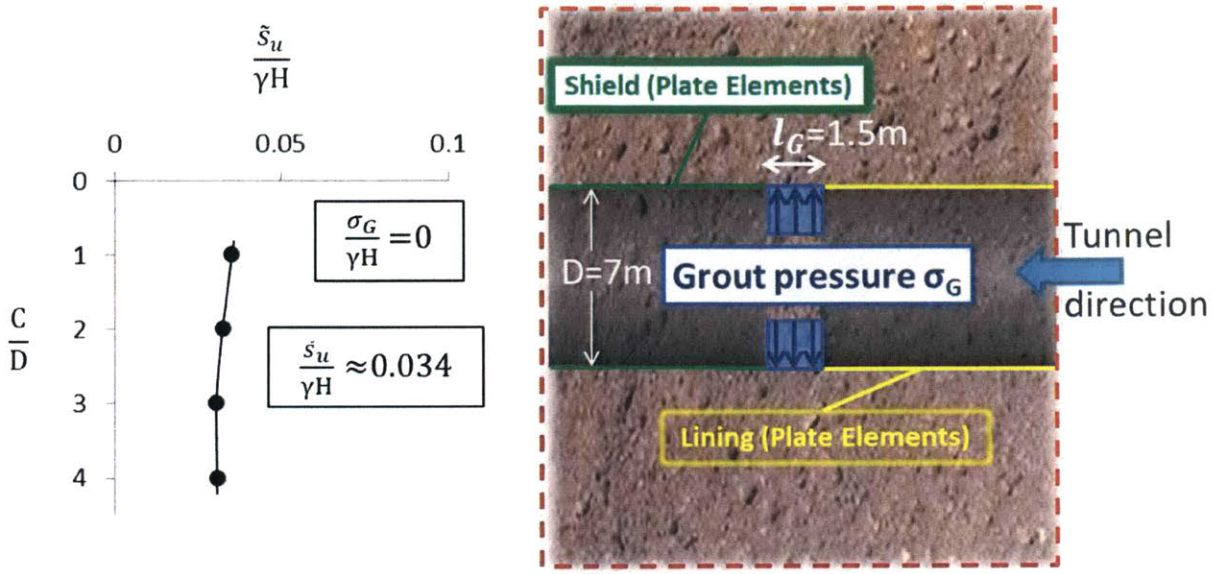

a) Stability for zero grout pressure b) 3D model schematic

Figure 4.6 Grout pressure a) stability analyses for zero grout pressure and b) schematic of 3D model used for stability and deformation analyses.

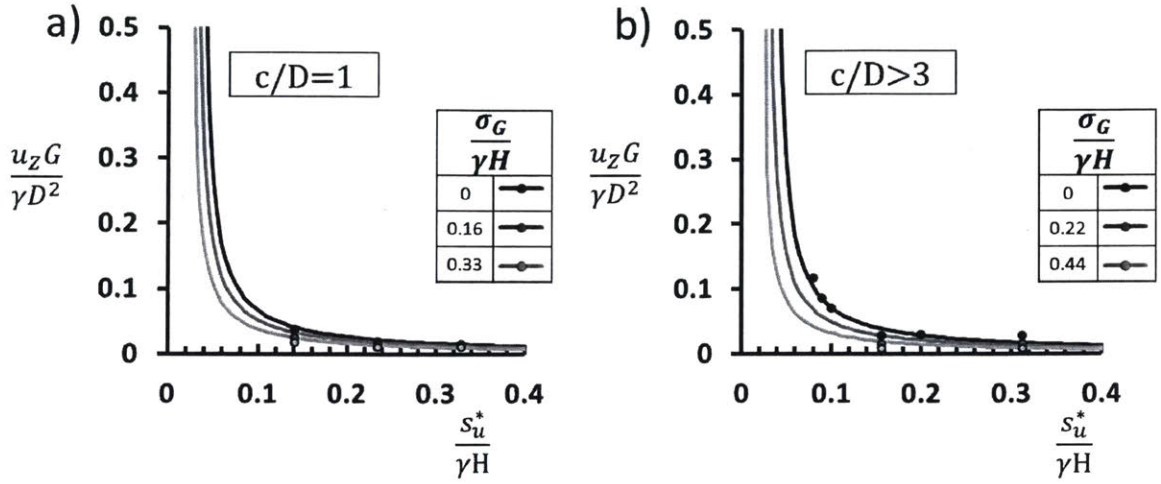

Rectangular Hyberbola

$$\frac{u_Z G}{\gamma D^2} = b\left[\frac{\gamma H}{\Delta s_u}\right]\left[1 - \frac{\sigma_G}{\gamma H}\right]$$

$$\Delta s_u = s_u^* - s_u$$

Fitted for the analysis data

$$b = 0.004$$

Figure 4.7 Computed deformations due to grout pressure fitted with rectangular hyperbola for a) shallow and b) deep tunnels

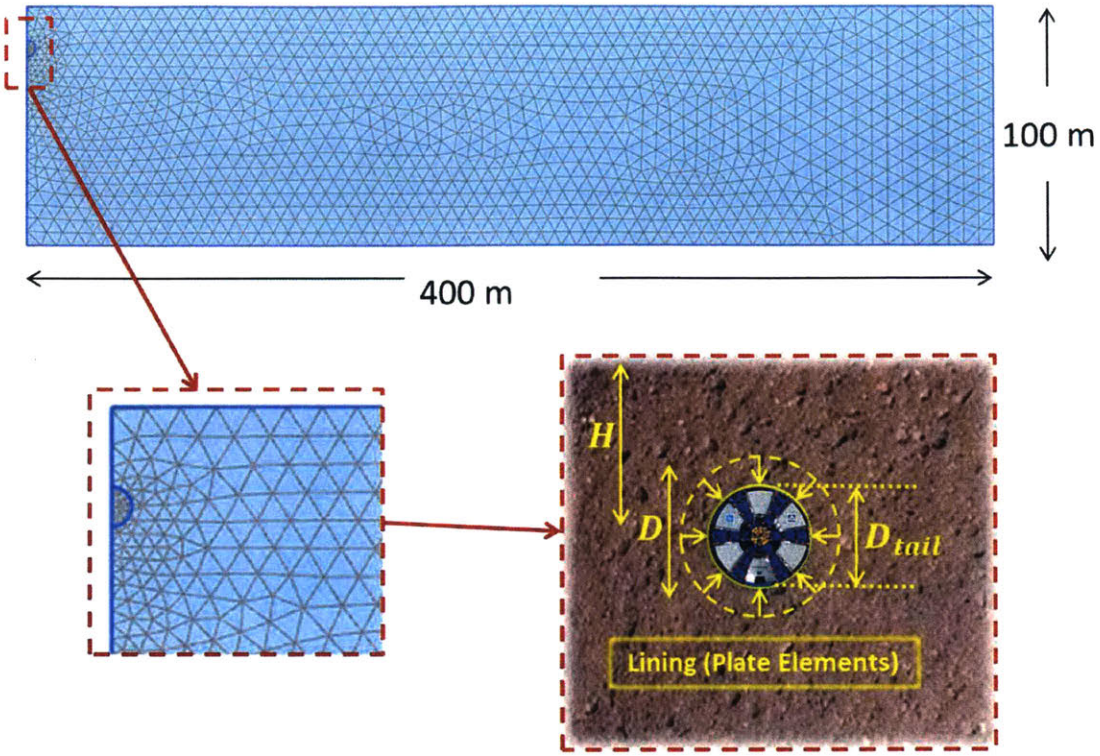

Figure 4.8 2D plane strain model used for calculating displacements due to the conical shape of the TBM

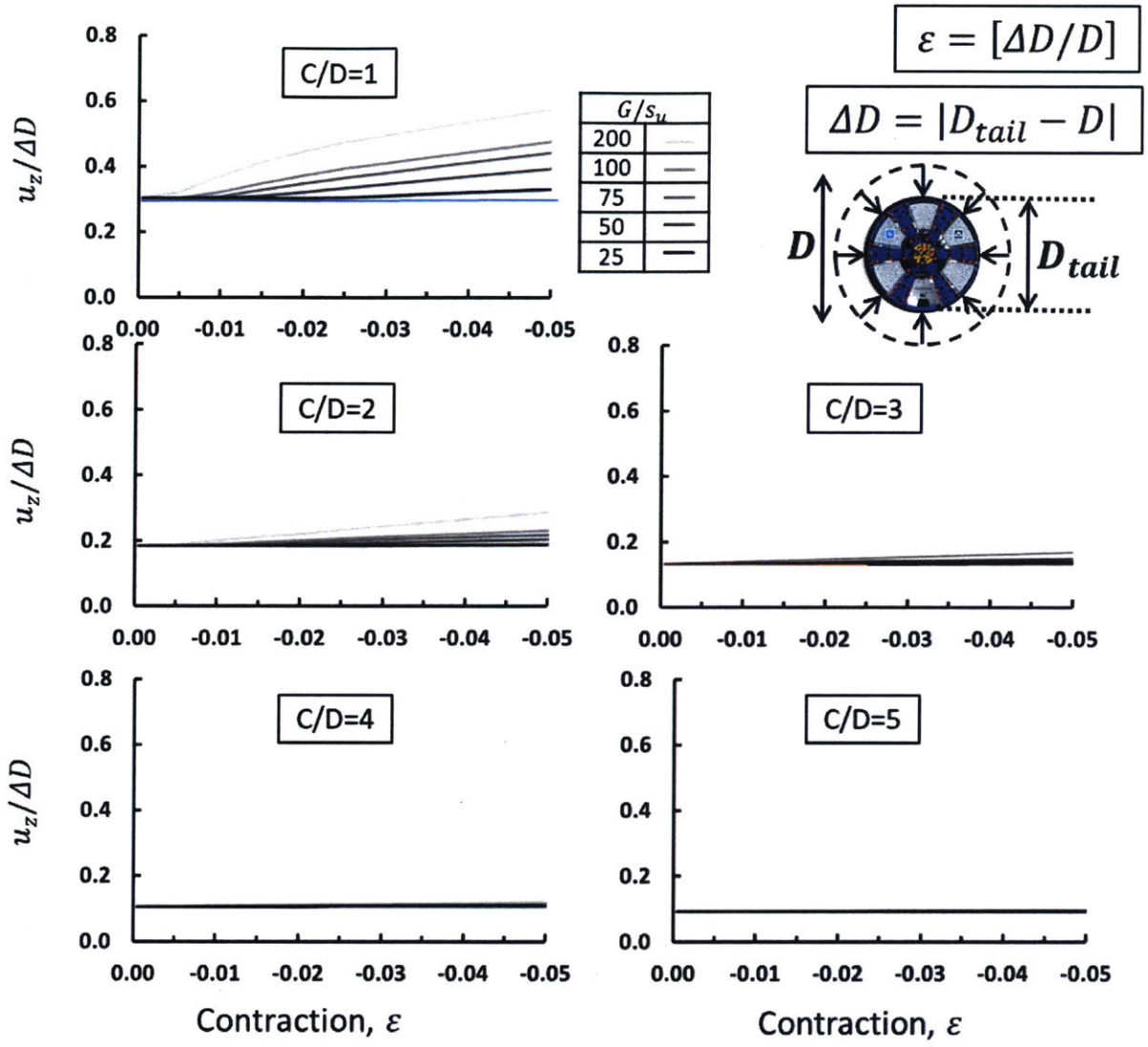

Figure 4.9 Computed surface settlements as a function of the cover depth ratio C/D, the shear stiffness over strength ratio G/S_u and TBM contraction

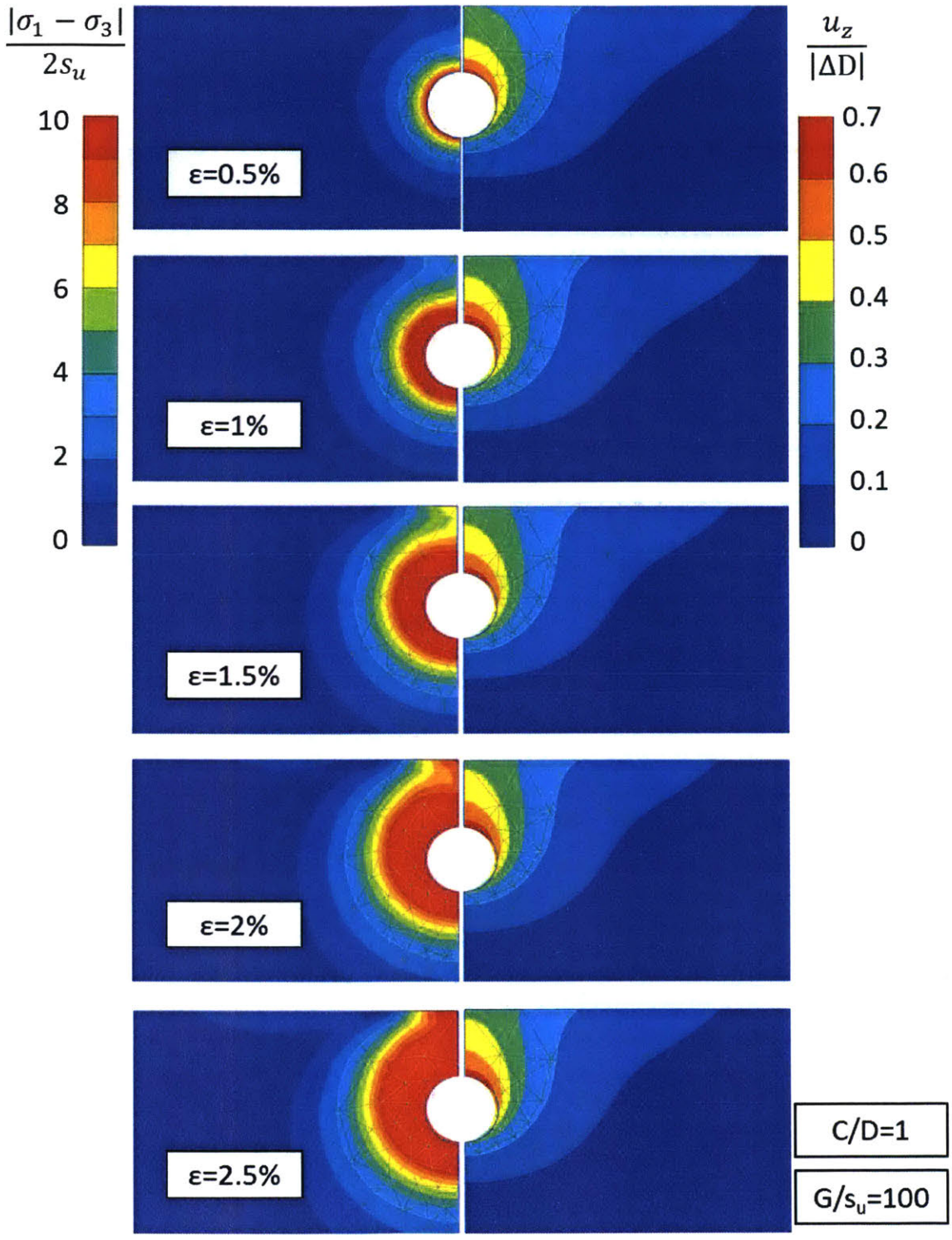

Figure 4.10 Mobilized shear stress on the left and normalized deformations on the right for the different applied contraction for C/D=1 and G/s_u=100

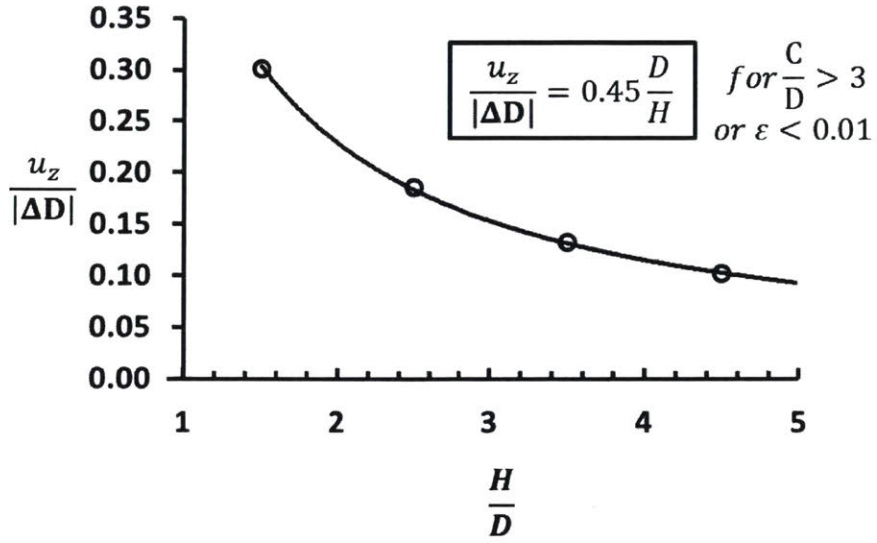

Figure 4.11 Computed minimum surface settlements as a function of the tunnel depth and TBM contraction

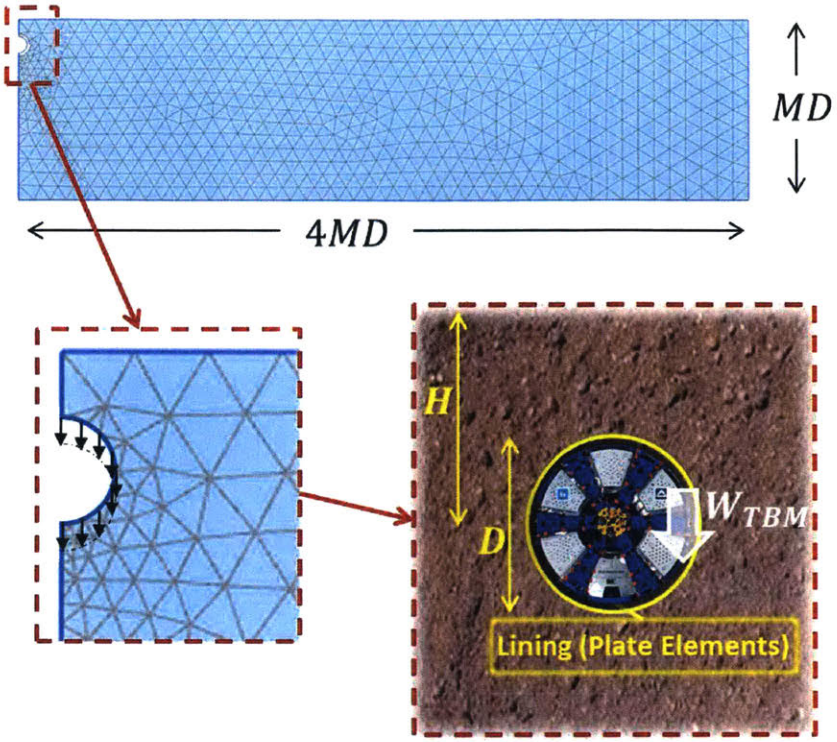

Figure 4.12 Schematic of the 2D plane strain model used to capture the isolated effect of the TBM weight

$$u_z = u_{zmax}\left(1 - \frac{W_{TBM}}{W_{soil}}\right) \Rightarrow \frac{u_{z,max}G}{\gamma D^2} = \left[3\log\left(\frac{MD}{H}\right) - 0.02\right] x10^{-3}$$

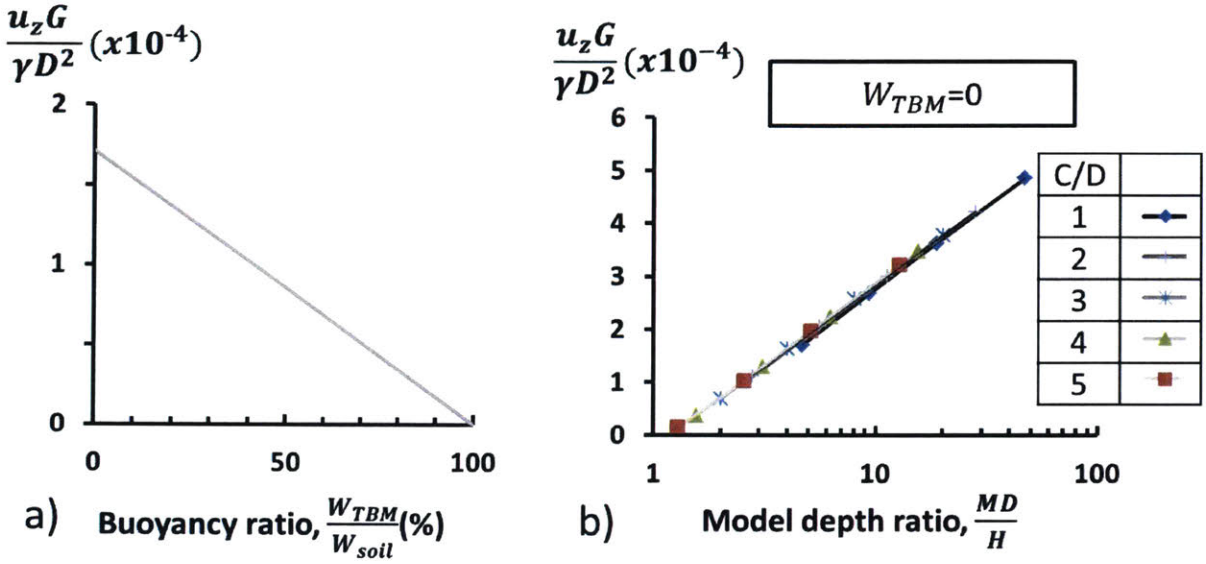

Figure 4.13 Computed maximum surface settlements as a function a) the machine weight b) the model depth and tunnel depth

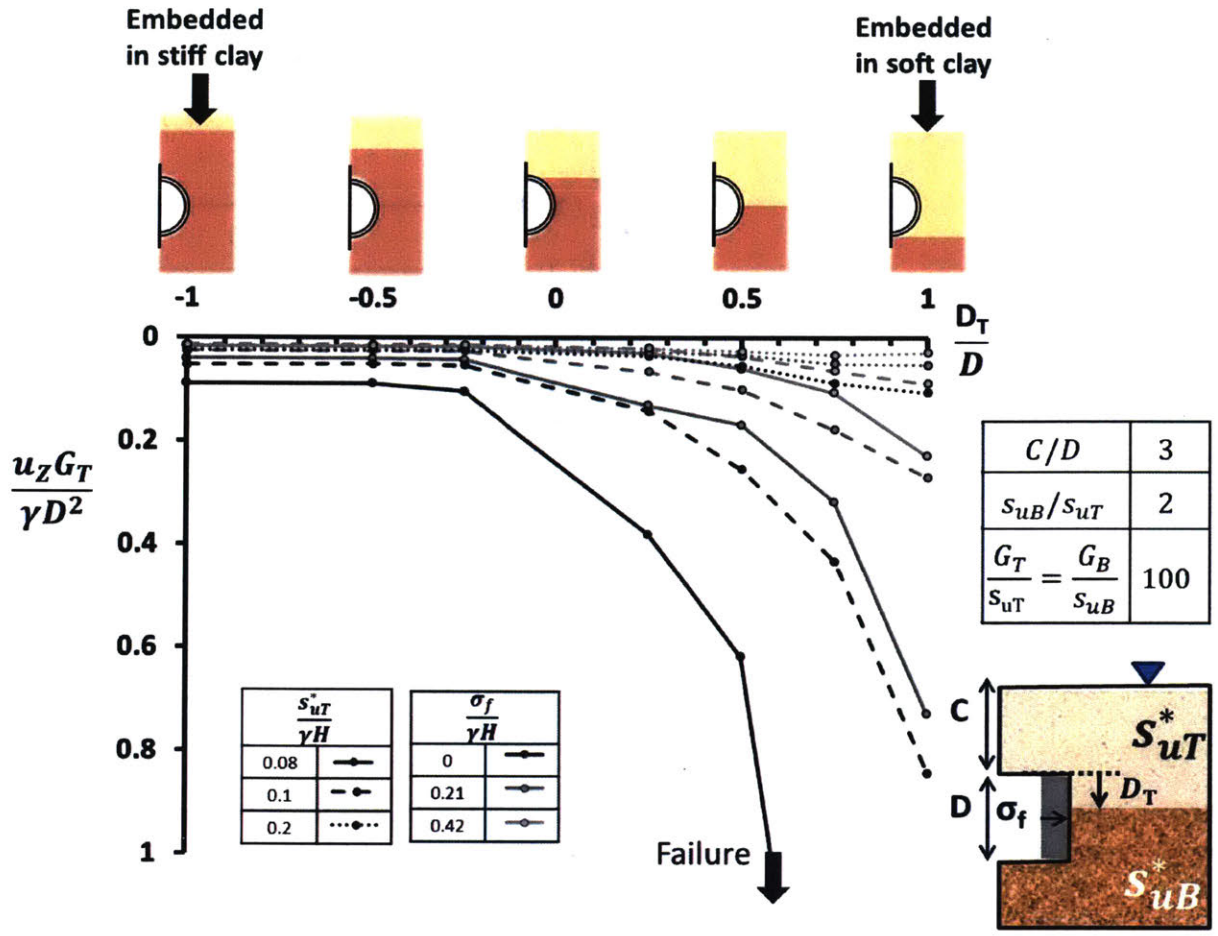

Figure 4.14 Computed deformations as a function of embedment ratio D_T/D, undrained strength ratio $s_{uT}/\gamma H$ and support pressure ratio $\sigma_f/\gamma H$, for strength ratio $s_{uB}/s_{uT}=2$ and cover depth ratio C/D=3

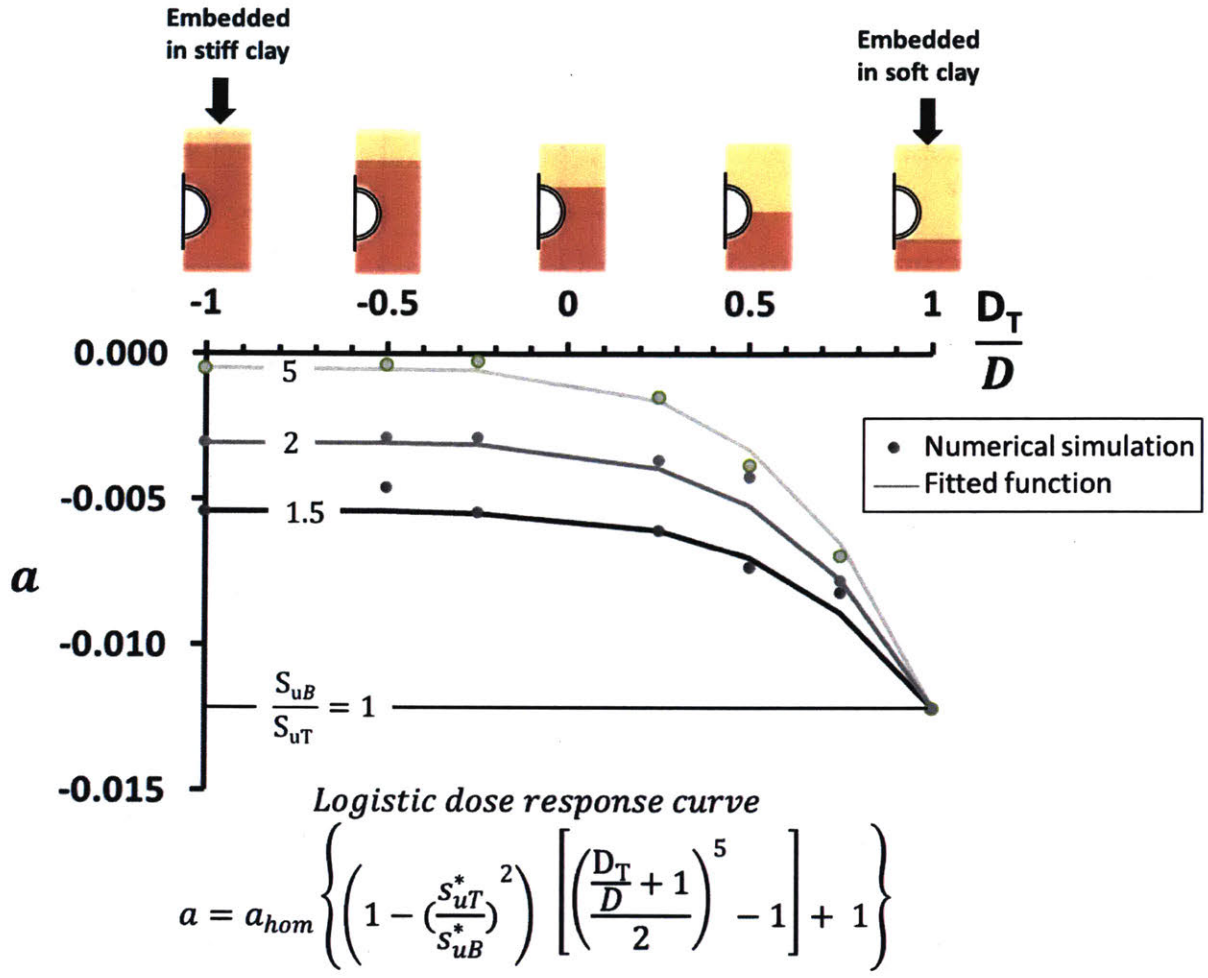

Figure 4.15 Plot of the fitted scaling variable α for each of the 20 scenarios examined corresponding to a unique combination of embedment ratio D_T/D and relative strength ratio s_{uB}/s_{uT}, fitted using the logistic dose response curve to describe the α parameter as a function of the embedment ratio D_T/D and strength ratio s_{uB}/s_{uT}

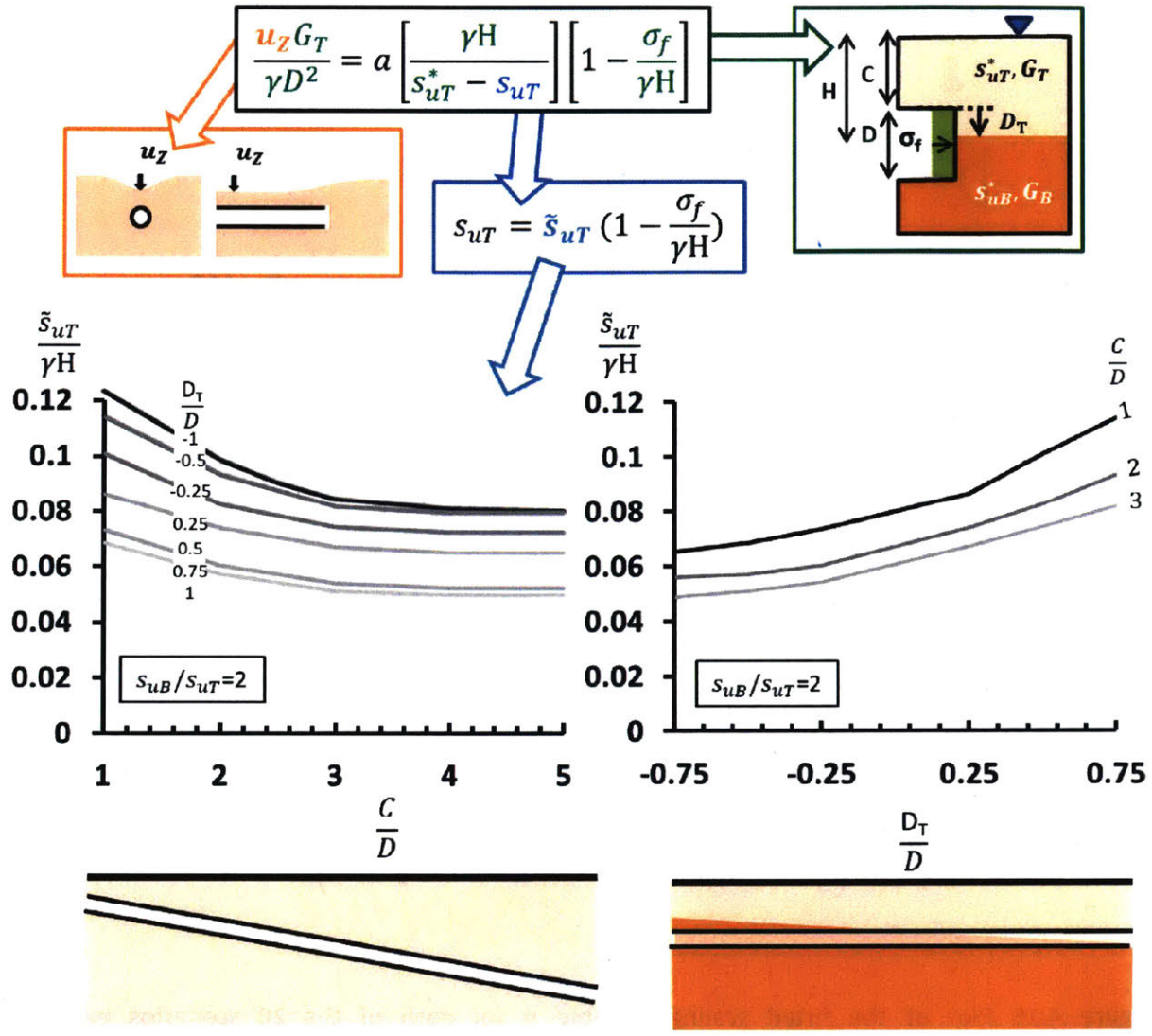

Figure 4.16 Illustrative methodology for calculating the induced deformation due to face pressure in mixed face conditions

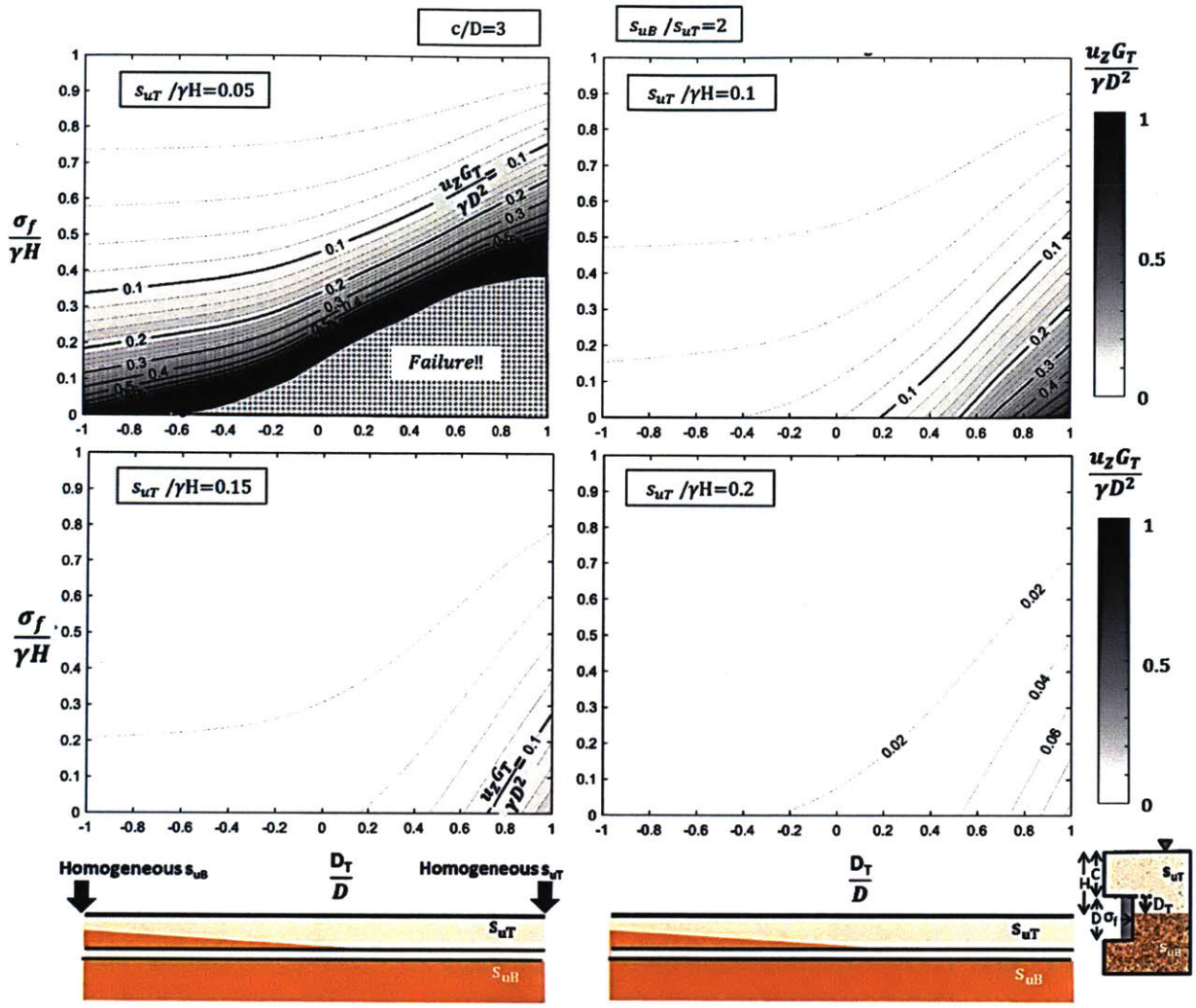

Figure 4.17 Proposed design charts with the method of displacements for two layered clays as a function of embedment ratio D_T/D and support pressure ratio $\sigma_f/\gamma H$, for strength ratio $s_{uB}/s_{uT}=2$, cover depth ratio C/D=3, and , undrained strength ratio $s_{uT}/\gamma H$= 0.05, 0.01, 0.015 and 0.02

5 Evaluation of Simplified Method for Predicting Surface Settlements due to Mechanized Tunneling in clay

5.1 Introduction

The goal of this chapter is to evaluate the proposed methodology defined in Chapter 4 for estimating ground surface settlements in clay. After studying separately each of four parameters that control the induced surface deformation we now combine their effects by superimposing to estimate surface settlements due to mechanized tunneling in clay. Table 5.1 shows the key equations derived from the simulations in chapter 4. The superposition principle is a reasonable approximation for small deformations (where most of the soil mass remains elastic) but can have shortcomings when dealing with simulations where there is a large zone of plasticity around the tunnel. However, even in these cases where the method will tend to under predict expected settlements the methodology can still be used as a qualitative guide to indicate critical sections of a tunnel project that require further attention and assist engineers in conducting quick estimates for control of ground deformations.

The goal of the current procedure is to predict realistically the surface settlements from basic knowledge of the soil properties (undrained strength), the dimensions and weight of the shield and key control parameters (face pressure, grout pressure). The proposed model focuses on the maximum ground settlement above the centerline of the tunnel, and addresses transitions in the soil profile (mixed face conditions). Here, we validate the methodology for three case studies of mechanized tunneling in clay: 1) Contract C300 (Ieronymaki et al., 2016), 2) contract

C933 for Downtown line in Kallang at Bendemeer, Singapore (Su, 2015), 3) northern section of the MRTA Blue Line in Bangkok, Thailand (Suwansawat, 2002, Suwansawat and Einstein, 2006).

5.2 Crossrail C300

The Crossrail C300 project involved the construction of twin tunnels for a high speed rail line crossing beneath central London (Figure 5.1a). The project is still under construction and is expected to become fully operational by 2019 (and will be known as Elizabeth Line). The Crossrail project contract C300 included construction of twin tunnel bores using 7.1m diameter EPB machines (Figure 5.2). Prior research has focused on the performance of these tunneling operations beneath Hyde Park. The current analyses focus on the first (WB) tunnel bore. Ieronymaki et al., (2016) have documented the TBM control parameters (σ_f, σ_G;Figure 5.3a) and tunnel advance rate (Figure 5.3b) for an 800m trajectory beneath Hyde Park (Greenfield site). For this section the applied face pressure, σ_f, remains almost constant at about 180 kPa (1.8 bar), while there is a high variation of the applied grout pressure which fluctuates from 60 kPa to 260 kPa (0.6-2.6 bar). Figure 5.1b shows a series of surface transections A-P, where settlements were monitored (in addition there was more complete subsurface data available for section F). The settlement measurements for the 9 monitoring sections are summarized in Figure 5.4. The maximum residual settlement at the surface above the tunnel centerline varies from 6 to 9mm. Figure 5.5 shows the subsurface stratigraphy in this area. The tunnel is excavated through units B and A3 of the London clay. Figure 5.6 summarizes the undrained shear strength profile in the London clay based on UU triaxial compression shear tests from the original site investigation (GCG, 2010). This figure shows that there is significant scatter in the

s_u of the high over-consolidated London clay. There is no clear distinction between the undrained strength properties of the main sub-units, but there is a reasonable linear variation with depth. The upper, lower bound and design line are:

Upper Bound: $s_u = 100 + 10z$ [kPa] (5.1)

Design Line: $s_u = 75 + 5.5z$ [kPa] (5.2)

Upper Bound: $s_u = 40 + 3.5z$ [kPa] (5.3)

Ieronymaki (2015) shows that there is little inherent anisotropy in the intact behavior of London clay (based on high quality data from block samples) hence, the results in Figure 5.6 are a good estimate of the average undrained shear strength and stiffness profile. The vertical drained stiffness of London Clay was estimated from an empirical relationship proposed by Stroud, 1989 relating the stiffness to the undrained shear strength from UU tests:

$$E_v' = 200 s_u \quad (5.4)$$

Based on this relationship the proposed design line for drained stiffness is:

$$E_v' = 15 + 1.1z \text{ [MPa]} \quad (5.5)$$

Ieronymaki (2015) estimated the equivalent isotropic stiffness parameters for the slightly anisotropic London clay, proposing that Eq.5.5 and a Poisson's ratio of v=0.244 can be used to approximate the London clay behavior. As a result the proposed design line for the shear modulus is:

$$G = 6 + 0.44z \text{ [MPa]} \quad (5.6)$$

The K_o value of London Clay was estimated from site investigation for Crossrail C300 (GCG, 2010) including Self-Boring Pressuremeter (SBP) tests and triaxial suction tests (on high quality samples), with an average value of K_o=1.

Figure 5.7 presents the bulk density for the London clay units corresponding to an average unit weight value, $\gamma = 20\frac{kN}{m^3}$ (GCG, 2010). By combining this data with the face pressure (Figure 5.3a) and the elevation data we can use results of chapter 3 to estimate face stability of the C300 tunnel). The computed stability strength ratio, $\widetilde{s_u}/\gamma H = 0.08$ for the unsupported case ($\frac{\sigma_f}{\gamma \mathrm{H}} = 0$) is obtained from Figure 3.17. This corresponds to stability ratios, $s_u/\gamma H$= 0.052 to 0.064 for the monitored face pressure range, $\frac{\sigma_f}{\gamma \mathrm{H}}$ = 130 to 230 kPa (based on Eq. 3.7: $s_u = \widetilde{s_u}\left(1 - \frac{\sigma_f}{\gamma \mathrm{H}}\right)$). Hence, the critical stability strength ratio is significantly lower, than the in situ strength, $s^*_{uH}/\gamma H \approx 0.4$ of the London clay (equivalent to a safety factor, FS= 6.5). The maximum induced surface settlements, are predicted along the WB alignment for the Hyde Park area using the proposed method of displacements developed in chapter 4 and are compared to gathered data from the 9 instrumented sections in Hyde Park using Position Leveling Points (PLPs) (Figure 5.1b) and prior predictions for the C300 tunnel (section F) using 3D finite element analyses by Founta and Whittle, 2016 (see Appendix A). The 3D model used by Founta and Whittle 2016 is presented in detail in Appendices A and B, discussing how it compares to measured transverse and longitudinal settlements.

Table 5.3 presents a summary of the predicted settlements by applying the proposed methodology for the 9 sections. The average soil properties (design line) estimated from the site investigation (GCG, 2010) as described above are used along with monitoring control data for face and grout pressure. The settlements due to face pressure are calculated using the critical strength ratio values from Figure 3.17 (homogeneous), the in-situ soil properties from Table 5.2, the monitoring control parameters from Figure 5.3a and the elevation data from Figure 5.5 as an input Eq. (4.3): $\frac{u_z G}{\gamma D^2} = a\left[\frac{\gamma \mathrm{H}}{\Delta s_u}\right]\left[1 - \frac{\sigma_f}{\gamma \mathrm{H}}\right]$. The settlements due to grouting of the tail void use the critical stability strength ratio for unsupported face, $\frac{\tilde{s}_u}{\gamma \mathrm{H}}$=0.34 as presented in chapter 4 and calculate the stability strength ratio from Eq. (4.5): $s_{uH} = \tilde{s}_{uH}\left(1 - \frac{\sigma_G}{\gamma \mathrm{H}}\right)$. The displacement due to grout pressure was calculated using Eq. (4.4): $\frac{u_z G}{\gamma D^2} = 0.004\left[\frac{\gamma \mathrm{H}}{\Delta s_u}\right]\left[1 - \frac{\sigma_G}{\gamma \mathrm{H}}\right]$. The settlements due to the conical shape of the shield were calculated using Eq. (4.7): $\frac{u_z}{\Delta D} = 0.45\frac{D}{H}$ and the effects of the TBM weight are ignored as they are minimal and favorable (<0.1mm) .

5.2.1 Comparison with Data and 3D FEA for Section F

Initially we present the predictions using the proposed methodology for section F of the Crossrail project in order to compare with prior work using a 3D FE model developed with Plaxis 3D^{TM} (Founta and Whittle, 2016). Founta and Whittle, 2016 studied the stratigraphy of section F in Hyde Park area (Figure A.1) using the M-C soil model with the design line soil properties as described in the previous paragraph (summarized in Table 5.2) based on site investigation data (GCG, 2010) and high quality laboratory shear tests as described in detail by Ieronymaki, (2015).

Figure 5.8 shows the comparison between our predicted maximum surface displacement, the longitudinal surface settlement trough predicted 3D FEA by Founta and Whittle, 2016 and monitoring data from PLPs for the instrumented sections shown in Figure 5.1 (Ieronymaki, 2015). The major components of deformation are the face pressure 1.3 mm and the TBM contraction 4.8mm. The settlement due the applied grout pressure is smaller and varies slightly due to the grout pressure fluctuation (see Figure 5.3) from 0.4 mm for σ_G=180 kPa to 0.5 mm for σ_G=80 kPa. The overall prediction of a 6.5 mm settlement is in good agreement with the 6.8mm measured data settlement for section F and the prediction from 3D FE model. The data from the other cross-sections have great scatter (5.9-9mm), but the median value (6.8mm) is close to our prediction.

5.2.2 Comparison with Data along Hyde Park

The method was then compared to PLP monitoring data for all A-P sections (Figure 5.9a) using the average design soil properties, the corresponding face and grout pressure (Figure 5.9 b) and the underground stratigraphy (Figure 5.9c) as input for the proposed equations. The surface settlements were predicted along this alignment and are in good agreement with the observed settlements at locations A-P. We can see that overall the predicted deformation remain almost constant at about 7mm although there are big variations in the monitored face pressures (130 to 250 kPa) and grout pressures (10 to 300 kPa). The small effect of the face and grout pressure on the surface deformations can be attributed to the high strength safety factor FS>6 for London Clay.

These results showcase how the proposed methodology can be applied in practice for estimating induced tunnel settlements in stiff clays. This methodology provides a valuable tool for estimating deformations and produces results comparable to complex 3D finite element simulations (Founta and Whittle, 2016). Further comparison is conducted to assess the accuracy of the proposed method in soft clays and mixed face conditions.

5.3 Downtown Line, C933, Singapore

Ong et al., (2016) and Su, (2015) have recently presented results that illustrate the difficulty of tunneling in mixed ground conditions. They present data for contract C933 of the Downtown Line (DTL) in Singapore. The section of interest involves tunneling using, 6.6m diameter, EPB machines that were launched from a shaft at the west end of the Bendemeer station. Each machine has a tailskin diameter, D_{tail}=6.58m while the tunnels are built using 1.4m wide rings, comprising 7 segments and 1 key. The two tunnels were built within 22m horizontal distance of the other with the Expo Bound tunnel (TBM2) generally positioned vertically above the bore of the Bukit Panjang tunnel (TBM1) for the examined 900m section of the tunnel alignment shown in Figure 5.10. The tunnels are fully embedded within a deep layer of Old Alluvium, a very stiff low permeability formation with very high strength. Su (2015) based on the site investigation (from SPT tests shown in Figure 5.11b) proposed the use of an undrained strength value, s_u=250kPa. Davies and Whittle, (2006) proposed the relationship s_u(kPa)=5.5N(bpf) for estimating the undrained strength, s_u from SPT tests, indicating that the selected value by Su (2015) falls in the mid-range for depths up to 15m deep and corresponds to the lower range for deeper locations. This value is also in close agreement with shear strength values (s_u≈300 kPa) from triaxial tests conducted by Chiam et al. 2003 for the Old Alluvium formation at a different

nearby location. The Old Alluvium unit weight, $\gamma = 20\ kN/m^3$ is based on the results shown in Figure 5.11a. The tunnels pass into soft marine clays of the Kallang formation between 700-800m from the launch site. The marine clays are high plasticity clays with w=60-70% and average (simple shear mode) undrained shear strength, s_u=20-50 kPa (increasing with depth) and unit weight, $\gamma = 16\ kN/m^3$ as shown in Figure 5.12. A linear dependency between the undrained strength with depth can be observed in Figure 5.12c and d which can be described by:

$$s_u = 18 + 1z \text{ [kPa]} \qquad (5.7)$$

where z is measured from the top of the Kallang formation at 98m elevation. Su (2015) selected a similar relationship to fit the data using: $s_u = 15 + 1.5z\ [kPa]$ as shown in Table 5.5. Sharma et al. 1999 estimated the deformation properties using pressuremeter and UU tests, reporting average values of E_u/s_u=170 for the Old Alluvium formation and 250 for the Kallang formation (corresponding to average values of G/s_u≈60 and 80 respectively). Su (2015) selected slightly different stiffness properties for the Old Alluvium and Kallang formations (shown in Table 5.5), however the data these values were based on were not presented in her thesis, so we could not validate these selections.

Table 5.4 summarizes the soil properties selected for the current work based on soil investigation data from the C933 project (Su, 2015) and recent soil investigations for the Singapore geological formations (Sharma et al., 1999). As shown in Figure 5.10, there is sand present between the Old Alluvium and the Kallang formations at certain locations from 500-

850m. For the purpose of these details are ignored and the model is applied assuming mixed clay face conditions only.

Figure 5.15 summarized the monitoring data for the section of interest as reported by Su, (2015). Figure 5.15a displays the maximum longitudinal settlements measured at locations along the tunnel alignment caused by TBM-1 alone (blue points) and combined total settlements after both TBMs have passed through (green points). The applied face pressure along the examined 900m window is presented in Figure 5.15b for TBM1 (blue line) and TBM2 (green line), while similarly the grout pressure is shown in Figure 5.15c.

5.3.1 Comparison with Data and 3D FEA for Array-1 and Array-2

First, we present predictions using the proposed equations at two instrumented sections, Arrays 1 and 2 (Figure 5.15) of the DTL project in order to compare with prior 3D Finite element analyses with the GeoFEA Finite Element Program (Su, 2015 see Figure 5.16 and Figure 2.37). Su (2015) studied these cases using the MC soil model with properties presented in Table 5.5.

The data at Array-1 show that both tunnels are embedded in the Old Alluvium with TBM-1 in homogeneous condition and TBM-2 encountering mixed face conditions as the sand layer[17] is less than one diameter above the tunnel crown. For Array-2, TBM-1 is fully embedded in the sand layer[18] while TBM-2 is embedded within Kallang (Figure 5.18c).

In order to estimate the settlements at Array-1 and Array-2 locations, we applied our proposed analytical method for estimating surface displacements (MoD) as described in chapter 4, using

[17] treated as Kallang for the purpose of this comparison

[18] since we treat sand as Kallang, TBM-1 is assumed to be in homogeneous conditions

the monitoring data from Figure 5.15, the stratigraphy from Figure 5.10 and the soil properties from Table 5.4. We assume independence of movements for the passage of TBM2 case and, as TBM1 is positioned below TBM2 for the sections of interest and hence, does not affect ground response due to TBM2. We can then uncouple the observed deformations by assuming that any increase in the observed settlement results can be fully attributed to the passage of TBM2.

The predicted settlements using our proposed method for the two tunnels (TBM1 and TBM2) in the two considered locations (Array 1 and Array 2) are shown in Table 5.6. For calculating the settlements due to the applied face pressure, the critical stability strength ratio for an unsupported face, $\frac{\tilde{s}_u}{\gamma \mathrm{H}}$, was found from results in Figure 3.17 and Figure 3.21 for the homogeneous and mixed face cases respectively. The critical stability strength ratio for the applied face pressure, σ_f, is calculated from eq. 3.7: $s_u = \tilde{s_u}\left(1 - \frac{\sigma_f}{\gamma \mathrm{H}}\right)$. Then the settlement due to face pressure was calculated for homogeneous and mixed face conditions using Equations: (4.3): $\frac{u_Z G}{\gamma D^2} = a\left[\frac{\gamma \mathrm{H}}{\Delta s_u}\right]\left[1 - \frac{\sigma_f}{\gamma \mathrm{H}}\right]$, (4.12) and (4.11): $a = a_{hom}\left\{\left(1 - (\frac{s^*_{uT}}{s^*_{uB}})^2\right)\left[\left(\frac{\frac{\mathrm{D_T}}{D}+1}{2}\right)^5 - 1\right] + 1\right\}$.

The embedment ratio for TBM-1 in the location of Array-1 is equal to zero ($\frac{\mathrm{D_T}}{D} = 0$) as the stratigraphic interface is located at the crown. The in-situ undrained strength of the top layer, s^*_{uT} was selected from Eq. 5.7 for the depth (C-0.5D) (z= C-0.5D-z1, where z1 is the depth of the top of the Kallang formation about 3.5 m), which corresponds to the average value assuming that the soil properties of the top layer have an effect up to one diameter above the tunnel. Hence, the average strength at the middle point of the affected area (C-D to C), i.e. depth of C-D/2 was used as an input. The deformations due to the grout pressure were calculated using

the critical stability strength ratio for an unsupported face, $\tilde{s}_u/\gamma$H=0.34 as presented in chapter 4 to calculate the stability strength ratio from Eq. (4.5): $s_{uH} = \tilde{s}_{uH}\left(1 - \frac{\sigma_G}{\gamma \mathrm{H}}\right)$. The displacements due to grout pressure were then estimated from Equation (4.4): $\frac{u_z G}{\gamma D^2} = 0.004\left[\frac{\gamma \mathrm{H}}{\Delta s_u}\right]\left[1 - \frac{\sigma_G}{\gamma \mathrm{H}}\right]$. The settlements due to the grouting of the tail void are quite small (≈0) as very high grout pressures were applied ($\frac{\sigma_G}{\gamma \mathrm{H}} \approx 1$). The settlements due to the conical shape of the shield were calculated using Eq. (4.7): $\frac{u_z}{\Delta D} = 0.45\frac{D}{H}$. We ignored effects of the TBM weight as there are quite small when compared to the other sources of deformation and their effect is favorable.

The comparison between the monitored data, the 3D FE predictions by Su, (2015) and the proposed MoD method are summarized in Figure 5.17. Generally our predictions are in good agreement with the monitored data apart from Array-2-TBM-1 case which is fully embedded within the sand layer and was treated as Kallang for this comparison. The predictions for the TBM-2 using our proposed method of displacements (MoD) are in close agreement with the monitored data for both Array-1 and Array-2 i.e. predictions show 3.9mm and 7.7mm, compared to measurements 4mm and 7mm, respectively and numerical results 4mm and 9.5mm predicted by Su, (2015). For the case of Array-1-TBM-1 we are predicting 3.2mm compared to 5mm measured and 3.5mm predicted by Su (2015). It should be noted that both our method and the 3D simulations by Su, (2015) underpredict by 2mm the settlement at this location, probably due to discrepancies in the representation of the stratigraphy.

5.3.2 Comparison with Data along the Alignment

The proposed methodology was applied to predict the settlements along the 900m alignment for TBM1 and TBM2 (Figure 5.18a and b). The deformations at each location were predicted by superimposing the calculated displacements due to the TBM conical shape (contraction) and the ones due to the applied face pressure. For the purpose of this comparison we ignored the settlements due to grout pressure (as they were found to be very small due to the high applied grout pressures). Overall, there is good agreement between the predictions and the observed settlements. The current predictions due to the TBM1 passage, agree with the monitored settlements for segments where the EPB is fully embedded within the stiff old alluvium formation (0 to 700 m), corresponding to homogeneous stiff clay conditions. However, as we encounter the sand layers and transition to the soft Kallang formation, we observe that we have excellent agreement for some locations (at 800m and 900m), but underestimate the settlements in other areas (700 to 900m). The discrepancy is mainly due to the presence of sand at those locations which induce settlements higher than those predicted, for the mixed clay face conditions. The comparison between the monitored data and the proposed method improves significantly when we compare deformations caused by TBM2, as TBM2 encounters only a small sand pocket in the location 700m, resulting in only a small discrepancy in this area.

5.4 Blue line, Bangkok

The performance of EPB tunneling for the Northern section of the MRTA Blue Line (Chaloem Rachamongkhon Line) was documented in a PhD thesis by Suwansawat, (2002). Data for the project were used by Suwansawat and Einstein (2006) to evaluate an ANN method for

predicting ground settlements (section 2.3.1). Figure 5.19, shows the overall project layout. The current research uses data from two sections: A) between Thiam Ruam Mit and Pracharat Bamphen stations; and B) between Ratchada and Lat Phrao Stations. Surface settlements along these sections were monitored at 50m intervals along the alignment. Figure 5.20 shows the stratigraphy along the Northern section (North of Rama IX station). The project involves parallel 6.43m diameter tunnel bores spaced at 15-20m apart, excavated primarily within a layer of stiff Bangkok clay with inverts 15-25m below the ground surface and most of the overlying soil comprising of softer marine silty clay. The current analyses consider only the effects of the first tunnel drive, southbound (SB) to avoid any interaction between the two bores during the second tunnel drive.

Figure 5.21 shows typical profiles of undrained shear strength for the two clay units as reported by Suwansawat, (2002) based on project design criteria and more recent investigations using field (vane shear tests) and lab tests (unconsolidated-undrained (UU) triaxial tests and consolidated undrained (CU) triaxial tests) in the vicinity of the MRTA project [19](see Figure 5.19) for Contract 2 of the Blue line extension project (AECOM, 2011). The soil properties reported by AECOM, (2011) are in close agreement with results from undrained triaxial tests by Seah and Lai, (2003) in the soft Bangkok clay layer. The results in Figure 5.21 show that the soft clay has a shear strength ranging from 20-25 kPa up to 40-45 kPa at 15m. The stiff clay typically has strength increasing from 60-80 kPa up to 125 kPa.

---

[19] Prior measurements show that Bangkok clay (Ladd et al., 1971, Seah and Lai, 2003) was approximately isotropic undrained shear strength and hence the values in Figure 5.21can be considered as average properties for modeling prurposes.

5.4.1 Comparison with Data along Section A and Section B

The proposed method of displacements is used to study the effect of mechanized tunneling using EPB shields in sections A and B. Section A started from a launch shaft inside the Thiam Ruam Mit station and progressed towards the Pracharat Bamphen station (Figure 5.22). A low face pressure (about 30 kPa→ $\sigma_f/\gamma H$=0.35) was applied during the initial drive comprising the first 60 rings (≈70m Figure 5.23b), as the backup equipment was not in place inside the tunnel and the temporary lining support system was not able to support high thrust forces. During the initial drive, shield operators experimented with various face pressures and penetration rate to determine which combination could minimize ground settlements. Suwansawat, (2002) reports that the grout pressure for the MRTA project were automatically controlled in the range, σ_G= 200 to 250 kPa (i.e. $\frac{\sigma_G}{\gamma \mathrm{H}}$= 0.5 to 0.9) for Section A (and B respectively).

In section A, we encounter mixed face conditions that affect face stability (Figure 5.23b). The transition from being partially embedded in the soft layer (D_T/D=0.35) to being fully embedded in the stiff layer (D_T/D=-0.35), results in a significant decrease of the critical face stability strength ratio for unsupported face ($\sigma_f/\gamma H$=0) $\tilde{s}_{uT}/\gamma H$=0.073 (estimated from Figure 3.21 for D_T/D=0.35, and s_{uB}/s_{uT}=2.7) to 0.043(for D_T/D=-0.35, and s_{uB}/s_{uT}=2.8). The corresponding critical strength ratio, $s_{uT}/\gamma H$ can then be estimated from Eq. (3.7): $s_{uT} = \tilde{s}_{uT}\left(1 - \frac{\sigma_f}{\gamma \mathrm{H}}\right)$. For D_T/D=0.35, $s_{uT}/\gamma H$= 0.065 (as $\tilde{s}_{uT}/\gamma H$= 0.073, and the applied face pressure 30 kPa, $\sigma_f/\gamma H$=0.34), while for D_T/D=-0.35, $s_{uT}/\gamma H$= 0.031 (as $\tilde{s}_{uT}/\gamma H$= 0.047, and face pressure 130 kPa, $\sigma_f/\gamma H$=0.34). Hence, the corresponding safety factor for face stability increases from FS=1.6 (for in situ strength ratio $s^*_{uT}/\gamma H$=0.106) at the launch site to FS=2.9 (for in situ strength ratio

$s_{uT}^{*}/\gamma H$=0.09) after 175m (75 rings). The observed increase in the safety factor (1.6 to 2.6) is reflected in the deformations that decrease to almost a half when the tunnel becomes fully embedded in the stiff layer.

The deformations at each location were predicted using the proposed method of displacements, as described in chapter 4 and illustrated in sections 5.2 and 5.3. The main factors controlling deformations were the applied face pressure and the conical shape of the shield (contraction), while the contribution of the grouting of the tail void to the total displacements was found to be minimal (i.e., less than 1mm). For the purpose of this comparison, we decided to ignore the effect of the TBM weight as it is also quite small when compared to the other sources of deformation.

Figure 5.23a, compares the predicted settlements using the proposed method of displacements to monitored deformations along the tunnel axis during the first drive for the SB tunnel (black points). The predictions use the design undrained shear strength and elastic shear modulus profiles reported by Suwansawat, 2002 (black dotted line) and soil properties based on soil investigations by AECOM, 2011 (blue line, Figure 5.21).

Our method under predicts deformations close to the launching site (i.e. 20-30mm compared to 30-60mm), as conditions present during the initial drive (excavating from a launch shaft, partial equipment use, learning curve of machine use) differ from the steady state conditions of a continued uninterrupted excavation considered in our proposed design method.

Further from the launch shaft we observe that the deformations decrease significantly and stabilize at around u_z =20mm (for a distance greater than 100 m from the shaft). The predictions using the proposed method of displacements converge to these measured values. Similar observations were made by Suwansawat, (2002) who studied the effects of the launching station on the magnitude of surface settlements. Figure 5.24 shows that larger oscillating settlements are generally measured for the first 500 m from the launching site for different sections of the MTRA project.

Figure 5.26 presents the first SB drive for section B, starting from a temporary launch shaft within the Ratchada station and directed towards the Lat Phrao station (Figure 5.25). During the initial drive (first 98 rings) the backup equipment was located at the surface and connected with cords and hoses to the EPB. The equipment was moved within the tunnel during a temporary inspection stop right after the EPB cut through the Khlong Naem Kaew bridge piles. In agreement with observations for section A, there is an underestimation of the measured settlements during the initial drive (Figure 5.26a). The proximity to the launch shaft, the temporary cessation of excavation and the differences in the excavation process are introducing additional factors that influence the surface settlements and are not taken into account in the proposed methodology. As the tunnel advances more than 100 m from the initial section, the monitored settlement stabilizes at around 12 mm which is reasonably predicted by the proposed methodology.

5.4.2 Comparison with ANN Model

Suwansawat, (2002) trained an ANN model using multiple variables such as the tunnel depth, distance from launching station, geology at tunnel crown and invert, water level from tunnel invert, face pressure, penetration rate and grouting pressure. Figure 5.27 compares his results for the case of an ANN trained with monitored data from section A, to predict settlements in sections A and B, to predictions using the proposed method of displacements. The ANN predicts very well settlements in section A, with a Root-Mean-Squared-Error, RMSE=7.3, but decreases in accuracy when applied to a different section, RMSE=16.2 for section B. Our predictions using the method of displacements have RMSE=15.2 and 10.9 for Section A and B respectively, which are comparable to the ANN method. Although, ANN predicts exceedingly well deformations within the same tunnel section the model was trained for (Suwansawat and Einstein, 2006) the current method matches or outperforms ANN's predictions when applied to different sections of the same project.

5.5 Conclusions

In the prior sections we presented examples of applying the proposed methodology for three cases studies involving homogeneous and mixed face conditions in clay: 1) Contract C300 (Ieronymaki et al., 2016), 2) contract C933 for Downtown line in Kallang at Bendemeer, Singapore (Su, 2015), 3) northern section of the MRTA Blue Line in Bangkok, Thailand (Suwansawat, 2002, Suwansawat and Einstein, 2006). Our method generally provides a good estimation of the monitored data, matching the performance of 3D FE simulations (Founta and

Whittle, 2016 and Su, 2015) and the ANN method (Suwansawat and Einstein, 2006). The main discrepancies related to the presence of sand layers in the stratigraphy (DTL project) and close proximity to the launching site. The proposed method is very simple to use as it does not require the calibration and running of sophisticated 3D models or access to the required database to calibrate ANN. As a result it can be a useful tool to engineers in practice as it offers direct immediate prediction requiring only basic information on soil properties, stratigraphy and tunnel control parameters.

Table 5.1 Components of surface settlements due to mechanized tunneling

Total deformation $u_z = \sum_{i=1}^{4} u_{zi}$		
i=1: Face Pressure		
$\frac{u_z G}{\gamma D^2} = 0.012\left[\frac{\gamma H}{\Delta s_u}\right]\left[1 - \frac{\sigma_f}{\gamma H}\right]$		$\Delta s_u = s_{uH}^* - s_{uH}$
i=2: Grout Pressure		
$\frac{u_z G}{\gamma D^2} = 0.004\left[\frac{\gamma H}{\Delta s_u}\right]\left[1 - \frac{\sigma_G}{\gamma H}\right]$		$s_{uH} = \tilde{s}_{uH}\left(1 - \frac{\sigma_G}{\gamma H}\right)$
i=3: Shield Weight		
$\frac{u_z G}{\gamma D^2} = (1 - \frac{W_{TBM}}{W_{soil}})\left[3\log\left(\frac{MD}{H}\right) - 0.02\right] x10^{-3}$		
i=4: Shield Geometry		
$\frac{u_z}{\Delta D} = 0.45\frac{D}{H}$	$for \frac{C}{D} > 3$ $or\ \varepsilon < 0.01$	$\varepsilon = [\Delta D/D]$ $\Delta D = \lvert D_{tail} - D \rvert$

- u_z [m] the maximum settlement at the surface occuring above the tunnel centerline
- σ_f [kPa] applied face pressure at the springline level
- σ_G [kPa] applied grout pressure at the springline level
- s_{uH} [kPa] critical undrained strength value at the springline (FS=1) calculated from the face or grout stability analyses
- $\tilde{s}_{uH}$ [kPa] critical undrained strength value for unsupported (i.e. σ_f *or* $\sigma_G = 0$) calculated from stability analyses
- s_{uH}^* [kPa] in-situ undrained strength of the clay at the springline
- G [kPa] in-situ shear modulus of the clay at the springline
- γ $[kN/m^3]$ average unit weight of the clay above the springline
- D [m] the shield diameter at the front section
- D_{tail} [m] the shield diameter at the tail section
- H [m] the depth to the tunnel springline
- C [m] cover depth of the tunnel
- γH [kPa] vertical geostatic stresses at the springline
- W_{TBM} [tone] the TBM weight
- W_{soil} [tone] the weight of the removed soil
- l_{TBM} [m] the TBM shield length

Table 5.2 Soil Properties for Crossrail C300, Hyde Park area used in 3D FE analyses (Founta and Whittle, 2016)

Formation	γ $[kN/m^3]$	E_u $[kPa]$	ν	φ [°]	s_u $[kPa]$
Made Ground/ Langley Silt	19.6	5	0.2	25	-
River Terrace	19.6	35	0.25	38	-
London Clay	19.6	15+1.1z	0.244	-	75+5.5z

Table 5.3 Example calculations with the method of displacements (MoD) for the Crossrail Project in Hyde Park area, using design soil properties from site investigation (GSC, 2010) and monitoring face and grout pressure data for sections A-P

	Project Specifics									
Section	H [m]	Dtail [m]	D [m]	C/D	σf [kPa]	σG [kPa]	γ [kN/m3]	s_u^* [kPa]	E' [kPa]	G [kPa]
A	33.8	7.05	7.1	4.3	157	114	20	261	52125	20951
B	31.7	7.05	7.1	4.0	167	82	20	249	49815	20022
C	29.4	7.05	7.1	3.6	174	126	20	236	47285	19005
D	29.8	7.05	7.1	3.7	162	117	20	239	47725	19182
E	32.5	7.05	7.1	4.1	180	167	20	253	50695	20376
F	33.5	7.05	7.1	4.2	180	130	20	259	51850	20840
G	34.0	7.05	7.1	4.3	180	97	20	262	52345	21039
H	35.3	7.05	7.1	4.5	189	103	20	269	53775	21614
P	35.3	7.05	7.1	4.5	195	190	20	269	53775	21614

	Face Pressure					Grout					Contraction		Total
Section	$\widetilde{s_u}/\gamma H$	su/γH	Δsu/γH	1-σf/γH	uz [mm]	$\widetilde{s_u}/\gamma H$	su/γH	Δsu/γH	1-σG/γH	uz [mm]	ΔD [m]	uz [mm]	uz [mm]
A	0.080	0.061	0.32	0.77	1.4	0.034	0.028	0.36	0.83	0.4	0.05	4.7	6.5
B	0.080	0.059	0.33	0.74	1.3	0.034	0.030	0.36	0.87	0.5	0.05	5.0	6.9
C	0.080	0.056	0.35	0.70	1.3	0.034	0.027	0.38	0.79	0.4	0.05	5.4	7.2
D	0.080	0.058	0.34	0.73	1.3	0.034	0.027	0.37	0.80	0.5	0.05	5.4	7.2
E	0.080	0.058	0.33	0.72	1.3	0.034	0.025	0.36	0.74	0.4	0.05	4.9	6.6
F	0.080	0.059	0.33	0.73	1.3	0.034	0.027	0.36	0.81	0.4	0.05	4.8	6.5
G	0.080	0.059	0.33	0.74	1.3	0.034	0.029	0.36	0.86	0.5	0.05	4.7	6.5
H	0.080	0.059	0.32	0.73	1.3	0.034	0.029	0.35	0.85	0.5	0.05	4.5	6.2
P	0.080	0.058	0.32	0.72	1.3	0.034	0.025	0.36	0.73	0.4	0.05	4.5	6.2

Table 5.4 Soil Properties at the DTL C933 based on site investigation (Su, 2015, Sharma et al., 1999) used as input for the proposed methodology

Formation	γ $[kN/m^3]$	E_u $[kPa]$	φ [°]	s_u $[kPa]$
Fill	19	10000	30	-
Kallang	16	250 s_u	-	18+1z
Sand (F1)	20	12000	30	-
Old Alluvium	20	170s_u	-	250

Table 5.5 Soil Properties for DTL C933 used by Su, (2015) in the 3D FEA

Soil Type	γ_{bulk} [kN/m^3]	E_u [MPa]	E' [kPa]	Φ' [deg]	c_u [kPa]	c' [kPa]	k_s [m/s]	K_0 -
Fill	19	10,000	8,000	30	30	0	10^{-6}	0.5
Clay	16	$400c_u$	$350c_u$	22	15+1.5y (y=98m RL)	0	10^{-8}	1
F1	20	12,000	10,000	30	-	0	10^{-6}	0.7
OA	20	150,000*	125,000*	35	250	10	10^{-8}	0.7

Table 5.6 Example calculations with the proposed method of computing ground displacements for DTL C933, Arrays 1 and 2

		Project Specifics										Mixed face	
Array	TBM	H [m]	Dtail [m]	D [m]	C/D	σf [kPa]	σG [kPa]	γ [kN/m3]	s_{uT}^{*} [kPa]	Eu [kPa]	G [kPa]	s_{uB}^{*} [kPa]	Dt/D
1	1	35	6.6	6.6	4.8	220	380	18	250	42500	14167	_	_
1	2	22	6.6	6.6	2.8	295	360	17	28	7100	2367	250	0
2	1	34	6.6	6.6	4.7	480	500	16	47	11750	3917	_	_
2	2	22	6.6	6.6	2.8	305	390	17	35	8625	2875	_	_

		Face Pressure					Grout					Contraction		Total
Array	TBM	$\widetilde{s_u}/\gamma H$	su/γH	Δsu/γH	1-σf/γH	uz [mm]	$\widetilde{s_u}/\gamma H$	su/γH	Δsu/γH	1-σG/γH	uz [mm]	ΔD [m]	uz [mm]	uz [mm]
1	1	0.080	0.052	0.34	0.65	1.3	0.034	0.014	0.38	0.40	0.2	0.02	1.7	**3.2**
1	2	0.068	0.014	0.06	0.21	12.9	0.034	0.001	0.07	0.04	0.6	0.02	2.7	**16.2**
2	1	0.080	0.009	0.08	0.12	3.3	0.034	0.003	0.08	0.08	0.7	0.02	1.7	**5.7**
2	2	0.088	0.012	0.08	0.14	5.0	0.034	0.000	0.10	0.00	0.0	0.02	2.8	**7.7**

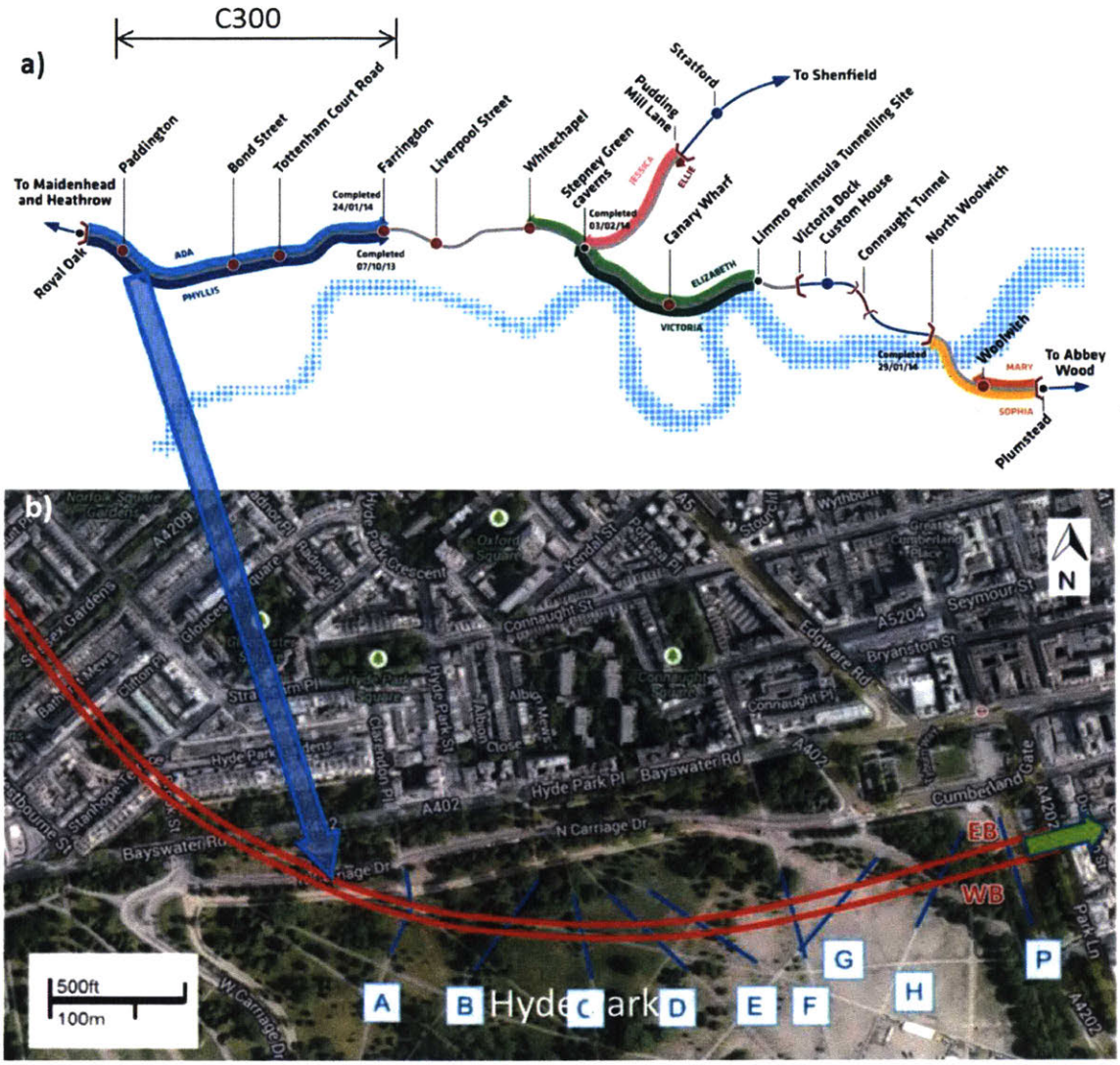

Figure 5.1 Regional map of Crossrail tunnels alignment a) Crossrail route map (Crossrail Project website:www.crossrail.co.uk) b) Location of the instrumented cross-sections A-P in Hyde Park area (Ieronymaki et al., 2016)

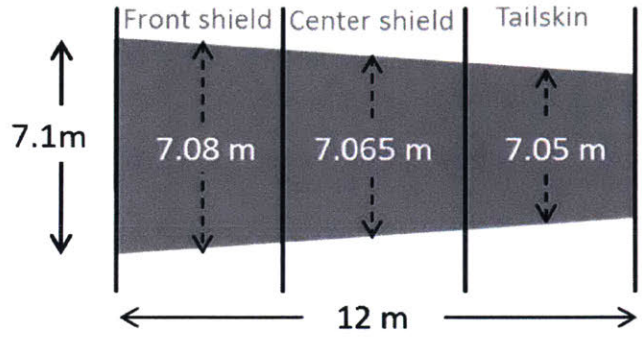

Figure 5.2 Herrenknecht EPB machine used for Crossrail (London)(source: Crossrail Report, 2012)

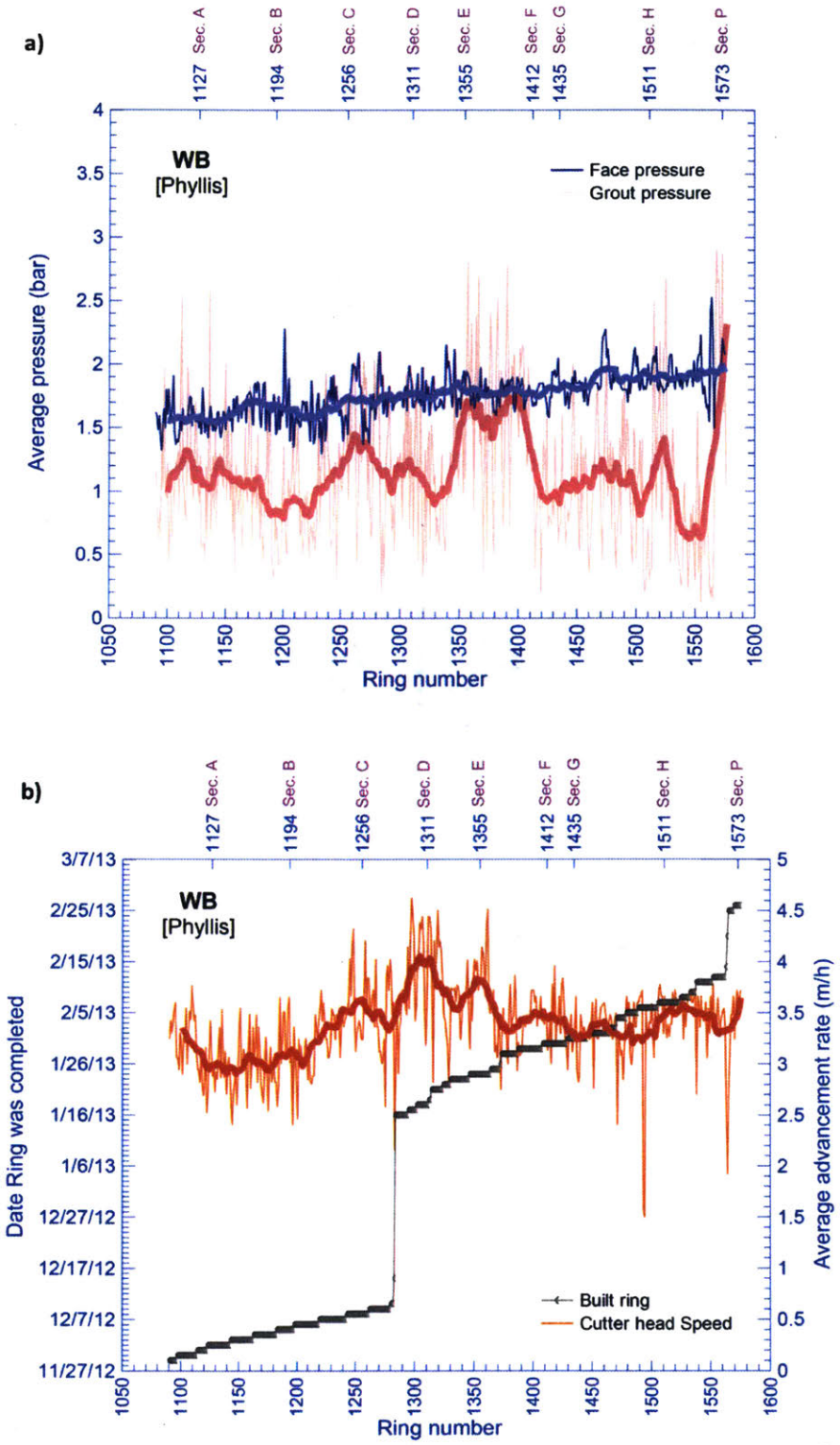

Figure 5.3 Crossrail tunnel Hyde Park are a) tunnel control parameters and b) tunnel construction data (Ieronymaki et al., 2016)

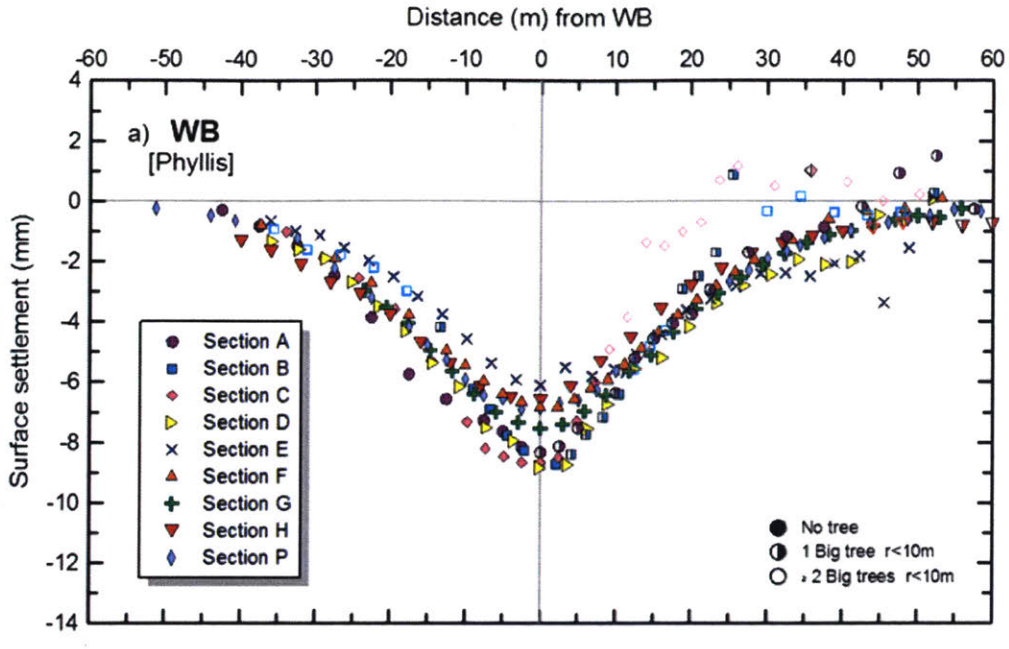

Figure 5.4 Monitored transverse surface settlement troughs for A-P section in Hyde Park area for the WB tunnel bore (Ieronymaki et al., 2016)

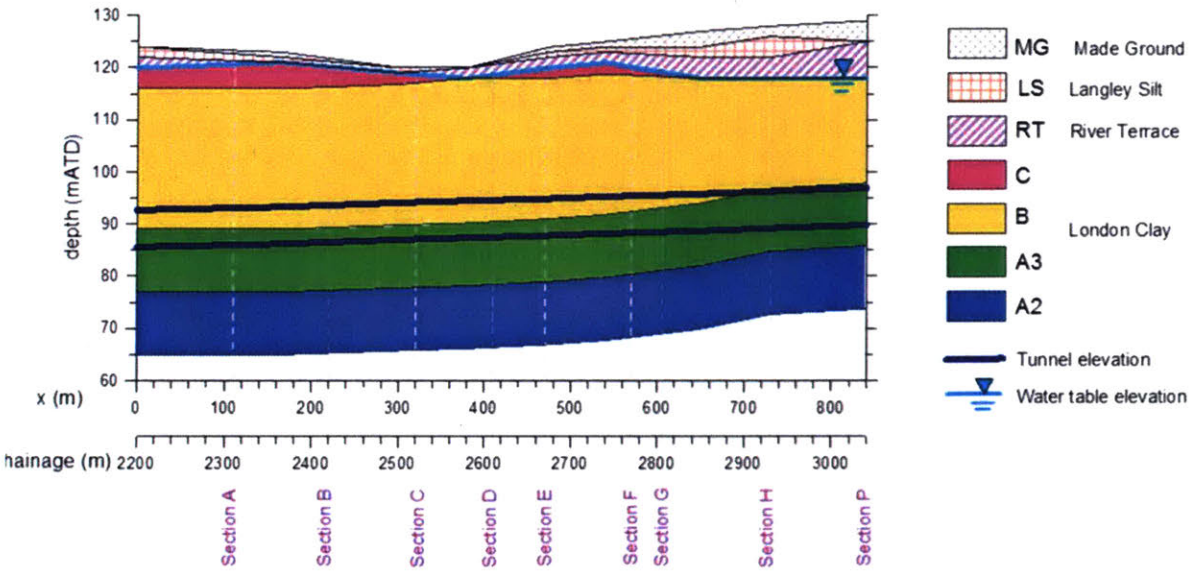

Figure 5.5 Soil stratigraphy for the Hyde Park area of the Crossrail Project (Ieronymaki et al., 2016)

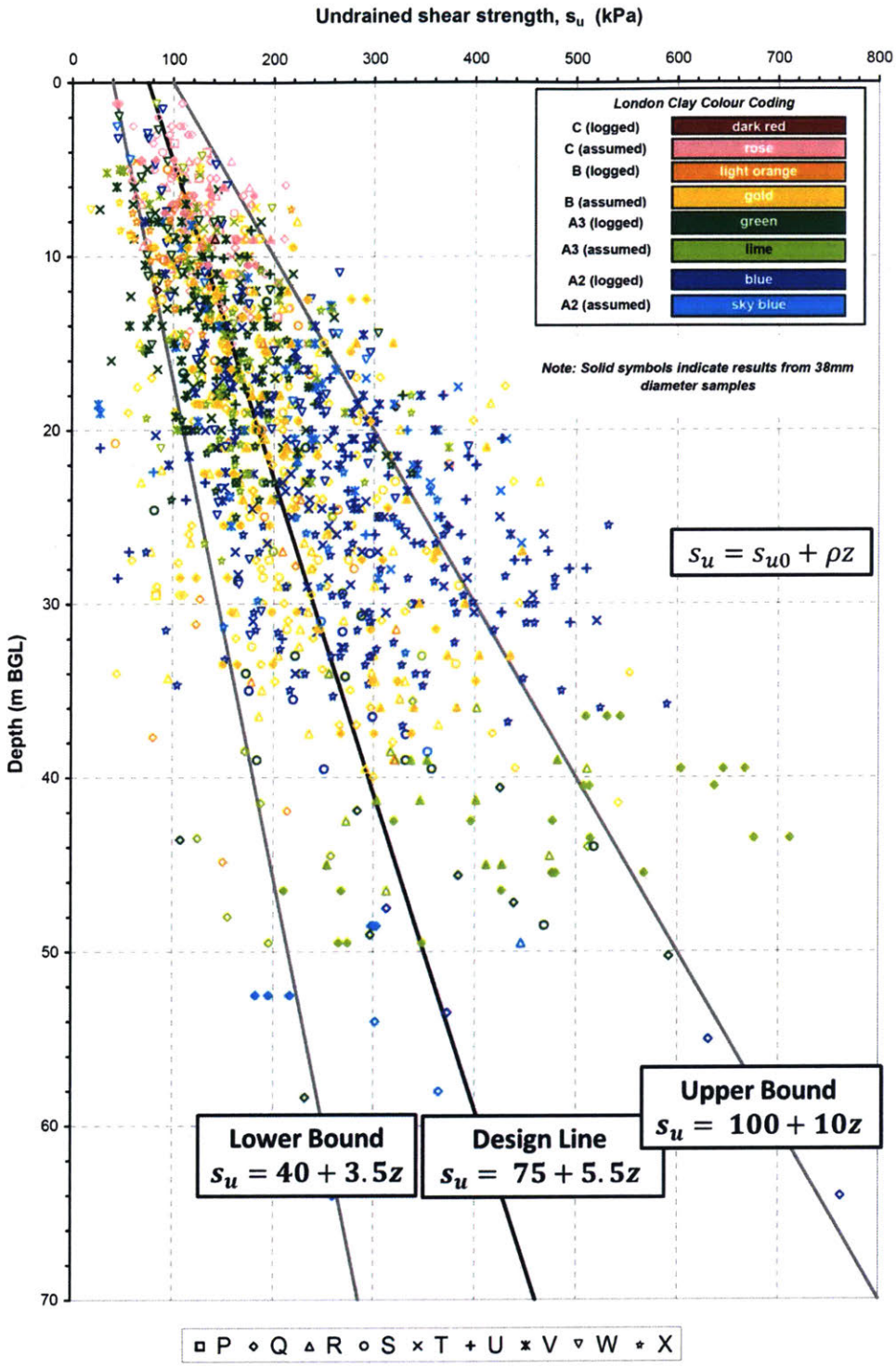

Figure 5.6 s_u vs depth from UU Triaxial tests (Section S includes Hyde Park) (GCG, 2010)

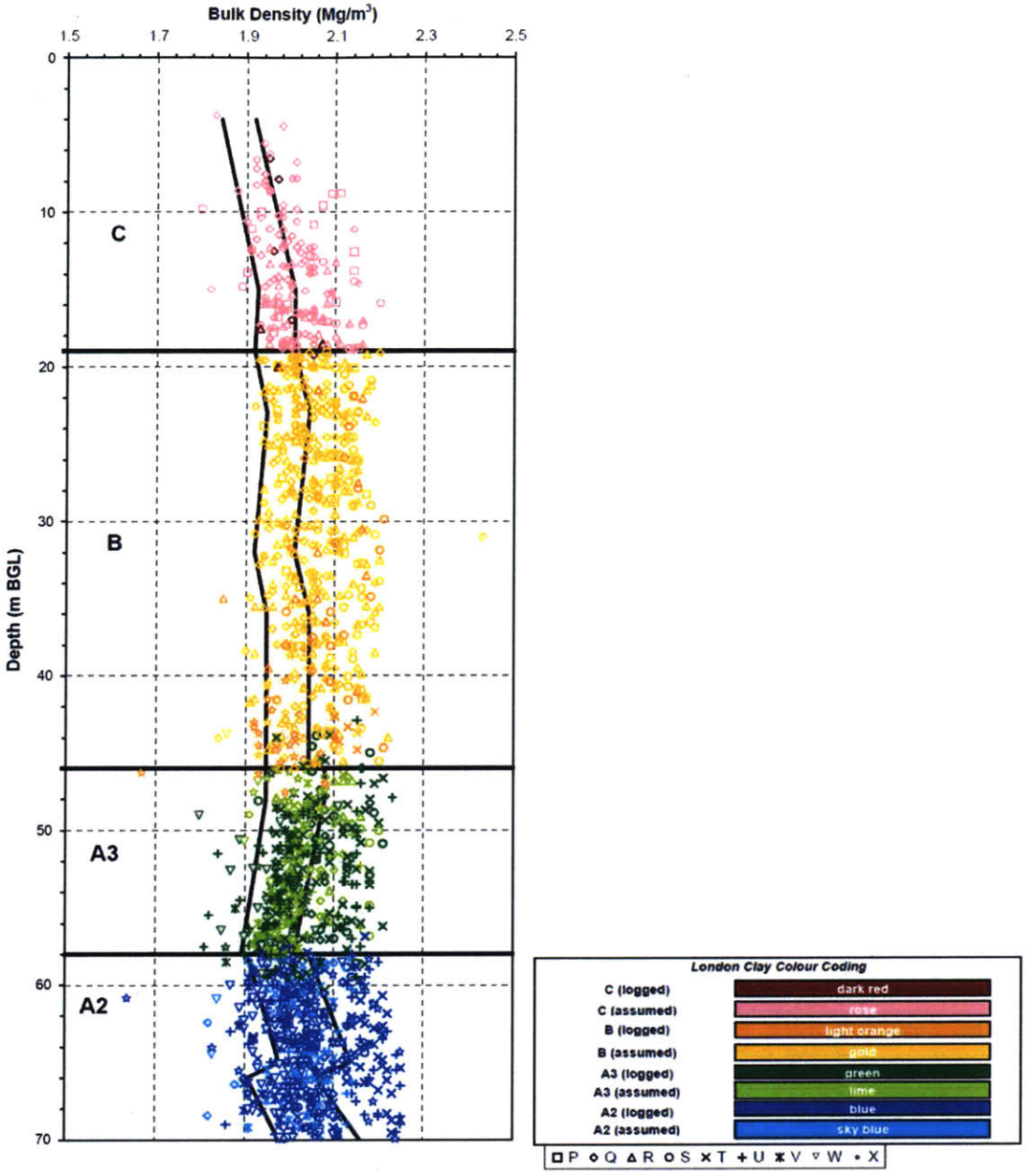

Figure 5.7 Bulk density (Section S includes Hyde Park) (GCG, 2010)

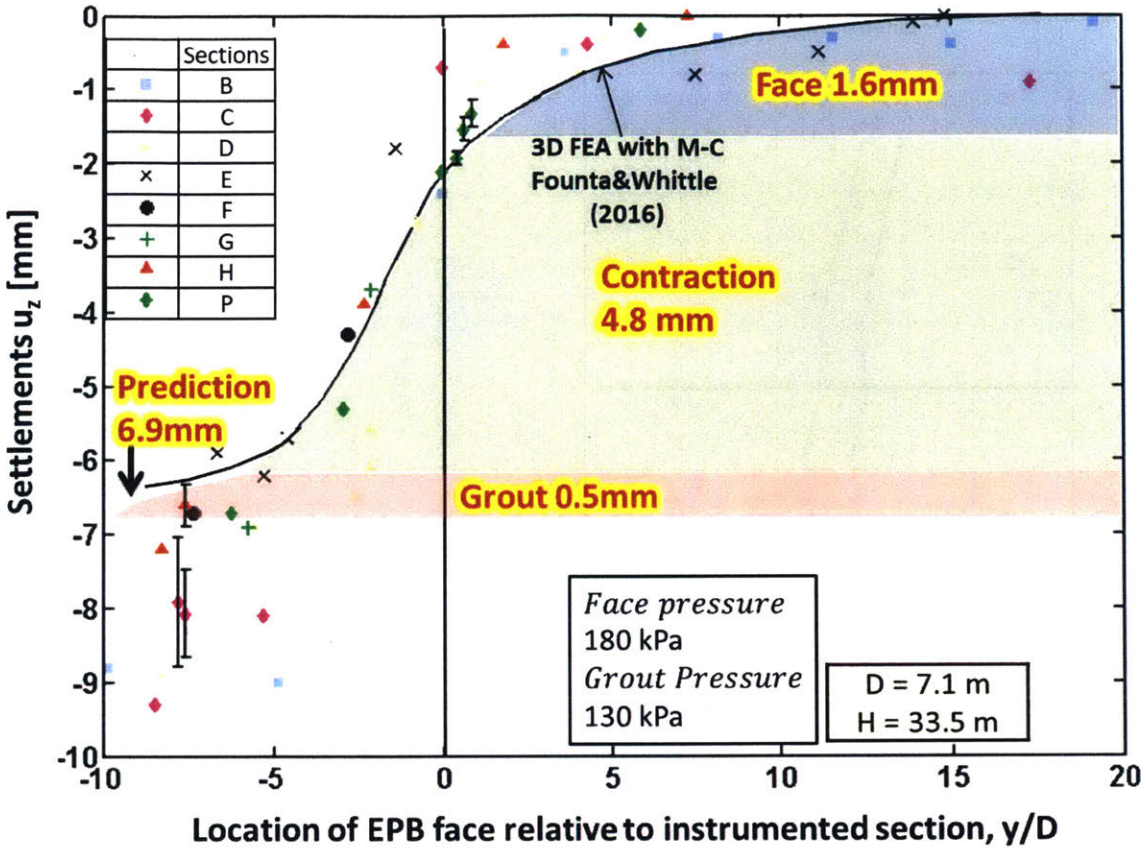

Figure 5.8 Application of method of displacements for section F in Hyde Park; comparison with 3D FEA by Founta and Whittle (2016) using the MC soil model, predictions from the proposed method and monitoring settlement data from the other instrumented cross-sections in the Hyde Park area.

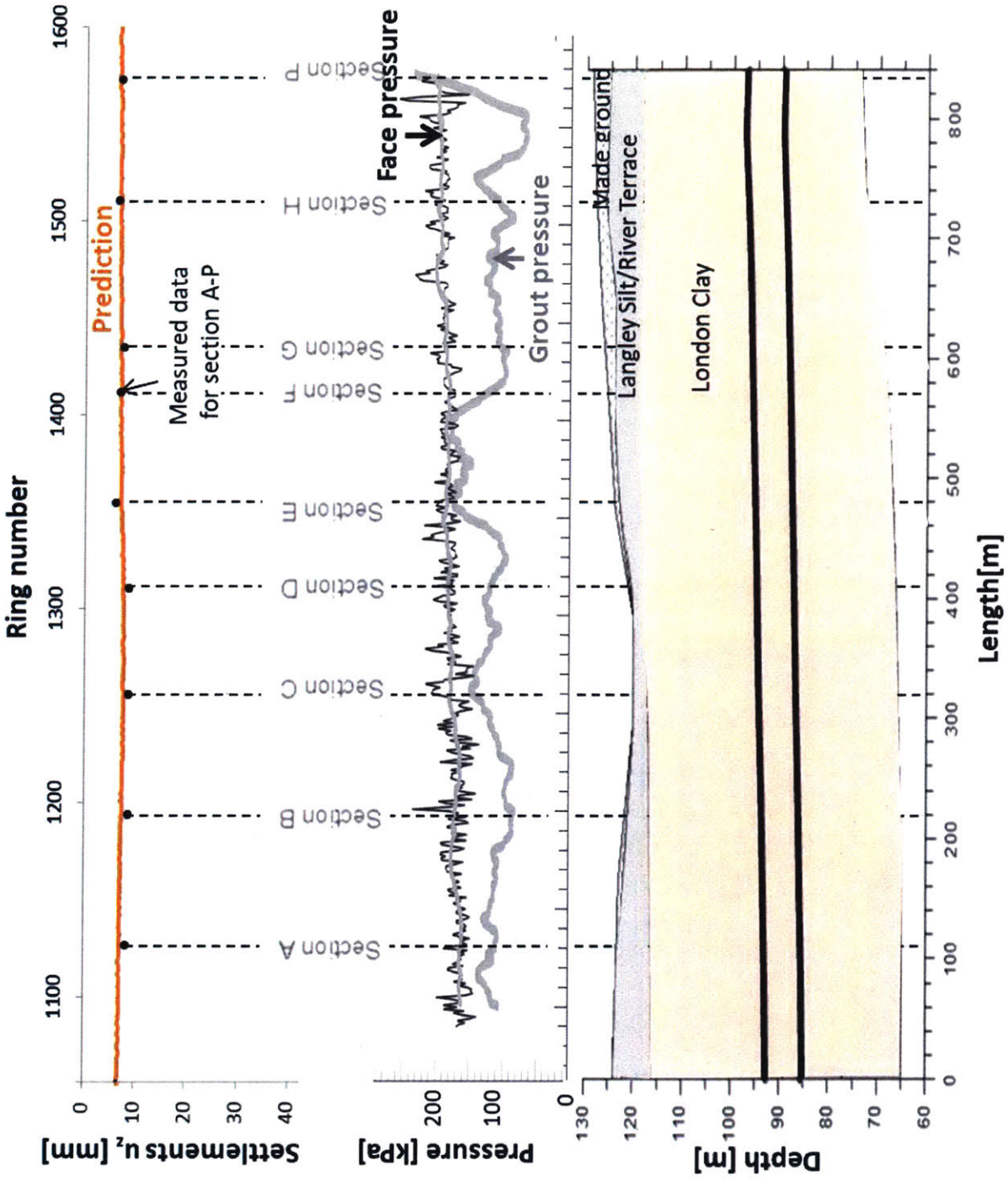

Figure 5.9 Application of method of displacements for the 9 section in Hyde Park Crossrail Project in London; effect of undrained strength profile

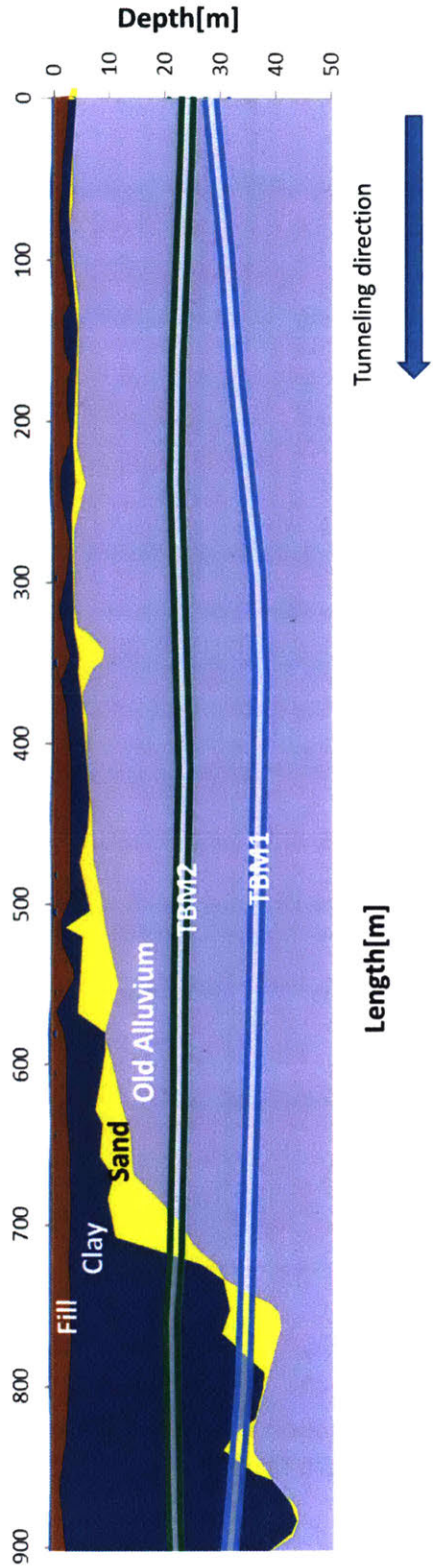

Figure 5.10 Soil stratigraphy of section of interest in the DTL project (Su, 2015)

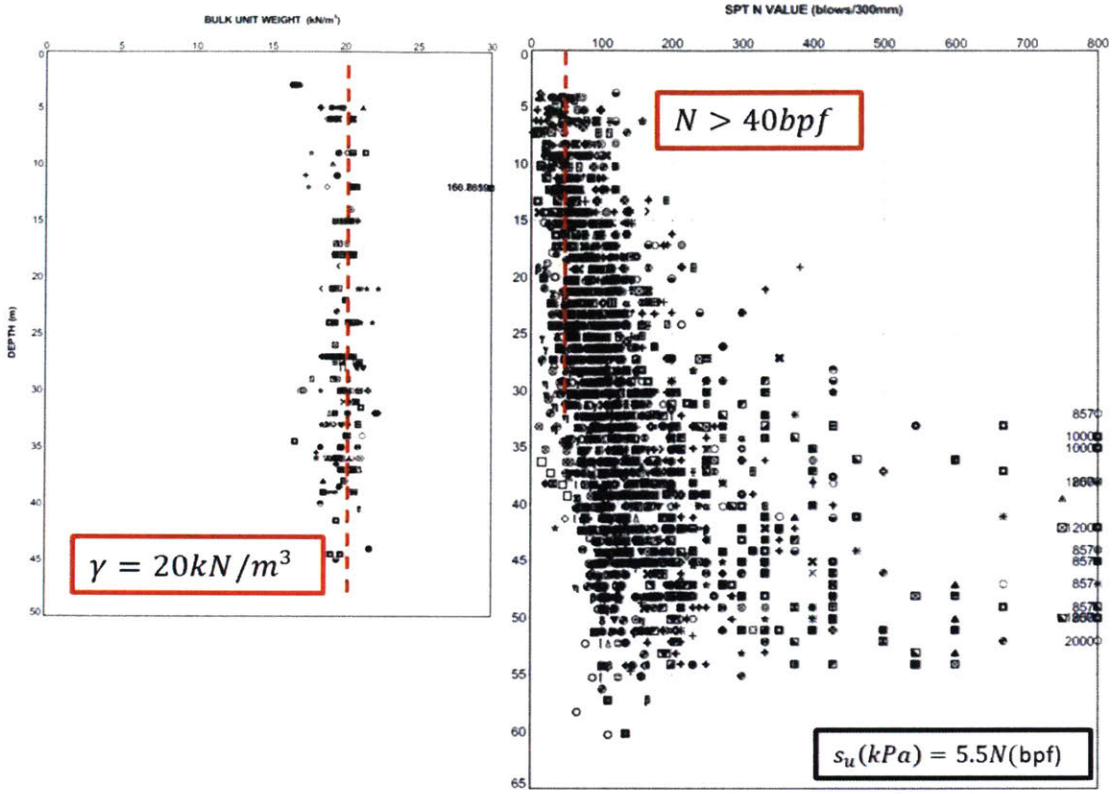

Figure 5.11 Bulk unit weight and SPT N value for old Alluvium unit (Su, 2015)

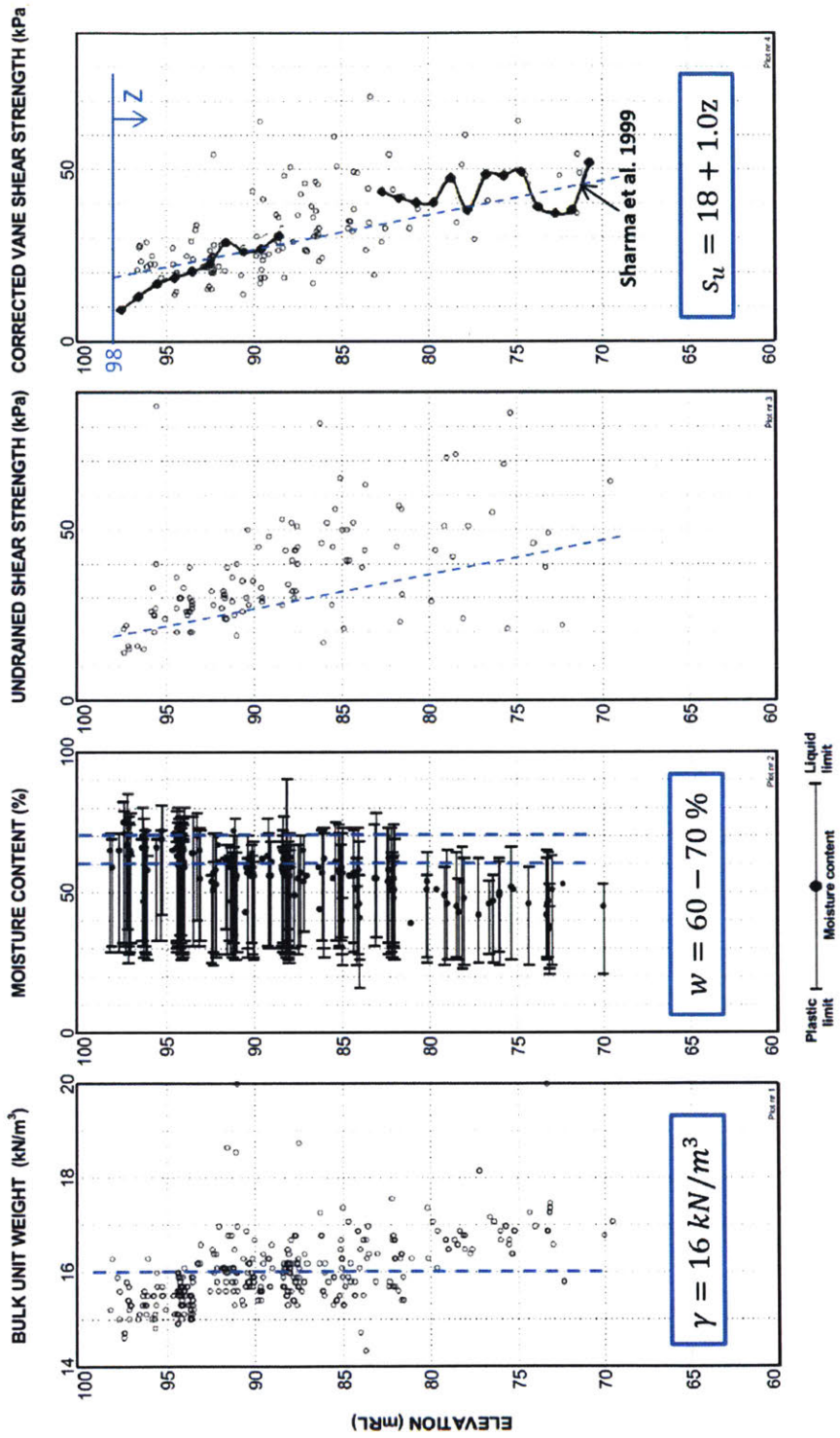

Figure 5.12 a)Bulk unit weight, b)moisture content and undrained strength from in-situ cone c)penetration and d)vane tests for Kallang clay (Su, 2015, Sharma et al., 1999)

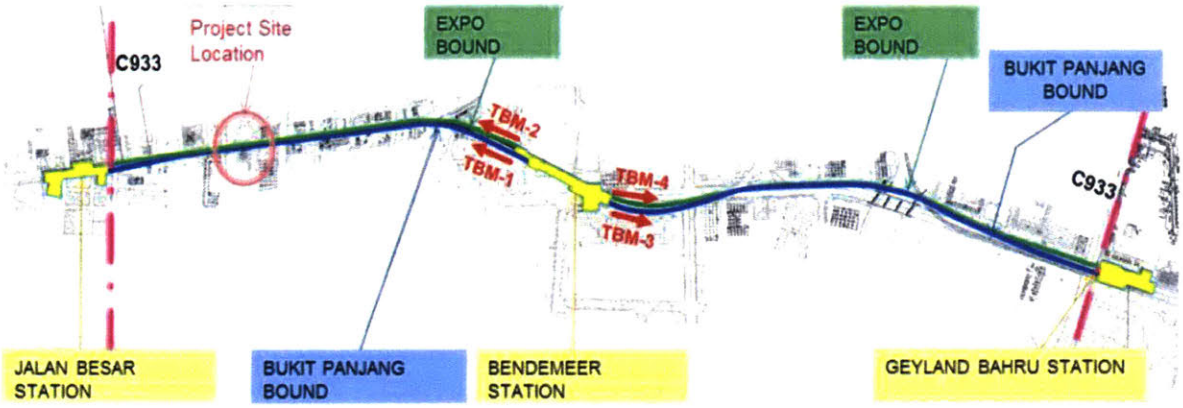

Figure 5.13 Site plan contract C933 DTL3 showing location of tunnel monitoring sections (Su, 2015)

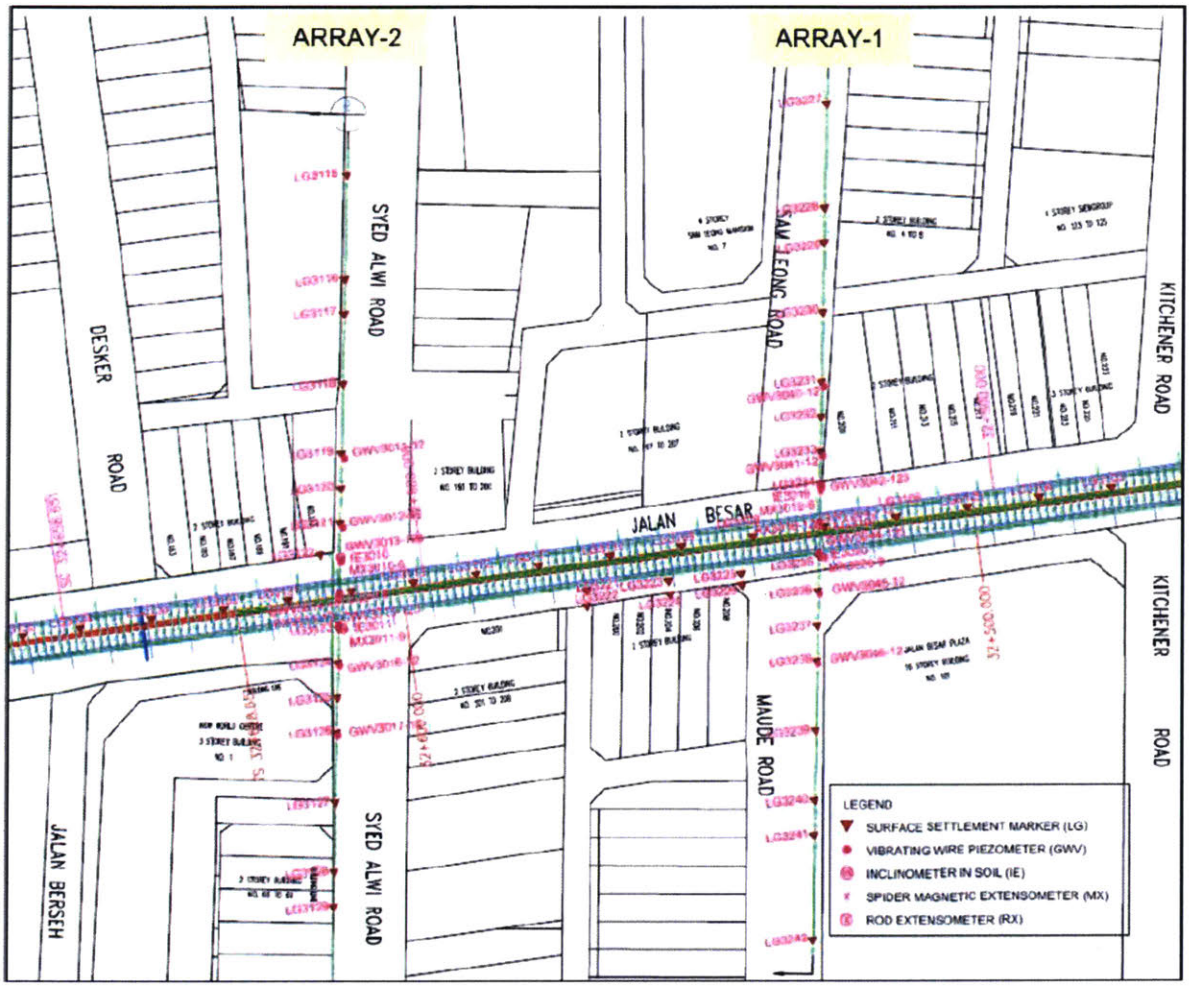

Figure 5.14 Detailed locations of instrumentation for arrays 1 & 2 (Su, 2015)

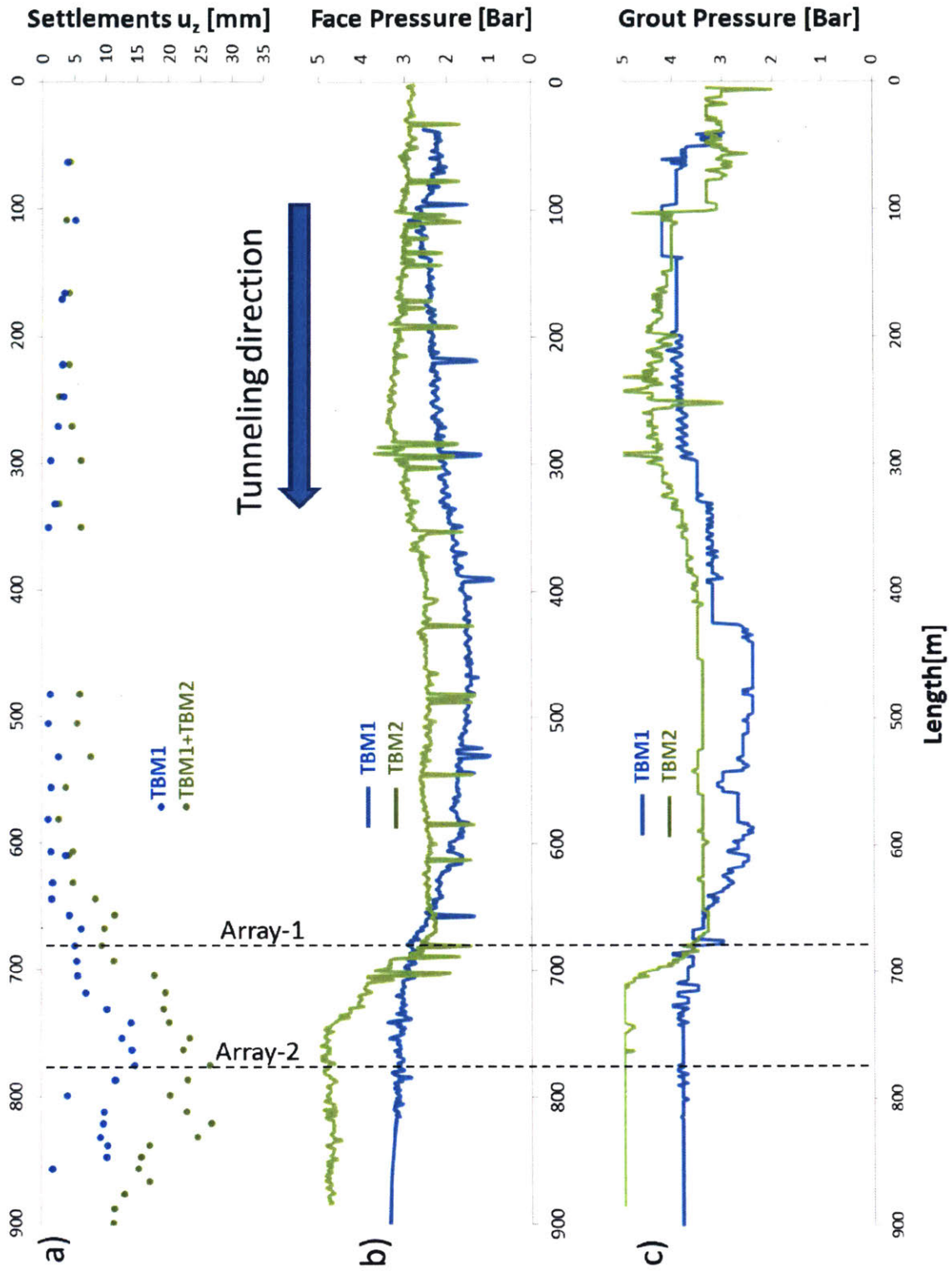

Figure 5.15 Monitored data for the DTL project in Singapore a) surface settlements in the Bendemeer station area b) face pressure and c) grout pressure (Su, 2015)

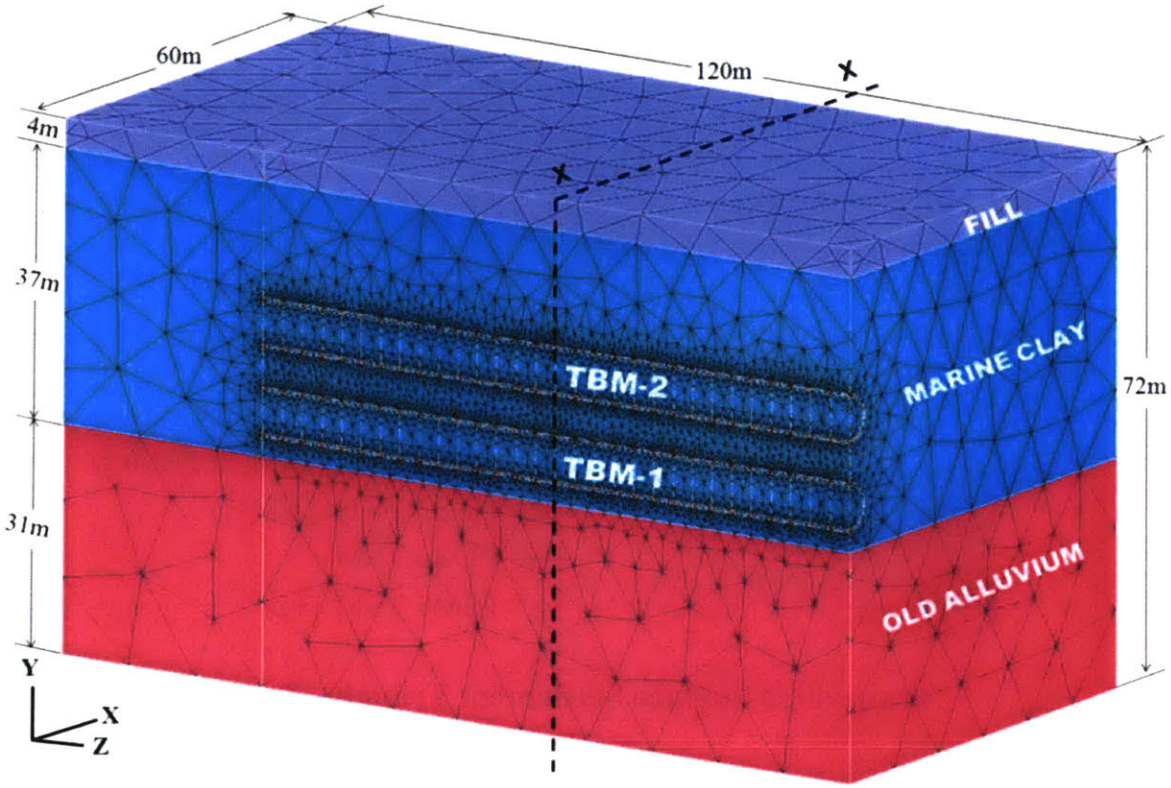

Figure 5.16 3D FE model developed with GeoFEA for Array-1 by Su, (2015)

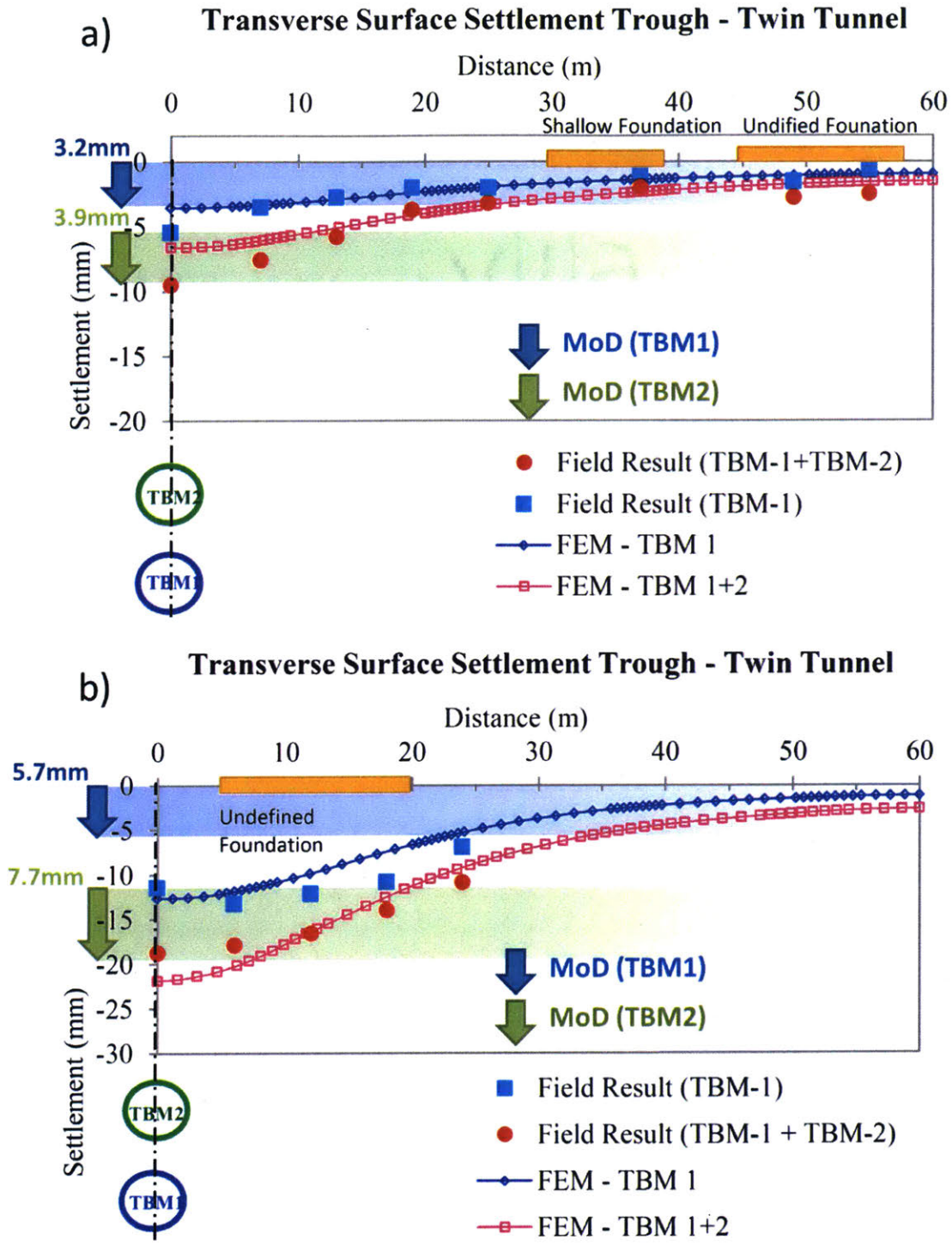

Figure 5.17 Monitored transverse surface settlements, 3D FE prediction with GeoFEA by Su, (2015) and predictions using the proposed method of displacements (MoD) for Arrays a) 1 and b) 2

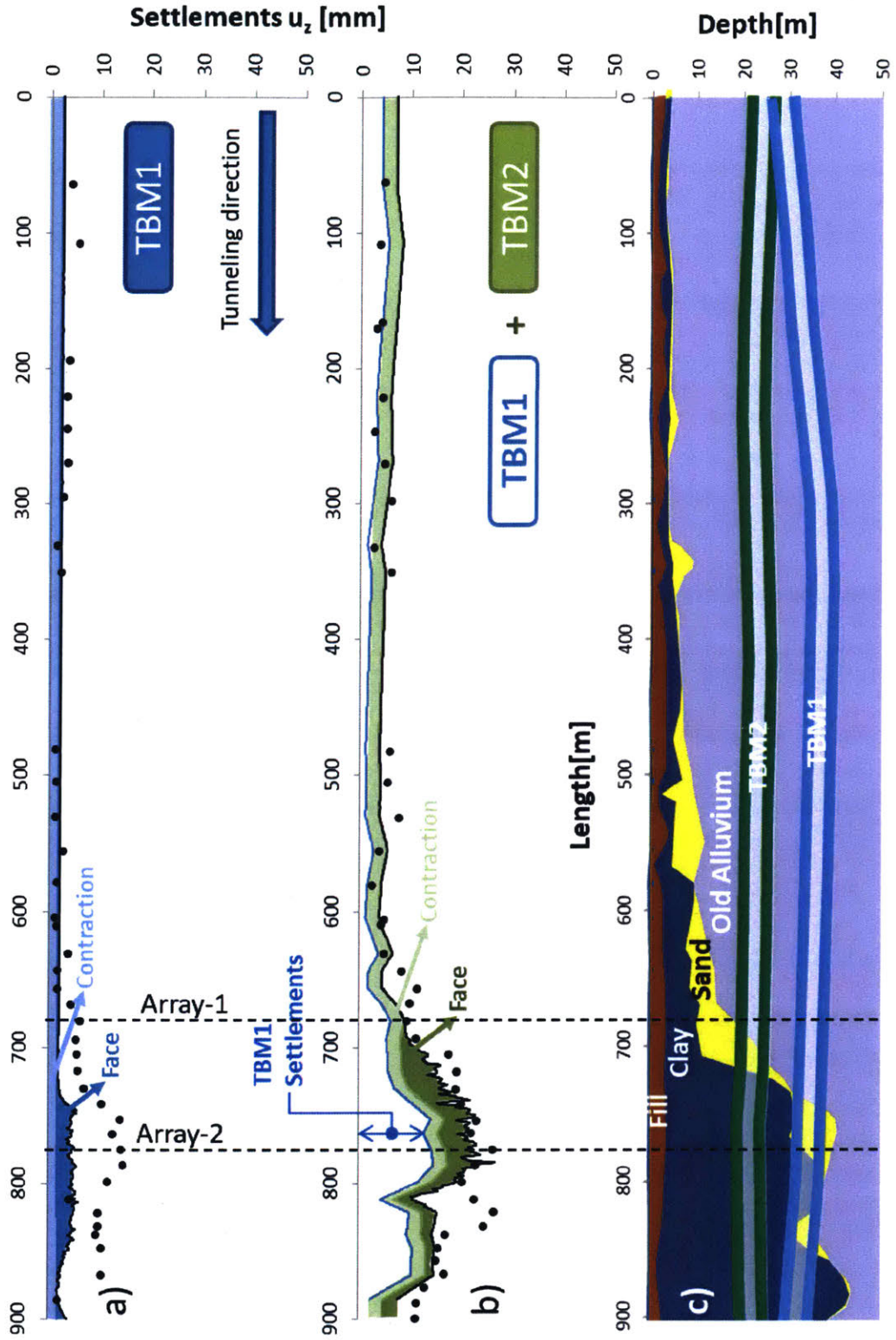

Figure 5.18 Application of method of displacements for the DTL Project a)TBM1 settlements b)TMB1 and TBM2 effect c) soil stratigraphy (Su, 2015)

Figure 5.19 MRTA project, location of north tunnel alignment (source: Suwansawat, 2002, AECOM, 2011 and Google maps, 2017)

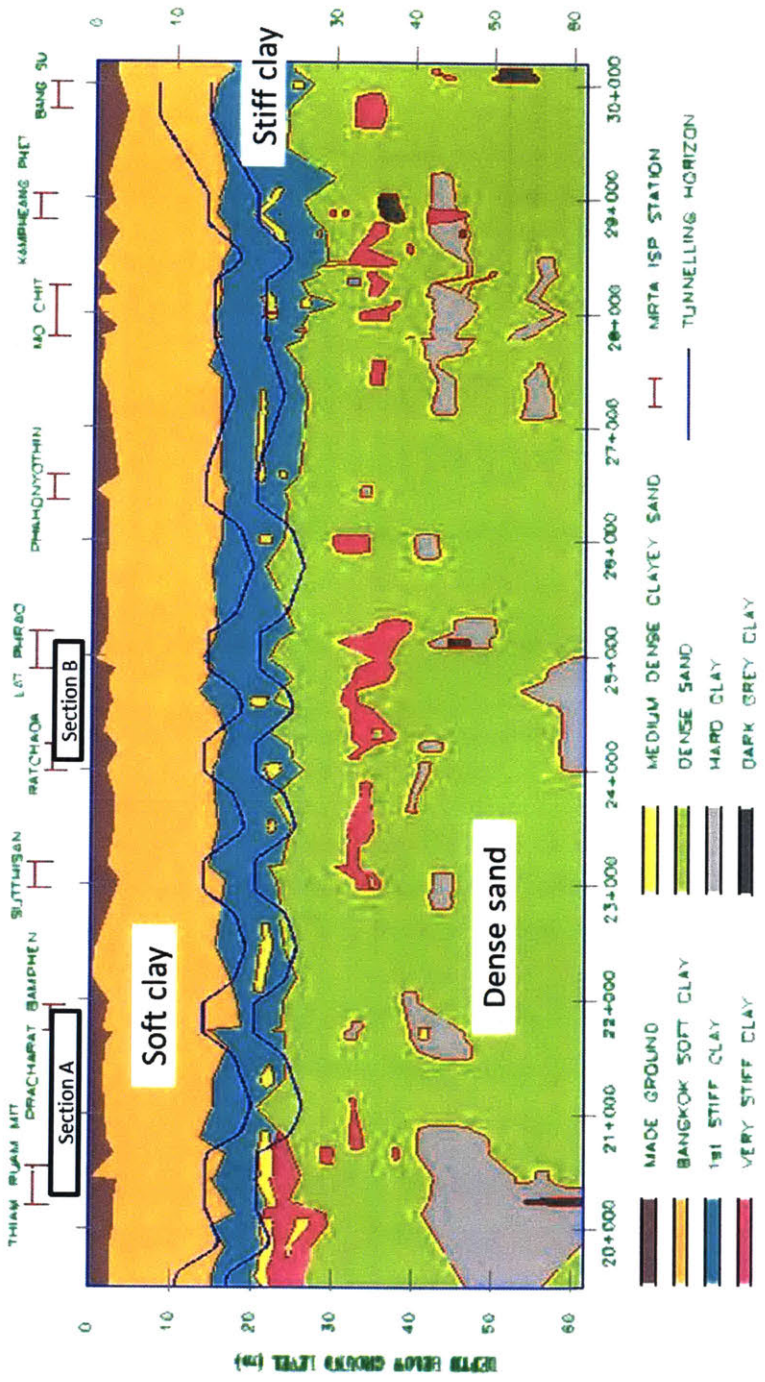

Figure 5.20 Northern tunnel alignment stratigraphy for MRTA project (source: Suwansawat and Einstein, 2006)

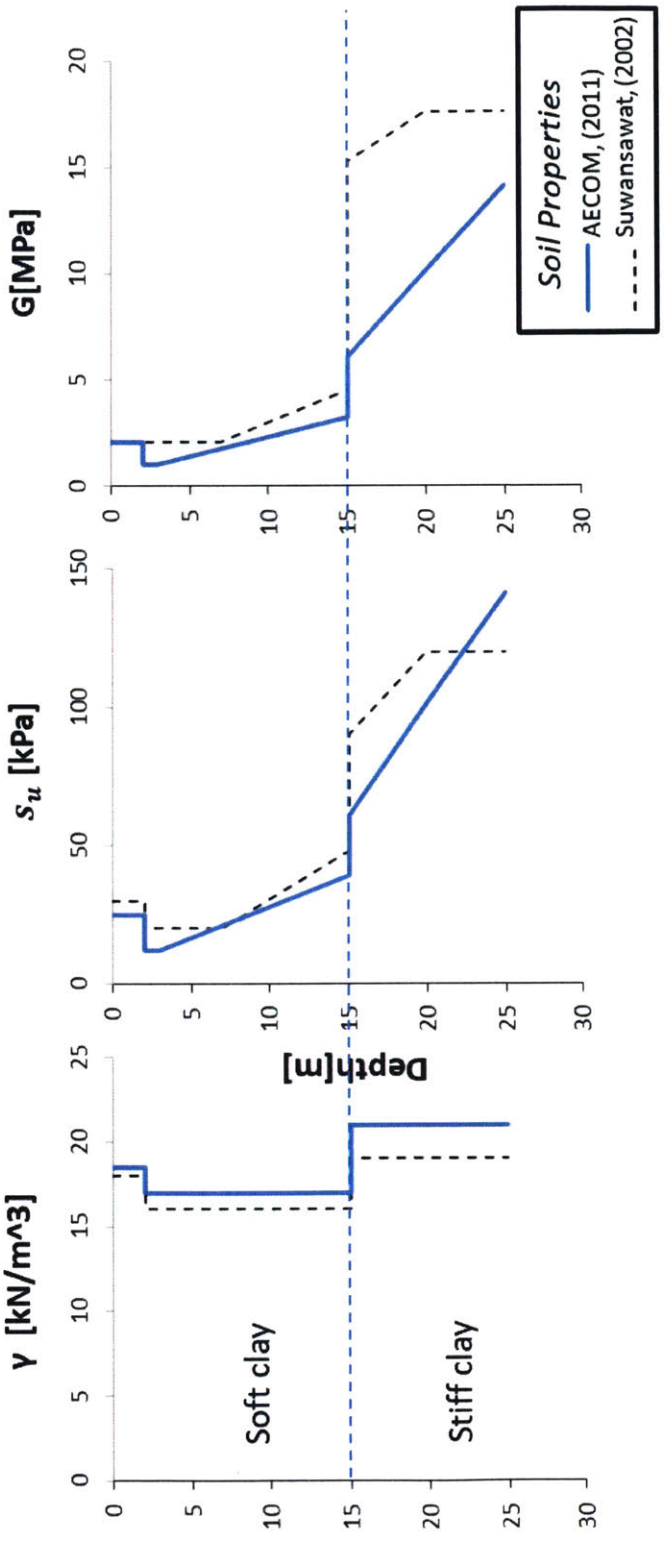

Figure 5.21 Soil Properties at the MRTA project area

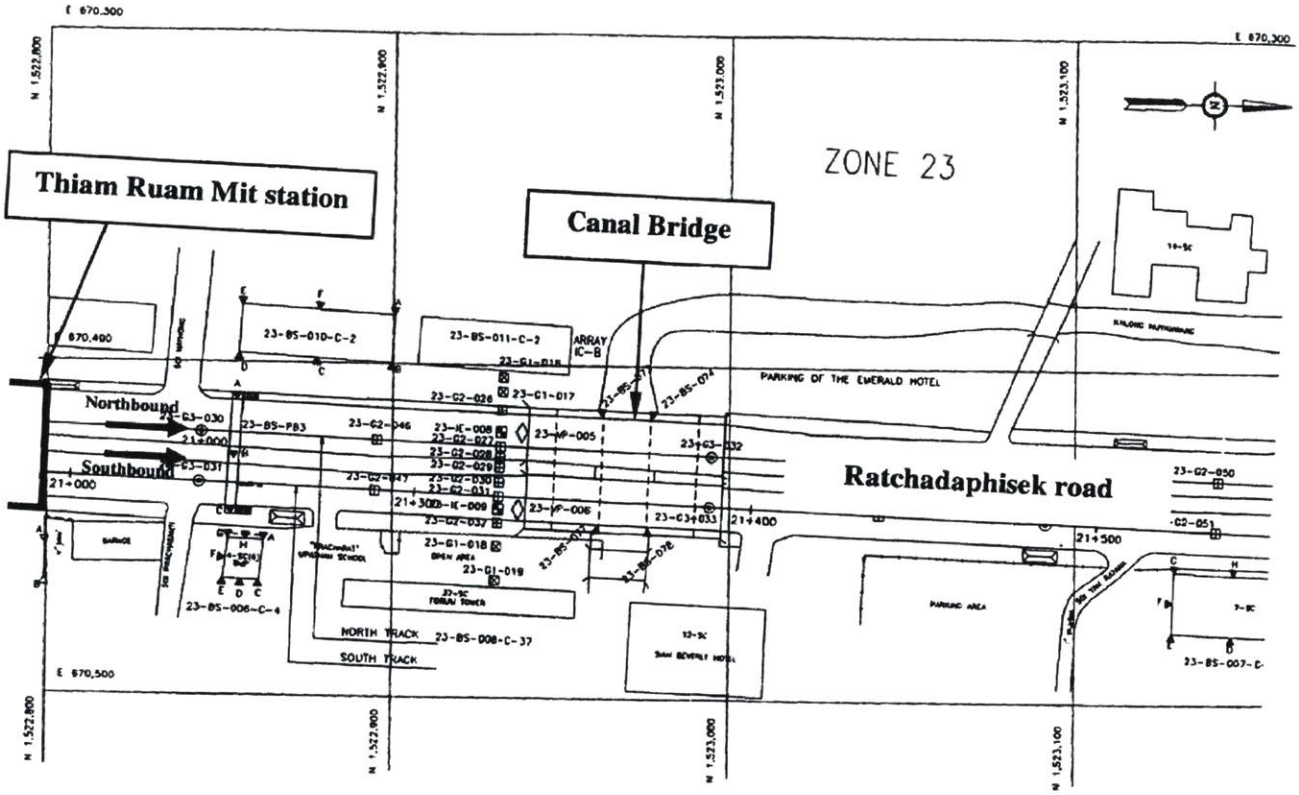

Figure 5.22 Map of initial drive of Section A starting from Thiam Ruam Mit Station (Suwansawat, 2002)

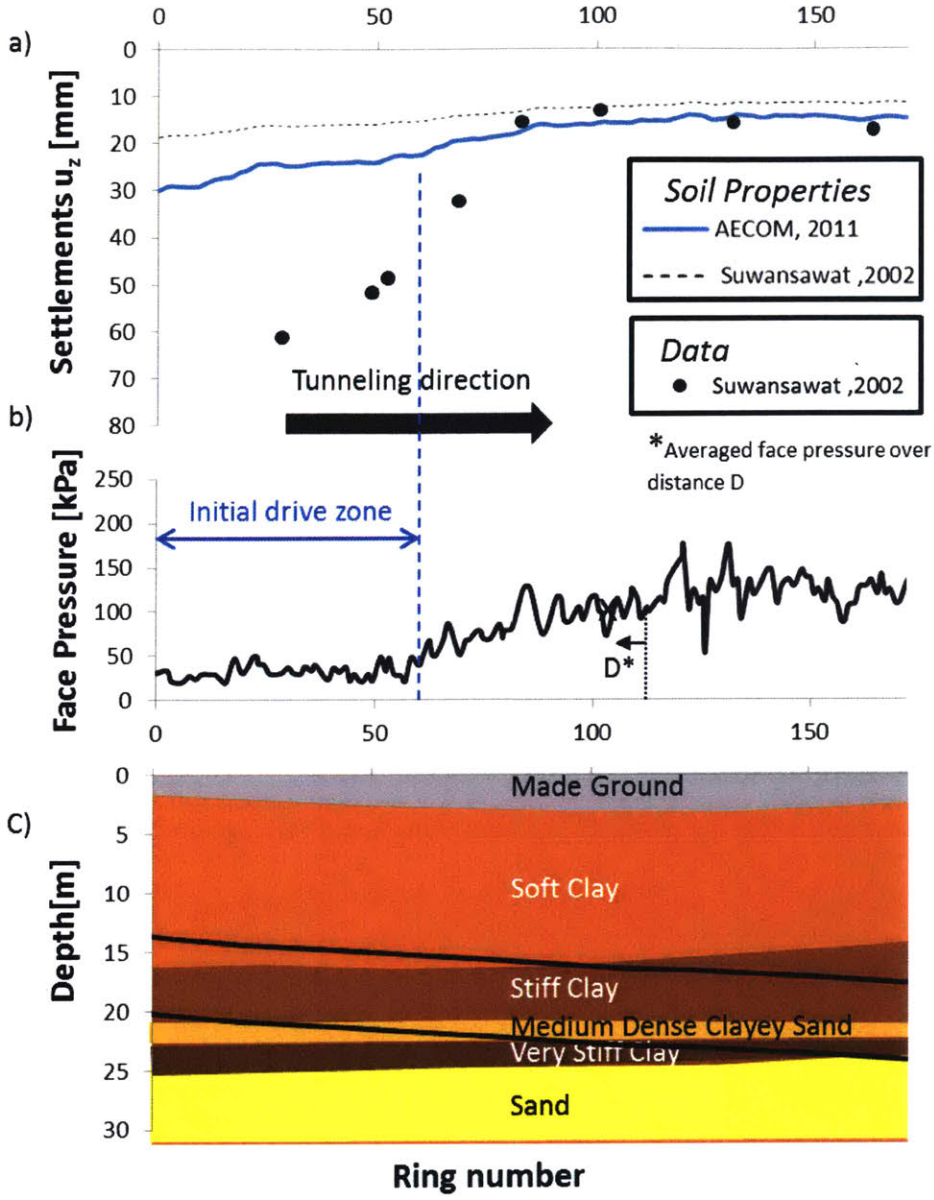

Figure 5.23 Section A of the MRTA project a) comparison of monitored data with method of displacements for SB tunnel b) measured applied face pressure and c) soil profile (Suwansawat, 2002)

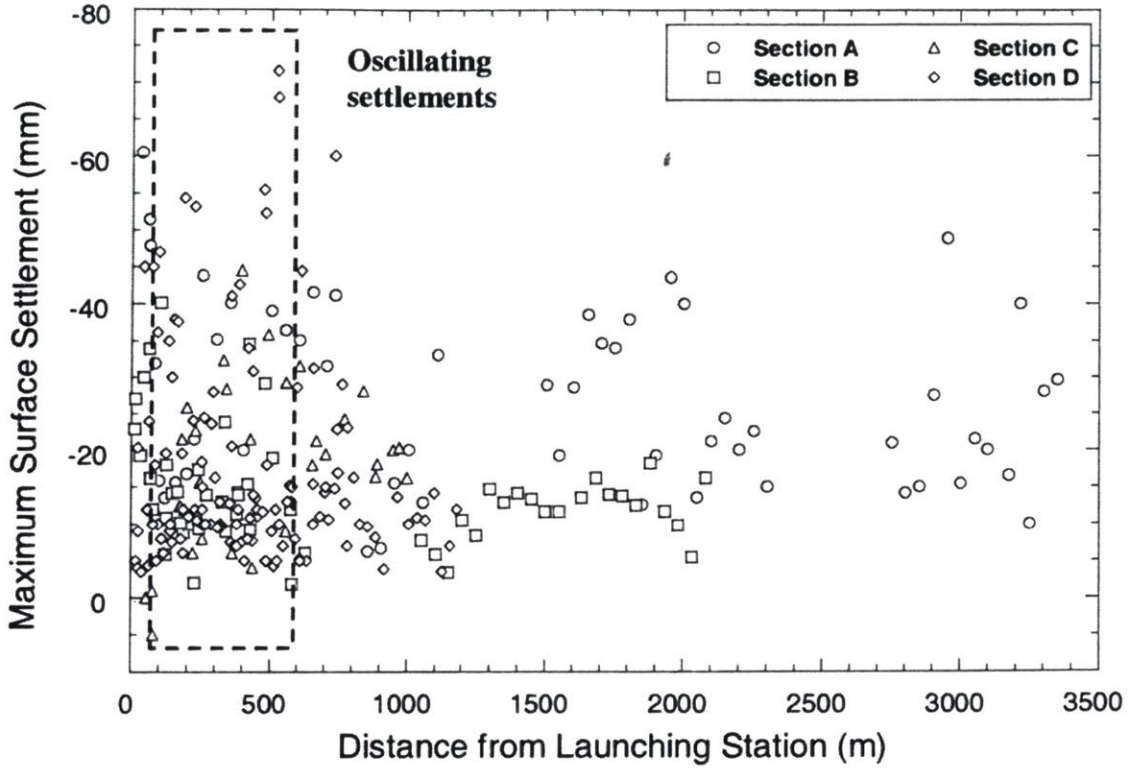

Figure 5.24 Effect of distance from launching station on surface settlements (Suwansawat, 2002)

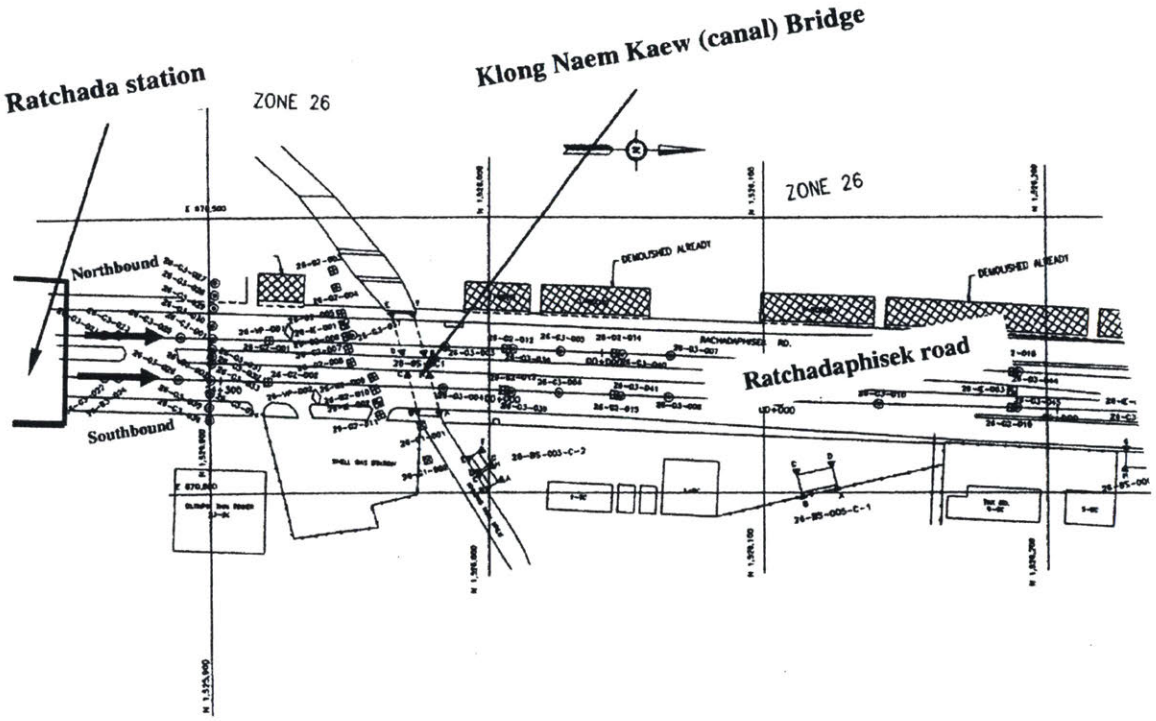

Figure 5.25 Map of initial drive of Section B starting from Ratchada Station (Suwansawat, 2002)

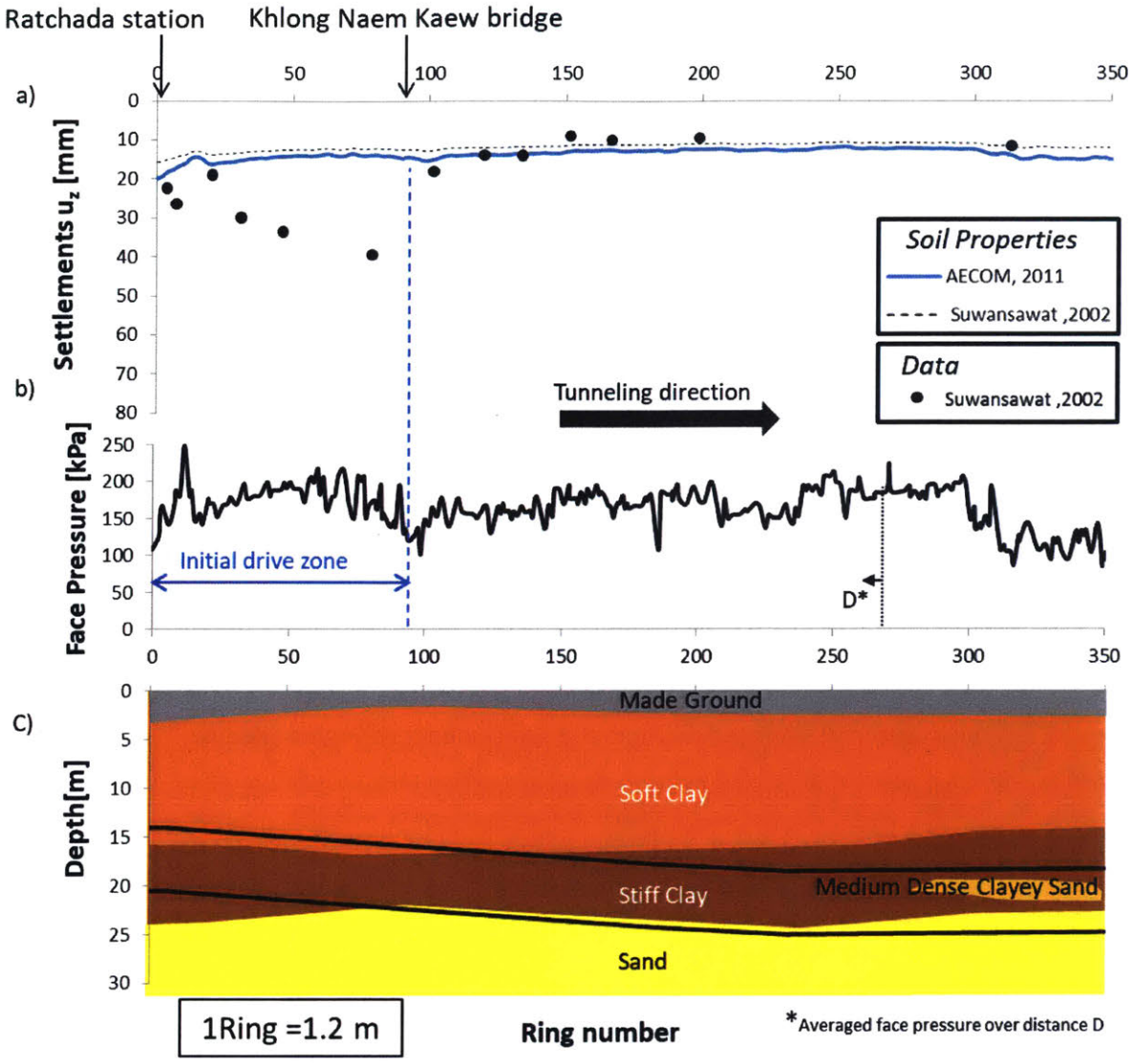

Figure 5.26 Section B of the MRTA project a) comparison of monitored data with method of displacements for SB tunnel b) measured applied face pressure and c) soil profile (Suwansawat, 2002)

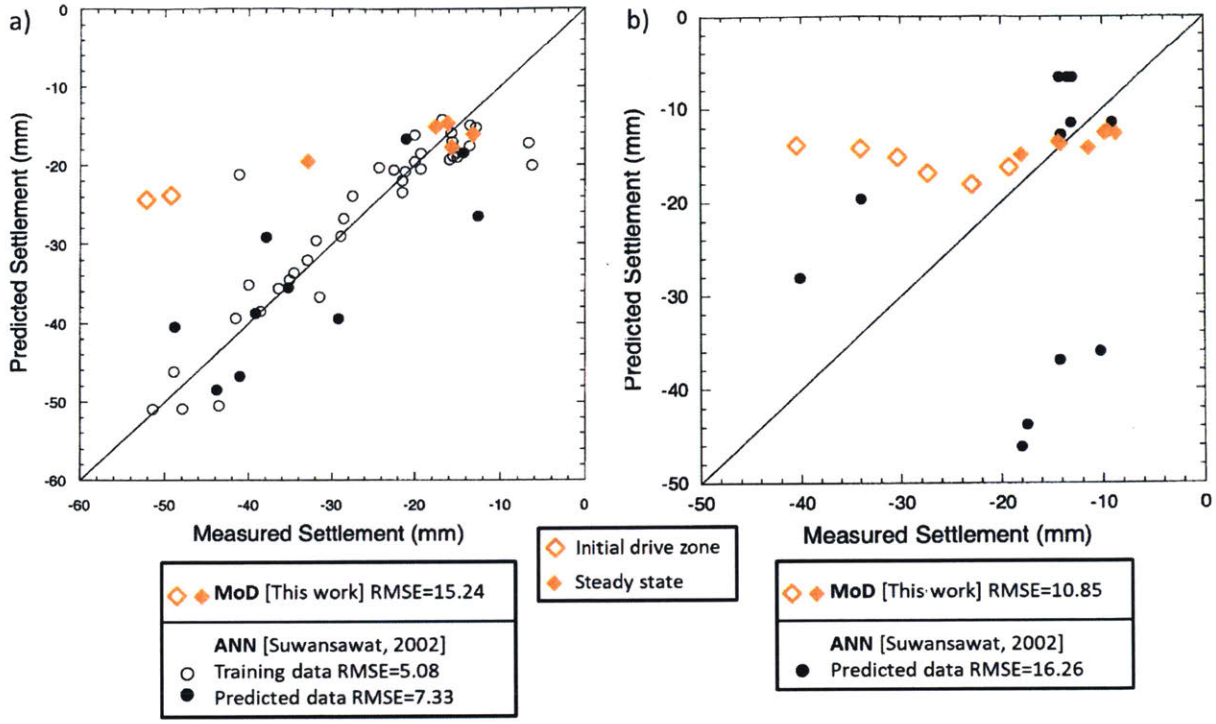

Figure 5.27 Comparison of proposed method of displacements with ANN method by Suwansawat, (2002)

6 Effects of Partial Drainage in Clays

6.1 Introduction

The prior analyses for tunneling in low permeability clay assume undrained shear conditions during tunnel construction. This basically assumes that there is no drainage occurring within the clay during the timeframe of construction and ignores long term movements associated with dissipation of excess pore pressures during construction. In practice, tunnel advance rates vary during construction and there are often delay periods (e.g. maintenance of the cutting head) when consolidation can occur. The importance of consolidation on ground deformations can be assessed by considering the role of partial drainage on ground movements for the steady advance of tunnels at different rates of excavation. For normal rates of production, we anticipate the ground response to be effectively undrained, while at very low advance rates conditions will approach drained conditions (zero excess pore pressures). Preliminary investigations on the effects of consolidation on surface deformations during mechanized tunneling have been conducted by Anagnostou (2008) using 3D Finite Element Analyses. He studied the case of an unsupported tunnel heading assuming seepage conditions at the face, impermeable conditions at the lining and using a linearly elastic soil model. Figure 6.1, shows that deformations generally increase for slower advance rate, v and higher hydraulic conductivity, k (smaller v/k ratios). However, the unrealistic heave deformations occurring after the lining installation (due to the assumption of elastic behavior), interfered significantly with the results closer to drained conditions (for $v/k<10^4$) resulting in severe underestimation of the overall expected deformations. Sitarenios et al., (2016) studied how partial drainage can affect face stability by computing the horizontal displacement at the tunnel face, U_f, from 3D Finite

Element Analyses, for tunnels with C/D=2 and advance rate v=1.5m/h (=36m/d). Figure 6.2 shows that generally the normalized horizontal deformations at the face increase for higher hydraulic conductivities, k. Sitarenios et al., (2016) observed an undrained-like behavior for low hydraulic conductivity values ($k<5*10^{7}$ m/s, see Figure 6.2 a and b) while deformations increased significantly for higher hydraulic conductivity values (Figure 6.2 c and d). As shown in Figure 6.2d, the case of a hydraulic conductivity $k=5*10^{5}$ m/s approaches drained conditions resulting in a highly unstable tunnel face (large horizontal deformations, U_f).

In this chapter we will conduct an initial assessment of partial drainage effects on surface deformations using the Mohr-Coulomb soil model for a typical tunnel case with C/D=3, D=7m with an unsupported heading (σ_f=0) assuming that the face acts as an impermeable membrane.

6.2 Methodology

The previously developed 3D Finite Element model (Figure 4.2) for studying induced deformations due face pressure in undrained conditions is extended to study partial drainage effects for different advance rates. The model simulates the excavation process as a sequence of discrete steps that involve the deactivation of an annulus of soil while impermeable plate elements are activated to model the TBM shield and lining. A constant face pressure boundary condition is applied at the newly exposed heading along with an impermeable boundary condition assuming zero water inflow into the tunnel.

The model considers undrained conditions for the first step and consolidation for each subsequent step with a time step referenced to the width of the lining ring (i.e. x hr/1.5 m advance rate). The model adopts the Mohr-Coulomb soil model with K_0 = 1.0 in situ stresses

assuming that the shear stiffness G and the friction angle ϕ remain constant with depth and that the groundwater table is coincident with the ground surface.

In the prior analyses undrained response of the clay is simulated using the M-C model with "method B" (Brinkgreve et al., 2012)., i.e. assuming the shear strength is controlled by total stresses such that $c' = s_u$ and ϕ' = 0. This same approach cannot be used when considering partial drainage/consolidation, as the shear strength of the clay is controlled by effective stresses. In order to simulate partial drainage, we use the MC model with "undrained method A" which uses the effective stress strength properties (ϕ', c') and calculates as an output of the analyses the total undrained shear strength. In order to match current results with prior undrained analyses using the "method B" (i.e. with input s_u) we estimated an equivalent undrained strength using method A, "s_u". Figure 6.3 shows the methodology followed for estimating the undrained strength at the springline (i.e. s_{uH}) based on the maximum shear stress computed along the tunnel axis at the level of the springline in undrained conditions. In this example the maximum shear stress, $\tau = (\sigma_1 - \sigma_3)/2 = 110\ kPa$, is computed at a distance y= 5 m in front of the face of the tunnel. The predicted and measured settlements can then be compared with prior results for s_u =100 kPa. Figure 6.4 compares the deformations computed for undrained conditions using "method A" and "method B" (fitted with Eq. 4.3). The comparison reveals a very close match between the two methods, which allowed us to relate the current results to our prior analyses.

We are then able to proceed with consolidation analyses examining the effect of partial drainage in clay. The methodology used for calculating the ground surface settlement above

the centerline of the advancing tunnel follows a similar procedure to that in section 4.1. For each advance step, Δy =1.5m, we applied a time increment corresponding to the examined advance rate, v= Δt / Δy. This process is repeated until a steady state was reached, where the incremental settlement troughs for successive steps remain the same. The total settlement $\boldsymbol{u_z}$ is then obtained by integrating the incremental settlements $\boldsymbol{\delta u_i}$ spatially along the TBM trajectory (Eq. 4.1).

The current analyses consider an array of different soil properties, i) friction angle ϕ=25°, 30° and 35°, ii) hydraulic conductivity k= 10^{-12} to 10^{-9} m/s (based on permeability range for clay minerals as presented by Casey, 2014, Figure 6.5), iii) a reference soil stiffness G/"s_u"=100 (used in our prior undrained analyses) and iv) tunnel advance rates, v = 0.3 to 100 m/d (corresponding to typical advance rates for mechanized tunneling in soft soils).

The selected advance rates correspond to typical ranges reported in the literature for mechanized excavations. Willis, (2013) reported average advance rates per week for soft ground conditions at 15 m/d and for mixed face conditions at 10 m/d based on collected data for 28 TBM machines used in metro sized projects worldwide, Figure 6.7. Roby and Willis (2014) made similar observations of average advance rates at 12m/d by examining advance rates from 40 EPBs in mixed face conditions. The Crossrail project data shows weekly advance rates ranging from 7 to 25m/d (Figure 5.3) while rates of 4 to 20 m/d were reported for the MRTA project in Bangkok (Figure 6.6). Table 6.1 summarizes the monitoring advance data for the three reference projects studied in chapter 5, along established hydraulic conductivity

properties for the local clay. The three projects have dimensionless advance rates, v/k= $10^{-4} - 10^{-5}$.

6.3 Results

Figure 6.8 summarizes the effects of partial drainage in clay for the combinations of the considered advance rates and soil properties examined. The maximum surface deformation is presented as the dimensionless group $u_z G/\gamma D^2$ (as in our prior undrained analyses) and is plotted as function of dimensionless ratio of the advance rate over hydraulic conductivity ratio v/k, for three different ratios of undrained shear strength or $s_{uH}/\gamma H$ or ϕ'. The deformations are not controlled directly by permeability k, but by the relative ratio v/k, such that ratios v/k > 10^7 correspond to undrained behavior, while for v/k < 10^3 excessive deformations occur (due to lack of face support) as we approach drained conditions. It should be noted that drained conditions for the unsupported case ($\sigma_f = 0$) examined for this comparison correspond to failure at the tunnel heading. This plot illustrates that there is a critical ratio (v/k = 10^4) that signifies the transition from stable conditions at the face, for fast advancing tunnels in low permeability soils, to collapse at the face occurring when dealing with slow advance rates or temporary stops in high permeability soils. Although, the three case studies from chapter 5 fall within the examined range for hydraulic conductivity and advance rates, the current results are not representative of their respective face support conditions (i.e. only examine unsupported face conditions, $\sigma_f = 0$) and in situ undrained strength (i.e. reference range of undrained strengths, "s_{uH}"/γH=0.18 - 0.25). Hence, we cannot estimate from the current analyses the effect of partial drainage for these cases.

Table 6.1 Average weekly advance rates for the three tunnel projects (Ieronymaki, 2015, Su, 2015, Suwansawat, 2002)

Project	Weekly advance rate[m/d]	Hydraulic conductivity [m/s]	$\frac{v}{k}$
Crossrail	10	10^{-9}	10^{5}
MRTA (Bangkok)	15	10^{-9}	$2\,x\,10^{5}$
DTL (Singapore)	10	10^{-8}	10^{4}

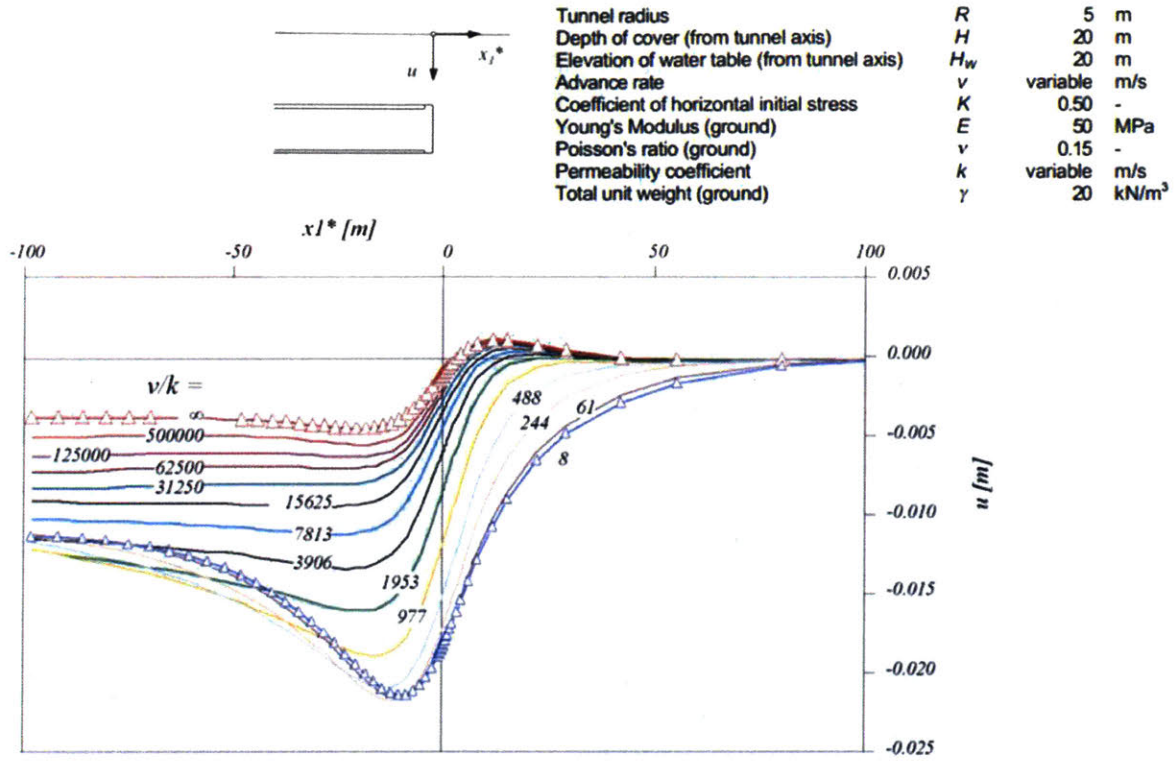

Figure 6.1 Effect of advance rate over hydraulic conductivity ratio v/k on longitudinal settlement trough for tunnels with impermeable lining and seepage conditions at the face assuming linear-elastic soil behavior (Anagnostou, 2008)

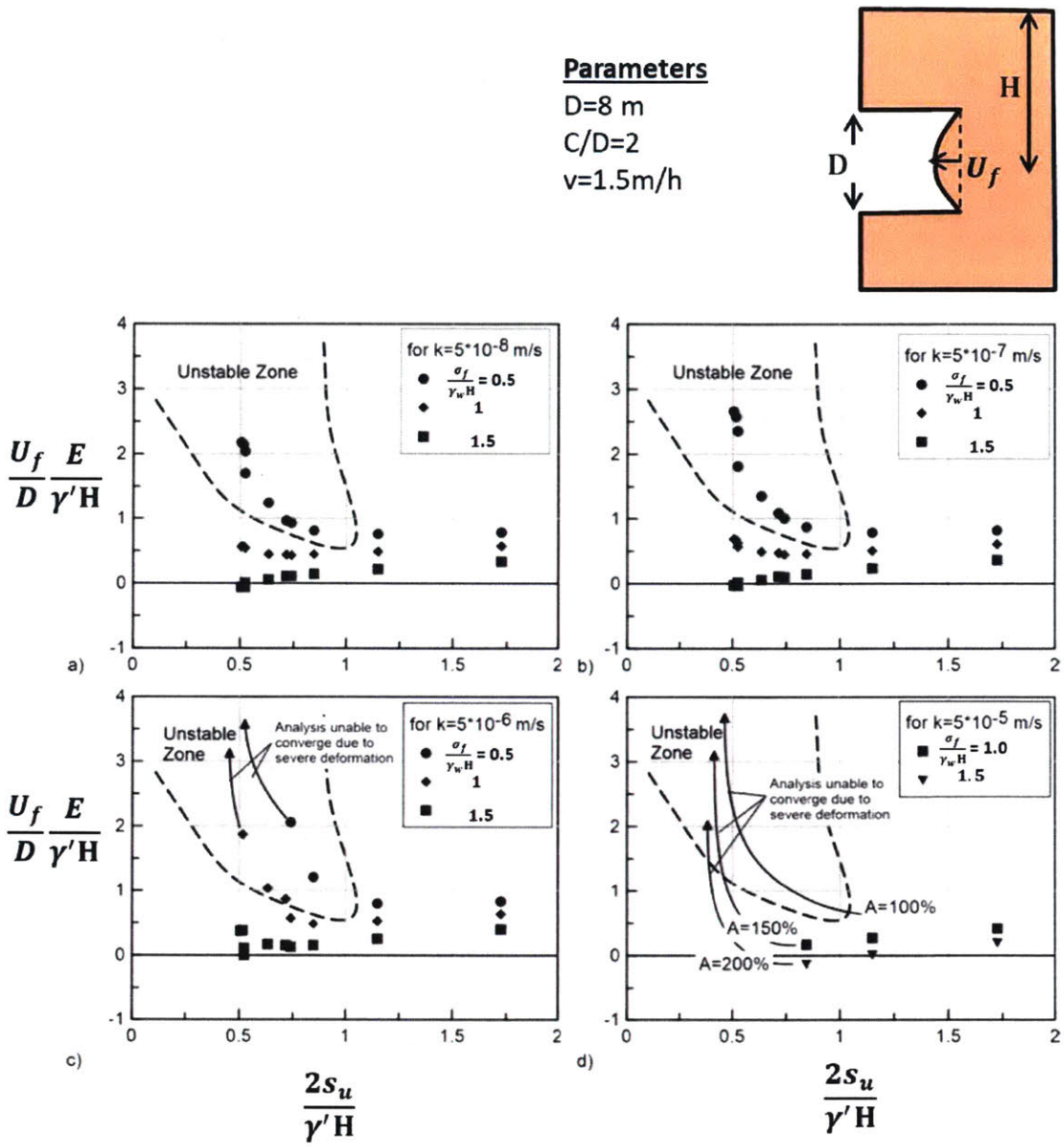

Figure 6.2 Effect of undrained strength s_u on the face stability/horizontal deformations at the face U_f for four hydraulic conductivity k values (Sitarenios et al. 2016)

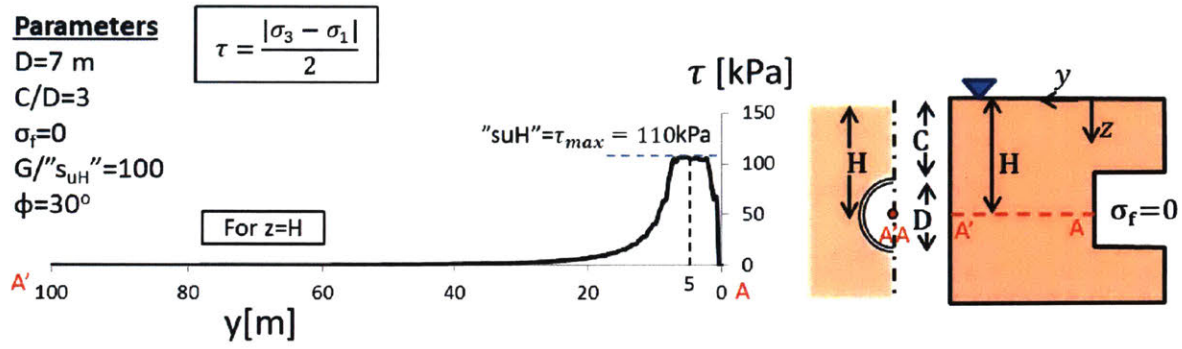

Figure 6.3 Example of methodology used to estimate the equivalent undrained strength "s_u" for undrained analyses using the M-C undrained A implementation

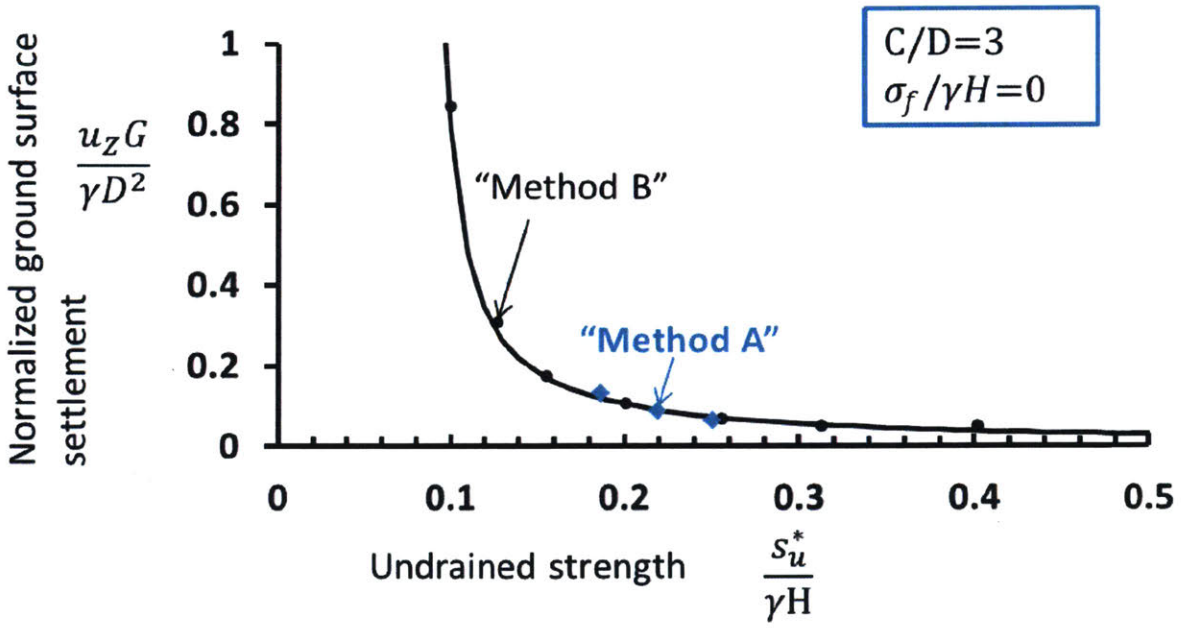

Figure 6.4 Comparison of "method A" and "method B" for undrained advance for the case of C/D=3

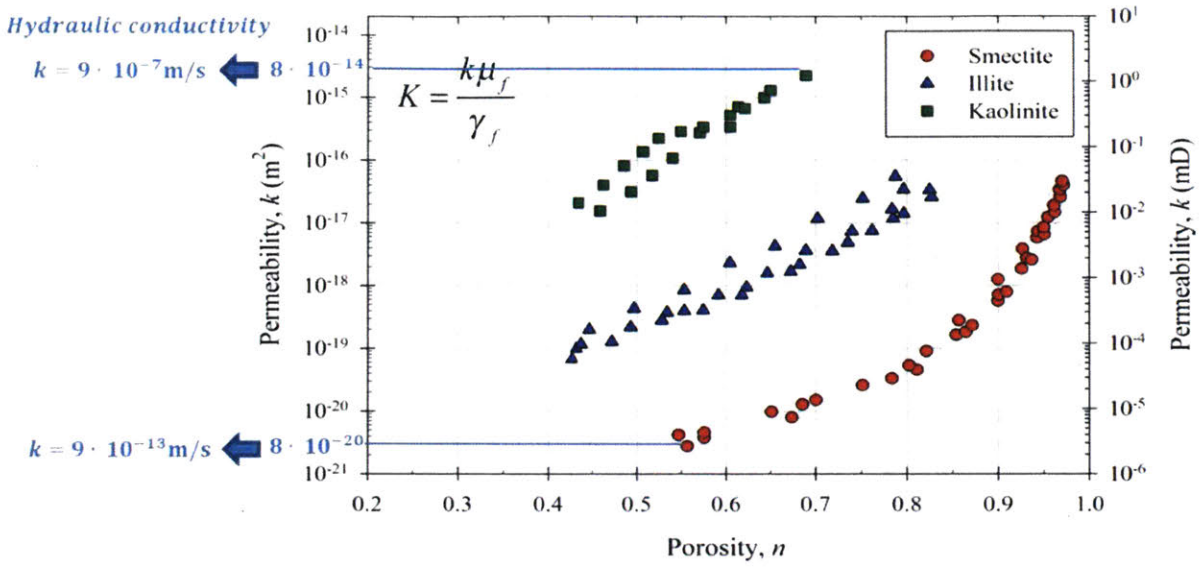

Figure 6.5 Recent measurements of intrinsic permeability for clay mineral (Casey, 2014) Hydraulic conductivity properties are estimated using specific weight of $\gamma_f=\gamma_w=9.8$ kN/m^3 and $\mu_f= \mu_W= 1$ mPa·s for water of 20.0 °C

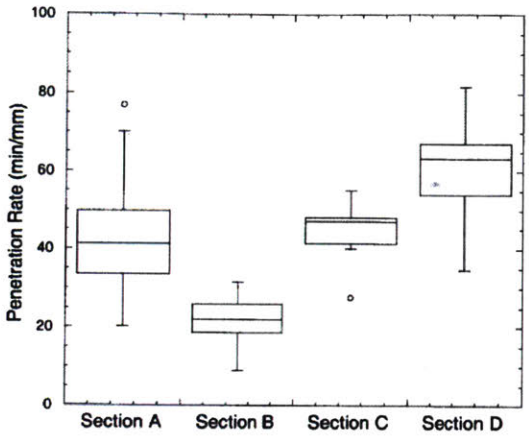

Figure 6.6 Ranges of penetration rate reported in the MRTA project by Suwansawat, 2002

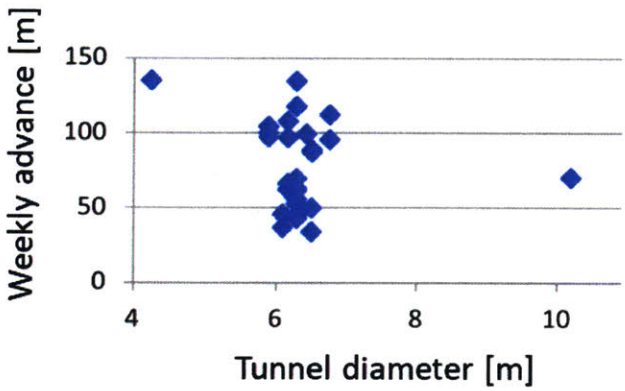

Figure 6.7 Ranges of weekly advance rates from metro-sized tunnels in homogeneous and mixed soil conditions (Willis, 2013)

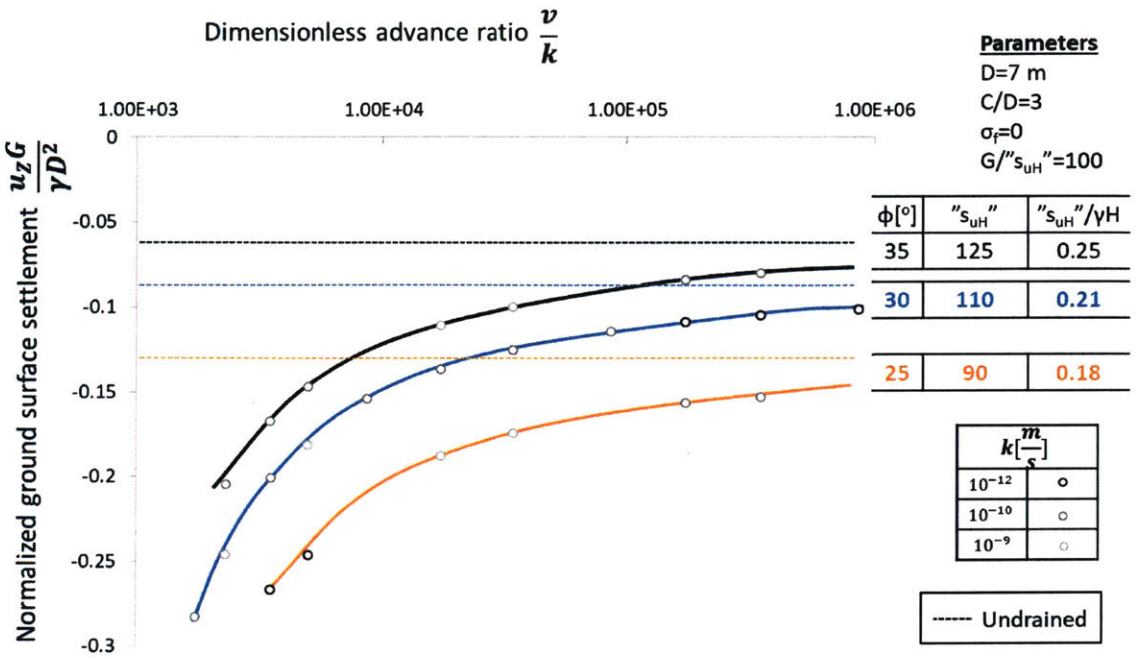

Figure 6.8 Effect of ratio of advance rate over hydraulic conductivity on computed ground deformations for different shear strength properties

7 Summary, Conclusions and Recommendations

7.1 Summary

The main goal of this research was to develop analytical methods for predicting ground deformations caused by closed-face mechanized tunneling in homogeneous and mixed face soil conditions. The ground deformations are closely linked to face stability conditions and hence are affected by the shear strength of the soil and the control of pressures in the closed face chamber. We then relate the ground deformations to the control parameters (face pressure, grout pressure), TBM cutting head, shield geometry, cover depth and tunnel diameter.

We studied face stability in a variety of soil conditions ranging from homogeneous conditions (clay and sand) to mixed face conditions in clay, i.e. a 2 layer system with contrasting shear strength. Stability analyses in homogeneous clay included both lined (immediate support directly behind the face) and unlined (no shield or lining system used) settings, using 3D and 2D plane strain FE models respectively. For low permeability clays, the analyses assume undrained conditions, and use the Mohr-Coulomb soil model in conjunction with a shear strength method (c-phi reduction) to induce a collapse mechanism. The results for the 2D (unlined) tunnel case match closely published upper and lower bound solutions using the numerical limit analyses (NLA) method (Wilson et al., 2011) (Figure 3.5), while the initial results from the 3D (lined) case compared well to prior studies from Davis et al., (1980); Sloan (2013); Mollon et al (2013); and Mair (1979)(Figure 3.11). The current analyses show that face stability is controlled by the undrained shear strength at the tunnel springline. For cover depth-to-diameter ratios C/D>3, instability invokes a local failure mechanism around the heading that does not reach the ground

surface. As a result, the ratio of the critical undrained strength to ensure stability over the geostatic stresses at the springline remains constant for deep tunnels (C/D>3). There is a linear dependency between the critical undrained strength at face and the applied face pressure (Figure 3.16).

The mixed face stability analyses consider a two layer ground profile with soft clay overlying stiff clay. The analyses showed that the presence of the soft clay above the tunnel does not affect face stability, when the distance between the tunnel cover and the two-layer interface is more than one diameter ($D_T/D < -1$). However, stability is affected as the tunnel approaches or intersects the overlying soft layer and is controlled by the soft layer until fully embedded. Similarly, the relative undrained strength ratio of the upper and lower clay layer is insignificant when the two-layer interface is ($D_T/D < -1$ or ($D_T/D > 1$). As shown in Figure 3.21, for cases where the top layer is more than one diameter above the tunnel crown only the undrained strength of the bottom layer controls face stability while for cases that the bottom layer is below the tunnel invert only the undrained strength of the top layer matters. The strength ratio becomes significant for geometries that the tunnel interacts with both layers. In that case there is a critical strength ratio for which the developed collapse mechanism extends only in the part of the face embedded within the soft layer and any further increase of the bottom layer strength will not have any effect on face stability (Figure 3.20).

Face stability in high permeability sand was considered, assuming the formation of an impermeable membrane (from the slurry) at the excavated face (typically applied by slurry pressure). The 3D FE analyses were performed using the c-phi reduction method as explained in

section 3.4. The initial analyses, conducted for dry conditions and a uniform face pressure distribution with depth, were compared against experimental model data by Chambon & Corte (1994), Kirsch (2010) and Plekkenpol et al (2006) and analytical studies by Anagnostou and Kovari (1996), Anagnostou (2012), Leca and Domieux (1990), Mollon (2010), Vermeer (2002) achieving very good agreement. The results confirmed prior observations from centrifuge tests by Chambon & Corte (1994), and 1g model tests by Kirsch (2010), and later studies by Vermeer and Ruse (2001) and Mollon et al (2011) that for common values of cover depth to diameter ratio, C/D>1, and friction angles, $\phi > 20^{o}$, face stability is independent of the ground cover. The parametric studies exploring the effect of the face pressure distribution on face stability compare well with similar work by Anagnostou and Perazzelli (2013), although they used a different methodology (limit equilibrium method with the method of slices) and assumed a rectangular cross section to approximate the tunnel face. We both find that the face pressure gradient has an adverse effect on stability, as higher average face pressure is required to ensure stability at larger pressure gradients. Finally, we examined the effect of the water level on face stability and found that stability depends only on the percentage of the face area that is submerged below water.

The 3D FE deformation analyses[20] studied the primary sources of settlement during a mechanized tunnel construction, including stress relief at the face due to soil removal, overcutting due to the conical shape of the shield, poor control of grout at the tail void and the buoyancy effect (due to lesser weight of the TBM compared to the excavated soil mass). These

[20] The analyses modeled soil behavior using the simple elastic perfectly plastic M-C soil model assuming G/s_u=100.

factors were initially studied separately and then their effects on ground surface deformations were superimposed assuming that the deformations were small enough to ensure elastic behavior. Although this assumption has potential shortcomings for larger deformations, it provides a reasonable quantitative approximation for the current range of conditions.

The deformations due to the applied face pressure, $\sigma_f/\gamma H$ are shown to be linearly dependent on the applied face pressure and inversely proportional of the strength difference between the in situ, $s_u^*/\gamma H$ and the critical stability strength, $s_u/\gamma H$ values. These results are very helpful in differentiating between cases that variations in face pressure have minor effects on deformations (when $s_u^* \gg s_u \rightarrow \frac{\Delta s_u}{\gamma H} \gg 0$) and cases that a very sensitive behavior is expected (when $s_u^* \rightarrow s_u \rightarrow \frac{\Delta s_u}{\gamma H} \rightarrow 0$) which require constant monitoring and careful adjustment of the face pressure during construction. Similarly, a linear dependency was shown between the applied grout pressure, $\sigma_G/\gamma H$ and the computed deformations due to grouting of the tail void. The deformations due to the shield conicity depend on the shield contraction and the tunnel geometry and not on the soil properties, due to the conservative assumption of zero gap formation between the surrounding soil and the shield. The buoyancy effect due to the lower TBM weight compared to the removed soil was found to be minor in comparison to the other three effects and it can be safely ignored.

The results from the proposed deformation analyses were then fitted with a closed-form equation in order to enable prediction of ground surface settlements in terms of the ground parameters and tunnel geometry. The proposed method illustrates how TBM control parameters (face pressure, grout pressure) and TBM shape are controlling tunnel stability and

surface settlements for different tunnel geometries and soil conditions. This can help tunnel engineers mitigate adverse effects such as excessive settlements or tunnel collapse, especially when dealing with sensitive urban environments.

The accuracy of the proposed solution is evaluated using data from three projects:

1. Crossrail C300 involving excavation in homogeneous stiff clay (Ieronymaki et al 2016),
2. DTL in Singapore involving mixed clay face conditions (Su, 2015), and
3. Blue Line in Bangkok (Suwansawat-Einstein, 2006) involving mixed clay face conditions.

Overall the proposed "method of displacements" achieves accurate predictions of the induced surface deformations in both homogeneous and mixed face conditions in the case of two layer clay formations. The method achieved an excellent prediction of the deformations monitored for the Greenfield Hyde Park location of Crossrail, where the tunnel was excavated in a homogeneous London clay profile. The predictions were comparable to results using a 3D FE model specifically developed to study the Hyde Park section by Founta and Whittle, 2016. Our method predicted very well the measured data for the DTL project in Singapore, apart from sections were a sand layer, present between the Kallang and Old alluvium formations was encountered at the tunnel face, which was not considered in our method. For the DTL case the predictions produced using our proposed method of displacements are comparable to results using a 3D FE simulation specifically developed to model the stratigraphy of the examined section (including the sand layer) by Su, 2015. Similarly, a good match with the recorded data was achieved for the Blue Line project, apart from the launching sections of the tunnel, where

non steady conditions were encountered (excavating from a launch shaft, partial equipment use, learning curve of machine use, equipment inspection stops) for which the proposed method is not applicable (as it simulates a continuous TBM advancement). Our predictions were compared to a trained ANN by Suwansawat-Einstein, 2006, using multiple variables such as the tunnel depth, distance from launching station, geology at tunnel crown and invert, water level from tunnel invert, face pressure, penetration rate and grouting pressure. Although, ANN provides excellent predictions of deformations within the same tunnel sections that the model was trained for (Suwansawat and Einstein, 2006) our method matches or outperforms ANN's predictions for different sections of the same project.

7.2 Conclusions

Current methods for predicting ground surface settlements include a variety of empirical and analytical solutions (e.g. Ieronymaki et al. 2016) that do not simulate effects of tunneling methods, as well as ANN techniques (Suwansawat-Einstein, 2006) that are trained on project specific data. Similarly, numerical predictions using 3D finite element methods generally focus on site specific conditions and soil properties and predict reasonably well the tunnel induced deformations (Moller 2006; Founta and Whittle 2016). These analyses require extensive fine-tuning which can be time consuming and resource demanding, making them impractical for use in the early stages of design. The current analyses use 3D finite element analyses to develop generic predictions that are then presented in the form of design methods for estimating ground settlements in terms of tunnel control parameters, tunnel geometry and easily defined design soil properties. Our method provides a valuable insight on how the parameters involved in a tunnel design will affect the expected deformations under both homogeneous and mixed

face conditions and is a first step in creating a global formula that can satisfactorily predict deformations in a range of soil conditions, requires a small number of input parameters and has been validated for three very different soil stratigraphies.

7.3 Recommendations for further research

The current study validated the proposed framework using three case studies. It would be very interesting to explore additional cases for which this methodology can be applied and assess its accuracy over a wider spectrum of conditions.

The proposed methodology focused on the behavior of cohesive materials (clays) in a variety of cases ranging from homogeneous to two layered profiles. Another direction for future research is to extend the current framework for frictional materials (sands) and also examine the interaction between cohesive low permeability and frictional high permeability layers and understand the mechanisms involved in collapsing the face and the induced surface deformations. This is a challenging case due to the contrasting permeability properties of the two soils layers that requires coupled consolidation analyses to model the partial drainage in the clay layer for different advance rates.

In addition our current method assumes a steady state advancement of the tunnel excavation. While this assumption was sufficient to obtain good predictions for most cases, our model unpredicted displacements for the beginning of a drive from a launching shaft, as shown in Figure 5.23 and Figure 5.26. An important direction for future research is to study how transient effects involving: i) starting from a launching shaft and ii) cutterhead gear repair involving temporary loss of face support are affecting the induced settlements.

References

Addenbrooke, T.I., Potts, D.M. & Puzrin, A.M. (1997) "The influence of pre-failure soil stiffness on numerical analysis of tunnel construction", Geotechnique, 47 (30), 693-712

AECOM (2011) "The MRT Blue Line Extension Project Contract 2: Underground Civil Works Sanam Chai – Tha Phra Section Geotechnical Interpretative Report"

Anagnostou, G. (2008) "The effect of tunnel advance rate on the surface settlements" In 12th international conference of IACMAG, Goa, India

Anagnostou, G. and Kovari, K. (1994) "The face stability of slurry-shield-driven tunnels" Tunneling and Underground Space Technology, 9(2), 165–174

Anagnostou, G. and Kovari, K. (1996) "Face stability conditions earth-pressure-balanced shields" Tunneling and Underground Space Technology, 11(2), 165–173

Anagnostou, G. and Kovari, K. (1996) "Face stability in slurry and EPB shield tunneling" Tunnels & Tunnelling International, 28(12), 27-36

Anagnostou, G. and Perazzelli, P. (2013) "The stability of a tunnel face with a free span and a non-uniform support", Geotechnique, 36(1), 40-50

Attewell, P. B. (1978) "Ground movements caused by tunneling in soil", Proc. International Conference on Lange Movements and Structures, J.D. Geddes (Ed), Pentech Press, London, 812-948

Attewell, P. B. and Woodman, J. P. (1982) "Predicting the dynamics of ground settlement and its derivatives caused by tunneling in soil", Ground Engineering, 15(8), 13-22, 36

Attewell, P. B. Yeates,J., Selby A.R. (1986) "Soil movements induced by tunnelling and their effects on Pipelines and structures", Blackie,Glasgow

Augarde, C.E., Lyamin, A.V., and Sloan, S.W. (2003) "Stability of an undrained plane strain heading revisited" Computers and Geotechnics, 30(5), 419–430

Bam Ferrovial Kier ,BFK (2012) "Status Report 2-Component grouting"

Bartlett, S.F. (2012) "Field Classification of Soil Using the USCS" Retrieved from http://www.civil.utah.edu/~bartlett/CVEEN6340/soildescription.pdf

Bathe, K.J., (1982) "Finite Element Procedures in Engineering Analysis", Prentice Hall, Englewood Cliffs

Bernat, S., Cambou, B. (1996) "Soil-structure interaction in shield tunnelling in soft soil", Computers and Geotechnics, 22 (3/4), 221–242, 1998.

Bernat, S., Cambou, B. (1998) "Soil-structure interaction in shield tunneling in soft soil", Computers and Geotechnics, 22 (3/4), 221–242

Bezuijen, A., van Seters, A. (2002) "The stability of a tunnel face in soft clay" Proceedings of the International Conference on Physical Modelling in Geotechnics (ICPMG'02), July 2002, St. John's, Newfoundland, Canada, 791-796

Black, M. (2012) "Crossrail: Geotechnical Sectional Interpretative Report1&2:Royal Oak to Liverpool Street"

Brinkgreve, R. B. J., Engin, E. and Swolfs, W. M. (2014) "Plaxis 2D Manual Anniversary Edition"

Brinkgreve, R. B. J., Engin, E., Swolfs, W., Waterman, D., Chesaru, A., Bonnier, P., and Galavi, V. (2012) "PLAXIS 3D 2012", Delft, the Netherlands: PLAXIS BV.

Brinkgreve, R. B. J., Bakker, H. L. (1991). Non-linear finite element analysis of safety factors" Proceedings of the international conference on computer methods and advances in geomechanics, Rotterdam, the Netherlands: Balkema, 1117–1122

Broere, W. (2001) "Tunnel Face Stability and New CPT Applications" PhD thesis, Delft University of Technology, Delft

Broere, W., Brinkgreve, R.B.J. (2002) "Phased simulation of a tunnel boring process in soft soil" Numerical Methods in Geotechnical Engineering, 529-536

Broms, B.B. and Bennermark, H. (1967) "Stability of clay at vertical openings" Journal of the Soil Mechanics and Foundations Division, 93(1), 71–94

Buckingham, E. (1914) "On physically similar systems; illustrations of the use of dimensional equations", Physical Review, 4 (4), 345–376

Burland, J. B., Standing, J. R., Jardine, F. M. (2001) "Building response to tunnelling: case studies from construction of the Jubilee Line Extension", London (Vol. 200). Thomas Telford.

Casey, B. B. A. (2014). The consolidation and strength behavior of mechanically compressed fine-grained sediments (Doctoral dissertation, Massachusetts Institute of Technology).

Civil Engineering and Development Department - The Government of the Hong Kong Special Administrative Region, CEDD (2015) "Catalogue of Notable Tunnel Failures - Case" Retrieved from http://www.cedd.gov.hk/eng/publications/geo/notable_tunnel.html

Celestino, T. B., Gomes, R. A. M. P. & Bortolucci, A. A. (2000) "Errors in ground distortions due to settlement trough adjustment" Tunnel. Undergr. Space Technol. 15(1), 97–100.

Chambon, P. and Corté, J.F. (1994) "Shallow tunnels in cohesionless soil: Stability of tunnel face" ASCE Journal of Geotechnical Engineering, 120, 1148–1165

Chiam, S.L., Wong, K.S., Tan, T.S. and Ni, Q., Khoo, K.S., Chu, J. (2003) "The Old Alluvium" Underground Singapore 2003 Engineering Geology Workshop

Clayton, C. R. I, Van Der Berg, J. P., Thomas, A. H.(2006) "Monitoring and displacements at Heathrow Express Terminal 4 station tunnels", Géotechnique, 56(5), 323 –334

Clough, G. W. and Leca, E. (1989) "With focus on use of finite-element methods for soft ground tunnelling", Review Paper in Tunnels et Micro-Tunnes en Terrain Meuble-du Chantier a la Theorie, Presse de l"Ecole National des Ponts et Chaussees, Paris, 531-573

Clough, G.W., Leca, E.(1993) "EPB Shield Tunneling in Mixed Face Conditions" Journal of Geotechnical Engineering, 119(10), 1640-1656

Crossrail data logs, 2013

Crossrail Project website, http://www.crossrail.co.uk

Dadvand, P., Rossi, R., Oñate, E. (2010) "An object-oriented environment for developing finite element codes for multi-disciplinary applications" Archives of Computational Methods in Engineering, 17 (3), 253–297

Davies, R.V., Whittle, A.J., (2006) "Nicoll Highway Collapse: Evaluation of Geotechnical Factors Affecting Design of Excavation Support System" International Conference on Deep Excavations 28-30 June 2006, Singapore

Davis, E.H., Gunn, M.J., Mair, R.J., and Seneviratne, H.N.(1980) "The stability of shallow tunnels and underground openings in cohesive material" Géotechnique, 30(4), 397–416

Deane, A. P., and Bassett, R. H. (1995) "The Heathrow Express Trial Tunnel". Proceedings of the Institution of Civil Engineers, Geotechnical Engineering, 113, 144-156.

Dias, D., Kastner, R., Maghazi, M. (1999) "Three dimensional simulation of slurry shield tunnelling", Geotechnical aspects of underground construction in soft ground, Tokyo, Rotterdam: Balkema; 351–6

Dias, D., Kastner, R., Maghazi, M. (2000) "Three dimensional simulation of slurry shield tunnelling" Proc. of the International Symposium on Geotechnical Aspects of Underground Construction in Soft Ground, 351–356

Do, N., Dias, N., Oreste, P., Djeran-Maigre, I., (2013) "3D Modelling for Mechanized Tunnelling in Soft Ground-Influence of the Constitutive Model" American Journal of Applied Sciences 10 (8), 863-875

FHWA (2011) "Technical Manual for Design and Construction of Road Tunnels - Civil Elements", http://www.fhwa.dot.gov/, U.S. Department of Transportation Federal Highway Administration, Bridge, Tunnels, Chapter 6, 7 and 9

Finno R. J. and Clough G. W. (1985) "Evaluation of Soil Response to EPB Shield Tunneling" Journal of Geotechnical Engineering Division, ASCE, 111(2), 155-173.

Founta V., Ninic J., Whittle, A.J., Meschke G., Stascheit J.(2013) "Numerical Simulation of Ground Movements Due To EPB Tunnelling in Clay" 3rd EURO:TUN conference: Computational Methods in Tunneling and Subsurface Engineering, Bochum Germany, in print.

Founta, V. (2013) "Numerical simulation of ground movements and structural forces in lining for Earth Pressure Balance (EPB) tunneling in clay", MSc Thesis, Massachusetts Institute of Technology, Cambridge, MA

Founta, V., Whittle, A.J., (2016) "3D finite element model for representing EPB tunneling in clay", World Tunnel Congress 2016, San Francisco, USA

Founta, V., Whittle, A.J., (2017) "Evaluation of 3D FE Predictions of Ground Movements Caused by EPB Tunneling In Stiff Clay", draft version

Galli, G., Grimaldi, A., Leonardi, A., (2004) "Three-dimensional modelling of tunnel excavation and lining", Computers and Geotechnics, 31(3), 171-183

GCG (2010) "Geotechnical Sectional Interpretative Report 1&2: Royal Oak to Liverpool Street, Volumes 1 and 2 Report" (No. 1D0101-G0G00-00549 and No. 1D0101-G0G00-00550)

Google Maps (2017) "MRTA: Blue line map" Retrieved from https://www.google.com/maps/@13.7814934,100.5074649,13z

Greenwood, J.D. (2003) "Three dimensional analysis of surface settlement in soft ground tunnelling", MEng Thesis, Dept. of Civil & Environmental Engineering, Massachusetts Institute of Technology

Hemphill, G. B. (2012). Tunnel-Boring Machines. Practical Tunnel Construction, 171-185.

Herrenknecht (2017) "Tunnelling: Future-oriented tunnelling technology for transport and supply for tomorrow" Retrieved from https://www.herrenknecht.com/en

Herrenknecht, M., Rehm, U., Liebler, B.C. (2004) "Tunnelling in changing geology" Underground space for sustainable urban development. In: Proceedings of the 30th ITA-AITES World Tunnel Congress, Singapore, 1, 611–621

Horn M., (1961) "Horizontal earth pressure on perpendicular tunnel face". In: Hungarian National Conference of the Foundation Engineer Industry, Budapest

Hu, X., Zhang, Z., Kieffer, S. (2012) "A real-life stability model for a large shield-driven tunnel in heterogeneous soft soils" Front. Struct. Civ. Eng. 2012, 6(2): 176–187

Ieronymaki, E. (2011) "Response of continuous pipelines to tunnel induced ground deformations", MSc Thesis, Dept. of Civil & Environmental Engineering, Massachusetts Institute of Technology

Ieronymaki, E.S. (2015) "Prediction and interpretation of ground movements due to tunneling in stiff clay and impacts on adjacent structures" PhD Thesis, Massachusetts Institute of Technology, Cambridge, MA

Ieronymaki, E.S., Whittle, A.J. and Simic, D. (2016) "Interpretation of Free-field ground movements caused by mechanized tunnel construction". ASCE J. of Geotechnical and Geoenvironmental Engineering

Jacobsz, S. W. (2002) "The effects of tunnelling on piled foundations" PhD thesis, Engineering Department, Cambridge University

Joseph, D.D., Yang, B.H.(2010) "Friction factor correlations for laminar, transition and turbulent flow in smooth pipes" Physica D: Nonlinear Phenomena ,239 (14), 1318–1328

Kasper, T. , Meschke, G. (2004) "A 3D finite element model for TBM tunnelling in soft ground" International Journal for Numerical and Analytical Methods in Geomechanics, 28, 1441–1460

Kasper, T., Meschke, G. (2006a) "On the influence of face pressure, grouting pressure and TBM design in soft ground tunnelling", Tunnelling and Underground Space Technology, 21 (2), 160–71

Kasper, T., Meschke, G. (2006b) "A numerical study on the effect of soil and grout material properties and cover depth in shield tunneling", Computers and Geotechnics, 33, 234-247

Kimura, T. and Mair R.J. (1981) "Centrifugal testing of model tunnels in soft clay" Proceedings of the 10th ICSMFE, 1, 319–322.

Kirsch, A (2008) "Experimental investigation of face stability of shallow tunnels in sand" W(H)YDOC 08: 3rd international workshop of young doctors in geomechanics, Nov 2008, Champs-sur-Marne, France, 61-64.

Komiya, K., Soga, K., Akagi, H., Hagiwara, T., Bolton, M. (1999) "Finite element modelling of excavation and advancement processes of a shield tunnelling machine", Soils and Foundations, 39 (3), 37–52

Ladd, C.C., Moh, Z.C., and Gifford, D.G, (1971)"Undrained Strength of Soft Bangkok Clay" Proceeding of Forth Asian Regional Conference on Soil Mechanics and Foundation Engineering, 1 , 135-140

Lambrughi, A., Medina Rodríguez, L., Castellanza, R. (2012) "Development and validation of a 3D numerical model for TBM–EPB mechanised excavations" Computers and Geotechnics, 40, 97–113

Laver, R.G. & Soga, K. 2012. Numerical simulation of long-term twin-tunnel behavior at St James's Park. Proc. Geotechnical Aspects of Underground Construction in Soft Ground, Rome, Ed. G. Viggiani, Balkema, 395-402.

Layman, R. (2011) "Short term vs. long term thinking: transit, the Washington Examiner, Fairfax/Loudoun Counties vs. DC", http://urbanplacesandspaces.blogspot.com/

Lyamin, A.V., and Sloan, S.W. (2002)(1) "Lower bound limit analysis using nonlinear programming" , International Journal for Numerical Methods in Engineering, 55(5), 573–611

Lyamin, A.V., and Sloan, S.W. (2002)(2) "Upper bound limit analysis using linear finite elements and nonlinear programming", International Journal for Numerical and Analytical Methods in Geomechanics, 26(2), 181–216.

Macklin, S. R. (1999) "The prediction of volume loss due to tunneling in overconsolidated clay based on heading geometry and stability number", Ground Engineering, April UK

Maidl, B., Herrenknecht, M., Anheuser, L. (1996) "Mechanised Shield Tunnelling", John Wiley & Sons, Technology & Engineering

Maidl, B., Herrenknecht, M., Maidl, U., Wehrmeyer, G. (2013) "Mechanised shield tunneling" John Wiley & Sons

Mair, R. J., Gunn, M. J. and O'Reilly, M.P. (1981) "Centrifuge testing of model tunnels in soft clay", Proc. 10th International Conference on Soil Mechanics and Foundation Engineering, Stockholm, Balkema, 1,323-328

Mair, R. J., Taylor, R. N. and Bracegirdle, A. (1993) "Subsurface settlement profiles above tunnels in clay", Geotechnique, 43 (2), 315-320

Mair, R.J. (1999) "Design and construction of tunnels in soft ground",Proceedings of the XIIth European Conference on Soil Mechanics and Geotechnical Engineering, Amsterdam, 3, 1915-1921

Mair, R.J. , Taylor, R.N.,Burland, J.B. (1996) "Prediction of ground movemetns and assessment of risk of buildings damage due to bored tunnelling , In: Mair, R.J. and Taylor R.N (eds), Geotechnical aspects of underground construction in soft ground, Proc. Int. Symp.,London, Rotterdam: Balkema

Mair, R.J. and Taylor, R.N. (1997) "Board tunneling in the urban environment", Proc. 14th International Conference on Soil Mechanics and Foundation Engineering, Hamburg, Balkema, 2353-2385

Marshall, R., Farrell, R., Klar, A., Mair, R. (2012) "Tunnels in sands: the effect of size, depth and volume loss on greenfield displacements" Geotechnique, 62, 385-399

Melis, M. (1997) "A selection and specifications of the EPB tunnelling machines for the Madrid Metro extension", Jornadas Tecnicas sobre la ampliacion del Metro de Madrid. Fundacion AgustÃn de Bethencourt y Comunidad de Madrid, Madrid, (1)

Melis, M., Medina, L., Rodríguez, J.M., (2002) "Prediction and analysis of subsidence induced by shield tunneling in the Madrid Metro extension" Canadian Geotechnical Journal, 39 (6), 1273-1287

Merritt, A.S., Mair, R.J. (2008) "Mechanics of tunnelling machine screw conveyors: a theoretical model" Géotechnique, 58(2), 79-94.

Möller, S.C. (2006) "Tunnel induced settlements and structural forces in linings" Doctoral thesis, Institute of Geotechnical Engineering, University of Stuttgart

Mollon G, Dias D, Soubra A.H. (2009) "Probabilistic analysis of circular tunnels in homogeneous soils using response surface methodology". Journal of Geotechnical and Geoenvironmental Engineering (ASCE), 135(9), 1314–1325

Mollon G, Dias D, Soubra A.H. (2010) "Face stability analysis of circular tunnels driven by a pressurized shield" Journal of Geotechnical and Geoenvironmental Engineering (ASCE), 136(1), 215–229.

Mollon, G., Dias, D., Soubra, A.H., (2010) "Rotational failure mechanisms for the face stability analysis of tunnels driven by a pressurized shield" International Journal for Numerical and Analytical Methods in Geomechanics, 35(12), 1363–1388

Morgenstern, N. R., Price, V. E. (1965) "The analysis of the stability of general slip surfaces" Geotechnique, 15(1), 79-93

Nagel, F., Meschke, G. (2011) "Grout and bentonite flow around a TBM: Computational modeling and simulation-based assessment of influence on surface settlements", Tunneling and Underground Space Technology, 26, 445-452

NFM Technologies (2017) "Soft ground machines", Retrieved from http://www.nfm-technologies.com/-Soft-ground-machines-.html

Nunes, M.A., Meguid, M.A., (2009) "A study on the effects of overlying soil strata on the stresses developing in a tunnel lining" Tunnelling and Underground Space Technology, 24(6), 716-722

Ong, C.W., Ee, J.P., Su, T., Yong, K.Y., Kulaindran, A., (2016) "A case study of twin bored tunnelling under mixed-face soil - Bendemeer MRT station project (Downtown Line 3), Singapore" The 15th Asian Regional Conference on Soil Mechanics and Geotechnical Engineering

Panet, M. and Guenot, A. (1982) "Analysis of convergence behind the face of a tunnel", Tunnelling'82, London, 197-20

Peck, R. B. (1969) "Deep Excavations and Tunnels in Soft Ground" Proceedings of the 7th International Conference on Soil Mechanics and Foundation Engineering, Mexico City, State of the Art Volume, 225-290.

Pestana, J.M. and Whittle, A. J. (1999) "Formulation of a unified constitutive model for clays and sands" International Journal for Numerical and Analytical Methods in Geomechanics, 23(12), 1215–1243

Pinto, F. (1999) "Analytical methods to interpret ground deformations due to soft ground tunneling", MSc Thesis, Dept. of Civil & Environmental Engineering, Massachusetts Institute of Technology

Pinto, F. and Whittle, A. J. (2013) "Ground movements due to shallow tunnels in soft ground: 1. Analytical solutions", ASCE Journal of Geotechnical and Geoenvironmental Engineering

Pinto, F., Zymnis, D. M. and Whittle, A. J. (2013) "Ground movements due to shallow tunnels in soft ground: 2. Analytical interpretations and predictions", ASCE Journal of Geotechnical and Geoenvironmental Engineering

Potts, D.M., Addenbrooke, T.I. (1997) "A structure's influence on tunnelling-induced ground movements", Geotechnical Engineering, ICE, 125(2), 109-125.

Pourtaghi, A. and Lotfollahi-Yaghin, M.A. (2012) "Wavenet Ability Assessment in Comparison to ANN for Predicting the Maximum Surface Settlement Caused by Tunneling" Tunnelling and Underground Space Technology, 28, 257-271.

Roby, J., Willis, D. (2014) "Achieving Fast EPB Advance in Mixed Ground: A Study of Contributing Factors" North American Tunneling 2014 Proceedings, 182-194

Sagaseta, C. (1987) "Analysis of undrained soil deformation due to ground loss", Geotechnique, 37 (3), 301-320

Salvucci, F.P. (2003) "The "Big Dig" of Boston, Massachusetts: lessons to learn", 29th ITA World Tunnelling Congress, Amsterdam, Claiming the Underground Space, Vol 1 and 2, 37-41

Savidis, S. A., and Rackwitz, F. (2004) "Geotechnical and environmental consideration by planning and construction of the transportation infra-structure in the centre of Berlin. "Proc., 5th Int. Conf. on Case Histories in Geotechnical Engineering , Paper 5.32, University of Missouri-Rolla, Rolla, MO

Schmidt, B. (1969) "Settlement and ground movement associated with tunnelling in soils", PhD Thesis, University of Illinois, Urbana

Seah, T. & Lai, K. (2003). Strength and Deformation Behavior of Soft Bangkok Clay. Geotechnical Testing Journal, 26(4), 421-431.

Selemetas D. (2006) "The response of full-scale piles and piled structures to tunnelling", PhD Thesis, University of Cambridge

Sharma, J. S., Chu, J., and Zhao, J. (1999) "Geological and geotechnical features of Singapore: an overview. " Tunnelling and Underground Space Technology 14(4), 419-431.

Shirlaw, J.N. (2008) "Mixed Face Conditions and the Risk of Loss of Face in Singapore" International Conference on Deep Excavations (ICDE 2008)

Sitarenios, P., Litsas, D., Kavvadas, M. (2016) "The interplay of face support pressure and soil permeability on face stability in EPB tunneling" World Tunnel Congress (WTC) 2016, San Fransisco

Sloan, S.W. (1988) "Lower bound limit analysis using finite elements and linear programming", International Journal for Numerical and Analytical Methods in Geomechanics, 12(1), 61–77.

Sloan, S.W. (1989) "Upper bound limit analysis using finite elements and linear programming", International Journal for Numerical and Analytical Methods in Geomechanics, 13(3), 263–282.

Sloan, S.W. (2013) "Geotechnical stability analysis" Geotechnique, 63(7), 531-572

Sloan, S.W., and Assadi, A. (1992) "The stability of tunnels in soft ground" In Proceedings of the Wroth Memorial Symposium on Predictive Soil Mechanics, Oxford, UK, 27–29 July 1992,Edited by G.T. Houlsby. Thomas Telford Ltd., London, 644–663.

Sloan, S.W., Randolph, M.F., (1982) "Numerical prediction of collapse loads using finite element methods", Int. J. Num. Analy. Meth. Geomech. 6, 47-76

Sousa, R.L., Einstein, H.H. (2012) "Risk analysis during tunnel construction using Bayesian Networks: Porto Metro case study" Tunnelling and Underground Space Technology, 27(1), 86-100

Standing, J.R., Burland, J.B. (2006)"Unexpected tunnelling volume losses in the Westminster area, London" Géotechnique, 56(1), 11-26.

Stroud, M. A. (1989) "The Standard Penetration Test - Its Application and Interpretation." Penetration Testing in the UK, Thomas Telford, London.

Su, T. (2015) "Study on Ground Behaviour Associated with Tunnelling in Mixed-Face Soil Condition" PhD Thesis, National University of Singapore, Singapore

Suwansawat, S., (2002) "Earth pressure balance (EPB) shield tunneling in Bangkok: Ground Response and Prediction of Surface Settlements Using Artificial Neural Networks" Doctoral Thesis, Massachusetts Institute of Technology, Cambridge, MA.

Suwansawat, S., and Einstein, H. H. (2006) "Artificial neural networks for predicting the maximum surface settlement caused by EPB shield tunneling" Tunn. Undergr. Space Technol., 21(2), 133–150.

Swoboda, G. (1979) "Finite element analysis of the New Austrian Tunnelling Method (NATM)" Proceeding of the third international Conference on Numerical Method in Geomechanics, Aachen, (2), 581-586

Swoboda, G., Abu-Krisha (1999), "Three-dimensional numerical modelling for TBM tunnelling in consolidated clay", Tunnel Undergr Space Technol, 14, 327–333

Talmon A.M, Bezuijen, A. (2002) "Muck discharge by the screw conveyor of an EPB Tunnel Boring Machine", Proceedings of 3rd International Symposium on Geotechnical Aspect of Underground Construction in Soft Ground, Toulouse, 1, 89-94

Tschuchnigg, F., Schweiger, H. F., Sloan, S.W., Lyamin, A.V., Raissakis, I. (2015) "Comparison of finite-element limit analysis and strength reduction techniques"Geotechnique, 65(4), 249-257

Vermeer P.A., Ruse N.M., Marcher T. (2002) "Tunnel heading stability in drained ground" Felsbau, 20(6), 8-18

Vermeer, P.A., Ruse, N. (2001) "Die Stabilität der Tunnelortsbrust in homogenem Baugrund." In: geotechnik, 24 (3), 186-193.

Verruijt, A. & Booker, J. R. (1996) "Surface settlement due to deformation of a tunnel in an elastic half-space" Geotechnique, 36 (4), 753-756

Verruijt, A. (1997) "A complex variation solution for a deforming tunnel in an elastic half-plane", International Journal for Numerical and Analytical Methods in Geomechanics, 21, 77-79

Vorster, T. E. B., Klar, A., Soga, K. & Mair, R. J. (2005) "Estimating the effects of tunneling on existing pipelines" J. Geotech. Geoenviron. Engng, 131(11), 1399–1410.

Whittle A.J., Sagaseta, C. (2003) "Analyzing the effects of gaining and losing ground," Soil Behavior and Soft Ground Construction, ASCE GSP No. 119, 255- 291

Willis, D., (2013) "Trends in performance of metro sized EPB TBMs: A study of worldwide advance rates" Rapid Excavation and Tunneling Conference 2013 Proceedings, 905-913

Wilson, D.W., Abbo, A.J., Sloan, S.W., Lyamin, A.V. (2011) "Undrained stability of a circular tunnel where the shear strength increases linearly with depth" Canadian Geotechnical Journal, 48 (9), 1328-1342

Wong, PB (2004) "Recommended Tunnel Construction Methods Study", Working Paper, Rev. 0

Woods, E., Battye, Bowers, K., Mimnagh , F. (2007) "Channel tunnel Rail Link section 2: London tunnels", Proceedings of the ICE - Civil Engineering, 160(6) , 24 –28

Yu, H.S. & Rowe, R.K. (1999) " Plasticity solutions for soil behavior around contracting cavities and tunnels" International Journal for Numerical and Analytical Methods in Geomechanics, 23(12), 1245-1279.

Zhang, D., Huang,H., Hu,Q., Jiang, F.(2015) "Influence of multi-layered soil formation on shield tunnel lining behavior" Tunnelling and Underground Space Technology, 47, 123-135

Zhao, J., Gong, Q.M., Eisensten, Z. (2007) "Tunnelling through a frequently changing and mixed ground: A case history in Singapore" Tunnelling and Underground Space Technology, 22(4), 388-400

Zymnis. D.M., Chatzigiannelis, I. & Whittle, A.J. (2013) "Analytical interpretation of ground movements caused by JLE tunnel construction in St James Park," Géotechnique.

Appendices

A. Evaluation of 3D FE Predictions of Ground Movements Caused By EPB Tunneling in Stiff Clay

Since their introduction in the 1970's, closed-face Earth Pressure Balance (EPB) machines have become widely used for soft ground tunnel construction. The EPB design relies on a screw conveyor system to regulate the pressure of the excavated soil/spoil within the head chamber and hence control stability at the face of the machine. One of the key design issues in the application of EPB machines is to establish how control parameters, including the advance rate, face pressure and grouting processes (used to compensate for the tail void at the rear of the shield and to infill gaps between the precast lining rings and surrounding soil) affect and/or control the far-field ground movements. For closed-face systems, short-term deformations are associated with ground losses at the face, overcutting and ploughing of the shield and poor control of grouting in the tail void; while long-term deformations can occur due to consolidation and creep within the surrounding soil (and are closely connected to the seepage boundary conditions;e.g., Laver & Soga, 2012). The control parameters for advancing the EPB machine can have a significant effect on the magnitude and distribution of the far-field deformations. Therefore, analyses of the ground response to tunneling require accurate modeling of the soil stratigraphy and constitutive behavior as well as the construction process. Finite element (FE) methods have been used to simulate tunnel construction since the early 1980s, but only a few studies involved three-dimensional modelling of mechanized tunneling (e.g., Finno and Clough 1985; Bernat and Cambou 1999; Swoboda and Abu-Krisha 1999; Dias et

al., 2000; Melis et al., 2002; Kasper and Meschke 2004; Möller 2006). In order to get a better understanding of the effect of the construction process and soil properties on the development of the ground deformations more comprehensive models of tunnel excavation and tunnel support are required in order to capture the 3D nature of mechanized tunneling and the effect of construction parameters such as advance rate, face and grout pressure.

The various models developed over the last decade, simulate the tunnel excavation with a step-wise procedure, where each step represents a fixed incremental advance equal to the width of the lining rings (or fraction thereof). The TBM is represented either as an advancing solid body (Kasper and Meschke 2004) or in a simplified process of element activation (Moller, 2006). A detailed representation of the tunneling process is important but simplified models have shown to yield equally good results with less computational effort (Founta et al. 2013). As a result, it is important to identify the key parameters necessary to achieve realistic predictions of tunnel-induced ground movements in order to achieve a balance between predictive capability and computational time/effort.

This paper evaluates the capabilities of a 3D finite element model, using a step-wise element activation approach (similar to Möller, 2006) to predict measured ground movements caused by EPB tunneling in a stiff, low permeability London clay for the Crossrail project. The current analysis considers a greenfield site beneath Hyde Park (Figure A.1a) and focuses on a 100m trajectory for the Westbound (WB) tunnel bore passing beneath a well instrumented section. The Crossrail project and the Hyde Park site instrumentation are described in detail by Ieronymaki et al. (2015). At this location the tunnel has a cover depth of 30m (33.5 m to

springline) and is excavated within the London Clay by an EPB machine (7.1 m diameter cutting wheel and 12 m long tapered steel shield). The mechanical properties of the London Clay are represented by a simple elastic, perfectly plastic soil model M-C (Mohr-Coulomb), that was calibrated to results of high quality laboratory shear tests.

The FE element model was developed with Plaxis 3D^{TM} software based on the dimensions and stratigraphy of the Hyde Park area using a simplified soil profile, Figure A.1b, comprising three soil units. The two upper units: Made Ground/Langley Silt and River Terrace are relatively permeable and are described using a linearly-elastic, perfectly-plastic; Mohr-Coulomb (M-C) soil model with drained effective stress properties, while the London Clay was simulated using the M-C model with undrained shear strength varying linearly with depth (Figure A.1c). The finite element model assumes undrained shear conditions within the clay (i.e., there is no migration of pore water within the clay mass over the time frame of tunnel construction), the groundwater table is coincident with the ground surface, initial pore pressures are hydrostatic within the clay and in-situ stresses are characterized by K_0 = 1.0 (based on site investigation data reported by GCG, 2010). Figure A.1d summarizes the soil properties used in the FE model

Figure A.2 depicts the internal boundary conditions used to represent the conical shape of the EPB tunnel-boring machine in the Plaxis 3D FE model. The 12 m long shield is represented by a set of 8 x 1.5 m long, curved plate elements to which appropriate contraction boundary conditions are applied in order to match the unstressed dimensions of the EPB shield. The 500 T weight of the shield is applied as a uniformly distributed load at the surface of the activated plate elements representing the shield. The FE model assumes symmetry by considering a half

section of the circular tunnel bore, with a rigid boundary at the base of the London clay (depth, 60 m) and a far field lateral boundary located 300 m from the tunnel centerline (to ensure accurate representation of far field ground movements). The model assumes no lateral displacements along the exterior vertical boundaries of the mesh. The face conditions are represented through a face pressure that increases hydrostatically with depth, with a selected value of P_g =180 kPa at the crown, based on the control data measured for the WB Crossrail tunnel in Hyde Park (Ieronymaki, 2015).

The simulation of the grout was an essential parameter for realistic representation of the EPB construction process. The basic FE model represents grout activation in two phases:

The freshly injected grout is assumed to behave as an incompressible fluid with very low stiffness and a unit weight 15 kN/m^3. This stage is assumed to extend over one tunnel segment (based on the tunnel advance rates and the reported grout setup properties), and is represented through a hydrostatically increasing radial pressure with an average value of P_g=140 kPa at the crown, based on the measured grout pressure in the Hyde Park (Ieronymaki, 2015).

In the hardened state the grout is simulated by activating solid elements along with cylindrical plate elements representing the lining to capture the grout-lining-soil interaction. Figure A.1e lists the lining properties and the set of grout properties derived from grout laboratory tests from the Crossrail project (BFK, 2012). The simulation of the EPB shield is one of the more challenging parts in the current numerical simulation. The 3D finite element model was created using Plaxis 3D (based on infinitesimal strains). The FE model assumes that there is no gap

between the surrounding soil boundaries and the front part of the EPB shield. The soil surrounding the middle and tailskin sections of the shield is assumed to follow a linear deformation path (conical surface) between the contact points with the shield (contracting in diameter from 7.08 m at the face to 7.05 m at the tail of the shield), Figure A.2. At the tail void there is a step change in diameter of 0.25 m (7.05 m to 6.80 m external diameter of the unstressed lining). The face of the EPM machine has the tendency to sink due to its weight distribution (the shield is heavier at the face to support the cutter head). As a result the shield ploughs through the soil in order to follow the predefined trajectory, while the current analysis assumes the machine follows a perfectly horizontal trajectory.

The goal of this 3D finite element model was to evaluate the accuracy of the predicted tunnel-induced ground movements for the case of mechanized construction in stiff clay. The predictions are evaluated through comparison with measured data of instrumented sections from the Crossrail Project. Ground deformations are examined along the longitudinal mid-plane of the FE model (x = 0 m) and at the mid plane transversal section y=0 (see Figure A.3), where results are least affected by the proximity to boundaries of the model.

Figure A.4a and b compare the computed residual vertical and horizontal components of surface deformations along the transverse mid-plane of the FE model (y = 0 m), when the EPB machine has advanced 75 m (i.e., y/D= 10.7, where D is the nominal diameter of the tunnel) beyond the instrumented cross-section. In terms of surface settlements, the computed centerline settlement of u_{z0} = 6.3 mm matches closely with the measured centerline settlement of 6.8 mm. However, the analysis overestimates the far-field settlements (x > 20m) by 1.0-1.5

mm. In terms of lateral displacements, the analysis seems to overestimate the displacements interpreted from inclinometer measurements (especially for the far field). The FE model produces a maximum displacement of u_x = 3.7 mm at x=30m. The maximum measured displacement is u_x = 2.9 mm at x=12 m and compares very well with the computed displacement of u_x = 3 mm at the same location. The small overestimation of the residual displacements in the far field can be partially attributed to the simplicity of the M-C soil model and the modelling approach for the excavation. Similar analyses conducted with a more complex soil model (Founta and Whittle, 2016) have shown improvement in capturing the shape of the surface settlement trough.

Figure A.5 presents the development of surface settlements above the centerline of the tunnel as the EPB traverses past the monitored location. The FE predictions are compared to data measured at 8 cross-sections within Hyde Park area (Ieronymaki, 2015) in order to get a better evaluation of the longitudinal settlement trough. Initially, very small settlements ($u_z \leq 2.5$ mm) occur as the EBP advances towards the mid-plane of the model (y/D = 0). The settlements increase significantly with the passage of the shield (y/D = 0 to 1.7) and continue to develop until they converge to the constant value of 6.3 mm after y/D>5. Although there is significant scatter in the measured data, the FE model provides a good prediction of the longitudinal settlement trough. The 3D model seems to capture accurately movements ahead of the EPB face (y/D<0) and during the shield passage (y/D = 0 to 1.7), while it stays within the data range but closer to the lower bound for measurements behind the shield (residual settlements). Overall, the FE model provides good predictions for surface displacements in the vicinity of the tunnel (x<10-15m), but overestimates the far field surface movements.

Figure A.6 a and b compare the computed subsurface deformations with measurements from multi-point extensometers and inclinometers at a well-instrumented section (F) in Hyde Park. The FE model is generally in very good agreement with measured sub-surface settlements above the tunnel axis (Fig. 6a). Data from EX4 (6 m offset from centerline) shows that the model tends to overestimate the settlements close to the tunnel lining and that the model anticipates heave below the springline (where the extensometer shows small settlements). These results reflect limitations in soil behavior modeling within the zone of yielding close to the tunnel lining (due to underestimation of the unloading modulus).

Comparisons with horizontal subsurface measurements, Figure A.6b, suggest that the FE model generally overestimates lateral movements within the clay (especially at elevations close to the tunnel springline (IN3 and IN4). However, these results are clearly affected by the boundary conditions: The inclinometers extend to a depth of 42 m where it is assumed that there is zero lateral displacement, while the FE model predicts significant inward movements at this elevation (6 – 7 mm). This mismatch can explain discrepancies for IN4 but the model clearly overestimates movements for IN3 (offset 6 m from the centerline of the tunnel). Hence, it appears that the FE model consistently overestimates the magnitudes of deformations in the near field around the tunnel partially due to the simplicity of the M-C model and/or other approximations in the boundary conditions of the model.

Numerical 3D finite element predictions of short-term (i.e., undrained) tunnel-induced ground deformations have been obtained by simulating the construction of the Westbound Crossrail tunnel in London Clay at a greenfield site 30m below the ground surface in Hyde Park. The FE

model uses the simple M-C soil model (calibrated for London Clay) and measured control parameters for the EPB tunnel boring machine. Comparisons with the measured ground movements show that the 3D FE model is capable of predicting the magnitude of the surface settlement above the centerline of the tunnel, but slightly overestimates far-field surface movements. Results in the sub-surface show good agreement with vertical displacements measured by extensometers. Overestimation of measured lateral displacements is partly due to discrepancies in the datum used for interpreting inclinometer readings. Overall the model provides a good prediction of the measured displacements due to mechanized tunneling in clay considering the simplicity of the M-C soil model and FE modelling approach. Although, a more comprehensive soil model can improve the predictive accuracy, this appears to have only marginal benefits when considering the additional complexity of the analysis (parameter calibration etc.), especially for a situation with small ground movements.

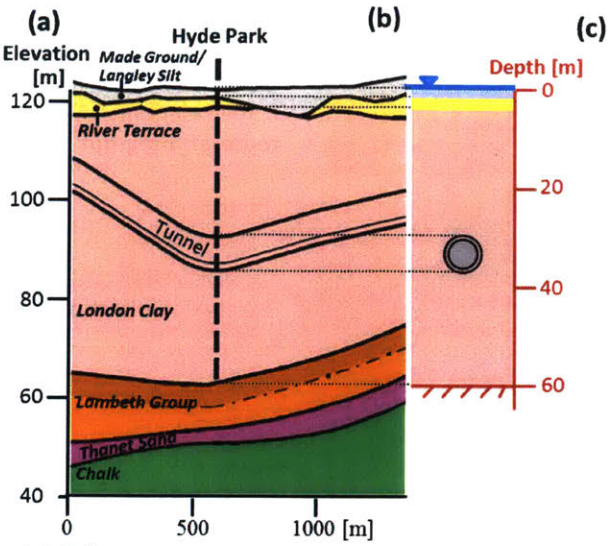

(c)

	Made Ground/ Langley Silt	River Terrace	London Clay
γ (kN/m^3)	19.6	19.6	19.6
c' (kPa) / s_u	0	0	0
ϕ' (°)	25	38	21
ψ(°)	0	0	3
E'_v (MPa)	5	35	15+1.1z
ν'	0.2	0.25	0.244
K_0	1-sinϕ=0.58	0.4	1
k_v (m/s)	10^{-5}	$5*10^{-4}$	--
e_o	0.65	0.5	0.65
Soil model	Mohr-Coulomb (Drained)		M-C (Undrained A)

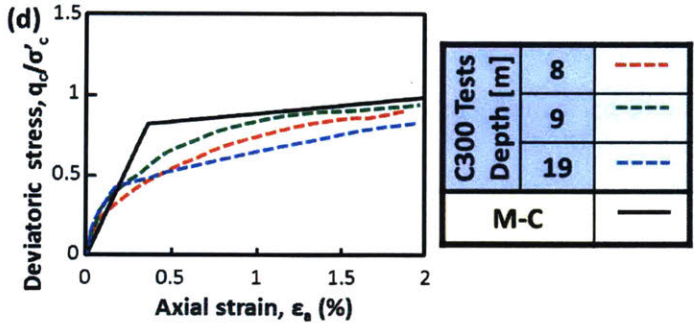

(e)

	Grout	Lining
Material Model	Linear Elastic	Linear Elastic
γ [kN/m^3]	16	25
E' [GPa]	1.5	25.4
ν'	0.20	0.15

Figure A.1 a) Longitudinal section of Crossrail below Hyde Park b) Simplified transverse section c) Soil properties d) Stress-strain curves for M-C vs C300 lab data (GCG, 2010) for London Clay and e) Properties of tunnel lining and grout

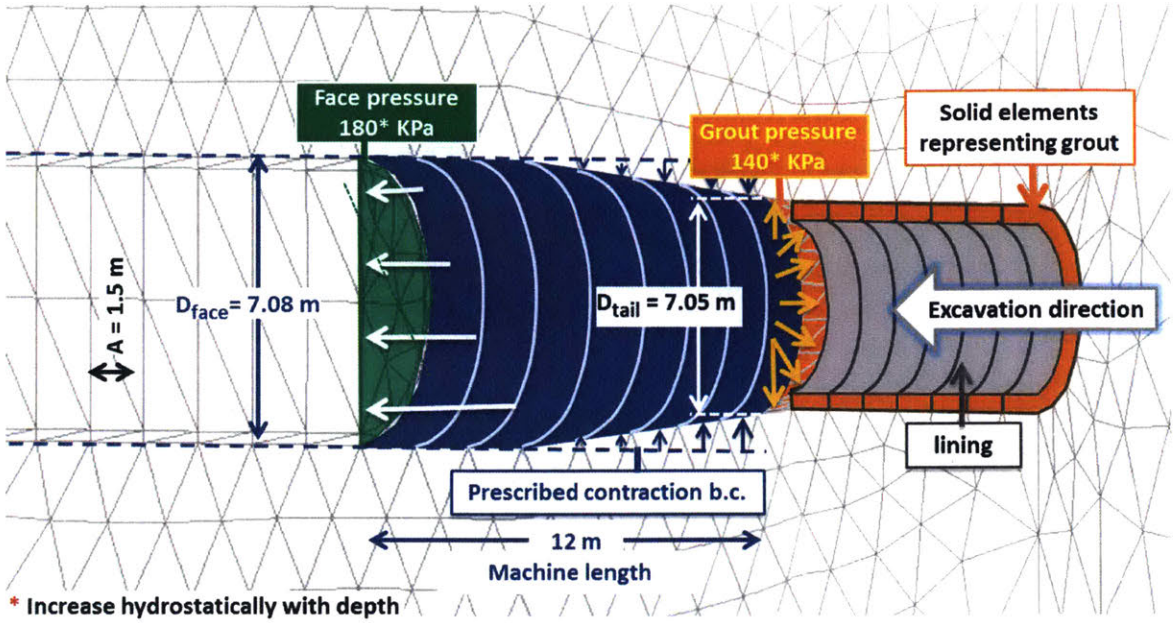

Figure A.2 Schematic representation of the FE basic model used for EPB tunnel construction

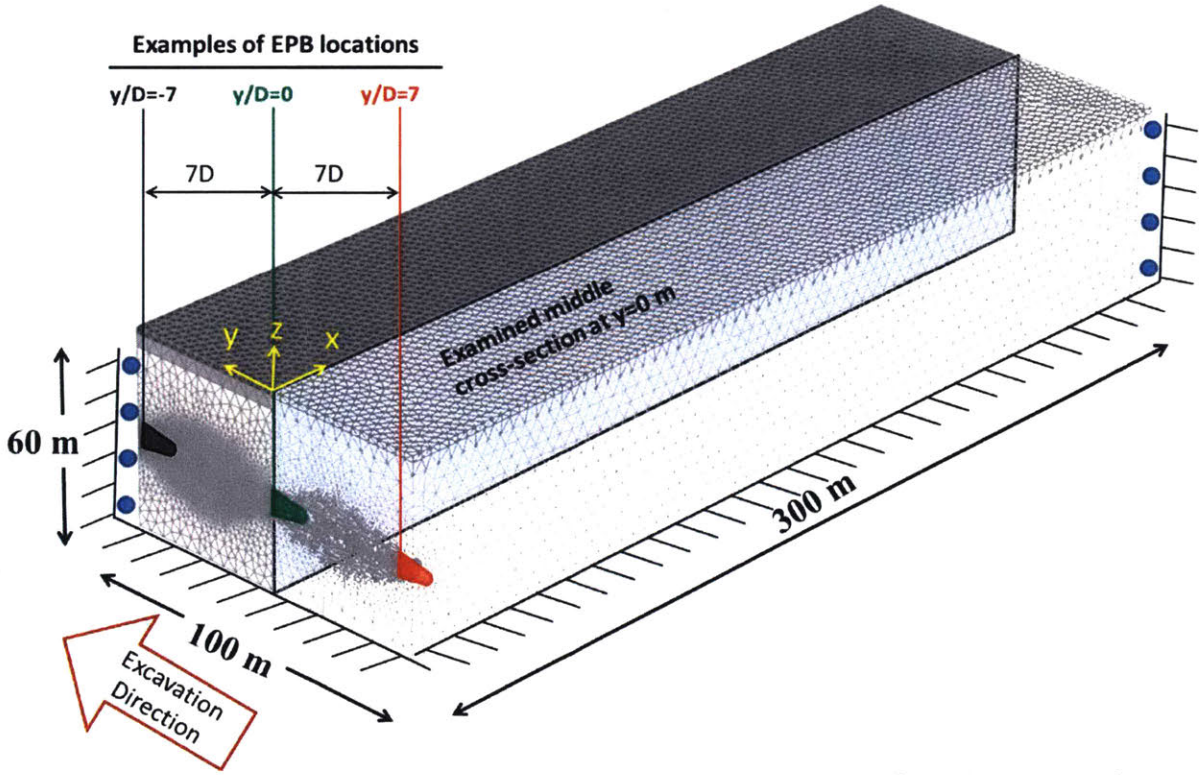

Figure A.3 3D FE model of EPB mechanized tunnel construction for WB Crossrail tunnel model)

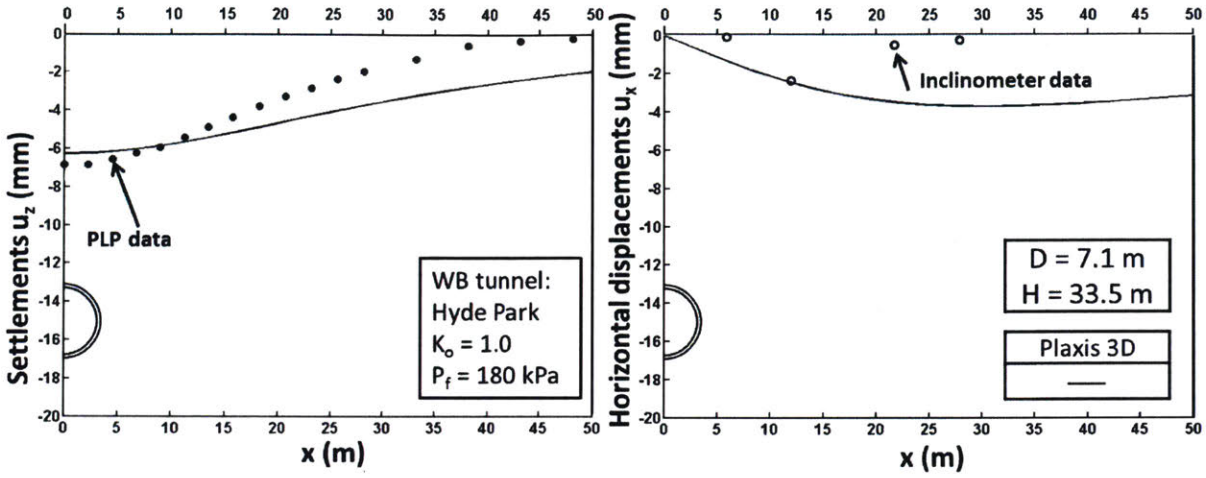

Figure A.4 Comparison of computed and measured surface displacements at the instrumented section due to construction of the WB tunnel

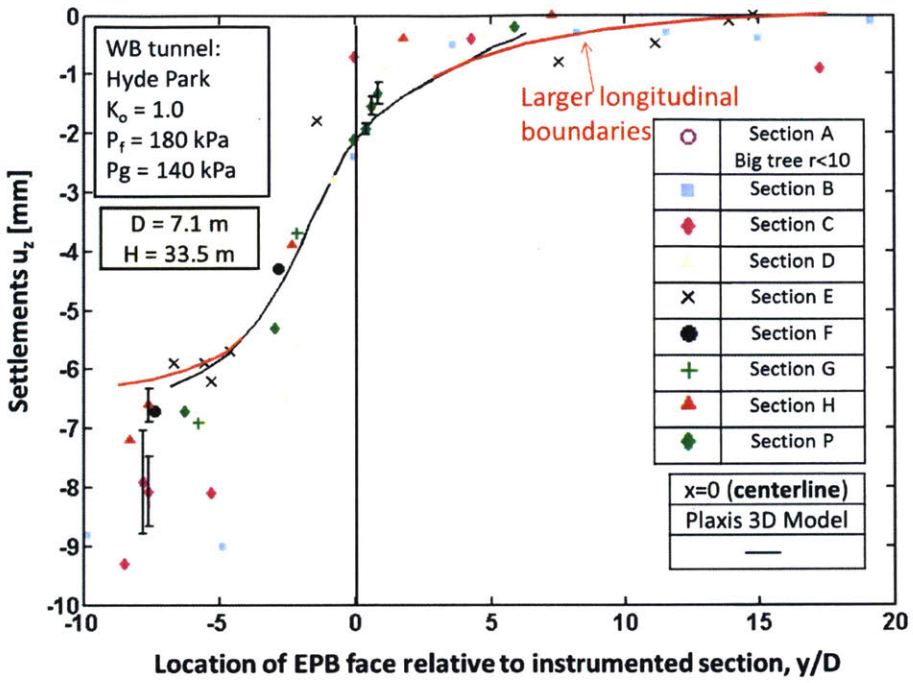

Figure A.5 Surface settlements development above the tunnel centerline as the EPB advances relatively with survey data from a series of transects within Hyde Park

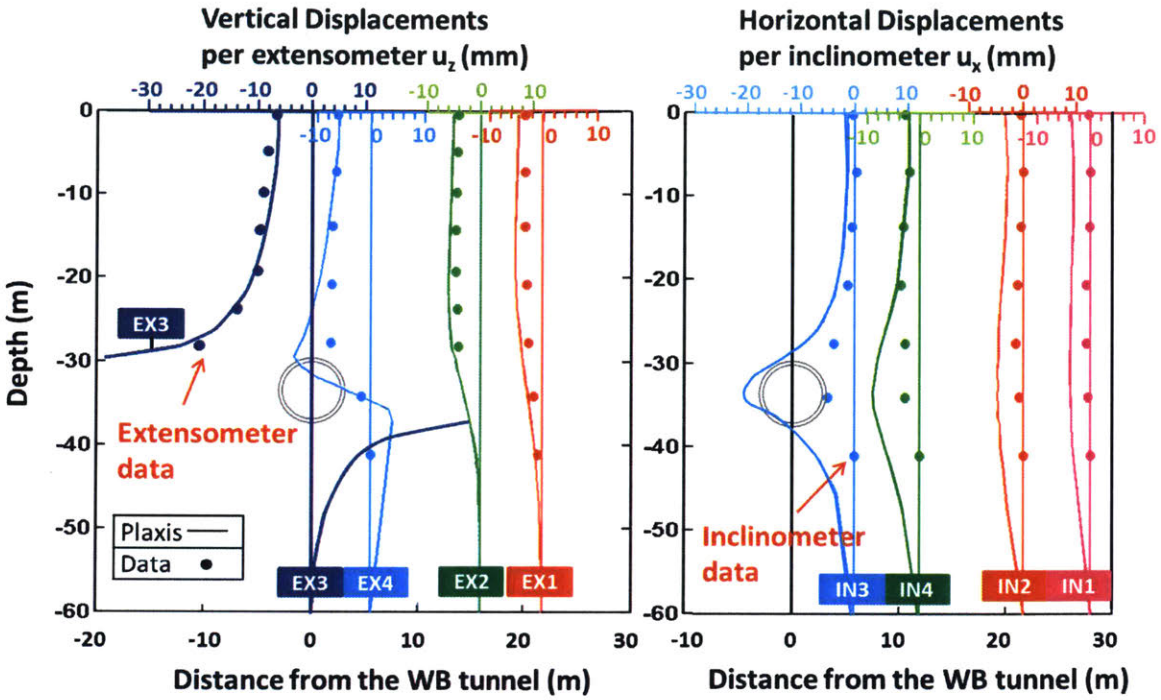

Figure A.6 Comparison of computed and measured subsurface deformations for WB Crossrail tunnel construction at instrumented Section F in Hyde Park; a) Vertical and b) Horizontal components

B. Comparative study and validation of a 3D FE model for representing EPB tunneling in clay using MC and MITS1 soil model

This section performs a comparative study on the performance of the 3D FE model presented in Appendix A for studying effects of mechanized excavation when using two different soil models. A simplified elastic perfectly plastic soil model (Mohr Coulomb) and a more elaborate one (MITS11) are calibrated to capture the London Clay behavior. The FE analyses focus on construction beneath Hyde Park, a 'greenfield' site to model the Westbound (WB) tunnel bore beneath one instrumented Section F (using Position Leveling Points (PLPs), inclinometers, extensometers and piezometers, Figure B.1).

The goal of this study is to assess the efficiency of the FE model and the effect of the considered soil models on the produced predictions. The FE element model was developed using Plaxis 3D software based on the dimensions and stratigraphy of the selected 100m window at the Hyde Park area (Figure 5.5). The model uses a simplified soil profile, Figure B.3, comprising three soil units. The two upper units: Made Ground/Langley Silt and River Terrace are relatively permeable and are described using a linearly-elastic, perfectly-plastic; Mohr-Coulomb (MC) soil model with drained effective stress properties. The London Clay was simulated using two different soil models: 1) the MC model with undrained shear strength varying linearly with depth and 2) the MIT-S1 soil model (Pestana and Whittle, 1999) with input parameters calibrated by Ieronymaki, 2015 corresponding to sub-unit B of the London clay. The finite element model assumes undrained shear conditions within the clay (i.e., there is no migration of pore water within the clay mass over the time frame of tunnel construction), the

groundwater table coincident with the ground surface with hydrostatic initial pore pressures, and in situ stresses are estimated by K0 = 1.0 (based on site investigation data reported by GCG 2010). Table B.1 summarizes the input parameters for the 3 soil units, while Figure B.2 presents a comparison between the behavior of MC and MIT-S1 at the tunnel crown.

Figure B.4 depicts the boundary conditions applied to represent the EPB tunnel-boring machine in the Plaxis 3D FE model. The 12 m long shield is represented by a set of 8 x 1.5 m long curved plate elements to which appropriate contraction boundary conditions are applied in order to match the unstressed dimensions of the shield. The 500 T weight of the shield is applied as a uniformly distributed load at the surface of activated plate elements representing the shield. The FE model (Figure A.3) assumes symmetry by representing a half section of the circular tunnel bore, with a rigid boundary at the base of the London clay (depth, 60 m) and a far field lateral boundary located 300 m from the tunnel centerline (to ensure accurate representation of far field ground movements). The model assumes no lateral displacements along the exterior vertical boundaries of the mesh. The face conditions are represented through a face pressure that increases hydrostatically with depth, with a selected value of p_g =180 kPa at the crown, based on the control data measured for the WB Crossrail tunnel in Hyde Park, Figure 5.3.

The simulation of the grout was an essential parameter for a realistic representation of the EPB construction process. The basic FE model represents grout activation in two phases:

1. The freshly injected grout is assumed to behave as an incompressible fluid with very low stiffness and a unit weight 15 kN/m3. This stage is assumed to extend over one tunnel segment (based on the tunnel advance rates and the reported grout setup properties),

and is represented through a hydrostatically increasing radial pressure with an average value of pg=140 kPa at the crown, based on the measured grout pressure in the Hyde Park (Figure 5.3).

2. In the hardened state the grout is simulated by activating solid elements along with cylindrical plate elements representing the lining to capture the grout-lining-soil interaction. A constant set of grout stiffness properties was derived by accounting for the grout laboratory tests from the Crossrail project (BFK, 2012) for an assumed average excavation advance rate of 0.75 m/h.

The grout stiffness was derived from the grout compressive strength lab tests (Figure B.5a) using the "ACI code" for concrete as an upper bound:

$$Ec = 4700 \cdot (fc)^{\left(\frac{1}{2}\right)} \quad MPa$$

and recommendations of van der Stoel and van Ree, 2000 for jet grouting columns as a lower bound:

$$Ec = 500(fc)^{(2/3)} \quad MPa$$

Based on the excavation data from Westbound Crossrail tunnel in Hyde Park the time required to build a ring is about 2 hours, so each excavation step corresponds to a time step of 2 hrs. As a result the stiffness of the first activated grout ring, located 2 segments (i.e. 3 m) behind the shield, and corresponds to a 2 hour offset. Figure B.5b depicts a comparison between the grout stiffness derived with all the aforementioned methods, as well as the constant set of grout

parameters selected for the finite element model (Table B.2). A constant value of grout stiffness is selected, which is initially closer to the upper bound and moves towards the lower bound for the following ring segments. Additionally a variation of the selected grout stiffness (Figure B.5c) is considered later on, as part of the performed parametric studies to evaluate the sensitive of the results to the grout stiffness.

The simulation of the EPB shield is one of the more challenging parts the current numerical simulation. The Plaxis 3D finite element program was created using Plaxis 3D and assumes infinitesimal strains and does not represent the EPB machine as a distinct structure. There are 3 simplifications used in the current model:

The FE model assumes that there is no gap between the surrounding soil boundaries and surface of the front shield. For the middle shield and tailskin section the soil follows a linear deformation path (conical surface) between the contact points with the shield (with a decreasing diameter from 7.08m to 7.05m over 12 m length of the shield), Figure B.4. At the tail void there is a step change in diameter of 0.25 m (7.08 m to 6.80 m for the unstressed lining).

As the EPB shield advances, shear stresses will develop along the shield-clay interface. In the current Plaxis model, these shear forces are bounded by undrained shear strength of the clay and are generated due soil movements towards the machine. The shear stresses generated due to the advancement of the shield are ignored, since the shield is not simulated as a distinct body. This approach ignores shear tractions at the shield-soil interface. These are expected to be small to ensure efficient advance of the TBM (lubrication was applied throughout ports in the shield)

The face of the EPM machine has the tendency to sink in to the clay due to its weight distribution (the shield is heavier at the face to support the cutter head). In practice, the machine is steered by a set of hydraulic jacks that control displacement rate at 22 locations around the circumference of the shield. The jacks are adjusted to compensate for the pitch of the machine and enable steering along prescribed arcs. The net effect is that the shield trajectory is defined but the machine ploughs through the soil at the centerline of the shield (i.e. is not necessarily horizontal). The current analysis assumes the machine follows a perfectly horizontal trajectory.

The goal of this initial 3D finite element model was to produce reliable predictions of the tunnel-induced ground movements and ultimately to establish how ground movements are related to EPB control parameters. The predictions are evaluated through comparison with measured data of instrumented sections. In order to assess the role of soil modeling, the movements predicted using a relatively advanced soil model, MIT-S1 (that has been well calibrated using laboratory element tests) are compared with results from the much simpler MC model. Ground deformations are examined along the longitudinal mid-plane of the FE model (x/D = 0 m) and at the mid plane transversal section y'/D=0, Figure A.3 (where D is the nominal diameter of the tunnel), where results are least affected by the proximity to boundaries of the model. Results were obtained at three reference locations of the EPB machine (highlighted in Figure A.3):

1. y'/D = 7.1, representing conditions where the EPB shield becomes fully embedded within the FE model

2. y'/D = 0.7 where the tunnel face approaches the central-plane of the model

3. y'/D = -6.8 is when the EPB machine exits the rear face of the FE model.

Figure B.6 compares the vertical and horizontal components of surface deformations along the transverse mid-plane of the FE model (y' = 0 m) at the three reference locations of the EPB machine (Figure A.3) for MC and MIT-S1 soil models for London Clay with measurements from surveys of Position Leveling Points (PLPs). In general, the MC model produces slightly larger far field settlements (x > 25-30m) and smaller centerline settlements compared to MIT-S1. Ahead of the advancing EPB machine (y'/D = 0.7), both models show very similar surface deformations (differing by less than 0.5mm). As the shield moves towards the central plane (y'/D = 0.7 to -6.8), there is a marked change in the surface settlement mode shape for the MIT-S1 model, such that the trough is narrower resulting in a slightly larger settlements for $x \leq 25$-30 m (at the centerline uz0 = 7.4mm for MIT-S1 versus uz0 = 6.3mm for MC) and slightly smaller far field settlements. Similar observations also apply to lateral displacements. The MIT-S1 predicts maximum lateral displacements u_x = 4.7mm at x = 20m from the centerline compared to u_x = 3.7mm at x=30m by MC.

Figure B.6 includes measured data from section F (PLPs and inclinometers) in Hyde Park recorded when the EPB machine has advanced 75 m (i.e. at y'/D= -10.7) past the instrumented cross-section. Comparisons with the finite element predictions show that both models estimate closely the measured centerline settlement (6.8 mm). The MIT-S1 shows a modest improvement in representation of the trough shape. The analyses appear to slightly overestimate the far-field settlements by 1.0-1.5 mm. The MC model seems to achieve a good

match of the inclinometer data close to the centerline, whereas both MIT-S1 and M-C overestimate horizontal surface movements in the far field (x>15 m).

Figure B.7 shows the longitudinal development of surface settlements relative to the EPB face location (y'/D). In this case, predictions are compared to data measured at the 9 cross-sections across Hyde Park area (Ieronymaki, 2015). For the MIT-S1 model, very small settlements (uz ≤ 3.5mm) occur as the EBP advances towards the mid-plane of the model (y'/D = 0.7). The settlements increase significantly with the passage of the shield (y'/D = 0 to -1.7) and continue to develop until they converge to a constant value after y'/D<-5. The MC model gives slightly larger longitudinal displacements for y'/D>2, due to the fact that for small strains the MIT-S1 has a stiffer behavior (Figure B.2). However, as the EPB advances forward approaching the middle cross-section, the strain level increases so MIT-S1 becomes softer due to the strain related stiffness behavior. During the passage of the EPB the settlement rate is similar for the 2 models, as displacements are mainly controlled by the imposed contraction boundary conditions used to simulate the shield, which are the same for the 2 models. As the EPB moves past the examined cross-section, for y/D<-3, the settlement rate decreases and finally becomes almost zero for both cases with MIT-S1 experiencing the slower settlement rate decrease. Although there is significant scatter in the measured data, MIT-S1 seems to capture more accurately movements ahead of the face (y'/D>0), while both models are in reasonable agreement with the measurements behind the shield (residual settlements). Overall, the differences in the representation of the non-linear stress-strain properties between the two models lead to small differences in the evolution of the longitudinal settlement trough.

Figure B.9 summarizes the interpreted tunnel cavity deformation mode shape parameters (ue, ud, Δuz; reported in Figure B.8) computed using the least square method applied to the displacements of the tunnel cavity. Uniform convergence (ue) is the dominant mode shape in the tunnel cavity deformations. This is not surprising given the fact that displacements are controlled primarily by the radial contraction boundary condition imposed along the shield. The results show that for both MC and MIT-S1 models the ovalization mode (ud) is negligible and there is a small translational effect associated with buoyancy (Δuz). The results for MC show a slightly larger residual convergence convergence (ue) and smaller vertical translation (Δuz) compared to MIT-S1. As the EPB approaches the reference cross-section (y'/D = 7 to 0) the two models give identical results for all three deformation parameters, due to the imposed boundary conditions as well as the small scale of the displacements. As the shield is passing from the examined cross-section (y'/D= 0—1.7) (ue) and (ud) remain identical for both MC and MIT-S1 as any difference is cancelled out by the imposed contraction boundary conditions representing the shield, such that for y'/D = -1.7 (the tail of the shield) the two models present essentially the same convergence (uε) and (ud). However as the imposed contraction boundary condition allows for vertical translation (Δuz), we notice that MIT-S1 producing slightly larger downward translation. As the EPB moves past the reference cross-section, the difference in behavior between the two soil models becomes obvious with MC developing a residual (ue) of 30.5mm compared to 27.5mm of MIT-S1. In terms of (Δuz) the initially developed difference during the shield passage now increases, with MIT-S1 translating downward by 6.7mm compared to 5mm for MC. A better understanding of the tunnel cavity deformations is given in Figure B.10, where we can observe the deformed tunnel cavity shape at y'/D = 0.7 (i.e. EPB

passing from the middle cross-section) and y'/D = -6.8 (i.e. exit of the EPB machine from the rear face). We can see that although the two models produce approximately the same inward movement at the crown and MC has a larger volume loss, the MIT-S1 gives slightly larger centerline surface settlement (although it has a smaller volume loss). This difference is associated with the different behavior of the two models that in essence results in small differences in the tunnel cavity deformation modes which propagate to different trough shapes at the surface.

Figure B.11 compares the computed subsurface deformations to those measured at section F. Uncertainties in the measured data are represented by error bars. The two soil models generate similar predictions in terms of lateral and vertical displacements and generally tend to slightly overestimate the measured behavior especially close to the tunnel axis. For y'/D = 0.7 both models achieve an excellent prediction of the observed movements. However, it should be noted that the movements are quite small (comparable to the error) and it is therefore difficult to draw certain conclusions. For y'/D = -6.8, the two models give identical results in the far field in terms of vertical displacements, while close to the tunnel centerline the MIT-S1 generally predicts slightly larger values. Overall, we can conclude that both models achieve very good agreement with the observed vertical subsurface movements. Comparison with horizontal subsurface measurements was produced using only the inclinometer data as is, assuming zero displacements at the base of the end inclinometers. The compared results show non-zero displacements extend below 40 m, hence, there is some remaining mismatch in the average of the measurements. Overall, agreement between the predicted displacements and the data is quite good.

In order to examine the effect of the initial grout stiffness on the computed settlements a slightly altered model was used as depicted in Figure B.12. In the altered model the grout is simulated as a one phase material by activating solid elements representing grout and plate elements representing lining directly behind the tail of the shield. In this way instead of assuming that the fresh grout had zero stiffness, we were able to examine the effect of the early age stiffness on the developed settlements. A plate element, representing the seal at the tail of the EPB was activated to ensure that there will be no leaking of the grout towards the face of the EPB. Figure B.13 shows a comparison of the surface vertical and horizontal displacements for grout stiffness ranging from 15 MPa till 100 MPa (see Figure B.5c) and a poison's ratio of v=0.5 (incompressible) for both MC and MIT-S1 soil models. As expected the settlements decrease as the grout stiffness increases. However we can note that for stiffness higher than 50 MPa the results are almost constant. This value is similar to the ground stiffness at the tunnel depth (52 MPa) indicating that once we reach the stiffness of the surrounding soil any further increase in the grout stiffness will have small or zero effect to the resulting displacements.

We can conclude that the proposed 3D numerical model can achieve good predictions of the measured surface and subsurface settlements. Based on the results, the soil model has a noticeable effect on the observed settlement troughs for both the transverse as well as the longitudinal direction. The small differences between the two soil models can be attributed to their differences in non-linear stress-strain properties. In terms of surface displacements, both MC and MITS1 models achieve a very good match with the measured data (less than 1.5 mm deviation), while MITS1 seems to provide a better representation of the trough shape. In terms

of subsurface displacements, both models show very good agreement with the measured settlements but tend to overestimate the horizontal components close the tunnel that can be partially attributed to the lack of a reference point to reset the inclinometer data. In the parametric studies examining the importance of early age grout stiffness, it was shown that developed settlements were greatly affected when the grout stiffness was lower than that of the surrounding soil, but any increase above that had a small effect on the results.

Finally, although MITS1 gives a slightly better prediction of the induced movements, MC can provide quite reliable results, so it should be used in case we want a quick prediction, especially when we don't have enough data available for the calibration of a more sophisticated model such as MIT-S1.

Table B.1 Soil properties used in Plaxis 3D Finite element model (source: Whittle et al. 2012)

	Made Ground/ Langley Silt	River Terrace	London Clay				
			M-C	MITS1			
γ (kN/m^3)	19.6	19.6	19.6	γ (kN/m^3)	19.6	ψ	2.00
c' (kPa) / s_u	0	0	0	ρ_c	0.4	r	0.00
φ' (^{o})	25	38	21	C_b	600	D_r	0.00
ψ (^{o})	0	0	3	P_{ref}/p_{atm}	12.93	w	1.00
E'_v (MPa)	5	35	15+1.1z	θ	0.45	ω_s	10.00
v'	0.2	0.25	0.244	2G/K	1.235	γ	0.00
K_0	1-sinφ=0.58	0.4	1	K_{oNC}	0.62	h_{po}	0.00
k_v (m/s)	10^{-5}	$5*10^{-4}$	--	Φ'_{cs}	21.0	p	2.80
e_o	0.65	0.5	0.65	m	0.4	e_o	0.65
Soil model	Mohr-Coulomb (Drained)		M-C (Undrained A)	φ_{max}	24.5	p_{atm}	100.0

Table B.2 Properties of tunnel lining and grout

	Material Model	γ [kN/m^3]	E' [MPa]	v'
Grout	Linear Elastic	16	1,500	0.20
Lining	Linear Elastic	25	25,400	0.15

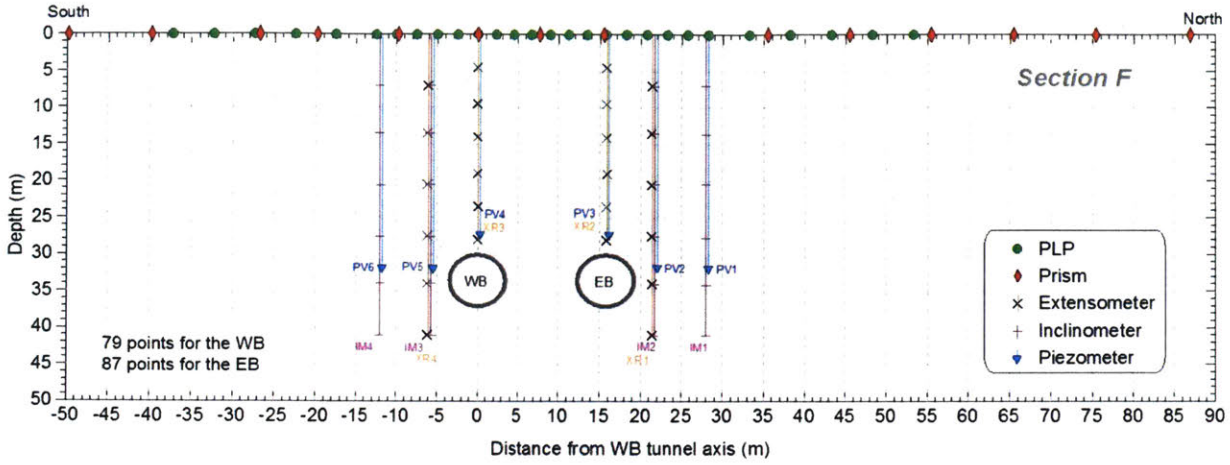

Figure B.1 Location of instrumentation for Section F in Hyde Park (source: Ieronymaki et al., 2015)

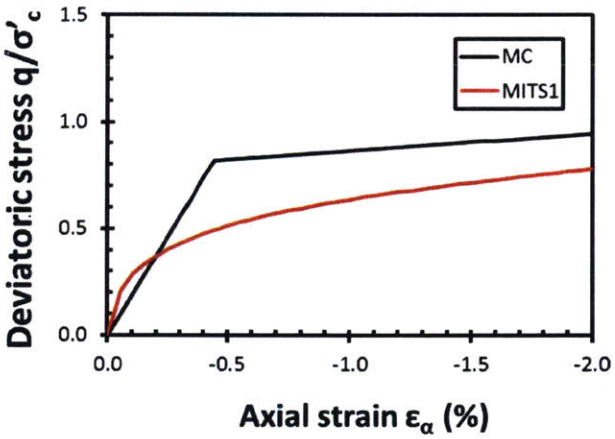

Figure B.2 Comparison of stress strain curves for MC and MITS1 at 30 m depth (crown of the tunnel)

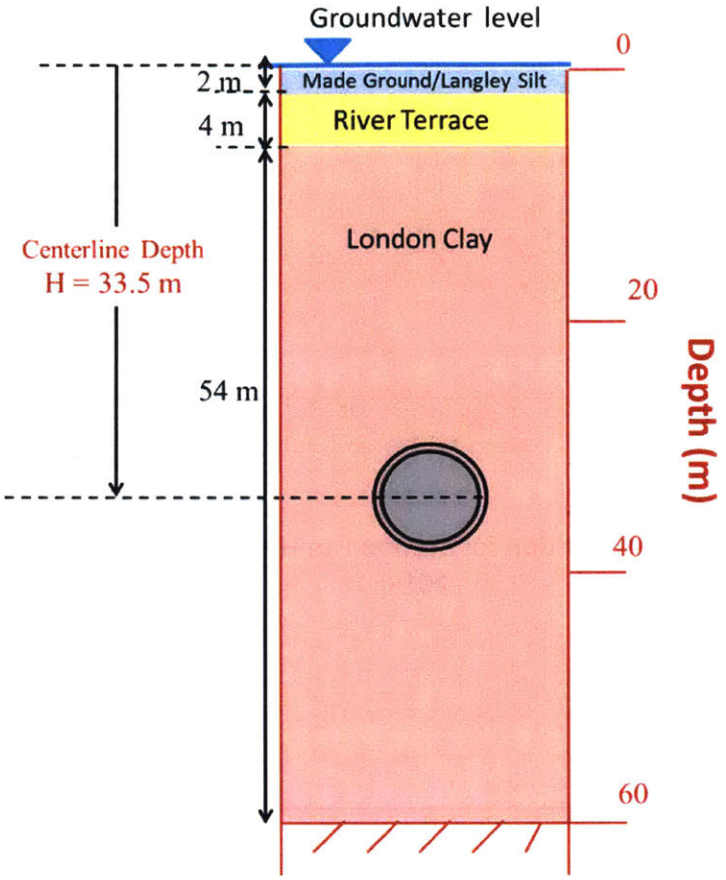

Figure B.3 Simplified soil profile used in Plaxis FE model based on Hyde Park Soil Stratigraphy

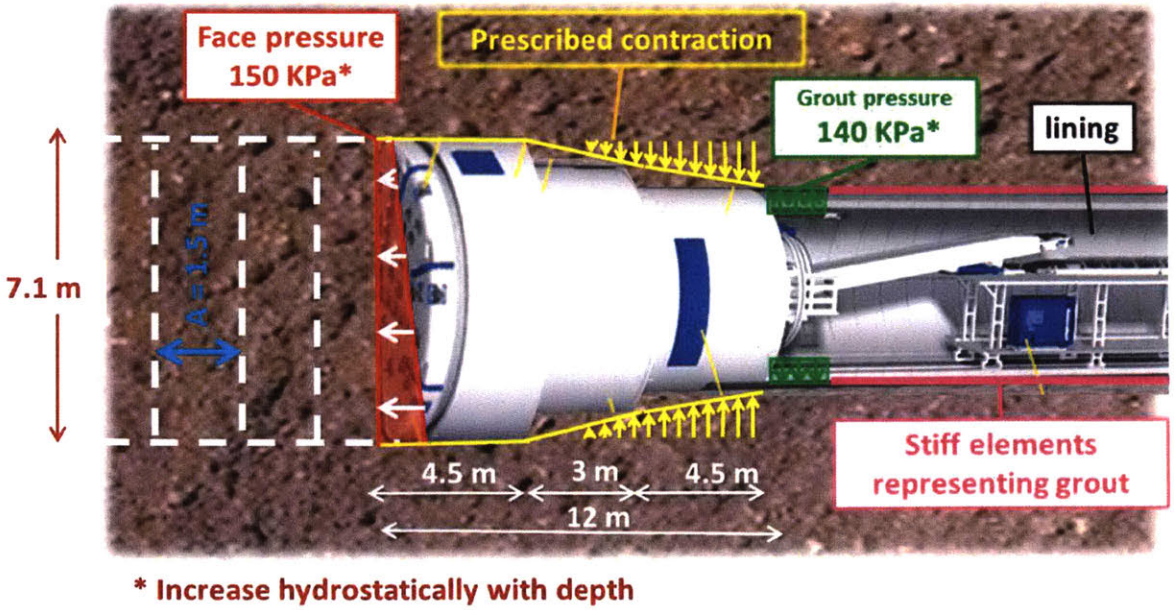

Figure B.4 Schematic representation of the FE basic model used for EPB tunnel construction (modified form FHWA)

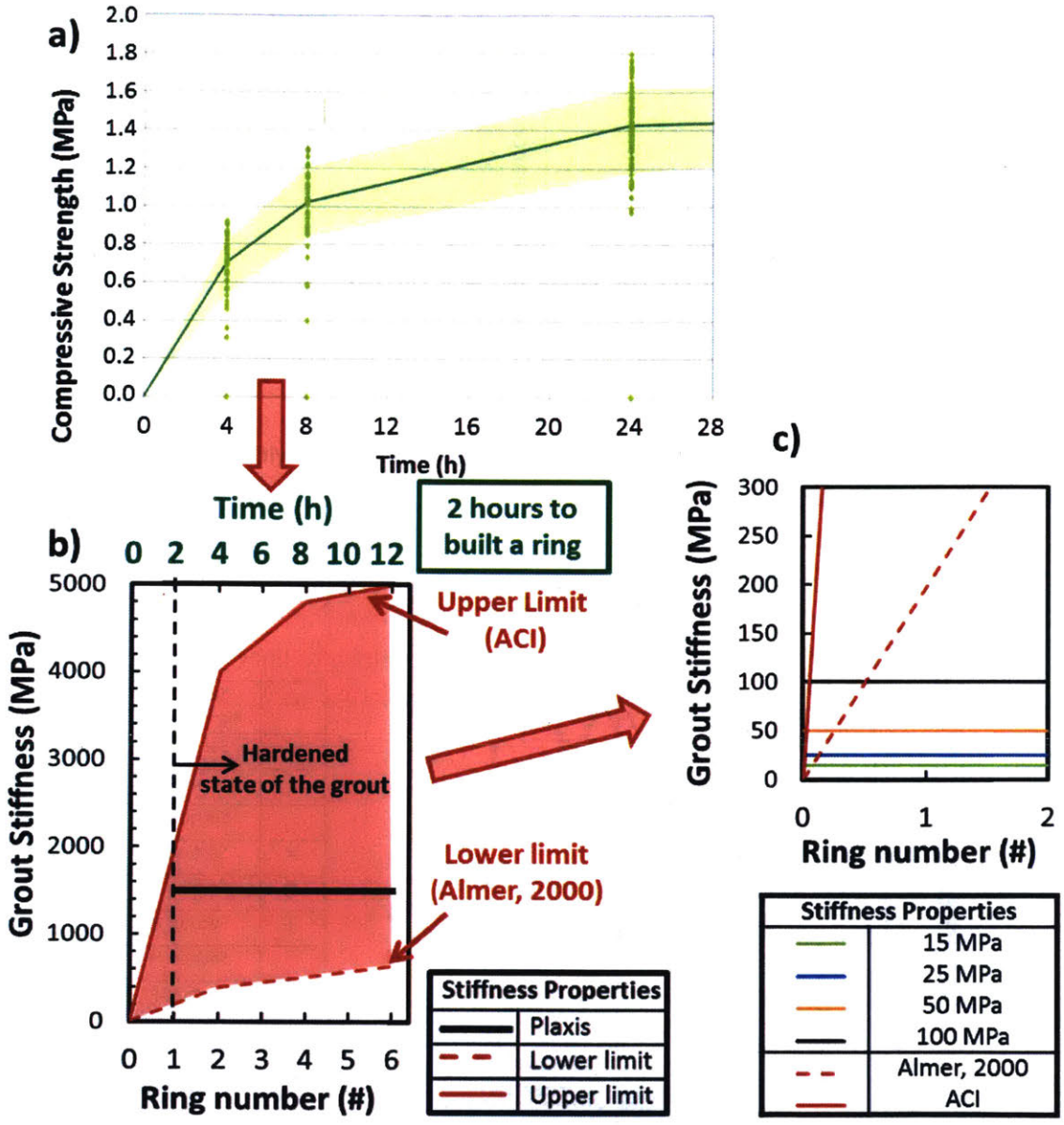

Figure B.5 Grout properties a) Compressive strength as a function of time (h) b) stiffness as a function of time for Van der Stoel and Van Ree (2000) and ACI compared to base case value c) stiffness range for parametric grout stiffness study.(Source: Crossrail Geotechnical report 2012-2013)

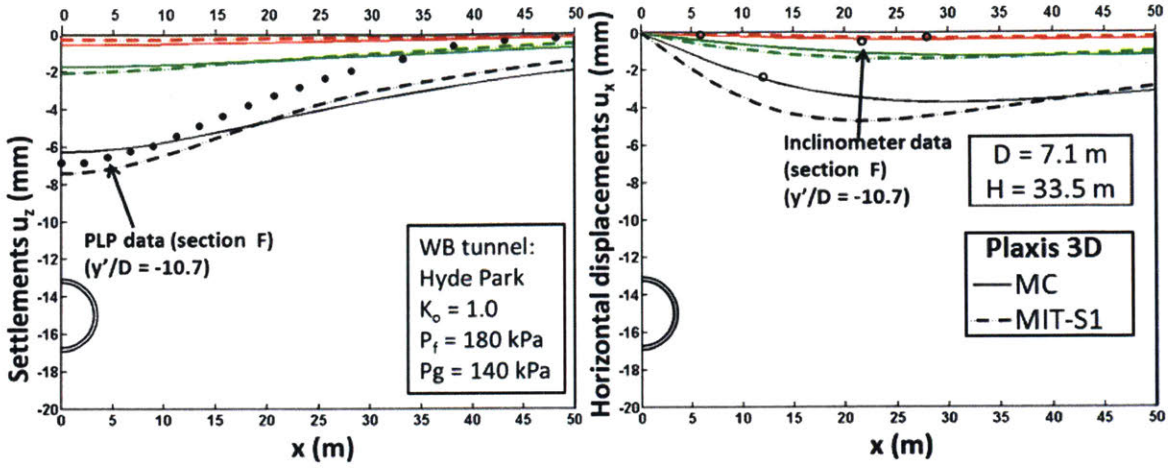

Figure B.6 Comparison of computed surface displacements using MC and MIT-S1 soil models to represent London clay

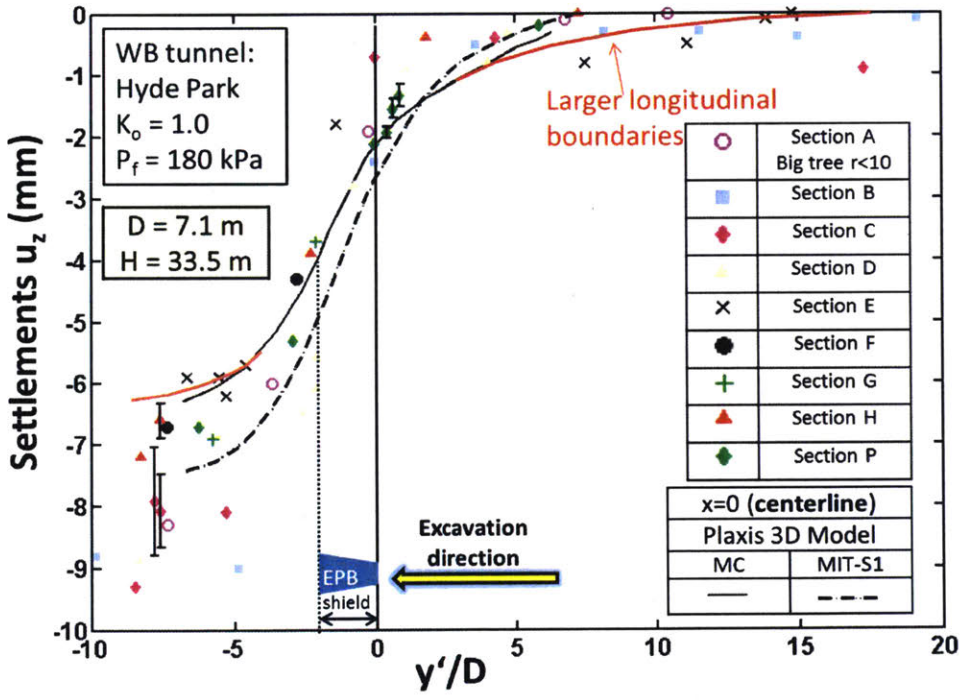

Figure B.7 Development of surface settlements as functions of the EPB face location at the centerline of the mid-plane of FE model for MC and MIT-S1 soil model compared to real data for the Hyde Park area

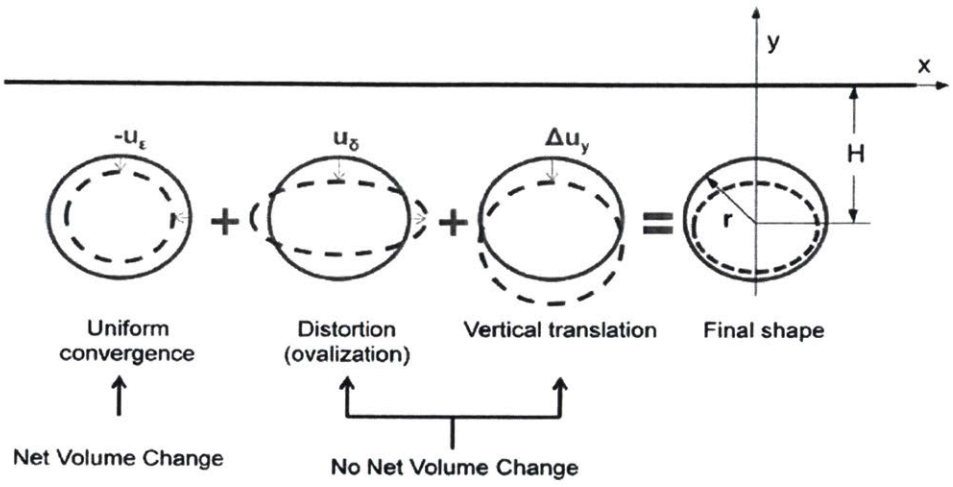

Figure B.8 Deformation modes around tunnel cavity (after Whittle and Sagaseta, 2003)

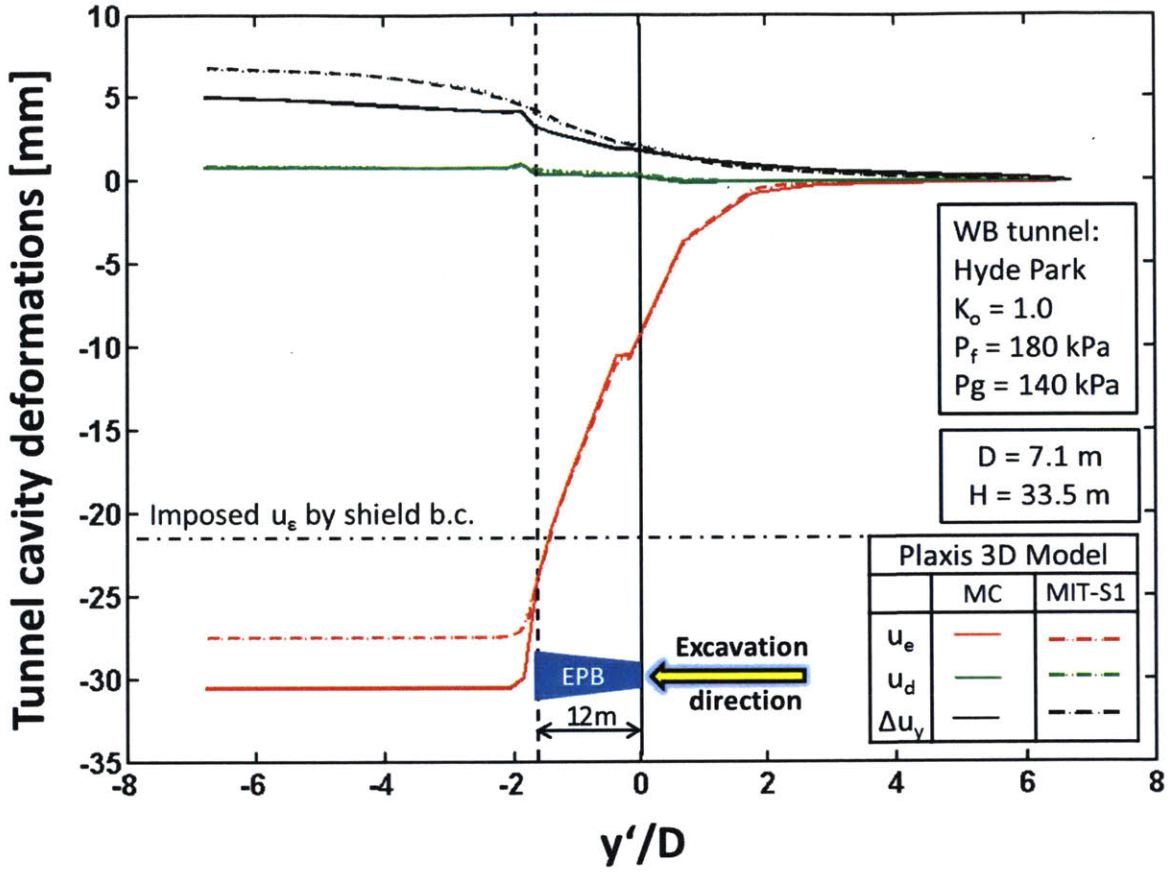

Figure B.9 Development of cavity deformation mode parameters as functions of the EPB face location at the mid-plane of FE model for MC and MIT-S1 soil model

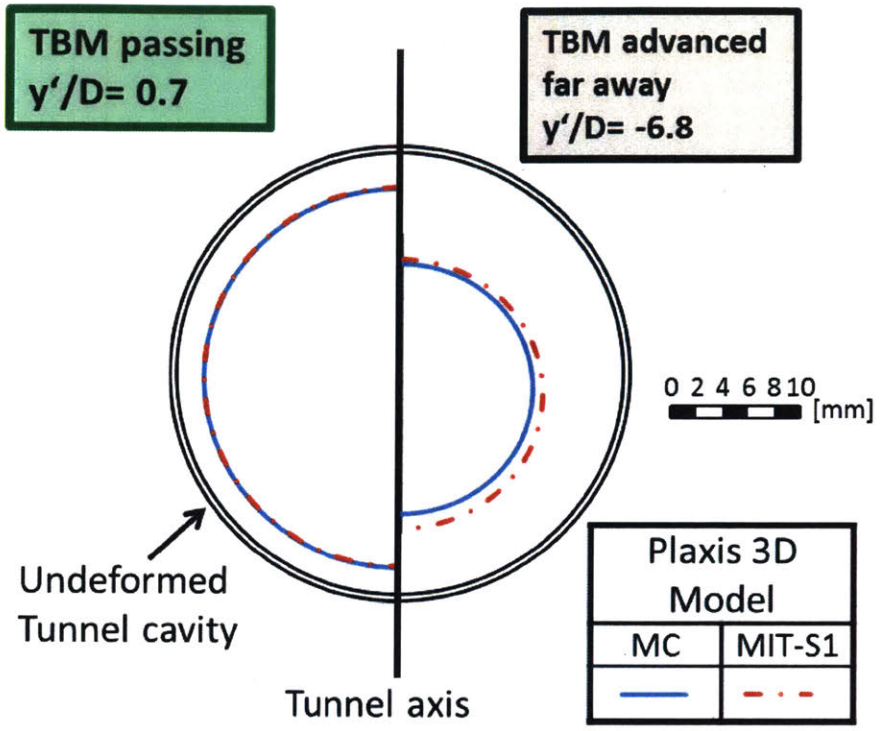

Figure B.10 Tunnel cavity deformations for y'/D=0.7(left) and y'/D=-6.8 (right) at mid-section of the FE model using MC and MIT-S1 soil models.

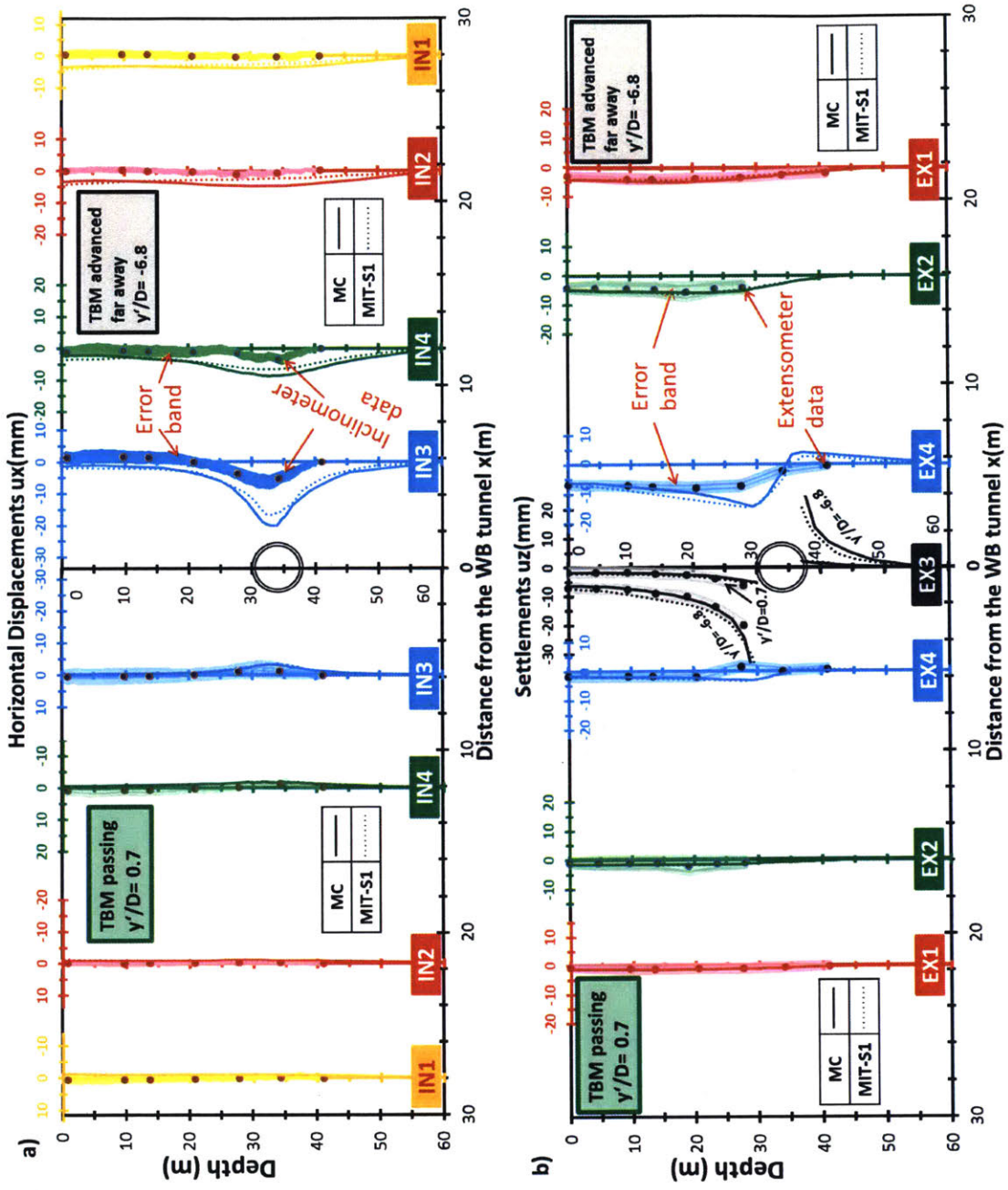

Figure B.11 Comparison of computed subsurface displacements: a) Vertical and b) Horizontal for y'/D=0.7(left) and y'/D=-6.8 (right) at mid-section of the FE model using MC and MIT-S1 soil models to the real data for the Hyde park cross-section F

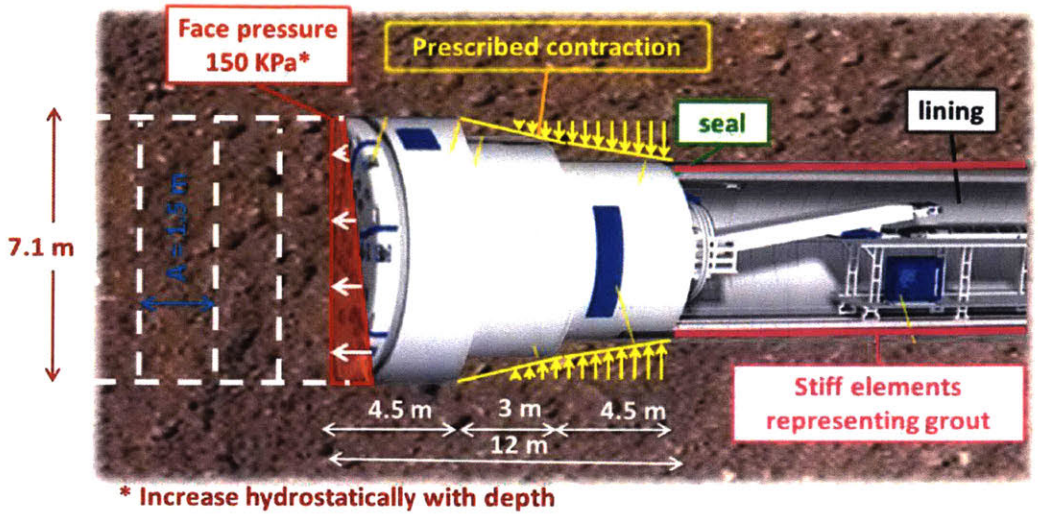

Figure B.12 Altered FE model used for the parametric studies of the grout stiffness

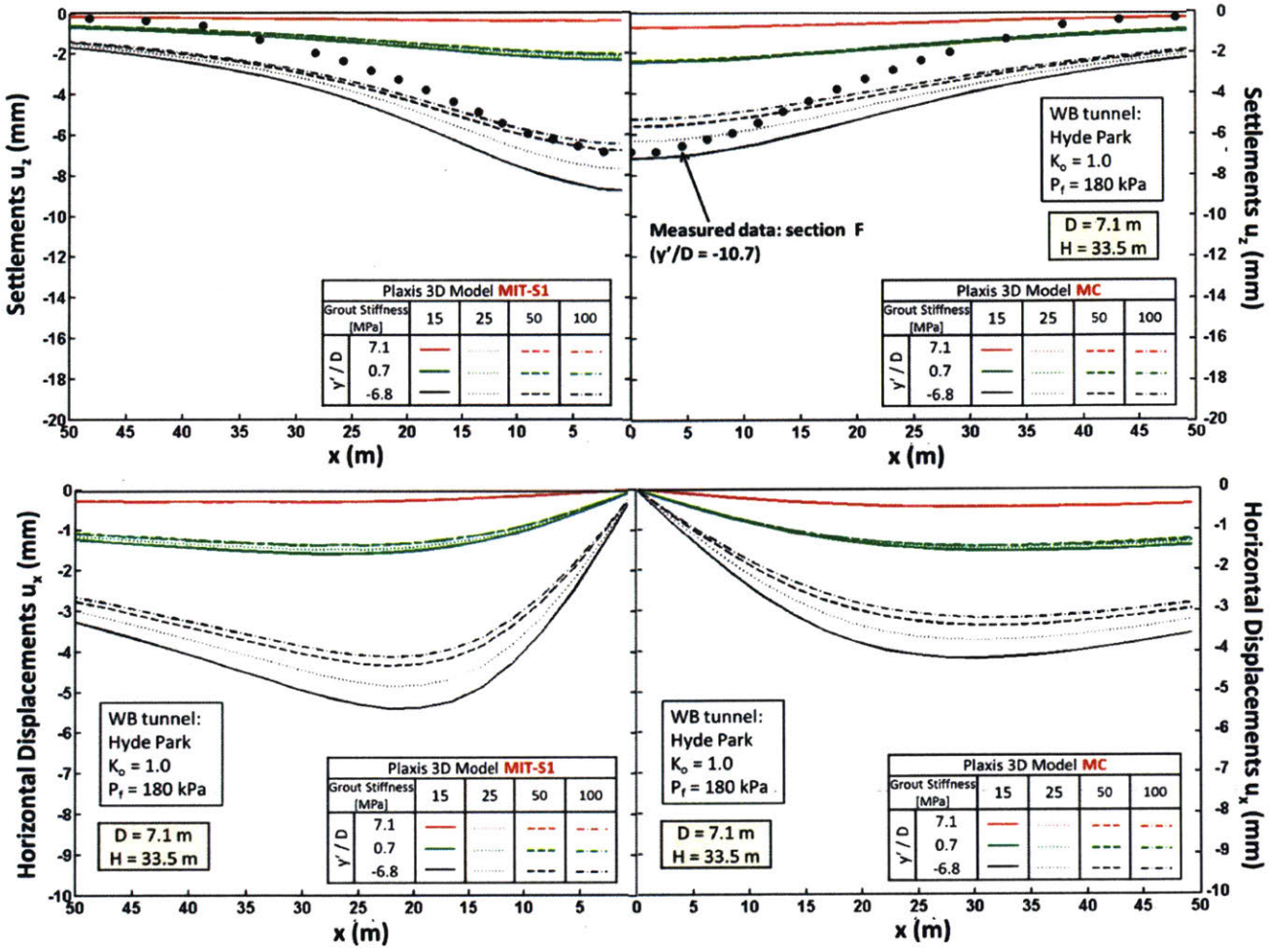

Figure B.13 Comparison of computed surface settlements using MC and MIT-S1 soil models for the FE model for grout stiffness ranging from 15 to 100 MPa.